1995

Wind And Wave Loading On A Compliant Off-shore Tower (theory And Experiment)

Mohammad Taghi Daneshvaran

NOTICE

The quality of this microform is heavily dependent upon the quality of the original thesis submitted for microfilming. Every effort has been made to ensure the highest quality of reproduction possible.

If pages are missing, contact the university which granted the degree.

Some pages may have indistinct print especially if the original pages were typed with a poor typewriter ribbon or if the university sent us an inferior photocopy.

Reproduction in full or in part of this microform is governed by the Canadian Copyright Act, R.S.C. 1970, c. C-30, and subsequent amendments.

AVIS

La qualité de cette microforme dépend grandement de la qualité de la thèse soumise au microfilmage. Nous avons tout fait pour assurer une qualité supérieure de reproduction.

S'il manque des pages, veuillez communiquer avec l'université qui a conféré le grade.

La qualité d'impression de certaines pages peut laisser à désirer, surtout si les pages originales ont été dactylographiées à l'aide d'un ruban usé ou si l'université nous a fait parvenir une photocopie de qualité inférieure.

La reproduction, même partielle, de cette microforme est soumise à la Loi canadienne sur le droit d'auteur, SRC 1970, c. C-30, et ses amendements subséquents.

Canada

Wind and Wave Loading on a Compliant Off-Shore Tower (Theory and Experiment)

by
Mohammad Taghi Siamak Daneshvaran

Faculty of Engineering Science
Department of Civil Engineering

Submitted in partial fulfillment
of the requirements for the degree of
Doctor of Philosophy

Faculty of Graduate Studies
The University of Western Ontario
London, Ontario
March, 1995

Name Mohammad T. Siamak Daneshvaran

Dissertation Abstracts International is arranged by broad, general subject categories. Please select the one subject which most nearly describes the content of your dissertation. Enter the corresponding four-digit code in the spaces provided.

Engineering (Civil)
SUBJECT TERM

0543
SUBJECT CODE

U·M·I

Subject Categories

THE HUMANITIES AND SOCIAL SCIENCES

COMMUNICATIONS AND THE ARTS
- Architecture 0729
- Art History 0377
- Cinema 0900
- Dance 0378
- Fine Arts 0357
- Information Science 0723
- Journalism 0391
- Library Science 0399
- Mass Communications 0708
- Music 0413
- Speech Communication 0459
- Theater 0465

EDUCATION
- General 0515
- Administration 0514
- Adult and Continuing 0516
- Agricultural 0517
- Art 0273
- Bilingual and Multicultural 0282
- Business 0688
- Community College 0275
- Curriculum and Instruction 0727
- Early Childhood 0518
- Elementary 0524
- Finance 0277
- Guidance and Counseling 0519
- Health 0680
- Higher 0745
- History of 0520
- Home Economics 0278
- Industrial 0521
- Language and Literature 0279
- Mathematics 0280
- Music 0522
- Philosophy of 0998
- Physical 0523
- Psychology 0525
- Reading 0535
- Religious 0527
- Sciences 0714
- Secondary 0533
- Social Sciences 0534
- Sociology of 0340
- Special 0529
- Teacher Training 0530
- Technology 0710
- Tests and Measurements 0288
- Vocational 0747

LANGUAGE, LITERATURE AND LINGUISTICS
- Language
  - General 0679
  - Ancient 0289
  - Linguistics 0290
  - Modern 0291
- Literature
  - General 0401
  - Classical 0294
  - Comparative 0295
  - Medieval 0297
  - Modern 0298
  - African 0316
  - American 0591
  - Asian 0305
  - Canadian (English) 0352
  - Canadian (French) 0355
  - English 0593
  - Germanic 0311
  - Latin American 0312
  - Middle Eastern 0315
  - Romance 0313
  - Slavic and East European 0314

PHILOSOPHY, RELIGION AND THEOLOGY
- Philosophy 0422
- Religion
  - General 0318
  - Biblical Studies 0321
  - Clergy 0319
  - History of 0320
  - Philosophy of 0322
- Theology 0469

SOCIAL SCIENCES
- American Studies 0323
- Anthropology
  - Archaeology 0324
  - Cultural 0326
  - Physical 0327
- Business Administration
  - General 0310
  - Accounting 0272
  - Banking 0770
  - Management 0454
  - Marketing 0338
- Canadian Studies 0385
- Economics
  - General 0501
  - Agricultural 0503
  - Commerce-Business 0505
  - Finance 0508
  - History 0509
  - Labor 0510
  - Theory 0511
- Folklore 0358
- Geography 0366
- Gerontology 0351
- History
  - General 0578
  - Ancient 0579
  - Medieval 0581
  - Modern 0582
  - Black 0328
  - African 0331
  - Asia, Australia and Oceania 0332
  - Canadian 0334
  - European 0335
  - Latin American 0336
  - Middle Eastern 0333
  - United States 0337
- History of Science 0585
- Law 0398
- Political Science
  - General 0615
  - International Law and Relations 0616
  - Public Administration 0617
- Recreation 0814
- Social Work 0452
- Sociology
  - General 0626
  - Criminology and Penology 0627
  - Demography 0938
  - Ethnic and Racial Studies 0631
  - Individual and Family Studies 0628
  - Industrial and Labor Relations 0629
  - Public and Social Welfare 0630
  - Social Structure and Development 0700
  - Theory and Methods 0344
- Transportation 0709
- Urban and Regional Planning 0999
- Women's Studies 0453

THE SCIENCES AND ENGINEERING

BIOLOGICAL SCIENCES
- Agriculture
  - General 0473
  - Agronomy 0285
  - Animal Culture and Nutrition 0475
  - Animal Pathology 0476
  - Food Science and Technology 0359
  - Forestry and Wildlife 0478
  - Plant Culture 0479
  - Plant Pathology 0480
  - Plant Physiology 0817
  - Range Management 0777
  - Wood Technology 0746
- Biology
  - General 0306
  - Anatomy 0287
  - Biostatistics 0308
  - Botany 0309
  - Cell 0379
  - Ecology 0329
  - Entomology 0353
  - Genetics 0369
  - Limnology 0793
  - Microbiology 0410
  - Molecular 0307
  - Neuroscience 0317
  - Oceanography 0416
  - Physiology 0433
  - Radiation 0821
  - Veterinary Science 0778
  - Zoology 0472
- Biophysics
  - General 0786
  - Medical 0760

EARTH SCIENCES
- Biogeochemistry 0425
- Geochemistry 0996
- Geodesy 0370
- Geology 0372
- Geophysics 0373
- Hydrology 0388
- Mineralogy 0411
- Paleobotany 0345
- Paleoecology 0426
- Paleontology 0418
- Paleozoology 0985
- Palynology 0427
- Physical Geography 0368
- Physical Oceanography 0415

HEALTH AND ENVIRONMENTAL SCIENCES
- Environmental Sciences 0768
- Health Sciences
  - General 0566
  - Audiology 0300
  - Chemotherapy 0992
  - Dentistry 0567
  - Education 0350
  - Hospital Management 0769
  - Human Development 0758
  - Immunology 0982
  - Medicine and Surgery 0564
  - Mental Health 0347
  - Nursing 0569
  - Nutrition 0570
  - Obstetrics and Gynecology 0380
  - Occupational Health and Therapy 0354
  - Ophthalmology 0381
  - Pathology 0571
  - Pharmacology 0419
  - Pharmacy 0572
  - Physical Therapy 0382
  - Public Health 0573
  - Radiology 0574
  - Recreation 0575
  - Speech Pathology 0460
  - Toxicology 0383
- Home Economics 0386

PHYSICAL SCIENCES

Pure Sciences
- Chemistry
  - General 0485
  - Agricultural 0749
  - Analytical 0486
  - Biochemistry 0487
  - Inorganic 0488
  - Nuclear 0738
  - Organic 0490
  - Pharmaceutical 0491
  - Physical 0494
  - Polymer 0495
  - Radiation 0754
- Mathematics 0405
- Physics
  - General 0605
  - Acoustics 0986
  - Astronomy and Astrophysics 0606
  - Atmospheric Science 0608
  - Atomic 0748
  - Electronics and Electricity 0607
  - Elementary Particles and High Energy 0798
  - Fluid and Plasma 0759
  - Molecular 0609
  - Nuclear 0610
  - Optics 0752
  - Radiation 0756
  - Solid State 0611
- Statistics 0463

Applied Sciences
- Applied Mechanics 0346
- Computer Science 0984
- Engineering
  - General 0537
  - Aerospace 0538
  - Agricultural 0539
  - Automotive 0540
  - Biomedical 0541
  - Chemical 0542
  - Civil 0543
  - Electronics and Electrical 0544
  - Heat and Thermodynamics 0348
  - Hydraulic 0545
  - Industrial 0546
  - Marine 0547
  - Materials Science 0794
  - Mechanical 0548
  - Metallurgy 0743
  - Mining 0551
  - Nuclear 0552
  - Packaging 0549
  - Petroleum 0765
  - Sanitary and Municipal 0554
  - System Science 0790
- Geotechnology 0428
- Operations Research 0796
- Plastics Technology 0795
- Textile Technology 0994

PSYCHOLOGY
- General 0621
- Behavioral 0384
- Clinical 0622
- Developmental 0620
- Experimental 0623
- Industrial 0624
- Personality 0625
- Physiological 0989
- Psychobiology 0349
- Psychometrics 0632
- Social 0451

ABSTRACT

The compliant tower is a slender jacket type structure which falls in the category of compliant platforms and is suited to deep water situations. Towers of this type resist the static loads through their stiffness while the first order wave loads are resisted primarily by inertia. Their typical first natural period is around 30 to 40 seconds and the second natural period is about 3 seconds so there would be little amplification of the response due to the first order wave forces. There is, however, dynamic amplification of the response due to the turbulent wind and nonlinear wave forces including the second order drift forces, and this response is significantly affected by the wave/motion induced drag damping.

This thesis investigates the importance of wind and wave loads on the model of a typical compliant tower. Numerical models both in frequency and time domains were developed to predict the response characteristics of the tower to the action of wave, wind and wind induced currents. The wave-structure interaction was incorporated using a modified form of the Morison equation.

In the first series of experiments, using a surface piercing cylinder supported from a heavy three point pendulum moving just above the water surface, the force and displacement time histories (free vibration) were recorded and the amplitude dependent damping forces were evaluated. Based on these experiments, the modified forms of the Morison's equation (relative velocity model and independent flow fields model) were used to derive the values of the force coefficients, C_D,C_M, and hydrodynamic damping. The experiment covered the structural oscillation in still water, and a variety of both regular and random waves. This work is believed to be the first which obtains the values of the drag coefficient in the case of structural motion in the presence of waves, and compares the results for both forms of the Morison's equation. These results are later used as input to the dynamic analyses performed in the last stage of this work.

The importance of second order drift forces including the free surface effect and bounded long waves were examined through another series of laboratory experiments. The drift forces on a surface piercing cylinder were measured and the results compared to different theoretical models. It was concluded that, in a deep water situation, it is the free surface effect which is responsible for most of the observed drift forces and the contribution of the bounded long waves is not significant.

The results obtained from above studies were employed to predict the response of the scaled model (1:150) of a simple cantilever compliant tower to different wind/wave states in both frequency domain (linearized load) and time domain (with and without the inclusion of the free surface drift forces). The theoretical response is then compared with the experimental results obtained in the wind/wave tank facility where the model was subjected to the combined action of the scaled random wave and wind loadings. The results obtained from the numerical simulations and experimental measurements compared well. The time domain results indicated that the inclusion of the free surface drift force in the numerical model improves the quality of the prediction in most cases. The significance of this force increases as the fundamental period of the structure increases. This study is believed to be the first to implement the contribution of the wind gust and second order drift forces in a numerical model where the numerical results are compared to experimental results obtained in a wind/wave facility.

Acknowledgements

I would like to express my gratitude to every one at the Boundary Layer Wind Tunnel Laboratory - faculty, staff, and students.

My sincere gratitude and appreciation goes to my supervisor Dr. Barry Vickery from whom I learned many things. His guidance, encouragement and most important of all, his tremendous support are deeply appreciated. His ability to find effective engineering solutions to complicated problems always amazes me.

I would also like to thank Mr. T. Eddy, Manager of the Boundary Layer Wind Tunnel Laboratory for his computer support. Mr. R. Morden was very helpful and his dexterity in computer programming always rescued me.

Mr. M. Young is also thanked for proofreading of this work. Technical support of Mr. J. Dafoe during the experimental part of this work is appreciated.

Above all, I thank my family here and back home, and very especially my wife, Maryam. She managed to work as a housewife, take care of our daughter, Saina, and at the same time study as a graduate student. I thank her for her support and understanding.

To the memory of my father Reza,
To my wife Maryam,
and my children Saina and Sina Daneshvaran

TABLE OF CONTENTS

LIST of APPENDICES

LIST of FIGURES

LIST of TABLES

CHAPTER 1

INTRODUCTION

1.1 Background

An offshore structure can be defined as one which has no fixed access to dry land and which is required to stay in position in all weather conditions. Most of them are used for the extraction and production of oil and gas from beneath the sea floor , but tl ere are some which are designed for deriving power from the sea .

Understanding about wave and wind induced loads, and resulting motions of offshore structures is important both in design and operational studies. In a hostile area like the North Sea, the significant wave height is larger than 2 m for 60 percent of the time. The mean wave period can range between 15 and 20 second in an extreme wave condition, and during most operational conditions the mean wave period is greater than 4 seconds. Environmental loads due to wind and current are also important. Extreme mean wind velocities about 40 to 45 m/s should be used in the design of an offshore structure in the North Sea. In spite of the knowledge and experience gained during the previous decade, the knowledge of some of the fundamental aspects of the wave loading mechanism is incomplete. Sometimes researchers are forced to resort to empirical and experimental approaches in order to validate results from mathematical model.

Furthermore, the experimental approach can sometimes lead to faster and more economical solutions compared to those obtained using mathematical solutions. On the other hand, one should be careful when applying results obtained from model studies to the full scale, due to their limited range of validity.

In brief, wind-wave testing facilities can be extremely valuable when used as a cross check for engineering predictions of response of offshore structures subjected to wind and wave loadings.

1.2 Classification of Compliant Offshore Platforms

With the recent technology and the need to search for oil and gas in increasingly deeper water, the requirement to develop deep water platform structures is steadily increasing. Economically , the classical stiff jacket type or gravity type structures are not suitable for deep seas and the compliant type structures are better economical alternatives. These structures are designed to resist the environmental loads through their inertia rather than their stiffness. Their fundamental periods of vibration are in the range of 30 to 100 seconds, these periods are longer than those associated with waves even in extreme weather situations, and as such there is little or no dynamic amplification of the response due to resonance.

Figure 1.1 compares the frequency ranges of different offshore platforms compared to the wind and waves. While first order wave forces do not cause dynamic response amplification in compliant structures, second and third order (wave drift and sum frequency) wave loads and wind loads can be important due to their dynamic magnification effects.

1.2.1 Compliant Tower

Historically compliant towers have been designed in several forms by different companies which can be classified as free standing guyed towers and flexible towers.

In this thesis the flexible compliant tower is considered. The typical structure studied herein has a period of 32 seconds. An example of the flexible compliant platform is the ROSEAU tower designed by E.T.P.M (Andrier et al., 1986). Figure 1.2 shows the general features and overall dimensions of the ROSEAU tower. It is designed for a 600 meter deep water in the gulf of Mexico. The base is rigidly anchored to the sea floor by piles. Most of the inertia of the structure is associated with the added mass produced by the water trapped in the stabilizer section, installed near the node of the second vibration mode. In this way the second natural frequency can be increased and moved to the right hand side of the wind and wave spectra to reduce resonance associated with first order wave load. During this study in order to simplify modelling and attain more accurate results on a slender structure, the proposed typical structure is designed without the stabilizer feature, and yet the structure has fist and second natural periods of vibration of 32s and 2.8s respectively.

The flexible tower has some advantages over the guyed type because it does not need guylines, and associated joint articulation problems, and has smaller displacements at the top mode level. Furthermore, the rigid clustered pile system at the sea bed reduces the localised bending of the conductors.

1.2.2 Tension Leg Platform

The tension leg platform is another type of compliant structure which is very useful in deep waters. It is restrained from oscillating vertically by pretensioned tethers. These are vertical anchorlines that are tensioned because platform buoyancy exceeds the platform weight. The T.L.P is compliant in the horizontal plane but quite stiff in the vertical direction.

These structures are economically viable because cost is only weakly dependent on water depth. One existing example is the six column Hutton T.L.P located in the North Sea in a water depth of 150 meters.

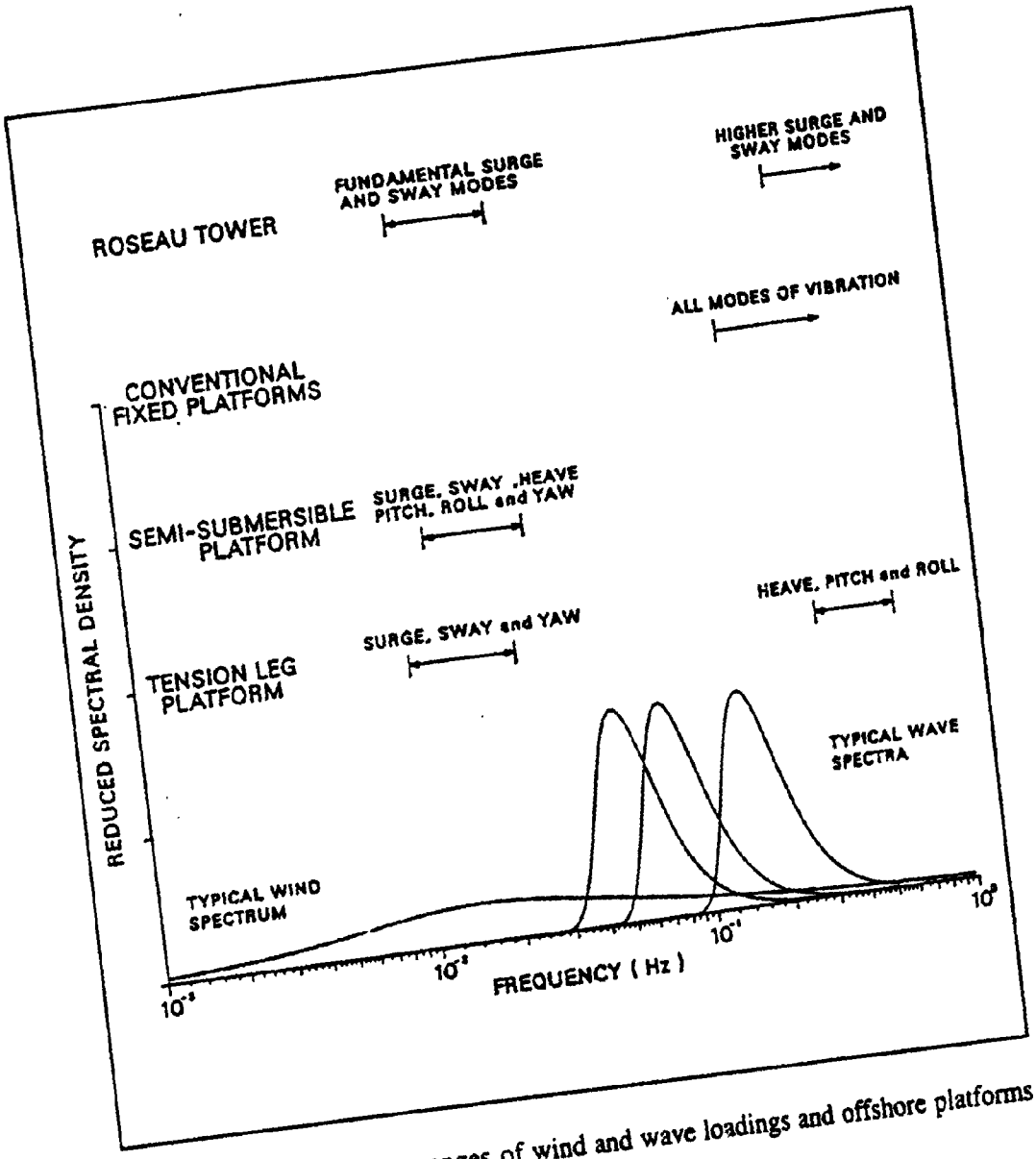

FIGURE 1-1: Frequency ranges of wind and wave loadings and offshore platforms (from Vickery, P.J. 1988).

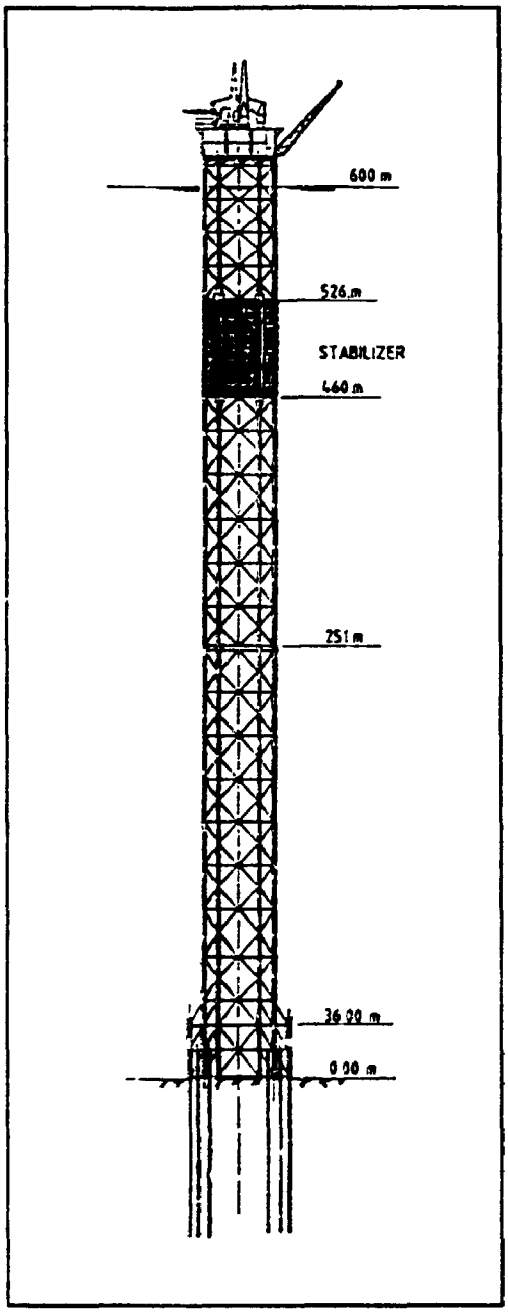

FIGURE 1-2: Roseau Platform in 600 m water (from Andrier, et al. 1986).

1.2.3 Semi-Submersible Platform

The semi-submersible platform is a free floating structure, kept in position by a spread mooring system (an alternative can be to use thrusters and a dynamic positioning system). This structure is compliant in all of it's degrees of freedom and can be mobile. Semi submersibles are able to withstand severe weather conditions relatively well and are capable of operating at depths up to about 300 meters.

1.3 Preview of The Thesis

The idea of the thesis is to study the drag and inertia type loading on a slender structure which is a scaled model of a typical compliant tower. The thesis investigates the effect of the nonlinear drag loading in both regular and random seas through the use of the Morison type relationship between velocities and load.

In the case of a structure oscillating in waves, usually a modified form of the Morison equation is used and the force coefficients are evaluated from fixed cylinder in waves or from surge tests. However due to the interaction between the cylinder motion and fluid motion it is not always appropriate to use these types of test to evaluate the force coefficient in a design situation (Moe,Verley, 1980; Bearman, et al, 1992).

The effect of the structural motion in still water and regular and random waves and the corresponding hydrodynamic damping is examined through the use of a surface piercing cylinder supported from a heavy parallel pendulum system moving just above the water surface. The drag coefficients were evaluated using the two different forms of the

modified Morison's equation (relative velocity and independent flow fields model) using both damping traces and by matching of the measured and computed force time histories. The effect of wave grouping on the low frequency drag type free surface forcing on a slender cylinder in bichromatic and random seas using different model extensions of Airy's linear wave theory and Stokes second order theory is discussed, and a theoretical high order model is developed. Using this model, numerical results are compared with experimental results obtained from experiments performed in the Wave Tank Facility at the Boundary Layer Wind Tunnel Laboratory at the University of Western Ontario. The model is based on the Chakrabarti's second order expansion (Connor, Gudmestad, 1986) for regular waves and it's accuracy in velocity prediction is confirmed using recent doppler velocimeter measurements (Bosma, Vugts, 1981).

Bounded long waves (subharmonics) are also investigated, and their contribution to the low frequency high order (2nd,3rd order) drag forcing is compared to the free surface low frequency force estimate. The effect of the free subharmonics generated by a first order wave signal at the wave tank (laboratory model) is also discussed.

The response of the scale model compliant tower to different wind-wave sea states is numerically predicted in both the frequency domain (linearized load) and the stochastic time domain where the nonlinear coupled drag force is considered, including the second order free surface effects. Finally the theoretical response predictions are compared to the experimental results obtained in the Wind Wave Testing Facility. The frequency domain solution follows the method suggested by Malhotra,Penzien (1970); Wu, McDermott (1976), where a uniform current field has been superimposed on the wave field. The time domain analysis model as given by Dao, Penzien (1980), and Andrier et al (1986) does not consider the free surface effects or wind loading. The time domain results given by Ng (1988) also do not consider the splash zone effects. In both of the models developed

in this study (frequency domain and time domain) the contribution of the wind loading to the response, estimated using the ESDU models of atmospheric turbulence (1985), is investigated.

This study is believed to be the first to suggest a model for the low frequency forcing in bichromatic and narrow-banded waves where the results are validated through comparison with the experimental results. The derivation of hydrodynamic damping and drag coefficients based on the reduced velocity and independent flow fields models, and the correlation of the results from both damping trace and matching of the force time history was satisfactory and is believed to be the first study to compare such results.

CHAPTER 2

GRAVITY WAVES, WIND AND THEIR LOADING

2.1 INTRODUCTION

In this chapter, a review of wind generated waves, wave theories, wave loading on slender bodies, and wind effects over ocean structures will be presented.

Wind is regarded as a random process and its structure is described using statistical methods. Wind speed can be treated as the superposition of a steady (mean) component and a zero mean turbulent component. The turbulent characteristics are explained using both single and multiple point statistics. The wind model used in this study employs the ESDU (1985a,b) data which rely on a series of world wide measurements for homogeneous terrains, and uses a form of Von Karman spectrum in the description of wind turbulence.

For the wind generated waves, the energy balance equation can be represented by three terms describing the energy input from the atmosphere, the transfer due to nonlinear wave to wave interactions and dissipation which is mainly due to wave breaking. The wind waves generated from this energy balance have periods in the range of 2 to 20 seconds.

The process of wind wave interaction is complicated and a complete mathematical description of the phenomenon does not exist, however, by using some reasonable assumptions it is possible to deal with these waves.

The wave loading on a slender cylinder is discussed using different extensions of linear wave theory (including second order models), group induced free surface forces in bichromatic and random waves are estimated. Contribution of free surface effects

(sharpening of the crest and shallowing of the trough), in regular waves is discussed. Generation of bounded and parasitic long waves (second order incident group induced waves) in physical models are reviewed. Their relative importance in deep water modelling carried out in this study is approximately examined (chapter 4). Finally, using order of magnitude analysis, the contribution of (natural) bounded long waves to the drag loading on a slender cylinder is compared to that due to the free surface effect.

2.2 REGULAR WAVE THEORY

There exists a number of wave theories which have been developed to cope with different conditions depending on wave height, period, and water depth.
Generally a boundary value problem (BVP) consisting of a partial differential equation and some specific boundary conditions related to the geometric boundaries of the problem must be solved. As will be explained in the next paragraphs, it is not, in general, possible to solve the complete boundary value problem, and some assumptions need to be made in order to solve the problem.

One of the approximate analytical methods for solving such a boundary value problem is the perturbation method which has different levels of approximation and leads to a closed form solution, where other quantities including water particle kinematics and pressure fields are provided. In perturbation methods, results of the first order solution (Airy wave theory) is required to enable the second order solution to be obtained (Stokes second order), etc.

It is assumed that the water is inviscid and incompressible and the flow is irrotational. The wave motion is 2-D (long crested) and takes place in the x-z plane with x axis along the mean water level and the z axis vertically upward. The ocean floor is flat

with the undisturbed depth of d. The waves are progressive in the positive x direction. Since the flow is irrotational, the problem is to determine the velocity potential ϕ (or equivalently stream function ψ) in the fluid domain. If the free surface is given by $z=\eta(x,t)$, then the boundary value problem in the 2-D case can be summarized as follows:

The Laplace equation which is a result of the continuity equation:

$$\nabla^2\phi=0 \qquad -d<z<\eta(x,t)$$
$$\nabla^2=\frac{\partial^2}{\partial x^2}+\frac{\partial^2}{\partial z^2} \tag{2.1}$$

where:

$$w=\frac{\partial\phi}{\partial z} \qquad \textit{velocity component , z direction}$$
$$u=\frac{\partial\phi}{\partial x} \qquad \textit{velocitycomponent , x direction} \tag{2.2}$$

The bottom boundary condition is:

$$\frac{\partial\phi}{\partial n}=\frac{\partial\phi}{\partial z}=0 \qquad \textit{at } z=-d \tag{2.3}$$

Where n is the normal to the bottom surface.

The free surface boundary condition is:

$$\frac{\partial\phi}{\partial t}=-g\eta-\frac{1}{2}(\nabla\phi)^2 \qquad \textit{on } z=\eta(x,t)$$
$$\frac{\partial\eta}{\partial t}+\frac{\partial\phi}{\partial x}\frac{\partial\eta}{\partial x}-\frac{\partial\phi}{\partial z}=0 \qquad \textit{on } z=\eta(x,t) \tag{2.4}$$

The first of the free surface boundary conditions expresses the continuity of pressure across the surface and the second expresses that there is no mass flux through the surface, or a fluid particle when on the surface, will remain there.

The solution of the complete problem is difficult since the free surface boundary conditions are nonlinear and would be satisfied on the unknown $z=\eta(x,t)$ which is always changing.

Using a Taylor's series to expand the free surface boundary conditions from the exact free surface to the plane z=0 (which is known), and using the perturbation method it is possible to break the problem in to the 1st, 2nd, ... orders. The first order solution (also known as Airy wave theory) is based on the assumption that the wave height is small compared to the wave length or water depth. It is a linearized solution and satisfies the free surface boundary conditions at the mean water level z=0. The second order solution is called stokes wave theory which satisfies the second order free surface boundary conditions on the mean water level. The perturbation parameter in the expansion is a small nondimensional parameter which in this case is wave slope $\varepsilon=kH/2$ (k is the wave number).

$$\phi = \sum_{n=1}^{N} \varepsilon^n \phi^{(n)}$$
$$\eta = \sum_{n=1}^{N} \varepsilon^n \eta^{(n)} \qquad (2.5)$$

Where $\phi^{(n)}$, $\eta^{(n)}$ are the nth order velocity and surface elevation approximations.

Substituting for ϕ and η from equation 2.5 into the above boundary value problem, yields:

$$\begin{aligned} \nabla^2\phi^{(1)} &= 0 \\ \frac{\partial\phi^{(1)}}{\partial z} &= 0 \\ \frac{\partial\eta^{(1)}}{\partial t} - \frac{\partial\phi^{(1)}}{\partial z} &= 0 \\ \frac{\partial\phi^{(1)}}{\partial t} + g\eta^{(1)} &= 0 \qquad on\ z=0 \end{aligned} \tag{2.6}$$

The two free surface conditions may be combined in to one (Poisson equation) by eliminating $\eta^{(1)}$ as follows:

$$\frac{\partial^2\phi^{(1)}}{\partial t^2} + g\frac{\partial\phi^{(1)}}{\partial z} = 0 \qquad on\ z=0 \tag{2.7}$$

The solution to the first order boundary value problem (equations 2.6,2.7) results in the velocity potential $\phi^{(1)}$:

$$\phi^{(1)} = \frac{gH}{2\omega}\frac{\cosh(k(z+d))}{\cosh(kd)}\sin(kx-\omega t) \tag{2.8}$$

where ω,k,H are the wave angular frequency, wave number and wave height respectively. The first order dispersion relation is

$$\omega^2 = kg\tanh(kd) \tag{2.9}$$

and the wave celerity is

$$C = \frac{\omega}{k} \tag{2.10}$$

The second order boundary value problem can be derived by the substitution of equation 2.5 up to order n=2 into equations 2.1 to 2.4. This approach assumes that the second order terms are one order of magnitude smaller than the first order terms and it is valid (convergence) when $H/d<<(kd)^2$, $H/L<<1$, and $kd<1$ (Chakrabarti, 1987). These conditions limit the validity of the second order approximation for shallow water situations.
The second order dispersion relation is the same as the first order one (As will be explained later).

Plane progressive waves in deep water are of particular interest in this thesis and in this case the first order velocity potential is a solution of the second order boundary value problem:

$$\phi = \frac{gH}{2\omega} \exp(kz) \sin(kx-\omega t) + O(\varepsilon^3) \qquad (2.11)$$

where O stands for order.
Substitution of ϕ in to the second order boundary value problem results in a second order wave elevation given as:

$$\eta = \frac{H}{2} \cos(kx-\omega t) + \frac{kH^2}{8} \cos 2(kx-\omega t) + O(\varepsilon^3) \qquad (2.12)$$

The second term is a nonlinear correction to the linear sinusoidal waves and is positive at wave crest area and negative at wave troughs so the crests will be steeper and the troughs will be shallower.

Based on the extension of linear theory, several engineering approximations are also available which give more favourable results. Among them is Chakrabarti's second order

method (Gudmestad, Connor, 1986) which is also hydrodynamically correct, and is used in this work to calculate the wave forces up to the free surface level.

2.3 STATISTICAL DESCRIPTION OF RANDOM WAVES

Ambient waves on the surface of the ocean are not only dispersive, but random. The generating mechanism is the wind on the water surface. The wind itself is random, when looked from the point of view of turbulent fluctuations and eddies which are important in generating waves. The randomness of ocean waves is then increased by their propagation over large distances in space and time, thus ocean waves must be described by their statistical properties.

The mechanism describing how energy and momentum in wind is transferred to sea waves is not a subject of immediate concern to the ocean engineers, but since it is at the root of the wave forecasting problem, it ultimately has an important effect on practical problems.

In practice, linear theory is often used to simulate irregular seas and to obtain statistical estimates of wave kinematics. If the irregular sea is assumed to be comprised of an infinite sum of sinusoidals, each of them associated with an independent random phase angle, then the use of central limit theorem indicates that the instantaneous wave elevation will be Gaussian. The wave elevation of the long crested irregular sea, which propagates in the positive x direction can then be written as:

$$\eta(t) = \sum_{i=1}^{N} A_i \sin(\omega_i t - k_i x + \phi_i) \qquad (2.13)$$

where $A_i, \omega_i, k_i, \phi_i$, and N are correspondingly the wave amplitude, frequency, wave number, random phase angle and number of components used in the analysis.

The random phase angles are uniformly distributed between 0 and 2π and are constant

with time. The wave amplitudes A_i are derived from the wave spectrum S(f) as:

$$A_i = \sqrt{2S(f_i)\Delta f} \tag{2.14}$$

where Δf is the frequency increment (resolution).

Since the instantaneous wave elevation is a zero mean Gaussian process, the variance when N goes to ∞ is:

$$\sigma^2 = \int_0^\infty S(f)\,df \tag{2.15}$$

The relationship between a time domain and a frequency domain representation of the waves is shown in Figure 2.1.

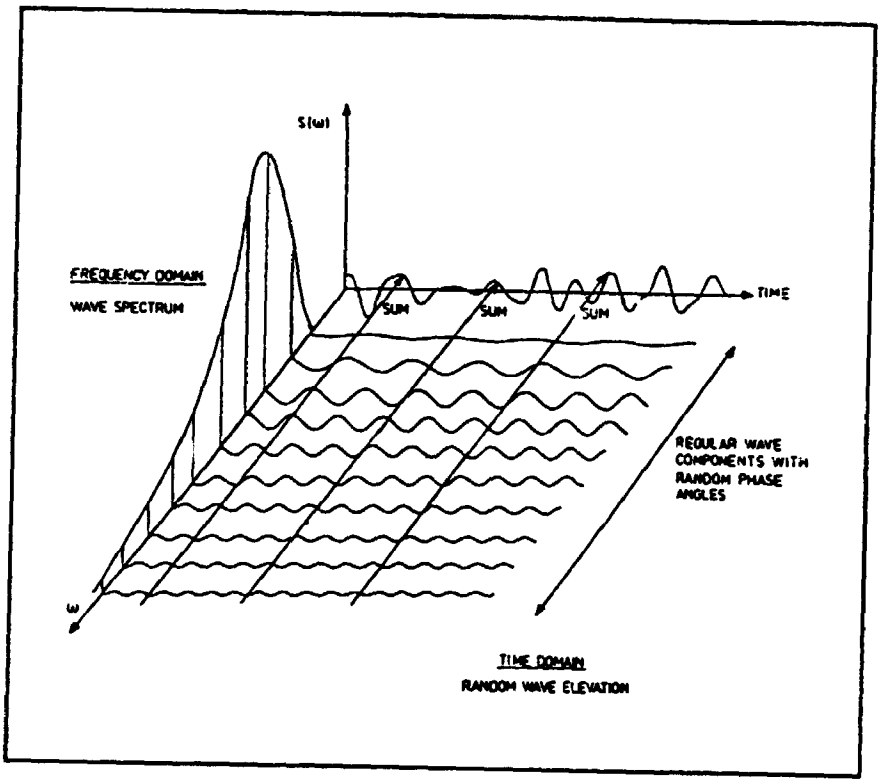

FIGURE 2.1: Relation between time domain and frequency domain representations of a long crested sea (from Faltinsen, 1990).

2.3.1 SHORT TERM STATISTICS

The wave spectrum can be obtained from wave measurements by different devices. The short term description of the sea is the basic input required to determine the response of a marine structure, and is a period of time short enough to make it possible to describe the sea as a stationary random process. The statistical properties of the sea may be regarded as constant over a period of time in the range of half an hour to 10 hours during which the significant wave height Hs (the mean of the highest one third of wave heights in a record) and mean wave period are constant. In this manner a sea can be simulated by the use of equation 2.13. This time history repeats itself every $1/\Delta f$ seconds. To prevent this repeatability a large number of components N is required. The approach taken in this study to eliminate the repeating wave train uses a random frequency at each frequency interval ($fi-\Delta f/2, fi+\Delta/2$), and then calculates S(f) at this frequency. The number of wave components should be about 800 or more depending on the minimum and maximum frequencies in the spectrum.

The selection of the minimum frequency is easy and depends on the spectrum but in general is about $f_{min}=f_z/2$ where f_z is the mean wave frequency defined as (Faltinsen, 1990):

$$f_z = \left(\frac{m_2}{m_0}\right)^{0.5}$$

$$m_i = \int_0^\infty f^i S(f)\, df \qquad (2.16)$$

For the maximum frequency, due to a slower rate of energy drop at higher frequency range, it would be an iterative procedure to find fmax and to make sure that the result do not depend on the selection of fmax.

2.3.1.1 WAVE SPECTRA

The mathematical formulation commonly used is of the general format shown as:

$$S_{\eta}(\omega) = a\omega^{-m}\exp[-a\omega^{-n}] \qquad (2.17)$$

where a,m,n are parameters of the spectrum.

The most common spectra models are P-M (Pierson-Moskowitz), Bretschneider, ISSC (International ship and offshore structures congress), ITTC (International towing tank conference), and the JONSWAP (joint North sea wave project).

The P-M energy spectrum was proposed in 1964 by Pierson & Moskowitz based on similarity theory of Kitaigorodskii and some measured data. It describes a fully developed fetch unlimited sea and its only parameter is the wind velocity.

The assumptions made on this spectrum are that wind is blowing on a large area for many hours with a constant speed. It is expressed as

$$S_{\eta\eta}(f) = \alpha g^2\omega^{-5}\exp[-0.74(\frac{\omega U_{wi}}{g})^{-4}] \qquad (2.18)$$

where α =0.0081, $S(f)=2\pi S(\omega)$.

Or expressing it in terms of peak frequency f_p (mode):

$$S_{\eta\eta}(\omega) = \alpha g^2 \omega^{-5} \exp\left[-1.25\left(\frac{\omega}{\omega_0}\right)^{-4}\right]$$

$$\omega_0 = \frac{0.877 g}{U_{w1}}$$

U_{wi} is the wind speed measured at 19.5 meters above sea level.

In this model, the wave celerity at the peak frequency is almost equal to the mean wind speed (the sea is assumed to be fully developed).

Bretschneider (1959,1969) reported another form for the spectral model:

$$S_{\eta\eta}(f) = \frac{H_s^2}{4\pi T_z^4 f^5} \exp\left[-\frac{1}{\pi}(fT_z)^{-4}\right] \qquad (2.20)$$

$$T_z = \left(\frac{m_0}{m_2}\right)^{0.5}$$

This model is also derived for a fully developed sea. It should be noted that although the above two spectral models are based on a fully developed condition.

Also the following empirical hindcasting equations has been given by Bretschneider (1959):

1-For the fully developed sea the relations are:

$$\frac{gH_s}{U_\omega^2} = 0.282 \qquad (2.21)$$

$$\frac{gT_s}{U_{w1}} = 6.776$$

2-For the partially developed sea:

$$\frac{gH_s}{U_\omega^2}=0.254$$
$$\frac{gT_s}{U_{w1}}=4.764 \qquad (2.22)$$

So knowing the mean wind speed at the level of 19.5 meter, the significant wave height and significant wave period (T_s=0.946T_p) can be defined for later use in a Bretschneider spectrum.

The 17th ITTC recommended the use of JONSWAP spectrum for limited fetch cases. It was developed from measurements made off the island of Sylt in the German Bight of the north sea (Hesslemann et al 1973). The spectrum has a variably higher but a narrower peak than the P-M and Bretschneider spectrum. The narrower peak in this spectrum is achieved by a frequency dependent factor that multiplies the spectral ordinate of the P-M/Br. form of equation. This model was employed in the theoretical and experimental course of this work and will be explained in Chapter 3.

Sometimes the effect of short-crestedness may be important. In this case the waves have directional characteristics in terms of the mean direction and the spread about the mean. Theoretically both mean direction and spreading function are frequency dependent, but in practice the 2-D wave spectrum is written as:

$$S_{\eta\eta}(f,\theta)=S_{\eta\eta}(f)\,G(\theta) \qquad (2.23)$$

Where θ is the direction of wave propagation in the sea.

Usually the mean direction is considered constant for all frequencies and a spreading function of the following form will be used:

$$G(\theta) = K(s)\cos^{2s}\left[\frac{1}{2}(\theta-\bar{\theta})\right] \quad for\ -\frac{\pi}{2} \le \theta \le \frac{\pi}{2} \tag{2.24}$$

where $\bar{\theta}$ corresponds to the mean wave propagation direction and K(s) is defined so that:

$$\int_{-\frac{\pi}{2}}^{\frac{\pi}{2}} S_{\eta\eta}(f,\theta)\,d\theta = S_{\eta\eta}(f)$$

$$or \tag{2.25}$$

$$\int_{-\frac{\pi}{2}}^{\frac{\pi}{2}} G(\theta)\,d\theta = 1.$$

Which leads to

$$K(s) = \frac{1}{2\sqrt{\pi}}\,\frac{\Gamma(s+1)}{\Gamma(s+\frac{1}{2})} \tag{2.26}$$

and Γ is the gamma's function.

It should be mentioned that spreading can cause an important reduction in the wave loading.

A narrow-banded spectrum is an spectrum whose energy is concentrated over a narrow

range of frequencies. The wave time history resembles that of a slowly varying group. A good approximation to the probability distribution function for the wave amplitudes (maxima) in the time history of a narrow banded Gaussian wave elevation, is the Rayleigh distribution

$$P(A) = \frac{A}{m_0} \exp\left(\frac{-A^2}{2m_0}\right) \tag{2.27}$$

In describing ocean waves usually wave height, H, is used instead of amplitude, A, and the above equation can easily be converted to a wave height distribution using:

$$H_{rms} = 2\sqrt{2m_0} = 2\sqrt{2}\,\sigma_\eta \tag{2.28}$$

where σ_η is the rms of wave elevation. Then P(H) is:

$$P(H) = \frac{2H}{H_{rms}^2} \exp\left(-\frac{H^2}{H_{rms}^2}\right) \tag{2.29}$$

also using this density function the relationship between significant wave height and Hrms may be obtained as:

$$H_s = 1.414 H_{rms} = 4\sigma_\eta \tag{2.30}$$

Some examples of wave elevation simulated from the same spectrum and duration are shown in Figure 2.2. It is seen that the largest amplitude in each time history (A_{max}) is different. When selecting a large number of such time histories it can be stated that these extreme values have their own probability distribution (Ochi, 1982). Practically the

expected A_{max} can be approximated as:

$$A_{max} = (2m_0 Ln\frac{t}{T_z})^{0.5} \qquad (2.31)$$

where T_z is the mean wave period as defined before (mean zero crossing period) and Ln is the natural logarithm.

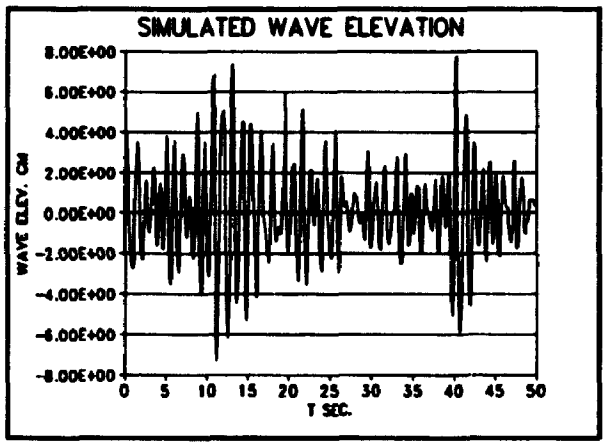

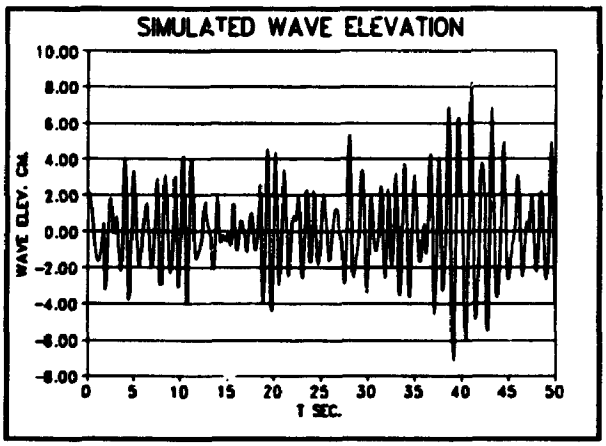

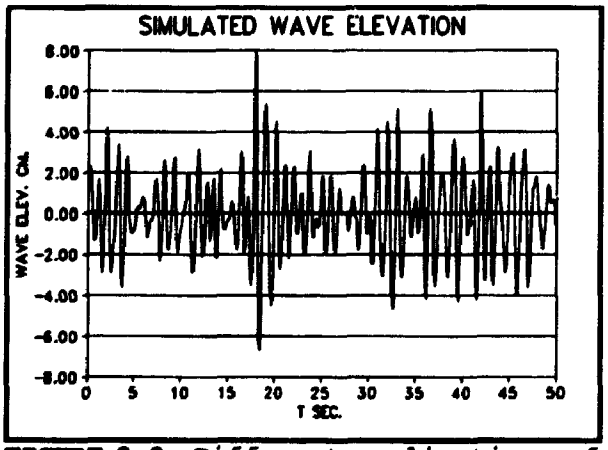

FIGURE 2.2: Different realizations of a wave record in model scale (Hs=9.95 cm.,Fp=0.81 Hz.), generated by a JONSWAP spectrum.

2.3.2 Long term statistics

The long term refers to events and extreme values related to a period of 20 to 100 years. The significant wave height and wave period vary in a long term sea description and in order to do an analysis on this basis a joint probability distribution of significant wave height and peak wave period is needed. This information can be provided from numerous short term statistics of the wave heights.

Usually a long term statistical method is preferred in the design of offshore structures. In this case when the design criteria for an structure is a single extreme wave, the extreme wave and its return period is needed in the analysis, and when the criteria is to use an spectral analysis, the extreme sea state is given in terms of a significant wave height and a peak period parameters as is done in Chapter 3 in dynamic analysis.

2.4 WIND EFFECTS ON OCEAN

2.4.1 GENERATION OF WIND WAVES

Energy is transferred from the turbulent wind to sea water both by pressure fluctuation and by the tangential shear stresses. The motion induced by shear stress mechanism is associated with vorticity but that of pressure fluctuation allows for irrotationality assumption. Once the seas start to grow there will be a feed back of the waves on to the wind (sheltering effect), which will produce pressure differences in an air flow. This sheltering effect is a function of the wave amplitude and there is always a balance in the relative importance of these two phenomena as the waves are growing to reach a fully developed state.

There exist different theories that try to explain the phenomena of growing of wind waves and among them are the resonance model, shear flow model and a combination of both models. In the next section a brief review of these theories will be given.

2.4.2 BRIEF REVIEW OF THE AVAILABLE THEORIES:

The resonance model was suggested by Phillips (1957). In this model the turbulent pressure fluctuation work on the surface and any interaction between wave field and pressure field is neglected which means it is an uncoupled model (excitation according to this theory is assumed to be independent of the response). According to this theory the pressure fluctuation in a turbulent wind field will contribute to the generation of waves in two different stages 1- The eddies in a turbulent wind and the associated pressure are being convected across the water by the mean wind. 2- The pressure field is not convected rigidly but due to eddy interaction, it slowly evolves in time. In this theory the resonance condition (Kinsman, 1965):

$$\left(\frac{g}{k}+\frac{\sigma k}{\rho}\right)^{0.5}=c(k) \qquad \sigma\text{-surface tension} \tag{2.32}$$

states that among the waves, those moving with the free water speed have the same convective velocity as the pressure forcing function and are in resonance with pressure field that generated them, continue to grow while other wave frequencies, called forced waves (as opposed to free waves), do not grow in time beyond a small upper bound.

The shear flow model which was suggested by Miles (1957,1959a,1959b) is based on the interaction of the mean flow and the waves and neglects the turbulent fluctuations in the wind field (except that without them the deriving mean flow could not exist). The

air flow is assumed to be incompressible and inviscid and its profile in the absence of the waves is U(z). The surface wave induced air flow disturbances are assumed to be two dimensional. The same as the previous model small amplitude theory is assumed in order to linearize the equations of motion. Under these conditions and neglecting the turbulent fluctuations in perturbation equations, the situation will lead to the inviscid case of the Orr-Sommerfeld equation:

$$(U-c)\frac{\partial^2\psi}{\partial^2 z} - [k^2(U-c) + \frac{\partial^2 U}{\partial^2 z}]\psi = 0 \qquad (2.33)$$

where ψ is the stream function

$$U(z) = \frac{u_*}{k}\ln(\frac{z}{z_0}) \quad k=0.4 \text{ Van Karman's constant} \qquad (2.34)$$

, z_0 is the effective roughness and u_* is the shear velocity (explained later). Here the air motion is coupled with a surface wave with a phase velocity of c and the wave extract energy from the mean flow:

$$\Delta E = \rho_a \overline{uw}(\frac{\partial U}{\partial z}) \qquad (2.35)$$

where $\overline{uw}$ is the Reynolds stress and ρ_a is air density.

Using the inviscid parallel flow assumption (Kinsman 1965), it can be shown that there exist a critical layer above which the Reynolds stress is zero and below that it is a constant. At the interface, the mean wind speed and the wave phase speed are equal. Lighthill (1962) proposed an easy approach for a better physical understanding of the process. Neglecting the turbulent and viscous diffusion, a combination of the pressure gradient and advection using Navier Stokes equations leads to the streamline pattern

shown in Figure 2.3. Again at the critical streamline $U(z_c)=c$, where the air particles are stationary in an average sense relative to the wave motion. Below $z=z_c$, there is a mean flow opposite to the mean wave motion and above $z=z_c$ there is a mean flow in the direction of the wave motion.

The third model suggested by Miles (1960) is a combination of both models and turbulent pressure fluctuations and shear stress act together. The resonance mechanism feed the sea surface with a broad banded energy spectrum, and the shear flow mechanism through its interaction with waves, acts as a modifying transfer function.

The time history of a particular wave component looks like Figure 2.4 which consists of three main phases, linear growth, transition and exponential growths which are not covered by the linear stability theory. In this figure ωt is the time required for a wave component to reach the transition. In case of strong wind (strong turbulent pressure fluctuation), the average transition time is about $\omega t=2\pi\ t/T=10^4$, and some of the wave components will become instable (breaking) even before reaching the exponential growth phase. Generally for wave components with $c/U(zc) > 0.8$ the generation mechanism is more governed by the resonance with the pressure fluctuations in the linear phase (Figure 2.5), and for shorter waves with $c/U<<1.$, the transition phase occurs sooner and as a result these components will experience a period of exponential growth.

The above mentioned three models are duration limited and site measurements corresponding to a duration limited theory is quite difficult. It can be stated that waves generated by the onset of wind on a fetch unlimited sea (duration limited) as a function

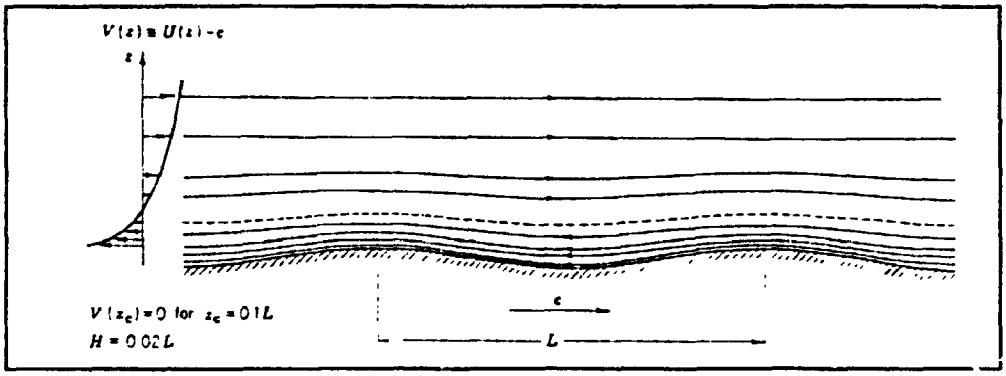

FIGURE 2.3: Mean shear flow for small wave heights (from Lighthill, 1962)

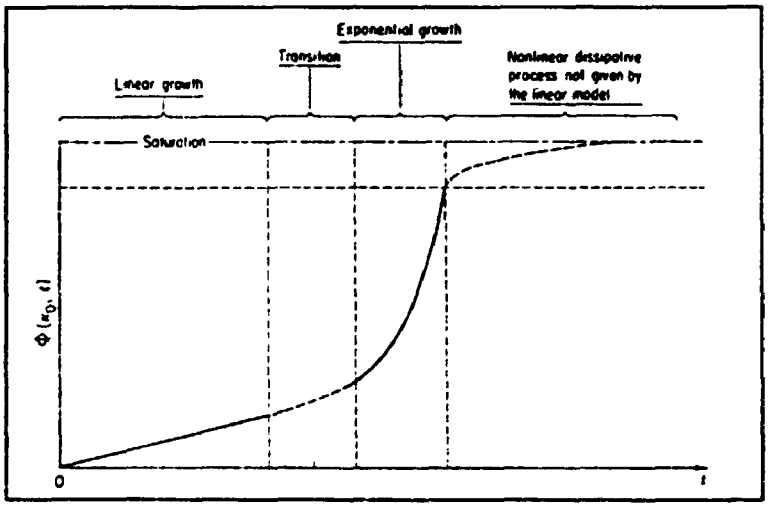

FIGURE 2.4: Energy growth of a wave component as a function of time. (from Wind waves, their generation and propagation on the ocean surface, by B. Kinsman, 1965).

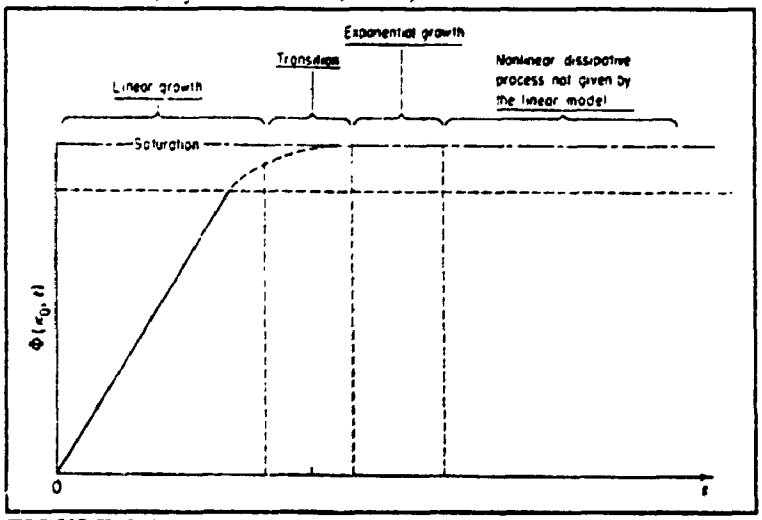

FIGURE 2.5: Energy growth of a wave component in strong wind (from Wind waves.... by B. Kinsman, 1965).

of time is similar to a fetch limited case under a steady wind as a function of space. Also there exist a number of observed spectra in fetch limited conditions under reasonably steady state winds. Phillips (1956) has shown that for a monochromatic wave in a linearized model, the duration D is dynamically equivalent to a fetch F as:

$$F=0.5C(k)\ D\ \ if\ F>L\ (wavelength),\ C(k)-phase\ vel. \qquad (2.36)$$

Using this relation and the available data on the fetch limited records, Phillips et al (1961) gave a proof for the existence of transition phase. From their model given a fetch distance, using the dispersion and phase velocity relations:

$$\omega^2=kg,\quad C(k)=\frac{\omega}{k} \qquad (2.37)$$

, it is possible to find the frequency which has just started the transition phase. In a growing sea, higher frequencies are either saturated or are growing exponentially till they break while lower frequencies (bigger waves) are still in a linear growth phase, and as the fetch F increases, the peak frequency fp decreases.

2.4.3 STATISTICS OF THE WIND

A fluctuating stationary velocity field for the wind can be expressed as a mean and a zero mean turbulent part. The mean component can be expressed by either a general logarithmic profile as given in (ESDU, 1982)

$$U(z)=2.5u_*(\ln\frac{z}{z_0}+34.5f_c\frac{z}{u_*}) \qquad (2.38)$$

where:

$$u_* = \text{friction velocity} = \left(\frac{\tau_0}{\rho}\right)^{0.5}$$
$$\tau_0 = \text{shear stress at surface}$$
$$z_0 = \text{roughness length}$$
$$f_c = \text{coriolis parameter} = 2\omega_e \sin\lambda$$
$$\lambda = \text{site latitude}$$
$$\omega_e = \text{earth angular velocity}$$

or by the power law:

$$\frac{U(z)}{U(z_{ref})} = \left(\frac{z}{z_{ref}}\right)^{\alpha} \qquad (2.39)$$

where $U(z_{ref})$is a reference velocity corresponding to z_{ref} and the exponent α is in the range of 0.1 to 0.15 for strong winds.

When considering the velocity distribution near the ground, contribution due to the Coriolis effects can be neglected and the log profile as given before can be written as:

$$U(z) = 2.5 u_* \ln\frac{z}{z_0} \qquad (2.40)$$

Due to the nature of the strong wind, the turbulent fluctuation are almost caused by mechanical stirring of the mean flow by surface friction and the atmosphere is assumed to be neutrally stable.

In this thesis the modelling of the wind is based on the ESDU procedure (Parts II,III, 1985) which basically uses the modified Von Karman types of spectrum and coherence functions (single and multiple points statistics) for modelling of the turbulent structure of

the wind.

On the basis of the definition of the friction velocity u_*, the surface drag coefficient (C_{10}) can be defined which indicates the level of roughness in ocean:

$$u^2_* = C_{10} U^2_{(z_{10})} \tag{2.41}$$

Amoroch and Devries (1980) suggested a relation in terms of $U(z_{10})$, which expresses this coefficient for low to high sea states. For the low sea states u_* and U_{10} have a linear relationship and C10 is constant (C_{10}=0.00104). For intermediate sea states where some of the wave components are still growing exponentially and full saturation is not yet met, C_{10} has a nonlinear relation with U_{10}. In the high sea states which correspond to high wind velocities (limited fetch and steady winds), most of the components have reached the saturation without even going through the exponential growth and again C_{10} has a linear relationship with U(10). Using the available data and a least square technique, C_{10} is expressed as:

$$C_{10} = 0.0015 \left(1+\exp\left(-\frac{U(10)-12.5}{1.56}\right)\right)^{-1} + 0.00104 \tag{2.42}$$

Turbulent intensity is a measure of the turbulent fluctuation and in strong winds (neutral stability) it mainly depends on the roughness length z_0 and increases with an increase in z_0. This quantity is a scaling parameter to define the velocity spectrum in the turbulent wind. The longitudinal turbulent intensity is given by:

$$I_u = \frac{\sigma_u(z)}{u_*} \frac{u_*}{U(z)} \tag{2.43}$$

where $\sigma_u(z)$ is the z dependent rms value of the longitudinal turbulence. ESDU (item 83045) describes $\sigma_u(z)/u_*$ on a semi-empirical basis as:

$$\frac{\sigma_u}{u_*} = \frac{7.5\eta\,(0.538+0.09\ln(\frac{z}{z_0}))^p}{1+0.156\ln(\frac{u_*}{f_c z_0})} \qquad (2.44)$$

where:

$$\eta = 1-\frac{6 f_c z}{u_*}\ ,\ p=\eta^{16} \qquad (2.45)$$

Also as given before:

$$\frac{u_*}{U(z)} = \frac{1}{2.5(\ln(\frac{z}{z_0})+34.5 f_c \frac{z}{u_*})} \qquad (2.46)$$

Equation 2.44 is based on the modification of the equation given by Harris and Deaves (1980), and in its derivation the asymptotic similarity theory was considered in order to be able to simulate conditions other than the fitted full scale data.

Using the strong wind data given by Shiotani (1975), Vickery (1983) suggested an empirical relationship to fit these data:

$$I_u(z) = 0.1(\frac{z}{80})^{-0.2}(\frac{u_{80}}{50})^{0.5} \qquad (2.47)$$

The estimated coefficient of variation in this relationship is about 5%.

In strong winds it is difficult to obtain spectral measurements when the length of the time history exceeds about 30 minutes, since after that the stationarity of the wind is in question. This limit on sample length combined with the need to have a resolution on the order of 0.01 Hz or smaller, will cause a variability (coefficient of variation) on the order of about 25% on a typical spectral estimate (Vickery, 1983).

Furthermore, the fact that in the lower frequency range of interest in this study, similarity relation is not valid, makes it quite difficult to describe the spectra by a universal relation (Simiu, Scanlan, 1986) and even the full scale results of Shiotani do not bring any confidence in the exact shape of the spectrum in this range (shape of the spectrum in this range varies strongly between sites and between the natural atmosphere and laboratory). The second scaling parameter necessary to define the wind spectrum, the length scale is explained in the next section.

2.4.4 SPECTRA OF THE HORIZONTAL GUSTINESS

The three most used equations for the spectrum of horizontal velocity are:

1- Due to Davenport (1961)

$$\frac{fS(f)}{\sigma_u^2} = \frac{79.2X^2}{(1+12\pi^2X^2)^{\frac{4}{3}}} \qquad (2.48)$$

2-Due to Harris (1971)

$$\frac{fS(f)}{\sigma_u^2} = \frac{3.66X}{(1+6\pi^2X^2)^{\frac{5}{6}}} \qquad (2.49)$$

3-Due to Kaimal (1972)

$$\frac{fS(f)}{\sigma_u^2} = \frac{2\pi X}{(1+3\pi X)^{\frac{5}{3}}} \qquad (2.50)$$

where X=fL′/U(z) and L′ is a length scale. This scale length corresponds to a wave length at which the reduced spectrum, $fS(f)/\sigma_u^2$, is maximum, and is called the characteristic length of turbulence:

$$L' = \frac{\lambda_m}{2\pi} \qquad (2.51)$$

Another definition of the length scale used is based on the spectral ordinate at zero frequency, and is called the integral length scale:

$$L = \frac{U(z)\,S(0)}{4\sigma_u^2(z)} \qquad (2.52)$$

At very low frequencies (less than about 1 cycle/hour), the spectra of wind turbulence are not strictly valid and the estimates of length scale based on zero frequency might have doubtful meaning. In the case of Harris and Kaimal spectra, the relation between L and L′ would be:

$$\begin{aligned} L' &= 1.09L \quad (Harris) \\ L' &= 0.64L \quad (Kaimal) \end{aligned} \qquad (2.53)$$

Vickery (1983), using the length scale data reported by Shiotani (1975), found an empirical relation for the variation of L with wind speed:

$$L=200\left(\frac{z}{80}\right)^{0.2}\left(U(80)/20\right)^{0.5} \tag{2.54}$$

Note that the length scale increases with height and wind velocity.

The ESDU model for integral length scale and spectra is derived from Deaves and Harris (ESDU 1974,1985) which itself is a modified form of the Von Karman spectrum. In this model the integral length scale is given (ESDU 1985) as:

$$L_u^x=\frac{A^{1.5}\sigma_u^{\,3}(z)}{k_z^{1.5}u_*^{\,2}\left(1-\frac{z}{h}\right)^2\left(\frac{dU(z)}{dz}\right)} \tag{2.55}$$

where:

$$\frac{dU(z)}{dz}=\frac{2.5u_*}{h}\left(\frac{1}{\frac{z}{h}}+5.75-7.5\frac{z}{h}-12\left(\frac{z}{H}\right)^2+4\left(\frac{z}{h}\right)^3\right) \tag{2.56}$$

$$k_z=0.2\left(1-\left(1-\frac{z}{z_c}\right)^2\right)^{0.5} \quad \text{when } z<z_c$$
$$k_z=0.2 \quad \text{when } z\geq z_c \tag{2.57}$$

$$A=0.115\left(1+0.315\left(1-\frac{z}{h}\right)^6\right)^{\frac{2}{3}} \tag{2.58}$$

$$\left(\frac{z_c}{h}\right)\ln\left(\frac{z_c}{z_0}\right)=0.65 \tag{2.59}$$

Also, the single point, along wind spectral density function is given as:

$$\frac{fS_u(f)}{\sigma_u^2}=\beta_1\frac{2.987\frac{n_u}{\alpha}}{\left(1+\left(\frac{2\pi n_u}{\alpha}\right)^2\right)^{\frac{5}{6}}}+\beta_2\frac{1.294\frac{n_u}{\alpha}}{\left(1+\left(\frac{\pi n_u}{\alpha}\right)^2\right)^{\frac{5}{6}}}F_1 \tag{2.60}$$

where

$$F_1=1+0.455\exp\left(-0.76\left(\frac{n_u}{\alpha}\right)^{-0.8}\right) \tag{2.61}$$

$$n_u=\frac{fL_u^x}{U(z)} \tag{2.62}$$

$$\beta_1=2.357\alpha-0.761\ ,\ \beta_2=1-\beta_1 \tag{2.63}$$

and

$$A=\alpha^{\frac{2}{3}}(0.3858-0.3298\alpha) \tag{2.64}$$

A good approximation for α is:

$$\alpha=0.535+2.76(0.138-A)^{0.68} \tag{2.65}$$

with

$$A=0.115(1+0.315(1-\frac{z}{h})^6)^{\frac{2}{3}} \qquad (2.66)$$

Note that when z/h tends toward one, β_1,β_2, and α asymptotically tend toward 1,0, and 0.747 respectively, which are Von Karman's equation parameters. This fact agrees with the results of the spectra measured at heights well above the layer nearest to the surface, and those results fit the Von Karman spectra quite well when plotted as reduced spectra vs. lnf. This fit suggests that the Von Karman formula is a good approximation. However, near the surface, the change of the shape of the spectrum indicates a nonlinear interaction between different frequency components and Von Karman model can be treated only as a first order approximation equivalent to a linear theory (Harris 1990).

The general form of the spectrum derived by Harris (1990) came from considering the auto-correlation function, $\zeta(\tau)$, of a random signal subjected to a nonlinear system, which for a wide class of nonlinearities, the auto-correlation of the output would be in the form of:

$$\rho(\tau)=\beta_1\zeta(\tau)+\beta_2\zeta^2(\tau)+\beta_3\zeta^3(\tau)+.. \qquad (2.67)$$

where the parameters $\beta_1,\beta_2,\beta_3,..$ are subjected to some constraints and boundary conditions depending on the nature of the experimental data.

A suitable form for $\zeta(\tau)$ is the Von Karman form for the auto-correlation function:

$$\zeta(\tau)=\frac{2}{\Gamma(\frac{1}{3})}(\frac{\alpha\tau}{2T_u})^{\frac{1}{3}}K_{\frac{1}{3}}(\frac{\alpha\tau}{T_u}) \qquad (2.68)$$

where α, as given before, is a normalizing parameter to make sure that the function $\rho_u(\tau)$ satisfies the relation:

$$\int_0^\infty \rho_u(\tau)\, d\tau = T_u \qquad (2.69)$$

T_u is the time scale of the longitudinal turbulence.

and $K_{1/3}$ is the modified Bessels function of second kind (order 1/3).

After doing some mathematical manipulation (Harris 1990), the coefficients β_i, can be determined. However, for all practical purposes, till now, a truncated series up to n=2 (ESDU, 1974,1985), has been used. It is worth noting that in this series solution, the role of higher order terms is to better simulate the behaviour in the higher frequency portion of the spectrum.

2.4.5 CORRELATION EFFECTS

The lateral dimension of the turbulence is the most important issue in determining the load time history on a structure and is demonstrated through the aerodynamic admittance function on the response history. In this regard, it would be necessary to define the concepts of coherence and/or correlation function between two different points on the structure. By definition, the correlation function is a measure of how velocities at two points are correlated;

$$\rho_{12} = \frac{\overline{u_1(t)\, u_2(t)}}{\sigma_{u1}\sigma_{u2}} \qquad (2.70)$$

The measure of this correlation in the frequency domain is expressed by the root coherence function, $\gamma_{12}(\Delta r,f)$, which is given as:

$$\gamma_{12}(\Delta r, f) = \left(\frac{CO_{12}^2(f) + QU_{12}^2(f)}{S_{11}(f)\,S_{22}(f)}\right)^{0.5} \qquad (2.71)$$

where

$S_{11}(f)$= wind spectrum at point 1

$S_{22}(f)$= wind spectrum at point 2

$CO_{12}(f)$= real part of the cross spectrum measured between 1, and 2

$QU_{12}(f)$= imaginary part of the cross spectrum measured between 1, and 2 (for application in this study it is usually small and therefore neglected).

In practice usually a simple form of the root coherence function is used (Davenport 1961):

$$\gamma_{12} = \exp\left(-C\frac{fr}{U}\right) \qquad (2.72)$$

where U is the average wind velocity at 1, and 2 and C is an experimentally observed coefficient between 10 to 12. This relation is suitable for most of the land based structures but in a compliant offshore structure, the situation is somewhat different (Vickery, 1982). The approximate wave length at which the wind loading can be dominant is around 1500 meters and higher ($\lambda = UT_0$, T_0 is the first natural period of the structure) and a typical turbulent scale length in strong wind is about 300 to 400 meters while a typical platform height is about 50 meters. In this environment, ($\lambda/z \approx 30$, $\lambda/L \approx 5$), the sea surface has an strong interaction with structure of turbulence (being relatively near to the surface) and also the Kolmogoroff region is away from this range. As a result the value of C and the form of the coherence function will be different (the previous form

will overestimate the real value in this range). A better root coherence function which more likely gives a better fit in this case over all the frequency range (Vickery, 1965) is:

$$\sqrt{Coh(f,\Delta)} = \exp\left(-\left(\left(\frac{\Delta}{L}\right)^2 + \left(C\frac{f\Delta}{U}\right)^2\right)^{0.5}\right) \tag{2.73}$$

The values of C were found from the value of the root coherence when f equals 0. and slope of $\text{Log}\sqrt{\text{Coh}(f,\Delta)}$, and are dependent on Δ/z (Vickery, 1983). Their fit for horizontal and vertical separations are respectively:

$$\begin{aligned} C &= 6 + 12\left(\frac{\Delta}{z}\right) \\ C &= 8 + 7\left(\frac{\Delta}{z}\right) \end{aligned} \tag{2.74}$$

Finally, the coherence model suggested by ESDU (1985) is given using the modified form of the Von Karman spectral equations which accounts for deviations from isotropic turbulence when getting near to the surface:

$$\gamma_{12}(\Delta, f) = \exp(-1.15\eta_1^{1.5}) \tag{2.75}$$

in which

$$\eta_1 = \left((0.747 r_g)^2 + \left(\frac{2\pi f C \Delta}{U_m}\right)^2\right)^{0.5} \tag{2.76}$$

where:

$$\begin{aligned} r_g &= \frac{\Delta}{2L_u^{\Delta}} \\ C &= \frac{1.6 r_g^{0.13}}{\eta^b} \\ \eta &= \left((0.747 r_g)^2 + \left(\frac{2\pi f \Delta}{U_m}\right)^2\right)^{0.5} \\ b &= 0.35 r_g^{0.2} \\ U_m &= \frac{U(z_1) + U(z_2)}{2}, \quad \Delta = (\Delta y^2 + \Delta z^2)^{0.5} \end{aligned} \tag{2.77}$$

$$L_u^{\Delta} = \frac{((L_u{}^y \Delta y)^2 + (L_u{}^z \Delta z)^2)^{0.5}}{\Delta} \qquad (2.78)$$

and Δ is the distance between points 1, and 2 and $L_u{}^y$, and $L_u{}^z$ are the principle length scales for the u component of wind velocity in the y, and z directions correspondingly. This form of the coherence function is complicated, but it accounts for the overestimation observed by the first model in the lower frequency range (Vickery P.J., 1988) and fits the experimental data quite well.

The real part of the cross spectrum between points 1, and 2 would be:

$$CO_{12}(\Delta, f) = \gamma_{12}(\Delta, f)\,(S_{11}(f) S_{22}(f))^{0.5} \cos\theta_{12} \qquad (2.79)$$

in which θ_{12} is the phase lag angle. The phase lag is zero for isotropic turbulence and is small in the high frequency range of the spectrum since in this range, the turbu. ce exhibits isotropic properties. Based on some experime l data (Rugby and Cranfield, ESDU 1986), θ_{12} is given as:

$$\theta_{12}(\Delta, f) = (1.3 \frac{\Delta z}{z_m})\,(c-1)^{0.7}\,(\frac{2\pi f \Delta z}{U_m}) \qquad (2.81)$$

where z_m is the average of z_1, and z_2.

For all practical purposes, the value of θ_{12} in this study is assumed to be zero.

2.5 WIND LOADING

2.5.1 INTRODUCTION

Offshore structures experience wind loading during different stages of their construction,

towing, and service. For compliant structures subjected to a wave loading with the peak wave period around 15 seconds, the wind loading may be the dominant one when the first natural period is between 20 to about 50 seconds (Vickery, 1982).

Generally, wind loading can be calculated by the methods given in the codes for single point and line like structures (Davenport, Hambly, 1984), but due to the fact that they do not sufficiently account for shielding and interference effects, they usually overestimate the load especially when the platform's geometry becomes more complex. In these cases wind tunnel simulation would be the best option to account for these effects.

2.5.2 MODELLING OF THE WIND FORCE

Wind loading consists of a drag component due to flow separation and an inertia component due to fluid body accelerations, however the latter is about two orders of magnitude smaller than the former one and often ignored in the analysis.

The drag induced wind load per unit area, assuming a wind field, U(t), acting on the center of the area is:

$$\frac{F_w}{unit\ area} = \frac{1}{2}\rho C_D U^2(t) \qquad (2.81)$$
$$where\ \ U(t) = U + u(t)$$

Upon substitution for U(t), the fluctuating part of drag force at time t on a surface A would be:

$$F(t) = \int_A \rho C_{D_i} U_i u_i(t) \phi(z)\, dA_i \qquad (2.82)$$

where on the platform $\phi(z)=1$.

The auto-correlation of this fluctuating force is:

$$R_{FF}(\tau) = \int_A \int_A \rho^2 C_{D_i} C_{D_j} U_i U_j R_{u_i u_j}(\tau) \phi(z_1) \phi(z_2)\, dA_i dA_j \qquad (2.83)$$

where $Ru_iu_j(\tau)$ is the cross-correlation of the fluctuating wind components.

Upon taking the Fourier transform of both sides and neglecting the quadrature (imaginary) part of the wind speed cross spectrum, the force spectrum will be:

$$S_{FF}(f) = \int_A \int_A \rho^2 C_{D_i} C_{D_j} U_i U_j CO_{12}(f)\, dA_i dA_j \qquad (2.84)$$

This double integral will be calculated numerically, discretizing the rectangular projected area of the structure in small rectangles.

The force spectrum for a point like structure is related linearly to the wind spectrum of longitudinal component, $S_{uu}(f)$, as:

$$S_{FF}(f) = (\rho C_D A U)^2 S_{uu}(f) \quad or$$
$$S_{FF}(f) = 4 \frac{\overline{F_D}^2}{U^2} S_{uu}(f) \qquad (2.85)$$

This equation is valid over a frequency range where the velocity fluctuations are fully correlated. The lack of a perfect correlation is accounted for by introducing an

aerodynamic admittance function $|\chi(f)|^2$ as:

$$S_{FF}(f) = 4\frac{\overline{F_D}^2}{U^2}|\chi(f)|^2 S_{uu}(f) \tag{2.86}$$

The admittance function is frequency dependent and decreases with increasing frequency. Vickery (1969) has suggested an empirical relationship based on a series of experiments as:

$$|\chi(f)|^2 = \left(\frac{1}{1+\left(\frac{2f\sqrt{A}}{U}\right)^{\frac{4}{3}}}\right)^2 \tag{2.87}$$

This function can be calculated analytically as:

$$|\chi(f)|^2 = \frac{\iint_{AA} \rho^2 C_{D_i} C_{D_j} U_i U_j CO_{12}(f)\, dA_i dA_j}{(\rho C_D A U)^2 S_{uu}(f)} \tag{2.88}$$

The double integral in the above equation should be calculated numerically. The wind forces calculated by this method, in combination with the allowance for the structural motion (aerodynamic damping), will be employed in dynamic analyses performed in Chapter 3. The above mentioned model is applicable for lattice model. In a bluf body, the pressure correlation is increased on the windward face and it is reduced on the leeward face, and in an average sense, the lattice model leads to good approximation.

2.6 WAVE LOADING ON SLENDER BODIES

Ocean waves are of special interest to marine engineers because of the interaction between these waves and structures on and beneath the free surface zone. In this section a brief review of the wave loading on slender bodies (circular cylinders) will be

presented.

2.6.1 INTRODUCTION

Assuming geometrical similarity, the magnitude of the unsteady wave force on a stationary member in a plane progressive wave system can be expressed as:

$$\frac{F}{\rho g D^3} = C_F\left(\frac{A}{L}, \frac{d}{L}, \frac{D}{L}, Re, \omega t\right) \qquad (2.89)$$

where D is the diameter of the member, A is the wave amplitude, L is the wave length, d is the water depth, and ω is the wave typical frequency. The relative magnitude of the viscous drag force and the inertia force on a stationary member is proportional to $\frac{U^2}{\dot{U}D}$

(U being typical fluid velocity). In an oscillatory flow, the oscillatory displacement of the fluid particles is proportional to the wave amplitude, hence the magnitude of the fluid velocity relative to the body would be ωA, and the ratio of the viscous to inertia force would be A/D. When the body is large, it is clear that the viscous effects are negligible. Assuming $\eta << (L,d)$, neglecting the second order effects, the force coefficient in an oscillatory flow would be:

$$C_F = C_1\dot{U} + C_2 U \qquad (2.90)$$

where C_1, C_2 are known as apparent mass and damping coefficients with the units $(\text{acceleration})^{-1}$, $(\text{velocity})^{-1}$ respectively, and depend on D/L ratio (diffraction parameter). They can be determined experimentally by measuring the amplitude and phase of the force acting on the body. When the body is small relative to wave amplitude, the viscous

effects dominate and the force can be given as:

$$f = \frac{1}{2} C_D \rho D |U| U \qquad (2.91)$$

where C_D is a drag coefficient.

When A/D is a quantity of order one, the situation due to the interaction of viscous and inertia effects is complex and is not yet fully understood. The current state of the art uses an equation which is a combination of these two effects:

$$F = \frac{1}{2} \rho C_D D |U| U + \frac{\pi}{4} D^2 \rho C_M \dot{U} \qquad (2.92)$$

In this semi-empirical engineering model, called the Morison equation (1950), the coefficients C_D, and C_M should be estimated experimentally. Many experiments have been done in order to verify Morison equation in this regime (Sarpkaya and Isaacson 1981). Some experiments confirm the equation and some other experiments consider it incomplete. But till today it has been used by engineers and has an important place in marine engineering codes.

Also a number of numerical works have been done to simulate the separated flow around marine structures and specifically circular cylinders. These methods include Single Vortex Method (Falinsen, Sortland, 1987), Discrete Vortex Method, Navier Stokes equation, etc. Most of them are limited to 2-D flow and are not powerful enough to be used directly without having some guidance from experiment. Generally, the Morison equation is considered to be valid when the ratio of $D/L<0.2$, i.e., the geometry of flow does not sensibly change by the presence of the structure.

2.6.2 MORISON EQUATION

In recent years many review papers (Hogben, 1976; Garrison, 1980; Sarpkaya, 1976) have been written to describe the wave force mechanism in slender offshore structures. In all of these papers the Morison equation (Morison et al, 1950) was the center of the discussion. It was often used to calculate the wave forces in circular members of fixed offshore structures. This equation is valid in a long crested wave, when a vertical surface-piercing column extends from sea bottom.

As was already mentioned, the wave induced force is comprised of two components, the first is the drag force and is related to the viscous and flow separation effects; the second is the inertia force which can be written as:

$$C_M \rho A \dot{U} = \rho A \dot{u} + C_A \rho A \dot{u} \qquad (2.93)$$

The first term on the right hand side represents the force associated with the pressure gradient induced by the undisturbed wave field on the member (Froud-Krylov force). The second term is due to the inertia associated with the motion of the mass of fluid particle in the presence of the member. The total force on the stationary member can be found by integrating this force along its length.

When considering the force on a vertical circular member the main parameters affecting the flow consist of:

Reynold's number, $Re = \frac{UD}{\nu}$, where U is the characteristic free stream velocity.

Fluid Keulegan-Carpenter number, $KC_f = \frac{U_0 T}{D}$, for ambient oscillatory planar flow

, $U=U_0\sin 2\pi\frac{t}{T}$, past a fixed body. T is period of fluid oscillation.

Reduced velocity, $U_r=\frac{UT_0}{D}$, when dealing with a responding cylinder (T_0 is the structural period).

Relative current number, $\frac{U_c}{U_0}$.

The C_D and C_M values are to be determined experimentally and are functions of the parameters described above. There exists a number of papers recommending different methods and justifications for their derivation and a detailed discussion of many of them can be found in Sarpkaya and Isaacson (1981), and Chakrabarti (1987).

The two most used techniques are:

1. Fourier averaging method which is applicable only when the wave kinematics are expressed in sinusoidal form (Chakrabarti 1987).

2. Least square method which is also applicable when the water particle kinematics are not sinusoidal, such as, when dealing with irregular waves and/or when using nonlinear wave theory to derive the kinematics of the flow.

In both of these methods C_D and C_M are found in an average sense per cycle (in reality these coefficients are time dependent).

Kaplan (1986) used a System Identification method to obtain the force coefficients. It is developed from the modern control theory and uses the measured force and velocity time histories to obtain the response of the system using Morison equation as its mathematical model with C_D,C_M unknown and tries to find the best fit for both measured force and

velocity simultaneously.

It is clear that when dealing with drag dominated flow where H/D is greater than 5 (drag force is large compared to the inertia force) the C_D coefficient can be found without scatter. In an inertia dominated range the inertia force is large relative to drag, and the C_M coefficient would be found without scatter. When viscous effects are negligible, using the linear diffraction theory, it is possible to show that Morison's equation is an asymptotic solution for small D/L ratio (Isaacson, 1979).

2.6.3 HYDRODYNAMIC FORCE COEFFICIENTS AND FLOW REGIMES

Determination of force coefficient in an unsteady flow is a difficult task. In an oscillatory flow the direction of the velocity vector at a point changes with time and as a result the starting separation point is not a fixed point any longer. One of the definitions of separation in unsteady flow as mentioned by Telionis (1981) is that in unsteady flow, the separation occurs when a singularity develops in the classical boundary layer equations, and in this case the point of zero skin friction may be called the detachment point.

The flow around a circular cylinder will not separate in an oscillatory fluid motion at very small KC_f numbers, however it will separate in a steady current. In the case of combined incident current and oscillatory fluid motion, the situation depends on the relative current number. If the combined flow velocity changes sign with time, there would be a possibility that the flow does not separate.

There are many studies which establish the variation of C_D and C_M with KC_f,Re, and the relative roughness, K/D. Sarpkaya's results (1976a,b,1986) seem to be the most comprehensive one in simple oscillatory flow. He studied different cylindrical members

at small KC_f numbers and a variety of Re numbers (without any ambient current) and reported that separation will start to happen at KC_f=1.25 [1]. He also found at very low KC_f numbers separation does not occur. Bearman et. al. (1981) studied the flow around a circular cylinder at KC_f=4, and reported that the pair of vortices generated during the first half cycle did not survive in the next half cycle because these vortices were convected back to the cylinder and their circulation was cancelled by the opposite vorticity of the boundary layer of the cylinder. Williamson (1985) reported a symmetric vortex shedding pattern for KC_f of 4. The results given by Bearman and Williamson suggest that at low KC_f numbers, there should be another parameter or parameters in addition to the KC_f number, which explain the initiation of the vortex shedding process (Faltinsen, 1990). An example is the Re number. So far a definitive analysis of the initiation of vortex shedding has not been given.

In an oscillatory nonseparated (small KC_f), laminar flow, Wang's analysis (1968) demonstrated that for high Re numbers, the drag coefficient on a cylinder can be written as:

$$C_D = \frac{3\pi^3}{2\,KC_f}\left[(\pi\beta)^{-\frac{1}{2}} + (\pi\beta)^{-1} - \frac{1}{4}(\pi\beta)^{-\frac{3}{2}}\right] \qquad (2.94)$$

where

$$\beta = \frac{Re}{KC_f} = \frac{D^2}{\nu T} \qquad (2.95)$$

This C_D differs from the Stokes solution for laminar unseparated flow. The drag

[1] at small KC_f numbers separation does not mean that vortex shedding process is clearly observed.

coefficient may be very large in this regime but it does not necessarily mean that drag force is large.

In a planar oscillatory separated flow at small KC_f numbers, the flow is symmetric at KC_f less than 7 (Faltinsen, 1990). In this range the flow oscillation governs and the inertia force is the primary component and after that, asymmetry starts to develop. As reported by Bearman (Faltinsen 1990), after a KC_f greater than 7 the majority of vortex shedding happens on one side of the member and the direction can be changed depending on the initial condition, and in this range the flow has a strong memory. In the intermediate range, when KC_f is between 5 and 25, drag and inertia forces are both of importance, and after 25 the flow is more quasi-steady and the wakes are more like the wakes in a steady situation.

As mentioned, Sarpkaya in his experiment (Sarpkaya, 1986) analyzed a cylinder in small amplitude flow for different KC_f numbers and β values. In the case of nonseparated laminar flow ($KC_f \approx 1$), his results were in agreement with Wang's formula and when KC_f is greater than 2, his C_D values begin to increase with KC_f (Figure 2.6). The relation between KC_f, and C_D around KC_f equal to 2 also depends on whether flow was separated before being turbulent or vice versa. It is clear that when turbulence occurs first, the C_D coefficient has a smaller minimum than the reverse case (Figure 4.26). At higher Re numbers. β=11240, the turbulence will take precedence.

As mentioned at high KC_f numbers, (KC_f>25), the flow tends to a quasi-steady situation and the drag force is the dominant component. This regime is very important for the prediction of wave loading on jacket platforms, compliant towers and riser systems in extreme sea states. The prediction of drag induced drift forces due to the free surface effect in compliant towers is especially sensitive to the C_D value. Here the variability of drag coefficient, is relatively large and typically for a KC_f equal to 100 and Re greater

than 10^6, C_D varies from 0.65 for smooth cylinder to 1.6 for a cylinder with k/D equal to 0.02.

The analytical solution for irrotational inviscid oscillatory flow past a circular cylinder yields a value of C_M=2.0 and it is the upper bound for the inertia coefficient. Usually the viscous and roughness effects decrease the C_M value, and its typical design value ranges from about 1.5 to 2.0.

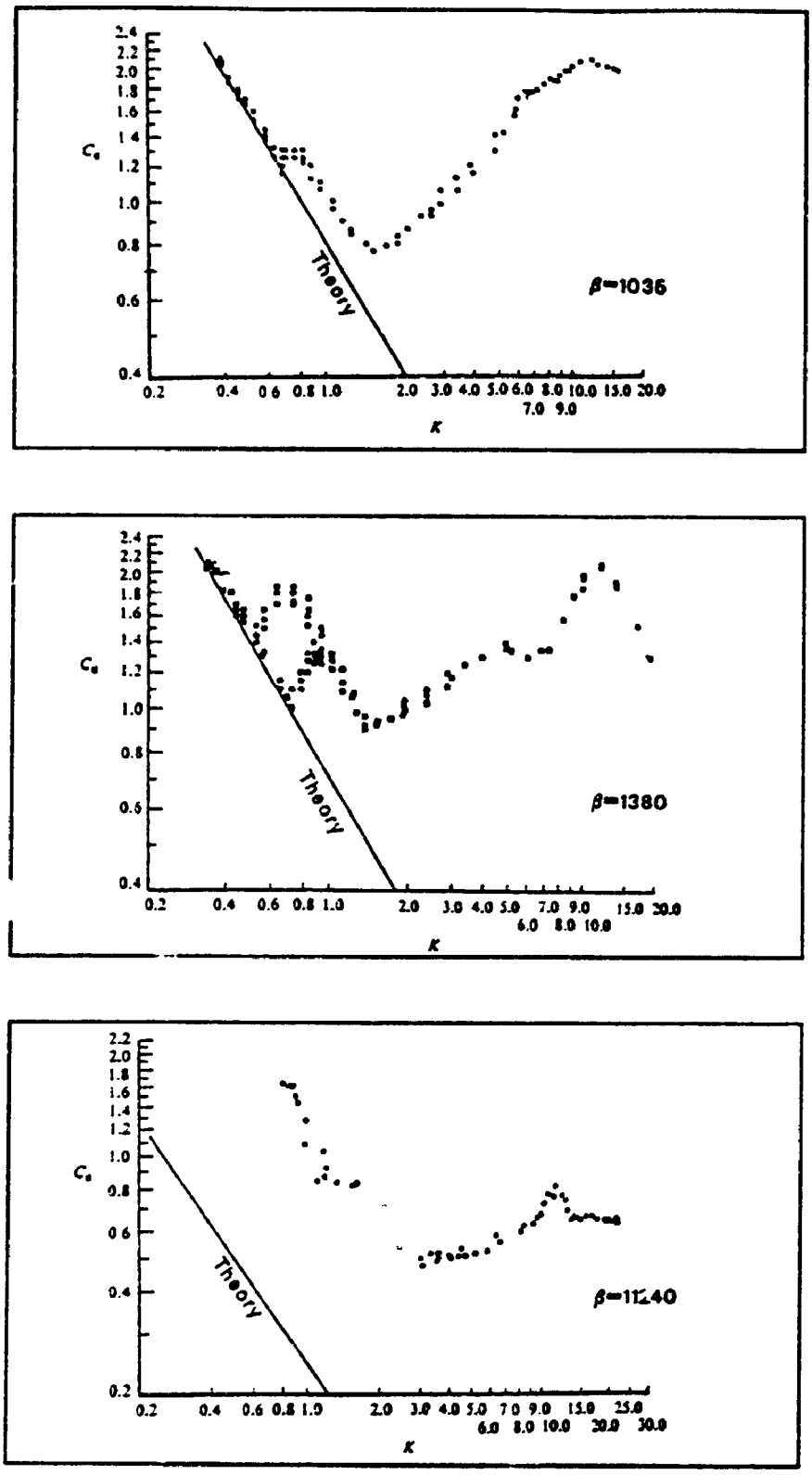

FIGURE 2.6: Drag coefficient derived from the rectilinear flow in low KC_r for smooth cylinder (from Sarpkaya, 1986).

2.6.4 MODIFIED FORMS OF THE MORISON'S EQUATION

When the member is moving in waves, the force and motion are dependent on the water particle kinematics as well as the velocity and acceleration of the member itself. In this case several modified forms of the Morison equation have been used. The most common models are:

1. The relative velocity model
2. Independent fields model

These models account for the wave structure interaction to calculate the hydrodynamic load on a nodal point of a compliant tower.

2.6.4.1 RELATIVE VELOCITY MODEL (RVM)

This form is given as:

$$f = \frac{1}{2}\rho C_D D\,|u-\dot{x}|(u-\dot{x}) + \rho\frac{\pi D^2}{4}(C_M\dot{u} - (C_M-1)\ddot{X}) \qquad (2.97)$$

where f is the force per unit length and $u, \dot{u}, \dot{x}, \ddot{x}$ are the velocity and acceleration corresponding to the fluid and structure respectively. It would be expected that this "quasi-steady" form would be valid at large values of KC_m (motion KC number defined as $2\pi x_0/D$), KC_f. In this model, the hydrodynamic drag and inertia coefficients are usually evaluated from a fixed cylinder in waves or from surge tests in still water. However, due to the interaction between the cylinder motion and fluid motion it is not always appropriate to use these types of tests to evaluate C_D, and C_M in a design situation.

Moe and Verley (1980), used this model to verify these coefficients in the case of an oscillating cylinder in the presence of current and the study indicated that they are different from those measured in surge tests in still water. Chakrabarti and Cotter (1984) reported that for the range of KC_f numbers encountered ($0<KC_f<40$), results of the surge test and the fixed cylinder test are still valid for the case of structural motion combined with the waves when KC_f number based on the maximum relative velocity at the centre of the cylinder is used. In the case of small cylinder motion (away from resonance) in the presence of waves, the flow seems to behave more like that of a fixed cylinder in waves rather than the simple surging motion (Chakrabarti and Cotter, 1984). In another study, Bearman et. al. (1992) measured the response of a responding cylinder in an U-tube oscillatory flow in the inline direction and concluded that the relative velocity model of Morison's equation agrees well with the experimental results. Also, the force coefficients derived from Morison's equation were found to be different from those measured on a fixed cylinder.

The relative velocity model, although being a natural extension of Morison equation, is somewhat heuristic and needs to be experimentally verified. In this case, the three important parameters are Kcf, $U_r=U_0T_0/D$ (reduced velocity), and KCm. It can be said that in the range of the Re numbers considered and a constant Strouhal number, the required time for a wake to develop is proportional to D/U_0, and as a result, KC_f would be proportional to (Laya et al, 1984):

$$KC_f \propto \frac{\textit{time available for development of a wake}}{\textit{time required for formation of a wake}}$$

Also, the reduced velocity may be interpreted in the same way as the KC_f number but the numerator in the above equation will change to the 'period of cylinder motion'. In cases where KC_f and U_r are both high enough (higher than around 10-15, which typically occurs for a compliant tower in a moderate to extreme sea states and KC_m big enough), it can be stated that the drag force would be better simulated by the superposition of two dependent quasi-steady flow fields (Laya et al. 1984). One due to an almost steady flow past a fixed cylinder and the other due to the slow oscillation of the cylinder in a relatively stationary water. In such a situation, wakes can properly develop and the relative model will probably be more appropriate.

2.6.4.2 INDEPENDENT FLOW FIELDS MODEL (IFFM)

This modification of the Morison's equation has been suggested by Moe and Verley (1980) when the conditions are such that the relative velocity model is not appropriate. They used it for a cylinder oscillating in steady flow in low Re number experiments. The concept is that there are two independent fields , a far field which is unaffected by the motion of the cylinder and a near field created by the motion of the cylinder itself. In case of waves the force can be modelled as:

$$f = \frac{1}{2}\rho D\left(C_{D1}\,|u|u - C_{D2}\,|\dot{x}|\dot{x}\right) + \rho\,\frac{\pi}{4}D^2\left(C_M\dot{u} - (C_M - 1)\,\ddot{x}\right) \qquad (2.97)$$

Since the motion consists of two different frequencies and two different time scales which can be treated independently, the drag coefficients can be found from two different sets of experimental data (C_{D1} from the fixed cylinder tests in waves, and C_{D2} from the

surge test with the KC and Re numbers related to the wavefield and cylinder motions).

Using the numerical values given by Moe and Verley (1980), Laya et al (1984) discussed the applicability of the two models. The cases of high KC_f and small U_r (corresponding to a superharmonically resonating drag dominated cylinder oscillating in a relatively slow far field flow), and low KC_f and high U_r (corresponding to low frequency cylinder oscillation in a high frequency far field flow oscillation), will make the assumption of quasi-steadiness to be invalid. Under these conditions, any vortex initiation due to the slow scale is interrupted by the fast scale motion and the water particles in the near field experience a rather chaotic flow pattern. They also reported that in smaller sea states the response predicted by the two models are close but for higher seas the damping predicted by the RVM is more than that of IFFM and, correspondingly, the RVM leads to smaller responses. In the case of the compliant tower, when dealing with random waves in smaller sea states, the use of the IFFM is acceptable but when moving towards the intermediate to higher sea states where the assumption of quasi-steadiness is approached, the use of the RVM is more reliable.

2.6.5 MORISON'S EQUATION IN RANDOM WAVES

In this study, the relative velocity model is used to calculate the hydrodynamic loading on the compliant tower. Except for very small KC_f numbers where the pressure drag damping is small due to the fact that vortices are not formed and separation has not occurred (laminar flow and stokes damping), this equation is valid and, as will be seen in Chapter 4, yields more uniform results for the C_D values in both regular and random waves.

The drag term in Morison's equation makes the loading highly nonlinear and to avoid

considering this coupled form and a lengthy time domain solution, approximations are often made to express this force in a series form and use the nonlinear spectral density calculations (Borgman, 1969; Connor 1980).

When the wave amplitude is much greater than the maximum displacement of the structure $\eta(t) >> x(t)$, the drag force can be decoupled using the Borgman approximation:

$$(u-\dot{x})|u-\dot{x}| = |u|u - 2|u|\dot{x} \qquad (2.98)$$

The first term can be represented by a polynomial :

$$u|u| = \sum_{n=0}^{N} C_n u^n \qquad (2.99)$$

and the problem is to minimize the function:

$$Q = \int_{-\infty}^{\infty} \left(\left[u|u| - \sum_{n=0}^{N} C_n u^n \right]^2 \frac{1}{\sqrt{2\pi}\,\sigma_u} \exp\left[-\frac{u^2}{2\sigma^2{}_u} \right] \right) du \qquad (2.101)$$

The last part of the integrand is the Gaussian probability density function. The values of C_n can be calculated by differentiating the above function with respect to C_n and setting the result equal to zero. The values of C_n are then obtained by forming a matrix equation and its inversion.

In cases where there's no current (u is a zero mean process), a quintic approximation would be (Gudmestad and Connor, 1984):

$$u|u| = \frac{3}{4}\sqrt{\frac{2}{\pi}}\,\sigma_u u + \frac{1}{2}\sqrt{\frac{2}{\pi}}\,\frac{u^3}{\sigma_u} - \frac{1}{60}\sqrt{\frac{2}{\pi}}\,\frac{u^5}{\sigma^3{}_u} \qquad (2.101)$$

and when a mean current U_c is also present a cubic approximation would be:

$$|u|u = -\frac{2}{3}\left(\frac{U_c}{\sigma_u}\right)^3\phi + \left[2\left(\left(\frac{U_c}{\sigma_u}\right)^2+1\right)\phi\right]\sigma_u u + \left(\Phi - 2\left(\frac{U_c}{\sigma_u}\right)\phi\right)u^2 + \frac{2}{3}\phi\frac{u^3}{\sigma_u}$$

where

$$\phi = \frac{1}{\sqrt{2\pi}}\exp\left(-\frac{1}{2}\left(\frac{U_c}{\sigma_u}\right)^2\right)$$

$$\Phi = \frac{2}{\sqrt{2\pi}}\int_0^{\frac{U_c}{\sigma_u}}\exp\left(-\left(\frac{t^2}{2}\right)\right)dt = 2erf\left(\frac{U_c}{\sigma_u}\right) \qquad (2.103)$$

Also, the method is able to evaluate the coefficients when u(t) is not a Gaussian process.

In Figure 2.7, the difference between different levels of approximation given above (linear,cubic,quintic) and the exact force as a function of u/σ_u is given. It is seen that the difference for high velocity ranges where $u/\sigma_u > 2.5$, is not negligible and as a result the Gaussian approximation (linearized drag) can not predict the extreme values properly. The second term of equation 2.98 is a damping term, and when u is Gaussian with a mean of U_c, the damping can be approximated as:

$$|u| = 2\left[\left(\frac{U_c}{\sigma_u}\right)^2+1\right]\sigma_u\phi + \left[\Phi - 2\left(\frac{U_c}{\sigma_u}\right)\phi\right]u + \phi\frac{u^2}{\sigma_u}$$

or to a zeroth order:

$$|u| = \left[\left(\frac{U_c}{\sigma_u}\right)\Phi + 2\phi\right]\sigma_u \qquad (2.105)$$

In many analyses, a constant damping term is used which in cases where there's no current would be:

$$|u| = \sqrt{\frac{8}{\pi}}\,\sigma_u \qquad (2.106)$$

Gudmestad and Connor (1980), proposed to use a hydrodynamic damping coefficient which was half the value given by Malhotra, and Penzien (1970).

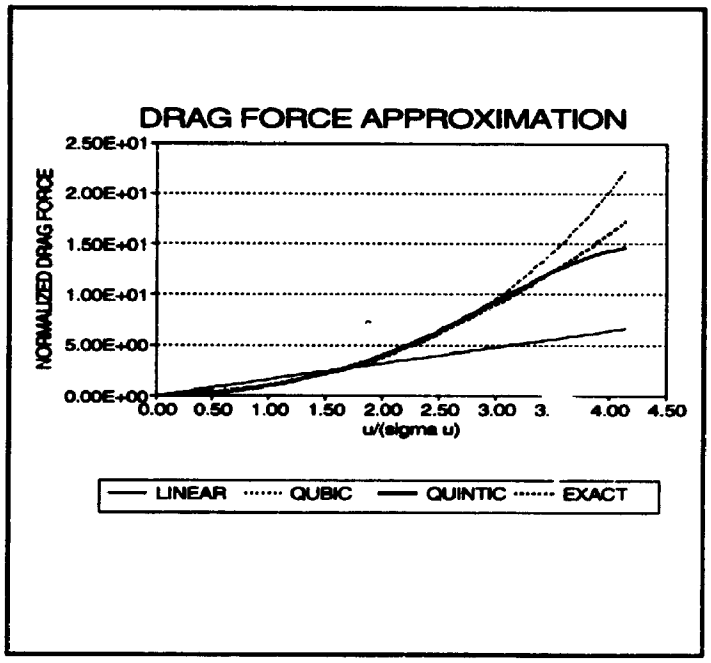

FIGURE 2.7: Different levels of drag force approximation

In reality, the hydrodynamic damping is a function of time but it has been shown by Blevins (1977) that for small structural motions, this constant damping assumption for a single degree of freedom model is close to the exact solution.

Dao and Penzien (1982) using the relative velocity model in random waves, considered the three cases of coupled nonlinear drag (exact), uncoupled nonlinear drag, and the linearized drag. For the latter two cases, they used a constant damping term.

The first two methods lead to response time histories which were quite close in r.m.s and mean extreme values but for high sea states where Hs/D >20, the mean extreme response for the uncoupled case can exceed the coupled one on the order of about 10 percent. The results obtained for the linearized method also showed nearly the same values for rms compared to the other two methods but the extreme values for higher sea states was underestimated by the linearized method on the order of 35 percent.

They also showed that the response extreme value statistics closely fit to the Gumble type I probability distribution.

The loading spectra, assuming that for a slender member the inertia and drag forces are independent, would be:

$$S_{FF}(\omega) = \left(\frac{1}{2}\rho C_{DD}\right)^2 \left[\left(\Phi\left(\left(\frac{U_c}{\sigma_u}\right)^2+1\right)+2\phi\left(\frac{U_c}{\sigma_u}\right)\right)^2 + 4\left(\Phi\left(\frac{U_c}{\sigma_u}\right)+2\phi\right)^2 \frac{S_{uu}(\omega)}{\sigma^2{}_u} + 2\Phi^2 \frac{(S_{uu}(\omega))^{*2}}{\sigma^4{}_u} + \frac{8}{3}\phi^2 \frac{(S_{uu}(\omega))^{*3}}{\sigma^6{}_u} + \frac{2}{3}\left(\left(\frac{U_c}{\sigma_u}\right)\phi\right)^2 \frac{(S_{uu}(\omega))^{*4}}{\sigma^8{}_u}\right] + \left(\rho\frac{\pi}{4}C_M D^2\right)^2 S_{uu}(\omega)$$

(2.107)

where the convolutions of $S_{uu}(\omega)$ are defined as:

$$(S_{uu}(\omega))^{*n} = \int_{-\infty}^{\infty} (S_{uu}(\omega))^{*(n-1)} S_{uu}(\omega-\lambda)\, d\lambda \qquad (2.108)$$

In the absence of current we have:

$$S_{FF}(\omega) = \frac{8}{\pi}\left(\frac{1}{2}\rho C_D D\right)^2 \sigma^4{}_u \left[\frac{S_{uu}(\omega)}{\sigma^2{}_u} + \frac{1}{6}\left(\frac{(S_{uu}(\omega))^{*3}}{\sigma^6{}_u}\right)\right] + \left(\frac{\pi}{4}\rho C_M D^2\right)^2 S_{\dot{u}\dot{u}}(\omega) \qquad (2.109)$$

It should be noted that the convolution terms $(S_{uu}(\omega))^{*n}$,n>1) are smaller compared to n=1, which represents the dominant wave frequency. However, due to their nonlinear effect, the convolution terms will cause peaks at multiples of peak frequency of the first order waves. Although their energy decreases as the frequency increases, these peaks usually contribute to the resonant response in the fixed jacket structures.

The current contributes to the even terms, and, as far as the compliant platform is of concern, it somewhat increases the low frequency portion of the wave force spectrum The higher order convolutions make the spectrum broader about the peak frequency. In the case of a compliant platform, although there is no peak due to these terms at $\omega<\omega p$, the force spectrum is not zero and a low frequency resonant response might still be important. There are other low frequency forcing contributions which will be discussed in later sections.

2.7 LOW FREQUENCY WAVE FORCING IN DRAG DOMINATED BODY

2.7.1 INTRODUCTION

The low frequency wave forcing is caused by the self and mutual interaction of different wave frequencies in a group.

As has been explained in the previous section, in the range where D/L< 0.2, the force is given by the Morison equation:

$$f = \frac{1}{2}\rho D C_D |u|u + \frac{1}{4}\rho \pi D^2 C_M \dot{u} \qquad (2.110)$$

In the above equation, drag forces dominate the body response for ratios of wave height to diameter (H/D) exceeding about 5 (Sarpkaya, Isaacson, 1981). In this section the phenomenon of low frequency forcing in a drag dominated body will be presented. The four main contributors to this phenomenon will be explained. Among them the contribution to the low frequency forcing due to the free surface effect and bounded long waves are investigated. The different engineering models for deriving the average force per wave at the free surface zone are discussed in Gudmestad, et al. (1986).

Measurements using LASER Dopppler Velocimeter (Anastasiou, et al 1982; Gudmestad et al, 1988) have indicated that the horizontal water particle velocity is smaller under crest and higher (more negative) under trough than predicted by the Stokes higher order theories. By correcting the Chakrabarties approximation (1971) for horizontal water particle velocities, Gudmestad and Connor (1986) developed a second order model which agrees well with the above mentioned experimental data. In this work, using the constant velocity model at the free surface (Faltinsen 1990) and the Chakrabarti's second order approximation, the force on a slender surface piercing cylinder in regular waves, is calculated (integrated to the current water level). The concept of the envelope of a narrow-banded process, using the Hilbert transform method is introduced and by extension of the above mentioned models to bichromatic and irregular waves, the low frequency forcing due to the free surface effects in deep water waves is explained.

2.7.2 DESCRIPTION OF THE LOW FREQUENCY FORCE

There are four main contributors to low frequency forcing in a surface piercing cylinder:

1) Due to the $u|u|$ term derived from the first order waves based on the integration of the drag force from seabed to the mean water level when integrating the exact force from seabed to mean water level.

2) Due to the $u|u|$ term derived from the integration of the wave force from zero (mean water level) to η (current water level).

3) Due to the bounded superharmonics which sharpen the crest and flatten the trough increasing the velocity at the crest region and decreasing it at the trough region.

4) Due to the bounded subharmonics (bounded long waves) which move with the group of first order waves and have a frequency equal to the frequency of the group.

The first factor broadens the force spectrum compared to the wave elevation spectrum and is accounted for by integrating the drag force between $-\infty$, and 0. This broadening effect can be expressed approximately by the higher order convolution of the velocity field (Gudmestad, Connor, 1983).

The third effect when implemented with the first order waves into the Morison equation and integrated from $z=0$ to $z=\eta$ will lead to a third order force (order of kH^4 and higher) which is negligible. The contribution to this integration when integrating from $z=-\infty$ to $z=0$ is equal to zero [2].

---

[2] This is the Stokes force which tends to zero as the water depth tends to infinity and is explained in section 2.7.4.

The fourth effect will be discussed in depth in section (2.7.8).

The second factor, the low frequency forcing (L.F.F) due to the free surface effect, is a result of the 'groupiness of the waves'. When an individual wave in a group passes a typical leg of an offshore structure , it will exert an average force. This force is a result of the change in the submergence length of the leg combined with the crest velocity being higher than the trough velocity. This average force, is a function of wave height and due to the modulation of the wave height in a first order wave group (a narrow banded process), the resultant force due to the passage of the group will be a function of this slowly varying envelope. This results in a low frequency forcing which is related to the convolution of slowly varying surface elevation envelope shown in Figure 2.8 (The model scale is 1:150).

Since the typical horizontal span of a compliant tower is about 40 meters compared to a 200 meters typical wave length of a deep water wave, the situation can be reasonably approximated as simultaneous crest loading which makes the study of a typical leg of such a platform reasonable.

2.7.3 MODELLING OF NONLINEAR WAVES

Deep water structures are dynamically more sensitive than structures in moderate water depths. In order to do an accurate time domain analysis, nonlinear effects must be considered. Among the nonlinear effects are the water surface elevation effects and the nonlinear water wave kinematics.

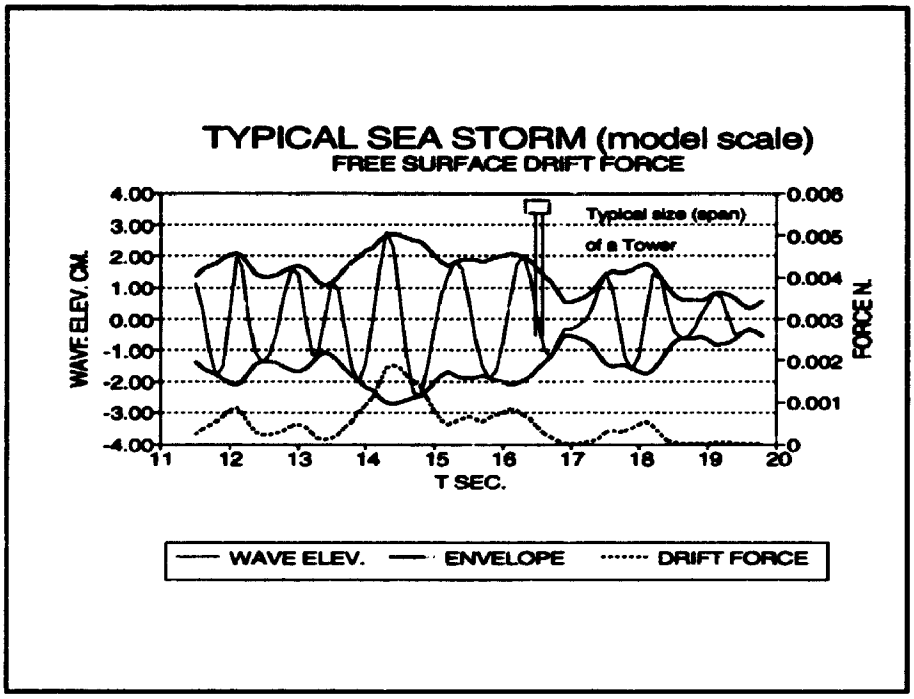

FIGURE 2.8: Free surface drift force on a typical offshore tower.

Usually, in deep water, different extrapolations of the Airy theory are used to predict the crest and trough velocities. Among the available first order engineering approximations are:

1-Direct extension of Airy's theory.

$$u = \frac{\pi H}{T} \frac{\cosh k(z+d)}{\sinh kd} \cos\theta \qquad (2.111)$$

2-Wheeler's stretching method (1970).

$$u = \frac{\pi H}{T} \frac{\cosh kz'}{\sinh kd} \cos\theta \qquad (2.112)$$
$$z' = \frac{zd}{d+\eta}$$

3-Chakrabarti's method (1971)

$$u = \frac{\pi H}{T} \frac{\cosh k(z+d)}{\sinh k(d+\eta)} \cos\theta \qquad (2.113)$$

4-Constant velocity field above the mean water level.

$$u = \frac{\pi H}{T} \frac{\cosh k(z+d)}{\sinh kd} \cos\theta \quad -d<z<0$$
$$u = \frac{\pi H}{T} \frac{\cosh kd}{\sinh kd} \cos\theta \quad 0<z<\eta \qquad (2.114)$$

where $\theta = kx - \omega t$

Prediction of the horizontal water particle velocity by the direct extension of the Airy's theory leads to higher crest velocity and lower (less negative) trough velocity compared to the experimental results obtained by the LASER Velocimeter. The difference between the predicted and experimental results increases with depth. Mathematically, this method

violates the free surface boundary condition as well as the local continuity condition (Laplace equation). However, in deep water waves, the difference given between the prediction given by the linear wave theory and higher order Stokes theories is small and makes this model popular for a first order wave analysis.

Wheeler's stretching method, where the linear velocity profile is stretched to the real surface, (Figure 2.9), predicts higher horizontal velocity under the trough and lower horizontal velocities under the crest compared to linear theory and higher order Stokes theories.

Chakrabarti's method, as is Wheeler's stretching method,is an extension of the linear theory but it takes care of the discontinuity in surface pressure and modifies it so that the dynamic boundary condition is satisfied. As in Wheeler's method, it predicts higher trough velocities and lower crest velocities than the linear theory and higher order Stokes theories.

In the fourth method, the fluid field at any point above the mean water level is considered to be equal to the fluid field at the point on the mean water level with the same horizontal coordinate (Figure 2.9).

Gudmestad and Connor (1986) examined the above methods and noted that none of them satisfy the continuity condition locally, and in addition most of them don't satisfy the nonlinear surface boundary conditions either. Using the second and third methods, they followed the classical steps to solve the full boundary value problem using the perturbation expansion. They come up with a second order solution which satisfies all the boundary conditions exactly except the continuity condition (Laplace equation) which was satisfied in an averaged sense[3] . They finally concluded that Chakrabarti's second order

[3] It follows the procedure used for the numerical solution of vertically averaged flow problems (Dean, 1965).

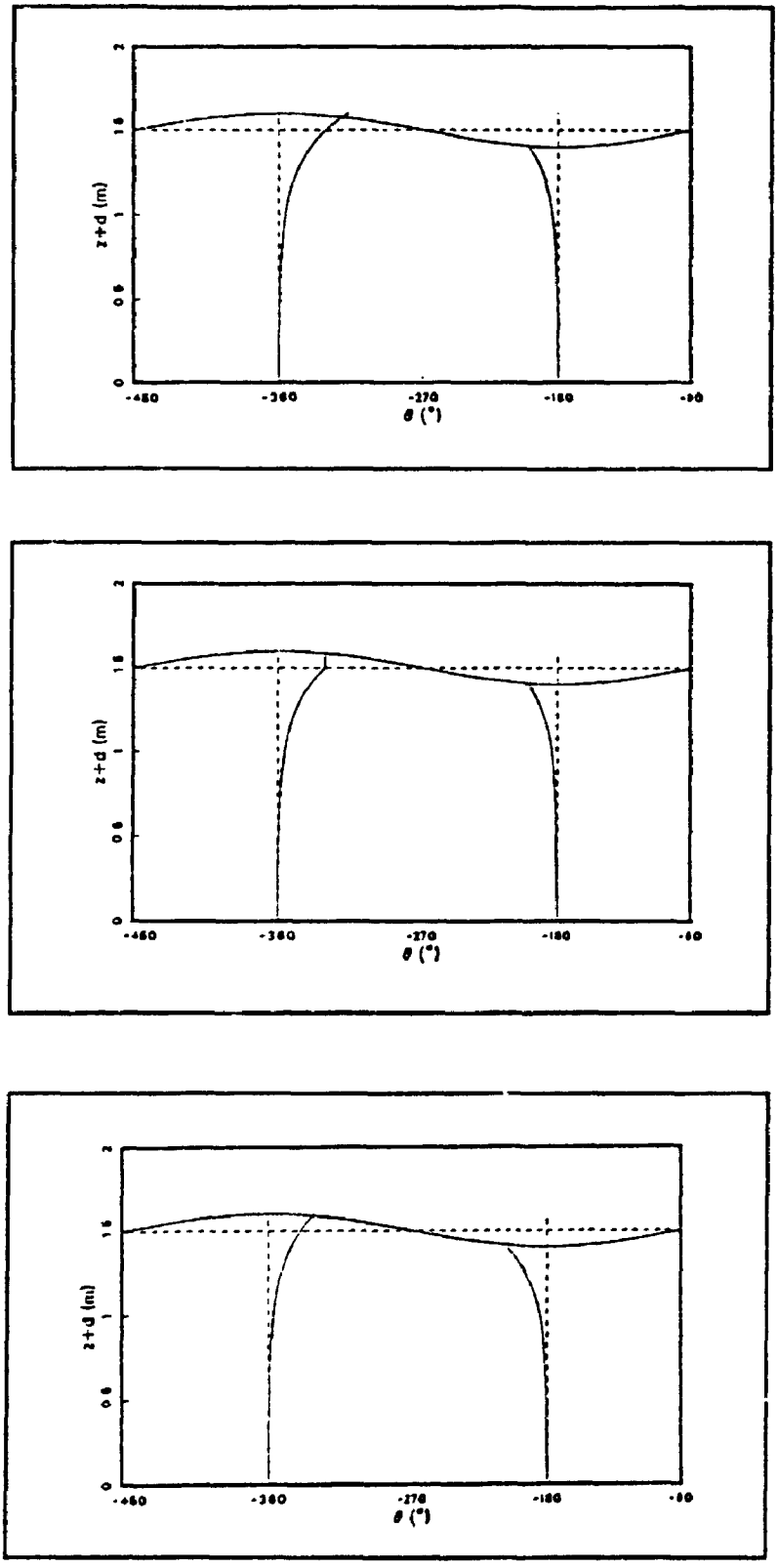

FIGURE 2.9: Different Models for wave kinematics. Extension of Airy's theory (top), constant velocity field in the waterline zone (middle), Wheeler's stretching method (bottom).

extension agrees best with the available experimental observations. This solution is given here in Table 2.1.

Figure 2.10 shows a comparison between different methods and recent measurements using LASER Doppler velocity meter.

As can be seen Chakrabarti's second order expansion, Gudmestad's method, is in close agreement with the experimental results and is based on a correct hydrodynamic description. In this study, this model is used to predict the drift free surface forces and will be discussed in section 2.7.5.

In irregular seas, the situation is more difficult and the existing experimental database is smaller. Discussion in the irregular case is still open and an analytical method does not exist. In industry, the fourth method given above (constant velocity field above the mean water level) is used when dealing with irregular waves, and yields conservative results (however, the prediction in this case is less conservative compared to the first method).

Gudmestad, in 1990, reported an irregular wave theory which is an extension of the second order method mentioned above for the prediction of velocity field. This method combines the use of a linear superposition of sinusoidal wave components for the generation of the irregular waves from a spectrum with the use of an adjustment for the description of the velocity field for each wave component. The velocity field for each component has two terms; the first term consistent with the Chakrabarti's proposal, and the second term which is a first order correction to Chakrabarti's proposal. The second term is required to satisfy the nonlinear free surface boundary conditions and average continuity condition. However, due to its slow convergence, it is only applicable to deep water waves.

TABLE 2.1: Second order Chakrabarti approximation for deep water regular waves.

$$\phi = -\frac{\pi H}{kT}\exp(kz)\sin(kx-\omega t) + \frac{1}{2}\frac{\pi H}{kT}\frac{\pi H}{L}\left[-\exp(kz) + \frac{3}{2}\exp(2kz) - \exp(4kz)\right]\sin 2(kx-\omega t)$$

$$\eta = \frac{H}{2}\cos(kx-\omega t)$$

$$u = \frac{\pi H}{T}\exp(kz)\,oc(kx-\omega t) + \frac{\pi H}{H}\frac{\pi H}{L}\left[-\exp(kz) + \frac{3}{2}\exp(2kz) - \exp(4kz)\right]\cos 2(kx-\omega t)$$

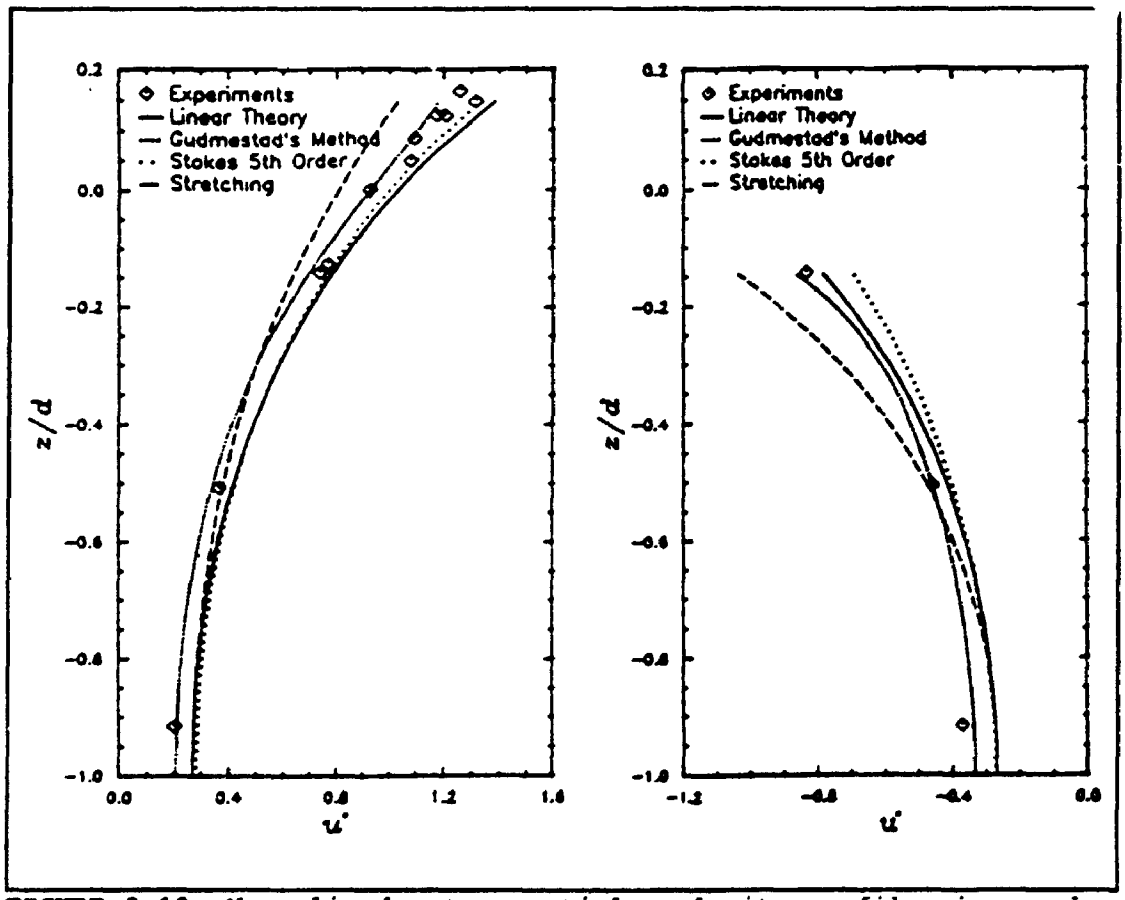

FIGURE 2.10: Normalized water particle velocity profiles in regular waves. Right: maximum horizontal velocity. Left: minimum horizontal velocity (from Gudmestad, 1990).

2.7.4 MATHEMATICAL DERIVATION

In the extension of small amplitude wave theory, using up to the second order term in wave amplitude (Stokes theory), the velocity potential and surface elevation can be written, using perturbation expansion in $\varepsilon=kH/2$;

$$\phi=\varepsilon\phi^{(1)}+\varepsilon^2\phi^{(2)} \tag{2.115}$$

$$\eta=\varepsilon\eta^{(1)}+\varepsilon^2\eta^{(2)} \tag{2.116}$$

Upon substitution of ϕ into the Laplace equation and considering the linear boundary condition at the bottom:

$$\frac{\partial\phi^{(n)}}{\partial z}=0 \quad at \quad z=-d \quad n=1,2 \tag{2.117}$$

and using the Taylor series and perturbation for the nonlinear kinematic and dynamic free surface boundary conditions, the first and second order problems would be:

$$\frac{\partial^2\phi^{(1)}}{\partial t^2}+g\frac{\partial\phi^{(1)}}{\partial z}=0 \quad at \quad z=0 \tag{2.118}$$

$$\eta_1 = -1/g \frac{\partial \phi_1}{\partial t} \qquad at \quad z=0 \tag{2.119}$$

and

$$\frac{\partial^2 \phi^{(2)}}{\partial t^2} + g\frac{\partial \phi^{(2)}}{\partial z} = -\eta^{(1)} \frac{\partial}{\partial z}\left(\frac{\partial^2 \phi^{(1)}}{\partial t^2} + g\frac{\partial \phi^{(1)}}{\partial z}\right) - \frac{\partial}{\partial t}\left(\left(\frac{\partial \phi^{(1)}}{\partial x}\right)^2 + \left(\frac{\partial \phi^{(1)}}{\partial z}\right)^2\right)$$

$$\eta^{(2)} = -1/g\left(\frac{\partial \phi^{(2)}}{\partial t} + \eta^{(1)} \frac{\partial^2 \phi^{(1)}}{\partial z \partial t} + 1/2\left(\frac{\partial \phi^{(1)}}{\partial x}\right)^2 + 1/2\left(\frac{\partial \phi^{(1)}}{\partial z}\right)^2\right) \qquad at \; z=0$$

Upon finding $\phi^{(1)}$, and $\phi^{(2)}$, the velocity potential up to second order in wave amplitude would be:

$$\phi = \frac{\pi H}{kT} \frac{\cosh ks}{\cosh kd} \sin\theta + \frac{3}{16} \frac{\pi H^2}{T} \frac{\cosh 2ks}{\sinh^4 kd} \sin 2\theta$$

and the surface elevation and horizontal water particle velocity up to the second order in wave amplitude would be (Chakrabarti, 1987):

$$\eta = \frac{H}{2}\cos\theta + \frac{\pi H^2}{8L} \frac{\cosh kd}{\sinh^3 kd} (2+\cosh 2kd)\cos 2\theta \tag{2.123}$$

$$u = \frac{\pi H}{T} \frac{\cosh k(z+d)}{\sinh kd} \cos\theta + \frac{3}{4} \frac{\pi^2 H^2}{LT} \frac{\cosh 2k(z+d)}{\sinh^4 kd} cos2\theta \tag{2.124}$$

For deep water , kd tends to infinity and the velocity potential would be:

$$\phi = \frac{\pi H}{kT} e^{(ky)} \sin\theta + O(\epsilon^3) \qquad (2.125)$$

Accordingly, the surface elevation is:

$$\eta = \frac{H}{2}\cos\theta + \frac{\pi H^2}{4L}\cos 2\theta + O(\epsilon^3) \qquad (2.126)$$

It can be shown (Newman, 1986), using the mixed boundary condition on the free surface that [4]:

$$\left(\frac{\partial}{\partial t} + \nabla\phi \cdot \nabla\right)\left(\frac{\partial\phi}{\partial t} + \frac{1}{2}\nabla\phi \cdot \nabla\phi + gz\right) = 0 \quad on\ z = \eta \qquad (2.127)$$

and taking advantage of the Taylor series expansion to expand equation 2.127 from the unknown free surface η to z=0, the 2nd order boundary condition would be:

$$\frac{\partial^2\phi}{\partial t^2} + g\frac{\partial\phi}{\partial z} + 2\nabla\phi \cdot \nabla\frac{\partial\phi}{\partial t} - \frac{1}{g}\frac{\partial\phi}{\partial t}\frac{\partial}{\partial z}\left(\frac{\partial^2\phi}{\partial t^2} + g\frac{\partial\phi}{\partial z}\right) = 0 + O(\epsilon^3) \qquad (2.128)$$
$$on\ z = 0$$

where ∇ is the 2-D gradient operator.

As mentioned before, in deep water waves, the direct substitution of the first order velocity potential, $\phi^{(1)}$, into the above equation will cause all second order terms to vanish. Hence $\phi^{(1)}$ is a solution of the second order boundary value problem. Also, the second order dispersion equation would be the same as the first order one:

---

[4] Dp/Dt=0 on z=η, substantial derivative of pressure on moving surface is equal to zero.

$$\omega^2 = kg \tag{2.129}$$

Using the above information, the total drag force due to a monochromatic wave system on the leg in finite water depth, d, would be:

$$F_D = \int_0^{d+\eta} \frac{1}{2} \rho C_D D \, |u^{(1)} + u^{(2)}| (u^{(1)} + u^{(2)}) \, ds \tag{2.130}$$

and since $u^{(2)} << u^{(1)}$, the Borgman approximation can be used to decouple this force as:

$$F_D = \int_0^{d+\eta} \frac{1}{2} \rho C_D D \, |u^{(1)}| u^{(1)} + 2|u^{(1)}| u^{(2)} \, ds \tag{2.131}$$

Splitting the integration into two parts from 0 to d, and from d to d+η

$$F_D = \frac{1}{2} \rho C_D \left(\int_0^d |u^{(1)}| u^{(1)} \, ds + \int_0^d 2|u^{(1)}| u^{(2)} \, ds + \int_d^{d+\eta} |u^{(1)}| u^{(1)} \, ds + \int_d^{d+\eta} 2|u^{(1)}| u^{(2)} \, ds \right.$$

(2.132)

The first integral is the drag force due to the first order waves. The second integral is the second order Stokes force due to the second order correction on the velocity field. The third integral is the force due to the free surface effects. The last integral is the Stokes force contribution on the free surface zone which is a third order quantity (a first order quantity would be of order H^2) and is negligible.

Upon substitution for $u^{(1)}$, and $u^{(2)}$ and after integration, the second order Stokes force would be:

$$F_D^{(2)}(St) = \frac{1}{64} C_D k H^3 g (\tanh kd) \frac{(3\sinh kd + \sinh 3kd)}{\sinh^5 kd} \cos\theta \cos 2\theta$$

(2.133)

Also, the corresponding Stokes inertial force in the Morison equation is:

$$F_I^{(2)}(St) = \int_0^d C_M \frac{\pi}{4} \rho D^2 \frac{\partial u^{(2)}}{\partial t} ds \qquad (2.134)$$

which upon substitution for $u^{(2)}$ would be:

$$F_I^{(2)}(St) = -\frac{3}{64} \pi D^2 \rho C_M \omega^2 H^2 \frac{\sinh 2kd}{\sinh^4 kd} \sin(2\omega t) \qquad (2.1\ 5)$$

Stokes second order drag and inertia forces are only important in shallow to intermediate water depths and in deep water as d goes to ∞ they tend towards zero because of the hyperbolic terms. In deep water waves, drag and inertia forces do not contribute to the low frequency forcing on the member.

For predicting the low frequency force due to the surface effects, analytical methods as well as the higher order engineering models can be used to integrate the $u|u|$ term. Using an extrapolation of the Airy theorem to model the velocity field between wave crest and trough in monochromatic waves, the $u|u|$ term can be analytically integrated over one wave, and then averaged to get the average force contribution when a single wave passes (Judge 1991).

Using the extrapolation of the Airy's theory (equations 2.111,2.114), the average drag force per wave would be:

$$\overline{F_D^{(2)}(fs)} = \overline{\int_0^{d+\eta} \frac{1}{2}\rho C_D D|u|u\, ds} \qquad (2.136)$$

Upon substituting for u, due to anti-symmetry, $\overline{\int_0^d \ldots |\cos\theta|\cos\theta ds}$ is zero. Using the constant velocity field at the free surface, the right hand side of equation 2.136 can be estimated as:

$$\overline{F_D^{(2)}(fs)} = \frac{1}{2}\rho C_D D\left(\frac{\pi H}{T}\right)^2 \left(\frac{\cosh kd}{\sinh kd}\right)^2 \overline{\eta|\cos\theta|\cos\theta} \qquad (2.137)$$

but:

$$\eta = \eta^1 = \frac{H}{2}\cos\theta \quad , \quad \overline{\cos^2\theta|\cos\theta|} = \frac{4}{3\pi} \qquad (2.138)$$

and using the dispersion equation:

$$\omega^2 = kg\tanh kd \qquad (2.139)$$

the average second order force per wave would be:

$$\overline{F^2{}_D(fs)} = \frac{1}{12\pi}\rho C_D D H^3 \frac{kg}{\tanh kd} \qquad (2.140)$$

and the force itself is:

$$F_D^{(2)}(fs) = \frac{1}{16}\rho C_D D k g H^3 \frac{1}{\tanh kd}|\cos\theta|\cos^2\theta \qquad (2.141)$$

Using the same procedure, the inertia force is:

$$\overline{F_I^{(2)}(fs)} = \overline{\int_d^{d+\eta} \frac{\pi}{4} D^2 \rho C_M \frac{\partial u}{\partial x} ds} \qquad (2.142)$$

After substitution for velocity and averaging (since $\overline{\sin\theta\cos\theta}=0$), the second order free surface inertia force does not contribute to the average force per wave and it is basically a double frequency phenomenon as:

$$F_I^{(2)}(fs) = \frac{\pi}{3\lambda} D^2 \rho C_M k g H^2 \sin 2\theta \qquad (2.143)$$

In a deep water situation, the velocity field would be:

$$u = \frac{\pi H}{T} e^{kz} \cos\theta \qquad (2.144)$$

Substituting for u in equation 2.136, and expanding the exponential function, e^{2kz} , in a Taylor series and taking the exact integration and averaging would yield:

$$\overline{F_D^{(2)}(fs)} = \frac{1}{12\pi} \rho C_D H^3 k g \left(1 + \frac{2}{15}(kH)^2 + \frac{4}{525}(kH)^4 + \ldots\right) \qquad (2.145)$$

This average force is derived using the extension of Airy's theory which does not satisfy the dynamic pressure boundary condition on the free surface. In the next section, the average force due to the free surface effect, based on the second order Chakrabarti method will be derived. In equation 2.145 the first term is the same as equation 2.140 , when considering it for deep water case and the second term is a fourth order quantity (k^3H^5) which is negligible.

$$\overline{F_D^{(2)}(fs)} = \frac{1}{12\pi} \rho C_D D H^3 k g + O(H)^5 \qquad (2.146)$$

Figure 2.11 presents the free surface drag and inertia forces induced by regular waves (equations 2.141, 2.143).

The first term of equation 2.145, as has already been shown, is derived when the same horizontal velocity as that of the mean water level is used between mean water level and instantaneous surface. This method is less conservative than extension of the Airy's theory.

In the case of a floating platform such as a semi-submersible, it is possible to find the mean viscous drag force on the surface zone of the platform which is part of the time in and part of the time out of water.

Second order drift forces derived based on the potential theory are proportional to the square of the wave height while the second order viscous drift forces are proportional to the cube of the wave height. As the wave height (sea state) get's bigger, these viscous effect will be dominating and more important.

2.7.5 SECOND ORDER CHAKRABARTI APPROXIMATION (GUDMESTAD AND CONNOR'S THEORY)

As has already been explained, Chakrabarti's second order approximation was confirmed by the recent DVM measurements in regular waves. This method has been used by the author to derive a more reliable relation for the average second order force in regular waves and then extended to the low frequency forcing in a narrow-banded sea. Using equation 2.132:

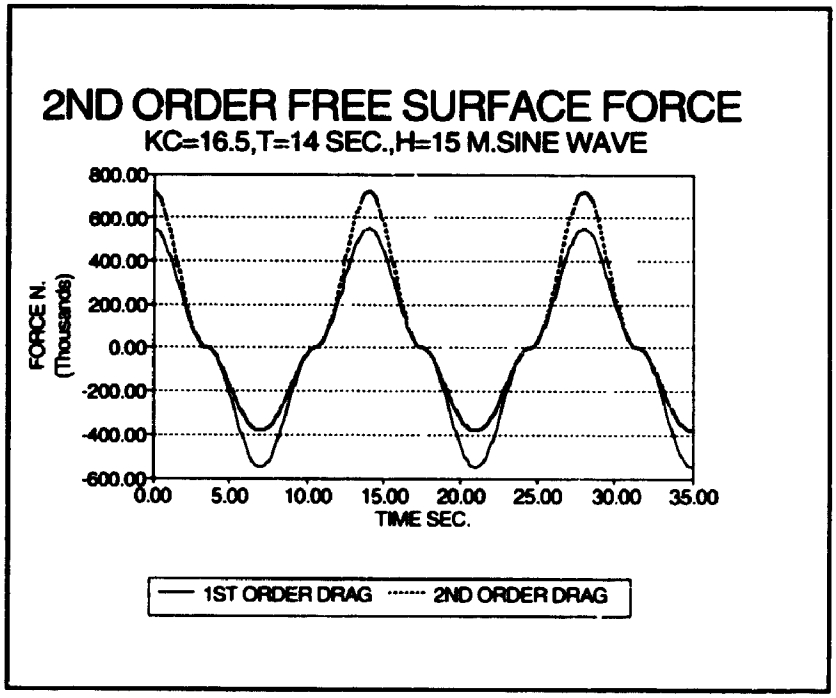

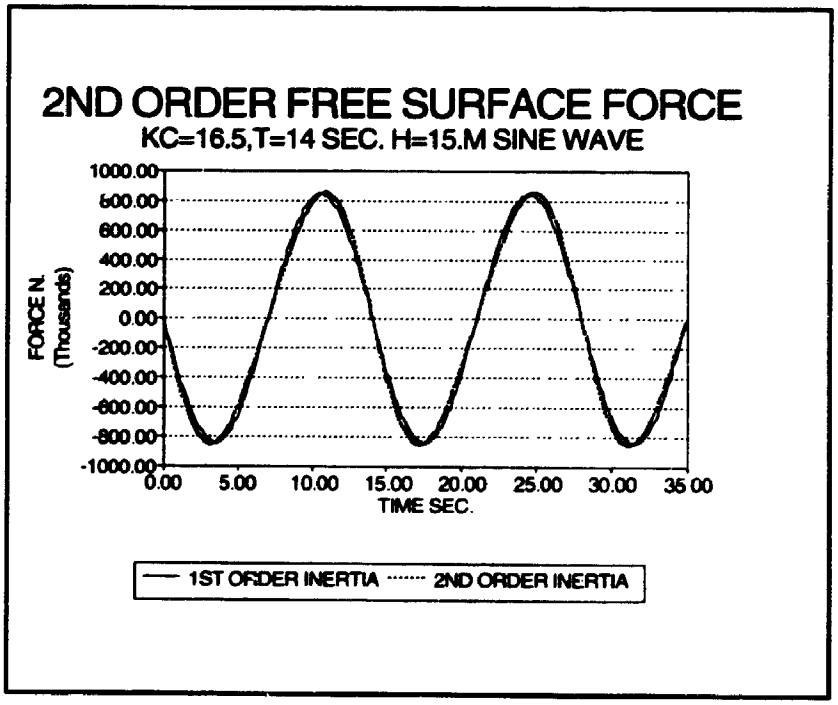

FIGURE 2.11: Free surface induced drag and inertia forces in regular waves

$$\overline{F_D} = \overline{\int_{-\infty}^{\eta} \frac{1}{2}\rho C_D D|u|u\,dz} = \frac{1}{2}\rho C_D D\left(\int_{-\infty}^{0}|u^1|u^1 dz + \int_{-\infty}^{0} 2|u^1|u^2 dz + \int_{0}^{\eta}|u^1|u^1 dz + \int_{0}^{\eta} 2|u^1|u^2 dz\right) \quad (2.147)$$

With the total 'deep water' velocity field given by the above method, (x=0 for simplicity):

$$u = \frac{\pi H}{T}\exp(kz)\cos(\omega t) + \frac{\pi H}{T}\frac{\pi H}{L}\left[-\exp(kz) + \frac{3}{2}\exp(2kz) - \exp(4kz)\right]\cos(2\omega t)$$

where the mean is average per wave.

And the surface elevation is:

$$\eta = \frac{H}{2}\cos(\omega t) \quad (2.149)$$

Again the mean of the first integral would be zero. The mean of the fourth integral has the form of:

$$\rho C_D D\int_0^{\eta} \frac{\pi H^3}{T^2 L}\left[-\exp(2kz) + \frac{3}{2}\exp(3kz) - \exp(5kz)\right]|\cos(\omega t)|\cos(2\omega t)\,dz$$

which upon expanding the exponential terms, multiplication ,averaging and integration leads to a fourth order force as:

$$-\frac{1}{16\pi}\rho C_D D\omega^2 H^3 (k^2 H^2) \quad (2.151)$$

The mean of the third .ntegral on the right hand side of equation 2.147, is the average of the second order forcing d"e to free surface effects (equation 2.146). The second integral is non-zero due to the fact that, in this theory, there is a decrease in horizontal velocity under the crest and an increase under the trough (more negative) compared to linear and higher order stokes theories. The second integral, knowing that:

$$\overline{|\cos(\omega t)|\cos(2\omega t)} = 0.212 \quad (2.152)$$

for finite depth would be:

$$\left(\frac{0.212}{8}\right)\rho C_D D\omega^2 H^3\left(-\frac{1}{5}+\frac{1}{2}\exp(-2kd)-\frac{1}{2}\exp(-3kd)+\frac{1}{5}\exp(-5kd)\right) \tag{2.153}$$

Note that kL=2π. When d is large the exponential terms inside the parenthesis tend to zero.

Finally the total average force in a regular wave for an infinite depth, to the fourth order would be :

$$\overline{F(t)} = \left(\frac{1}{12\pi}-\frac{0.212}{40}\right)\rho C_D D\omega^2 H^3 - \frac{1}{16\pi}\rho C_D D\omega^2 H^3 (k^2H^2)$$
$$= 0.0212\rho C_D D\omega^2 H^3\left(1-\frac{47.112}{16\pi}k^2H^2\right) \tag{2.154}$$

Note that, this force, in the case of a deep water structure, is about 20% smaller than the force predicted by the constant velocity field model and as the depth of submergence decreases the difference between the two models decreases.

It should be mentioned that the error in the following simplification

$$\frac{1}{2}\rho C_D D\overline{\int_0^{\eta}\left(\frac{H\omega}{2}\right)^2|\cos\omega t|\cos\omega t\,dt} - \frac{1}{12\pi}\rho C_D D\omega^2 H^3 \tag{2.155}$$

is less than 2% which is the difference between force evaluation by direct extension of Airy's theory and the constant velocity field model.

Following this approach and developing a method to extract the surface elevation envelope from a bichromatic or an irregular (narrow-banded) sea, it would be possible to

determine the time history of the slowly varying force.

2.7.6 ANALYSIS OF THE LOW FREQUENCY FORCING USING THE CONCEPT OF ENVELOPE IN BICHROMATIC AND RANDOM WAVES

2.7.6.1 BICHROMATIC WAVE

So far the discussion was centered on a monochromatic wave system. In this section, a simple approximation was used to derive an expression for the free surface low frequency forcing in a bichromatic wave, and the result was compared to the result obtained by employing the envelope concept.

Assuming a deep water wave field comprised of two close frequencies ω_1, and ω_2:

$$\eta = \frac{H}{2}\sin\omega_1 t + \frac{H}{2}\sin\omega_2 t \qquad (2.156)$$

$$u = \frac{H\omega_1}{2} e^{k_1 z}\sin\omega_1 t + \frac{H\omega_2}{2} e^{k_2 z}\sin\omega_2 t \qquad (2.157)$$

The velocity field can be simplified to:

$$u = \frac{H}{2}\omega_0 e^{k_0 z}(\sin\omega_1 t + \sin\omega_2 t) = H\omega_0 e^{k_0 z}\sin\omega_0 t\cos\frac{\Delta\omega}{2} t \qquad (2.158)$$

where:

$$\omega_0 = \frac{\omega_1+\omega_2}{2} \quad , \quad k_0 = \frac{k_1+k_2}{2} \qquad (2.159)$$

Upon substitution of equation 2.158 into Morison's equation and considering only the drag force (in a drag dominated member), the free surface force would be:

$$F(t) = \frac{1}{2}\rho C_D D \int_0^{\eta} H^2 \omega_0^2 e^{2k_0 z} \left|\cos\frac{\Delta\omega}{2}t\right| \left(\cos\frac{\Delta\omega}{2}t\right) \left|\sin\omega_0 t\right| (\sin\omega_0 t)\, dz \tag{2.160}$$

Using the constant velocity field model, this force can be written as:

$$F(t) = \frac{1}{2}\rho C_D D H^2 \omega_0^2 e^{2k_0 z} \left|\cos\frac{\Delta\omega}{2}t\right| \left(\cos\frac{\Delta\omega}{2}t\right) \left|\sin\omega_0 t\right| (\sin\omega_0 t)$$
$$\left(H\cos\frac{\Delta\omega}{2}t \sin\omega_0 t\right) dz \tag{2.161}$$

Upon using the following Fourier expansions in equation 2.161:

$$\begin{aligned} \left|\cos\theta\right|\cos^2\theta &= \frac{4}{3\pi} + \frac{8}{5\pi}\cos 2\theta + \frac{8}{35\pi}\cos 4\theta + \ldots \\ \left|\sin\theta\right|\sin^2\theta &= \frac{4}{3\pi} + \frac{8}{5\pi}\sin 2\theta + \frac{8}{35\pi}\sin 4\theta + \ldots \end{aligned} \tag{2.162}$$

the drift force would be:

$$F(t)_{(ref)} = \frac{1}{2}\rho C_D D \omega_0^2 H^3 \left(\frac{16}{9\pi^2} + \frac{32}{15\pi^2}\cos\Delta\omega t + \frac{32}{105\pi^2}\cos 2\Delta\omega t\right)$$

(2.163)

On the other hand the average force for a wave of amplitude E(t) using the constant velocity field model was:

$$F(t) = \frac{2}{3\pi}\rho C_D D\omega_0^2 E^3(t) \qquad (2.164)$$

In the case of the bichromatic wave, E(t) is the envelope of the surface elevation η:

$$\eta = \frac{H}{2}(\sin\omega_1 t + \sin\omega_2 t) = H\cos\frac{\Delta\omega}{2}t\sin\omega_0 t$$
$$E(t) = \left|H\cos\frac{\Delta\omega}{2}t\right| \qquad (2.165)$$

Upon substitution in equation 2.164:

$$F(t) = \frac{2}{3\pi}\rho C_D D\omega_0^2 H^3\cos^2\frac{\Delta\omega}{2}t\left|\cos\frac{\Delta\omega}{2}t\right| \qquad (2.166))$$

and upon performing the Fourier expansion,the expression for the free surface low frequency forces given by the envelope approach would be:

$$F(t)_{(fsf)} = \frac{2}{3\pi}\rho C_D D\omega_0^2 H^3\left(\frac{4}{3\pi} + \frac{8}{5\pi}\cos\Delta\omega t + \frac{8}{35\pi}\cos 2\Delta\omega t + ..\right) (2.167)$$

Note that this equation is the same as the drift force already calculated in equation 2.163.

2.7.7 ANALYTICAL DERIVATION OF THE ENVELOPE FUNCTION, E(t), FOR BICHROMATIC AND RANDOM WAVES

Derivation of the wave elevation envelope for an irregular sea is one of the main issues in calculating the low frequency forces acting on the legs.

Considering a wave group with an envelope of E(t), it is not difficult to show that the low frequency portion of the square of the surface elevation is half of the square of the envelope, E(t).

$$L.F.[\eta^2(t)] = \frac{1}{2}E^2(t) \qquad (2.168)$$

This envelope can be derived analytically by using the Hilbert transform technique. Assuming $\eta(t)$ to be the wave elevation time history of an irregular sea, its Hilbert transform is a real valued, time domain function, $\hat{\eta}(t)$, and X(t) would be an analytical function given as $X(t) = \eta(t) + i\hat{\eta}(t)$. From mathematical point of view, the modulus of X(t) is the envelope of $\eta(t)$, and the phase of E(t) is the phase of X(t). From physical point of view, this modulus is equivalent to the vectorial addition of velocity and elevation at time t (total energy).

The Hilbert transform of $\eta(t)$ is defined as the convolution of $\eta(t)$ and $\frac{1}{\pi t}$:

$$\hat{\eta}(t) = \int_{-\infty}^{\infty} \frac{\eta(s)}{\pi(t-s)}\,ds \qquad (2.169)$$

In brief the Hilbert transform of the function $\eta(t)$ is equivalent to passing $\eta(t)$ through a system which leaves its magnitude (Fourier transform or spectrum) unchanged but will shift its phase by the value of $\frac{\pi}{2}$ at each positive frequency. In other words when the signal is $\sin\omega t$, its Hilbert transform would be $\cos\omega t$ and vice versa.

Using this property and noting that Hilbert transforms are linear operators the envelope of the bichromatic wave system becomes:

$$\eta(t) = \frac{H}{2}(\sin\omega_1 t + \sin\omega_2 t) \qquad (2.170)$$

would be the modulus of X(t):

$$X(t) = \frac{H}{2}(\sin\omega_1 t + \sin\omega_2 t) + i\frac{H}{2}(\cos\omega_1 t + \cos\omega_2 t) \qquad (2.171)$$

Which on squaring the real and imaginary parts, adding them and finally taking the square root will lead to the envelope function:

$$E(t) = |X(t)| = |H\cos\frac{\Delta\omega}{2}t| \qquad (2.172)$$

In the case of an irregular sea, the sea surface elevation at a fixed point can be simulated using:

$$\eta(t) = \sum_{i=1}^{N} a_i \sin(\omega_i t + \phi_i) \qquad (2.173)$$

Where a_i , ϕ_i are the amplitude and random phase for each component.

Taking the Hilbert transform of $\eta(t)$, its imaginary part would be:

$$\tilde{\eta}(t) = \sum_{i=1}^{N} a_i \cos(\omega_i t + \phi_i) \qquad (2.174)$$

and its envelope square is:

$$E^2(t) = \eta^2(t) + \tilde{\eta}^2(t) = \sum_{i=1}^{N} \sum_{j=1}^{N} a_i a_j \cos(\Delta\omega_{ij} t + \Delta\phi_{ij}) \qquad (2.175)$$

Thus the square root of $E^2(t)$ would be the analytical envelope function for a general irregular wave train. With this envelope, the low frequency forcing due to the free surface effects would be given by equation 2.163.

In equation 2.163, a mean wave frequency is used which is defined on the basis of

$$\omega^2 = \left(\frac{m_1}{m_0}\right)^2 \quad or \quad \omega^2 = \frac{m_2}{m_0} \quad where \; m_i = \int_0^{\infty} \omega^i S(\omega)\, dw \qquad (2.176)$$

The second form (zero crossing frequency) is preferred and gives better results.

Figure 2.12 presents the time history of a random sea and its envelope which is calculated by the above mentioned method. The corresponding predicted drift force spectrum is also shown in the same Figure.

In chapter four the numerical evaluation of the envelope of a given sea state in time domain, using harmonic analysis is described. The corresponding low frequency forces are then compared to the experimental results obtained in the wind/wave tank facility.

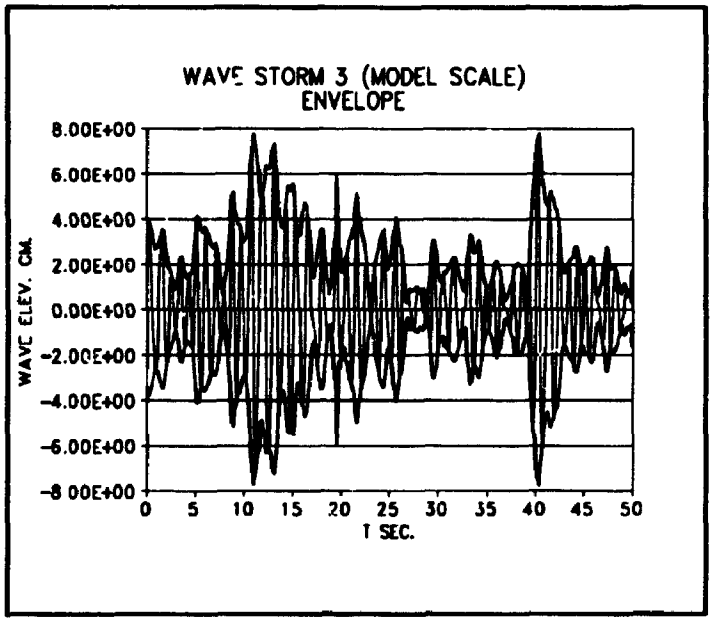

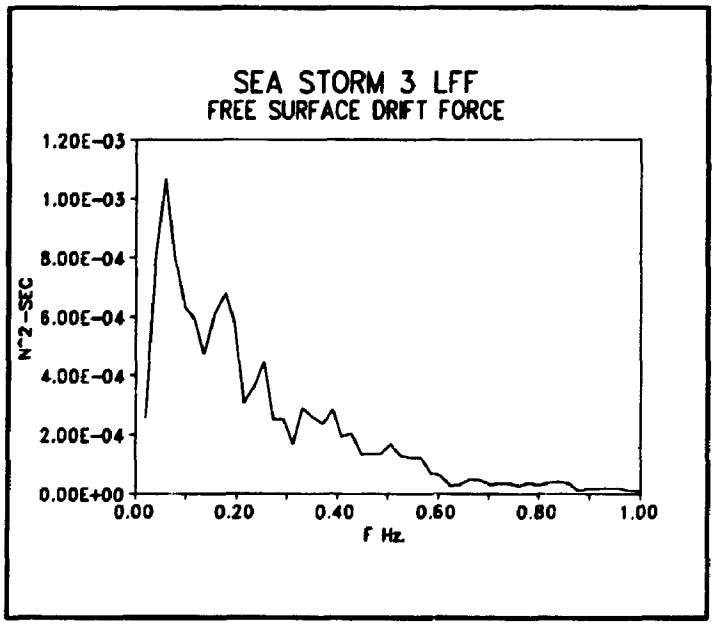

FIGURE 2.12: Envelope of wave elevation in a random sea and the corresponding free surface drift force spectrum

2.7.8 BOUNDED LONG WAVES AND THE ASSOCIATED FORCE

Bounded long waves in the natural sea and physical models and their loading on slender drag dominated surface piercing cylinder are investigated in following sections.

2.7.8.1 INTRODUCTION AND BACKGROUND THEORY

The description and reproduction of grouped waves and all the second order grouped induced waves are important for the response evaluation of the offshore structures. In this section the generation of the long waves in nature and in the laboratory and their mathematical derivation are reviewed.

For simulation of wave fields in numerical and experimental models the first order approximation is often used. In order to describe the natural waves in an irregular sea, the Laplace equation with the related boundary conditions often needs to be solved. The mathematical solution to this problem is available by the use of the regular perturbation technique or by the application of momentum equations . The solution of this problem up to the second order brings about two new waves for each pair of frequencies - the bounded long wave or subharmonic (Bowers, 1977; Ottesen Hansen, 1978), and the bounded super harmonic (Sand, Mansard, 1986).

Longuet Higgins, and Stewart (1964) reported that the variation of the radiation stress in grouped waves is the reason for the formation of long period waves. These waves are bounded to the groups and travel with the group velocity. Their typical periods are from 20 to 100 seconds (full scale).

The second harmonic is basically a double frequency phenomenon which sharpens the crest of the first order waves and flattens the trough. Their typical periods are from 2 to

10 seconds.

Figure 2.13 shows a review of the first and second order phenomena for a pair of frequencies fn,fm. This figure shows that the second harmonic include self interaction terms 2fn, and 2fm (Stokes waves), and the mutual component, fn+fm, which forms another grouping pattern in itself.

In this work, the first kind of waves, the long period waves are of interest. On the basis of the linearity of the first order problem in $\phi^{(1)}$, each of the wave components (sinusoidals) in an irregular sea can be treated separately and then added to obtain the velocity potential due to all of the components. Once the velocity potential, $\phi^{(1)}$, is known, the second order problem can be solved with the related boundary conditions to find $\phi^{(2)}$ and finally $\eta^{(2)}$ (Otteson Hansen, 1978) as:

$$\eta(x,t) = \sum_{n=1}^{N} a_n \cos(\omega_n t - k_n x + \phi_n) \qquad (2.177)$$

$$\eta^{(2)} = \sum_{n=1}^{N-1} \sum_{m=n+1}^{N} a_n a_m G_{nm} \cos\left((\omega_n - \omega_m)t - (k_n - k_m)x + (\phi_n - \phi_m)\right) \qquad (2.178)$$

where G_{nm} is the transfer function which will be discussed later. These are the incident natural bounded long waves, set down, which are responsible for part of the drift force and low frequency resonant response for compliant structures. From the above equation it is clear that they are of a second order nature and the amplitude is proportional to the square of the wave heights. It is also possible to show that they travel with the group velocity and that they follow groups (Mansard and Sand, Sub. and super harmonics in natural waves). In the next section, the velocity field due to this incident wave is used to see whether the corresponding slowly varying force is important in slender structures.

Generally, when a first order wave train is generated in a wave tank by a first order signal, automatically a group of second order waves other than the bounded long waves will be generated. This phenomenon happens due to the use of the first order signal, and a second order signal is necessary to remove the other generated long waves which do not exist in nature. The second order control signal required is described by Bowers (1980), and Sand (1982). A brief explanation follows.

The equations describing the situation in a wave flume with a given type of wave board are the same as equations 2.1 to 2.4 except for the addition of a new boundary condition at the position of the wave generator (Figure 2.14). This boundary condition states that at the front of board the velocity normal to the board at every point is equal to the velocity of fluid in the same direction (Barthel et. al., 1983):

$$V_n = u\cos\theta - v\sin\theta \qquad (2.179)$$

where u, and v are the horizontal and vertical first order water particle velocities.

The position of the wave generator is given as:

$$X(z,t) = f(z)X_0(t) \qquad (2.180)$$

where $X_0(t)$ is a generalised coordinate for the motion of the board, and f(z) is a function depending on the geometry of the paddle.

Again, the solution leads to a first and a second order problem. After solving the first order problem and substituting the first order velocity potential and control signal, $\phi(1)$ and $X_0^{(1)}$, into the second order problem, the solution results in some sinusoidal terms with sum and difference frequencies.

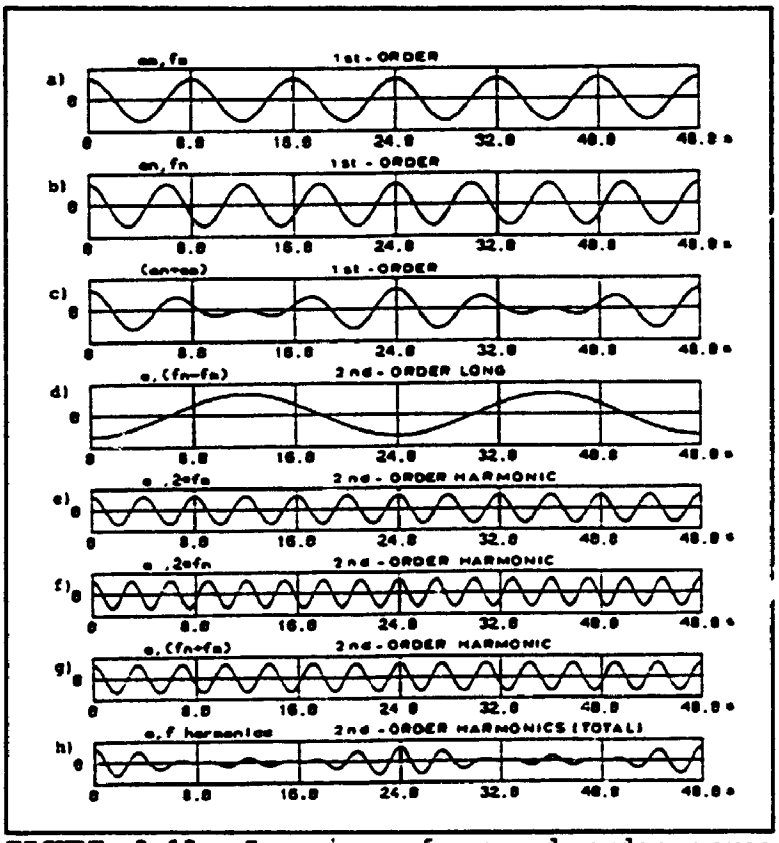

FIGURE 2.13: Grouping of second order waves induced by first order bichromatic waves (from E.P.D.Mansard, et al., 1987)

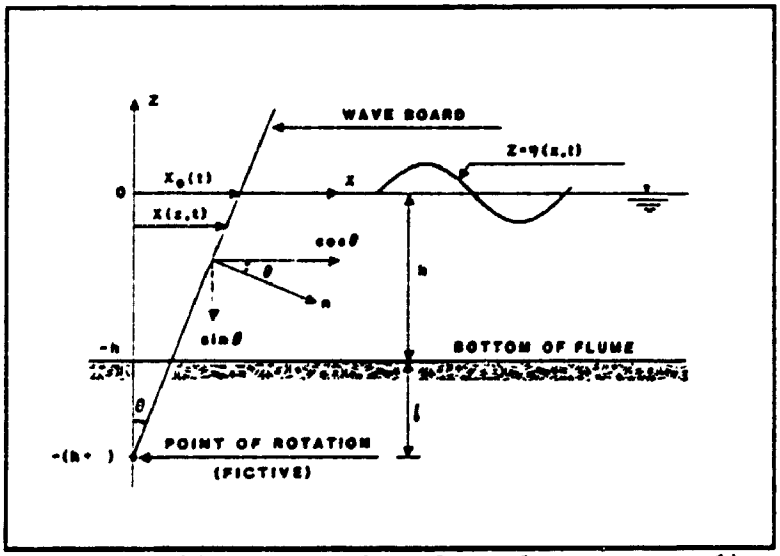

FIGURE 2.14: Wave board and corresponding boundary conditions (from Barthel, et al., 1983).

Since only difference terms contribute to long waves, it is possible to solve the second order problem by ignoring sum terms and find the second order signal $X_0^{(2)}$,$\phi^{(2)}$ and $\eta^{(2)}$ on the condition that no free long waves are allowed to occur. The complete solution can be found in Barthel et. al. (1983), but the general procedure is mentioned here.

1) Solve the 1st order problem which results in $\phi^{(1)}$,$X_0^{(1)}$.

2) Solve the second order problem considering the additional condition that no free long waves are permissible,i.e. finding the second order signal $X_0^{(2)}$.

Due to the linearity of the second order problem in $\phi^{(2)}$, it is possible to write the total velocity potential as the superposition of three different velocity potentials:

$$\phi^{(2)} = \phi^{(21)} + \phi^{(22)} + \phi^{(23)} \qquad (2.181)$$

From these three potentials, $\phi^{(21)}$ is the one which generates the second order bounded long waves and doesn't need to satisfy any boundary condition at the wave board.

$\phi^{(22)}$ has to satisfy the complete boundary condition at the wave board due to the first order motion of the wave board, and due to the already generated long waves. This boundary condition is:

$$\phi_x^{(22)} = -X_0 \left(f(z) \phi_{xx}^{(1)} - \frac{1}{h+1} \phi_z^{(1)} \right) - \phi_x^{(21)} \qquad at\ x=0 \qquad (2.182)$$

The first two terms will generate two different free long waves. The first is associated with the local disturbances at the board location and goes to zero as the waves are propagating along the tank (local disturbance wave), and the second is due to the first order displacement of the wave board (displacement wave). The third free long wave is due the third term in the above equation and it is associated with the already generated

bounded long wave, it is called a parasitic long wave. They are called free since they do not move with the first order wave group and they have a different phase velocity.

All of these three spurious long waves should be removed by means of a second order paddle signal $X_0^{(2)}$. So the last part of the second order problem in $\phi^{(23)}$ would be solved to find $X_0^{(2)}$ for a correct generation of grouped waves with only the natural bounded long waves.

The solution for $\phi_{nm}^{(21)}$ for a pair of frequencies fm, and fn is given by Otteson Hansen (1978) as:

$$\phi_{nm}^{(21)} = \frac{\Delta\omega_{nm}}{\Delta k_{nm}} G_{nm} \frac{\cosh\Delta k_{nm}(z+h)}{\sinh\Delta k_{nm}h} a_m a_n \cos(\Delta\omega_{nm}t - \Delta k_{nm}x + \Delta\phi_{nm}) \quad (2.183)$$

$G_{nm}h$ is a dimensionless transfer function and is given as:

$$G_{nm}h = \frac{\frac{4\pi^2 D_n D_m \Delta k_{nm}h\cosh(\Delta k_{nm}h)}{\cosh(k_n h + k_m h) - \cosh(\Delta k_{nm}h)} + \frac{\Delta k_{nm}h(D_n - D_m)(k_n hD_m + k_m hD_n)\coth(\Delta k_{nm}h)}{2D_n D_m} - 2\pi^2(D_n D_m)^2 \Delta k_{nm}h}{4\pi^2(D_n - D_m)^2\coth(\Delta k_{nm}h) - \Delta k_{nm}h} \quad (2.184)$$

where

$$D_n = \left(\frac{h}{g}\right)^{0.5} f_n \quad (2.185)$$

$$D_m = \left(\frac{h}{g}\right)^{0.5} f_m \quad (2.186)$$

g = gravity constant

h = water depth

The final solution for $\phi^{(21)}$ is found by superposition of all combinations of the first order

components (fm, and fn) in the wave spectrum i.e.

$$\phi^{(21)} = \sum_{n=1}^{N-1} \sum_{m=n+1}^{N} \phi_{nm}^{(21)} \qquad (2.187)$$

where N is the total number of wave components

Also the total bounded long wave elevation would be:

$$\eta^{(2)} = \sum_{n=1}^{N-1} \sum_{m=n+1}^{N} \eta_{nm}(t) \qquad (2.188)$$

For a pair of components fn, and fm the first order elevation would be:

$$\eta^{(1)} = a_n \cos(\omega_n t - k_n x + \phi_n) + a_m \cos(\omega_m t - k_m x + \phi_m) \qquad (2.189)$$

and the corresponding bounded long wave elevation is:

$$\frac{\eta_{nm}}{h} = \frac{a_n a_m}{h^2} (G_{nm} h) \cos(\Delta\omega_{nm} t - \Delta k_{nm} x + \Delta\phi_{nm}) \qquad (2.190)$$

The nondimensional transfer function is shown in Figure 2.15 for various ratios of long wave frequency to short wave frequency, $\Delta f/f$.

In nature, wave groups may contain typically from 4 to 10 waves, which means that $\Delta f/f$ ratio would be in the range of 0.1 to 0.25.

It is seen from the figure that the bounded long wave amplitude is greatly amplified in shallow water situation. This figure can be used to find the amplitude of a bounded long wave in a natural wave train.

In deep water waves which are the subject of this thesis, the free displacement waves

seem to be more important and the function of the second order signal is to remove these waves . The bounded long waves are small in a deep water situation and, as will be shown later, their effect on the low frequency forcing on a drag dominated body is negligible.

In model tests in deep water simulations with a first order paddle signal, long waves are generally exaggerated (Sand, 1982) and as a result the sway motions measured for sensitive compliant structures is also exaggerated.

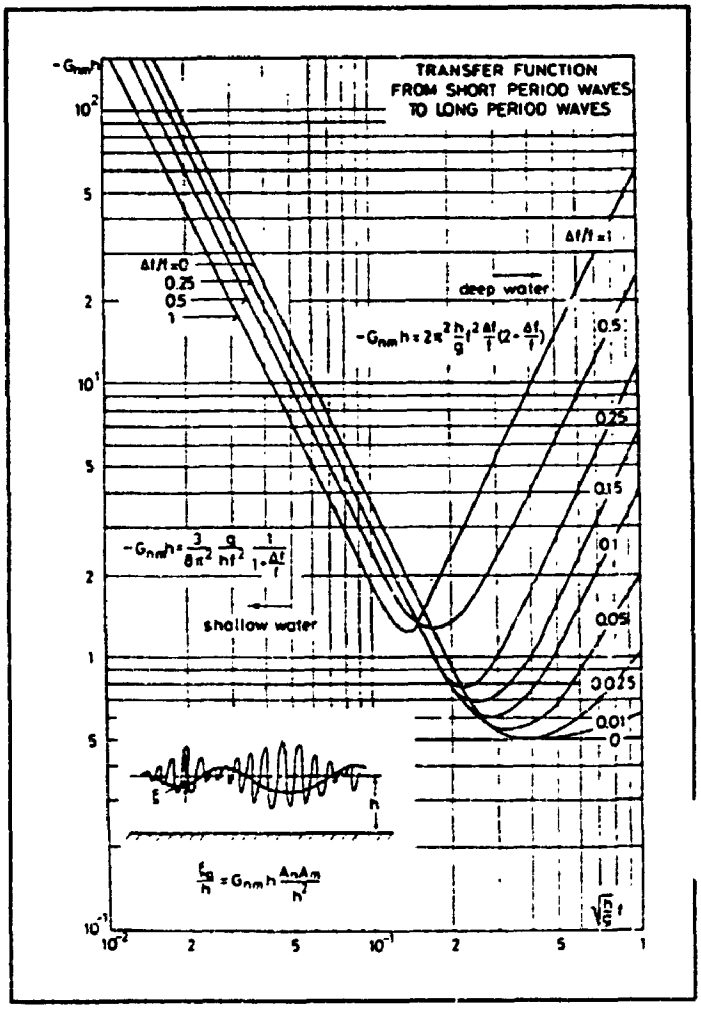

FIGURE 2.15: Second order incident wave (bounded long wave) transfer function induced by a bichromatic wave system (from S.E. Sand, 1982).

2.7.8.2 BOUNDED LONG WAVES AND THEIR CONTRIBUTION TO THE LOW FREQUENCY FORCING ON A DRAG DOMINATED MEMBER

Assuming m=1, and n=2 , the total velocity field due to the superposition of the first order wave group and the associated bounded long wave will be given. The drag term in Morison's equation is used to derive the total low frequency forcing due to both free surface effect and bounded long waves. Finally a comparison is made regarding the relative importance of these two effects.

For simplicity, it is assumed that the two first order wave components have an equal wave height, H, which simplifies the analysis but does not reduce its generality.
The transfer function $G_{nm}h$ is given in equation 2.184. After doing some mathematical rigour for deep water situation G_{12} would be:

$$G_{12}=\frac{2\pi^2}{g}(f_2^2-f_1^2) \qquad (2.191)$$

Noting that:

$$\omega_1^2=k_1 g \quad , \quad \omega_2^2=k_2 g \quad , \quad \Delta k_{12}=\frac{4\pi^2}{g}(f_2^2-f_1^2) \qquad (2.192)$$

and

$$D_2-D_1=\left(\frac{h}{g}\right)^{0.5}(f_2-f_1) \qquad D_1=f_1\left(\frac{h}{g}\right)^{0.5} \qquad (2.193)$$

The velocity due to this second order bounded long wave is

$$u^{(2)} = \eta_{12} \bar{u}_{(k1,k2)} \Delta\omega_{12} e^{\Delta k_{12} z} \qquad (2.194)$$

where $\bar{u}$, a correction factor to the hyperbolic velocity profile which is induced by the long waves, is given by:

$$\bar{u}(k1,k2) = 1 + \left(\frac{K_1 K_2 (1 - T_1 T_2)}{16\pi^2 D_1 D_2 G_{12} h} - \frac{\pi^2 (D_2 - D_1)^2}{G_{12} h}\right)\left(\frac{k_{12} h \tanh k_{12} h}{4\pi^2 (D_2 - D_1)^2}\right) \qquad (2.195)$$

where:

$$K_i = k_i h \qquad T_i = \tanh k_i h \qquad (2.196)$$

For deep sea, the velocity correction factor would be:

$$\bar{u}(k_1, k_2) = 1 - \frac{\Delta k_{12}}{4 G_{12}} \qquad (2.197)$$

which upon substitution for G_{12}, this correction factor would be less than one, but the value of one is used in order to be on the conservative side.

Note that the linear dispersion equation for deep see condition has been used for the above derivations. Hence the velocity would be:

$$u^{(2)} = a_1 a_2 G_{12} \bar{U}_{12} \Delta\omega_{12} e^{z\Delta k_{12}} \cos(\Delta\omega_{12} t - \Delta k_{12} x + \Delta\phi_{12}) \qquad (2.198)$$

Upon substitution and assuming $a_1=a_2=H/2$:

$$u^{(2)} = -\frac{1}{8g} H^2 (\omega_1+\omega_2) (\Delta\omega_{12})^2 e^{z\Delta k_{12}} \cos(\Delta\omega_{12} t - \Delta k_{12} x + \Delta\phi_{12}) \quad (2.199)$$

From now on, x is set to zero and the notation is simplified as:

$$\Delta k_{12} = \Delta k \quad \Delta\omega_{12} = \Delta\omega \quad \Delta\phi_{12} = \Delta\phi \quad (2.200)$$

The velocity field due to the first order wave group, on the condition that $\Delta\omega/\omega$ is less than 0.25, which is the case in grouped waves in sea, can be written as equation 2.158:

$$u^{(1)} \approx \frac{\omega_0 H(t)}{2} e^{k_0 z} \cos(\omega_0 t + \phi_0) \quad (2.201)$$

$$\phi_0 = \frac{\phi_1+\phi_2}{2}$$

where

$$H(t) = 2H \cos\left(\frac{\Delta\omega}{2} t + \frac{\Delta\phi}{2}\right) \quad (2.202)$$

By doing a simple order of magnitude analysis, it can be shown that $u^{(1)} >> u^{(2)}$, since $u^{(2)}$ is a second order quantity.

The load per unit length on a drag dominated surface piercing leg according to Morison's equation would be:

$$F_{unit} = \frac{1}{2} \rho C_D D |u^{(1)} + u^{(2)}| (u^{(1)} + u^{(2)}) \quad (2.203)$$

In the above equation, the addition of a superharmonic (sum effect) to the velocity field would result in a high frequency phenomena which is of no interest in this study. Since u(1)>>u(2), the Borgman approximation reduces equation 2.203 to:

$$F_{unit} = \frac{1}{2}\rho C_D D\left(u^{(1)}|u^{(1)}| + 2u^{(2)}|u^{(1)}|\right) \tag{2.204}$$

The total low frequency forcing now would be:

$$L.F.\ [F(t)] = L.F.\left(\frac{1}{2}\rho C_D D\int_{-\infty}^{\eta} F_{unit}\,dz\right) \tag{2.205}$$

where L.F. stands for the low frequency part, or

$$L.F.\ [F(t)] = L.F.\left(\frac{1}{2}\rho C_D d\left(\int_{-\infty}^{0}|u^{(1)}|u^{(1)}\,dz + \int_{-\infty}^{0} 2u^{(2)}|u^{(1)}|dz + \int_{0}^{\eta}|u^{(1)}|u^{(1)}\,dz + \int_{0}^{\eta} 2u^{(2)}|u^{(1)}|dz\right)\right) \tag{2.206}$$

The low frequency forcing due to the first term on the right hand side has already been discussed in sections 2.6.5, 2.7.2 and leads to the high order convolution integrals in force spectral analysis.

By an order of magnitude analysis, the fourth term is shown to be a fourth order quantity and is negligible compared to the other terms.

The second term is a second order force and is due to the bounded long waves. In the following, the magnitude of this force is compared to that of the free surface force.

Substituting $u^{(1)}$, and $u^{(2)}$ into the second term and integrating with respect to z and

noting that:

$$\frac{3k_2-k_1}{2} > k_2 \ , \quad k_2 g = \omega_2^2 \ , \quad \omega_2 > \omega_0 \tag{2.207}$$

it is easy to show that the low frequency portion of the second term is smaller than:

$$\frac{1}{2}\rho C_D D\left(-\frac{H^3}{2}(\Delta\omega)^2\left|\cos\left(\frac{\Delta\omega}{2}t+\frac{\Delta\phi}{2}\right)\cos(\omega_0 t+\phi_0)\right|\cos(\Delta\omega t+\Delta\phi)\right.$$

(2.208)

Also when we integrate with respect to z, and use a constant velocity field model at the water line zone, the third term would be:

$$\frac{1}{2}\rho C_D D\left(\omega_0^2 H^3\left|\cos\left(\frac{\Delta\omega}{2}t+\frac{\Delta\phi}{2}\right)\right|\cos^2\left(\frac{\Delta\omega}{2}t+\frac{\Delta\phi}{2}\right)\left|\cos(\omega_0 t+\phi_0)\right|\right.$$
$$\left.\cos^2(\omega_0 t+\phi_0)\right)$$

(2.209)

Now perform a simple Fourier analysis and expand the above two equations using:

$$\left|\cos\theta\right| = \frac{2}{\pi}+\frac{4}{3\pi}\cos 2\theta-\frac{4}{15\pi}\cos 4\theta \quad \ldots \tag{2.210}$$

$$\left|\cos\theta\right|\cos^2\theta = \frac{4}{3\pi}+\frac{8}{5\pi}\cos(2\theta)+\frac{8}{35\pi}\cos(4\theta)-\frac{1}{40\pi}\cos(6\theta) \quad \ldots$$

(2.211)

the low frequency forcing due to the second term would be:

$$L.F.\ F_{BLW} = -\frac{1}{2}\rho C_D \frac{H^3}{2}(\Delta\omega)^2\left(\frac{4}{3\pi^2}+\frac{56}{15\pi^2}\cos(\Delta\omega t+\Delta\phi)\right.$$
$$\left.+\frac{4}{3\pi^2}\cos(2\Delta\omega t+2\Delta\phi)-\frac{4}{15\pi^2}\cos(3\Delta\omega t+3\Delta\phi)\ \ ..\right.$$

(2.212)

and the low frequency forcing due to the third term, including the mean force, would be:

$$L.F.\ F_{surf.} = \frac{1}{2}\rho C_D D H^3(\omega_0)^2\left(\frac{16}{9\pi^2}+\frac{32}{15\pi^2}\cos(\Delta\omega t+\Delta\phi)+\frac{32}{105\pi^2}\cos(2\Delta\omega t+2\Delta\right.$$
$$\left.-\frac{1}{30\pi^2}\cos(3\Delta\omega t+3\Delta\phi)\right)\ \ ..$$

(2.213)

As can be seen by equations 2.212, 2.213, the ratio of the force amplitudes at the corresponding frequencies is:

$$\frac{F^{BLW}_{i\Delta\omega}}{F^{surf.}_{i\Delta\omega}} = \left(\frac{1}{2}\right)\left(\frac{\Delta\omega}{\omega_0}\right)^2\left(\frac{A_i}{B_i}\right) \qquad (2.214)$$

where A_i, and B_i are the amplitudes of the corresponding harmonics given in equations 2.212,2.213 respectively.

Since, in nature, groups typically contain from 4 to about 10 waves, the frequency ratio would be:

$$0.1 < \frac{\Delta\omega}{\omega_0} < 0.25 \qquad (2.215)$$

Upon substitution of equation 2.215 in equation 2.214, maximum of the ratio of the forces due to the bounded long waves and free surface effect, for the zero (mean), first, second, and third harmonics would be 2.35%, 5.5%, 13.4%, 24.4% respectively. It is seen that for higher harmonics, the contribution due to the bounded long waves decreases, and from the point of view of the structural response, the third and higher harmonics (even in the case of free surface forcing) are very small and therefore insignificant. The total drift force due to both contributions from free surface and bounded long waves is found by superposition of all the combinations of the first order components (f_m, and f_n) in the narrow banded wave spectrum. The above argument is valid for every single pair of frequencies. So the low frequency force due to bounded long wave is, at most, around one tenth of the water line contribution, and since the free surface drift force itself is small and is only important in high sea states, the contribution of bounded long waves is negligible.

CHAPTER 3

DYNAMIC ANALYSIS

3.1 INTRODUCTION

The analysis of wind and wave loads are of fundamental importance in the design of offshore structures from the view point of safety, serviceability and economy of the structures.

The rational approach considers the stochastic nature of the individual environmental loads and their combination together with the dynamic character of the structural response. An accurate representation of the stochastic nature of these loads is important when the dynamic and nonlinear effects of the response is required. In this context, dynamically sensitive deep water compliant towers become more attractive. These platforms respond to the excitation by some kind of soft rigid body modes as well as structural oscillations and withstand the external loading, highly through their inertia rather than their stiffness.

Typically, the period of the fundamental vibration mode is longer than the peak period of the first order waves, and period of the second vibration mode is shorter than the peak period of the wave energy spectrum. Nonlinearities of the sea loading as discussed in chapter 2, are mainly associated with the drag term of the Morison's equation as well as the effect of the variation of the wave elevation(free surface effects), and increases with the slenderness of the members.

The dynamic analysis of the compliant tower can be performed in time and frequency domain. Here these analyses are referred to as nonlinear stochastic time domain analysis and frequency domain analysis. In the former the nonlinearities associated with the system

loading is considered, while in the latter, the system and loading is linearized and the relation between the system response and applied loads, using the principle of superposition, is given by a linear transfer function and the possible nonlinear loads should be expressed by higher order statistics (convolution).

Significant efforts (Taylor, Rajagopalar, 1982 a,b; Wu, McDermott, 1976; Borgman, 1976; Malhotra, Penzien, 1970; Dao, Penzien, 1980) have been done to express the nonlinear force and developing computer based methods for rational stochastic, dynamic analysis of offshore platforms.

The principal intent of this chapter is to introduce the above mentioned two methods and demonstrate the effect of nonlinearities in the wave load formulation and the effect on structural responses with the variation of sea states. The wind and wave storms were adopted from ESDU data (ESDU 1985) and JONSWAP spectrum respectively. The dynamic analyses are performed on a 1:150 scaled model of a typical compliant tower.

3.2 SYSTEM MODELLING FOR DYNAMIC ANALYSIS

The use of the scaling laws in the analysis and design of engineering systems is well known. When, for example, analytical tools are insufficient to allow detailed calculations of a proposed large scale system, a scale model may be constructed and laboratory measurements performed with proper scaling relations, to predict the full scale behaviour. In the next two sections a typical compliant tower is roughly calculated to be able to safely resist wind/wave loads on the basis of a typical extreme wind loading and single wave theory with assumed design values for H_s,T_p corresponding to a 50 year return period in the Gulf of Mexico. This deep water tower is then scaled using the scaling laws and is reduced to a single stick model on which the detailed dynamic analysis and experiments are performed. It is worth to mention that the stick model used is a hollow

aluminum rod with a diameter of 1.905 cm which is the same as the member used for other experiments performed in this thesis, including experiments to evaluate CD,CM coefficients and low frequency forcing, explained later in chapter 4.

3.2.1 SIMPLIFIED CALCULATION OF A TYPICAL COMPLIANT TOWER

After doing some preliminary analysis for dimensioning of the tower Figure 3.1 shows the general tower dimensions as well as the platform's.

The base of the structure is rigidly fixed to the sea bottom by deep penetration of pile clusters so that no articulation is allowed for. The water depth for the assumed structure is 610 meters with a free board of about 20 m. The design parameters are: Tp=14. sec., Hs=15. m., wind speed=50. m/sec C_M=1.8, C_D=1.4. Mass of the platform is $1*10^7$ kg. Also dimension of the jacket members are:

Eight main legs, D(outside)=2.5 m., t=0.1 m.

Diagonal bracing, D=1.0 m., t=0.05 m.

In the last 45 meters the diameter of the main legs are increased to 3.25 m.

The analysis was done using one mode shape:

$$\phi(z)=1-\cos(\frac{\pi z}{2L}) \qquad (3.1)$$

to calculate the stiffness and mass of the structure in the wet condition (members filled). The geometric stiffness was also taken in to consideration.

The first natural period of such an structure would be about 32. sec. Calculation of the structure for strength was done using the equivalent static force approach:

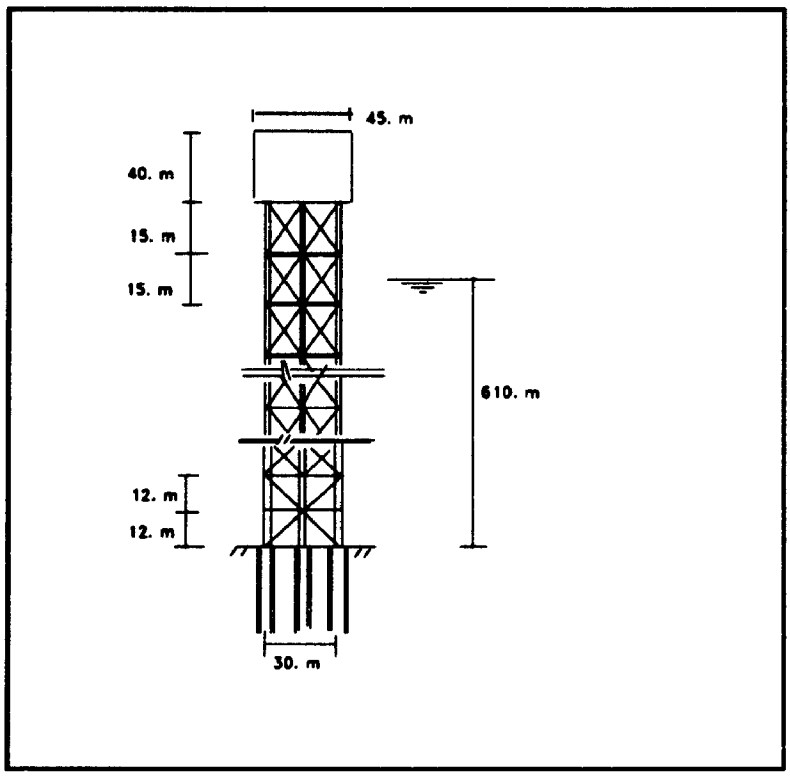

FIGURE 3.1: Typical Compliant tower.

$$F^*_{total}=\overline{F^*_{wt}}+[(2\overline{F^*_{wt}}ig\gamma)^2+(g\sigma^*_{wa}\frac{1}{[1-(\frac{f_{wa}}{f_0})^2]})^2]^{0.5} \qquad (3.2)$$

where $\overline{F^*_{wt}}$ is the generalized mean force due to wind, i is the turbulent intensity (typically 10%), g is the peak factor (typically 3), σ^*_{wa} is the rms of the generalized wave force and γ is a coefficient bigger than one (typically 1.1) to account for the low frequency forcing of the wind.

In the inertia dominated regime (T_p=14 sec, T_0=32 sec) most of the wave loading is resisted by the inertia loads and the value of the admittance function H(ω) (its modulus) is about 0.24.

Using the values given above, the computed mean wind force and wave rms force would be about $5*10^6$ N, $6.64*10^6$ N respectively. On this basis a maximum deflection of 6.4 meter (including mean wind drift) was calculated. The stress calculation was done using this approach and the columns at the base of the tower under the joint action of the axial force (compression) and moment were the critical members and needed to be modified. For the last 45 meter of the tower the legs diameter was increased in size, and also additional lateral bracing was needed to meet the stability (buckling) requirement.

For this rough analysis no allowance was made for the soil-pile-structure interaction which mostly reduce the moments at the base of the tower as well as it's natural frequency.

For scaling of this tower and reducing it to a single cantilever model it was necessary to find the integrated hydrodynamic effect of all of the bracing in the horizontal and vertical

planes and express them in terms of the equivalent main legs. An analysis was done to find their integrated contribution to the wave loading (considering an interaction factor for the reduction of loading due to their tandem effects). The total number of equivalent columns including main legs turned out to be 14.8 legs. Another analysis was also done based on their contribution to the generalized mass and in this case the total equivalent columns turned out to be 14.1 and finally the value of 14.4 were used for scaling of the structure.

3.2.2 SCALING OF THE TOWER

The description of the model and instrumentation is given in chapter 4, however the model used for the dynamic analysis is briefly explained in here.

The tower was modeled at a geometric scale of 1:150. This scaling was chosen on the basis of the frequency range of the paddle generated waves and length scale of the turbulent wind in the wind/wave flume at the Boundary Layer wind tunnel Laboratory at the University of Western Ontario. After accounting for Froud scaling, the velocity, mass, force and pressure scaling would be $(SL)^{1/2}$, $(SL)^3$, $(SL)^3$, $(SL)^2$.

Also considering the equivalent column factor given in previous section, using the mass and stiffness of the prototype, the mass and stiffness for the cantilever model were calculated. These values were used to design the stick model which will be described in chapter 4 as well as in the next section.

3.3 STRUCTURE IDEALIZATION, MODE SHAPES AND NATURAL FREQUENCIES

The stick model of the tower used, is the instantaneous tangent to the tip of the cantilever

model mentioned above. This simplified model is designed to have the same dynamic characteristics as the cantilever model as far as the displacement response at the tip (deck level) is concerned. The length of this model is S=2L/3, where L is the length of the cantilever model (650/150). Figure 3.2 shows this model as well as it's 2-D lumped mass idealization which has two degree of freedom at each node (rotation and translation). The descretized model was reduced to one degree of freedom at each node level using dynamic condensation method (Guyan, 1965; Paz, 1991). The effect of the axial static load to the first order was also considered in the analysis which in this case was important specially for its contribution to the first mode. Figure 3.3 shows the mode shapes and natural frequencies for the first four modes of the model.

3.3.1 EQUATIONS OF MOTION

The governing equations of motion for a line like multidegree of freedom system are:

$$m\ddot{X}+c\dot{X}+kX=p \tag{3.3}$$

where m is the mass matrix, c is the structural damping matrix, k is the stiffness matrix and p is the force vector due to the hydrodynamic loading. The displacement, velocity, and acceleration vectors are X, $\dot{X}$, $\ddot{X}$ respectively.

The equations of motion were decoupled using the mode superposition procedure (Clough, Penzien, 1975) introducing the following coordinate transformation:

$$X=\Phi Y \tag{3.4}$$

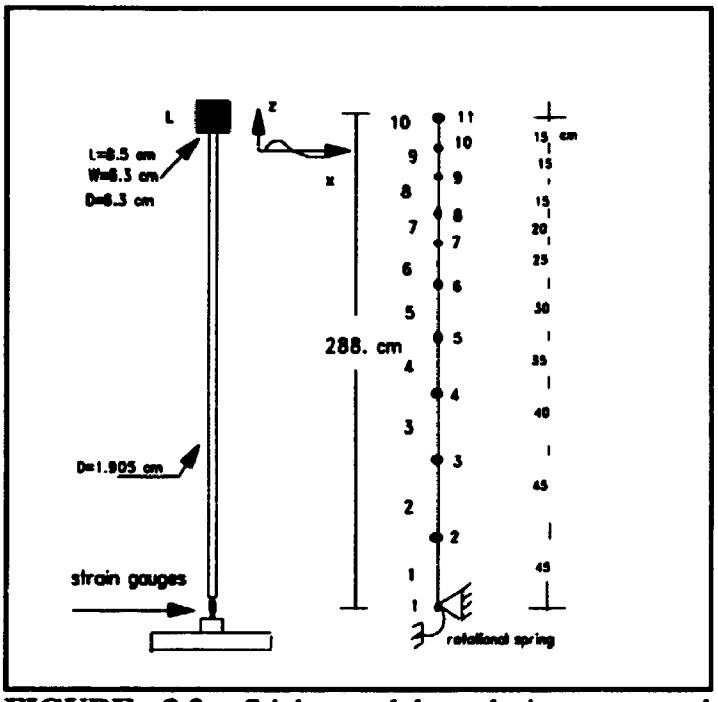

FIGURE 3.2: Stick model and its structural discretization.

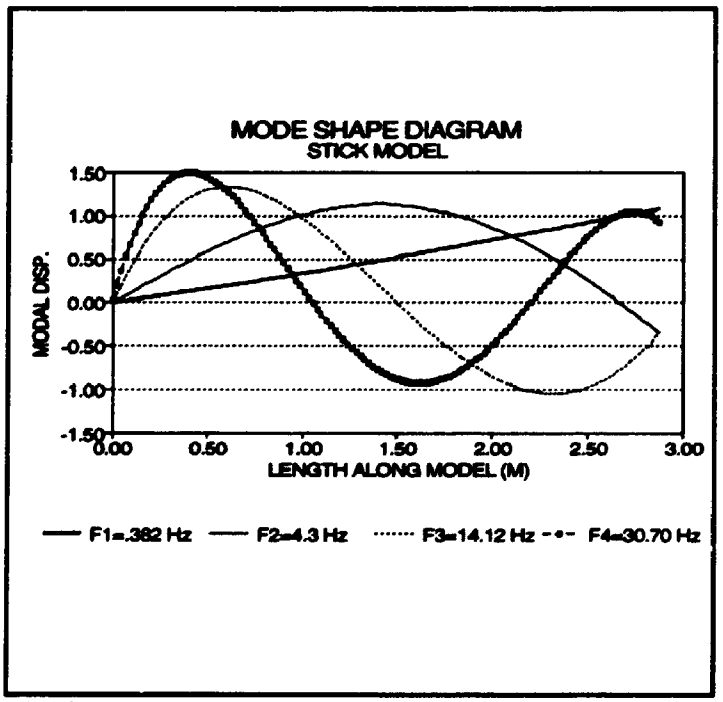

FIGURE 3.3: Mode shapes and natural frequencies

where Φ is the modal matrix obtained in the solution of the undamped free vibration system. Considering a linear viscous damping model (proportional damping), the modal mass, damping and stiffness would be:

$$M_n = \{\phi_n\}^T [m] \{\phi_n\} \tag{3.5}$$

$$C_n = \{\phi_n\}^T [c] \{\phi_n\} = 2\xi \omega_n M_n \tag{3.6}$$

$$K_n = \{\phi_n\}^T [k] \{\phi_n\} \tag{3.7}$$

The generalized force would be

$$P_n = \{\phi_n\}^T \{p(t)\} \tag{3.8}$$

The force vector p(t) expresses the effect of all environmental loads such as wind wave and current.

The set of uncoupled equations is solved and the solution in geometric coordinate would be obtained using equation 3.4.

3.4 FREQUENCY DOMAIN ANALYSIS

The use of spectral approach in dynamic analysis of offshore structures is quite common (Malhotra and Penzien, 1970; Moan et al, 1975). Using the mode superposition procedure (Clough, Penzien), the response is calculated by means of a linear transfer function.

The nonlinear hydrodynamic drag loading is linearized by either the equivalent linearization (Berge, Penzien, 1974; Foster, 1970) or by power series expansion and applying a weighted residual procedure (Gudmestad, Connor, 1983).

Depending on the relative magnitude of the water particle velocity and maximum velocity of the structure one of the linearization schemes mentioned above can be used. It is

obvious that linearization is only an approximation and for high waves considerable errors may be introduced. However the frequency domain analysis can be carried out rapidly and is economical computationally.

3.4.1 DESCRIPTION OF LOADS

The loading consists of wind, current and gravity waves.

As has been explained before the generation of the gravity waves from wind has a complex energy transfer process. A wind blowing over water will, by a variety of mechanisms, cause waves to grow. The wave height is dependant on:

1- The time for which the wind has blown.

2- The length of water in line with the wind, called fetch.

3- The wind speed

4- The width of water perpendicular to the wind

If the wind blows for a long duration with a long fetch, the wave height will reach an equilibrium in which the energy input to the waves by wind equals the energy dissipation by wave breaking and viscous effects. This type of sea state is known as fully developed and is characterized by a wide range of wave periods within the sea. Usually the wind does not blow for a sufficient duration or over a sufficient fetch to generate a fully developed sea. The sea is then said duration or fetch limited. Under these condition the wave heights are lower and the range of wave periods in the sea is narrower than the fully developed case. In this study the waves are considered to be long crested and Gaussian. the spectrum used is a JONSWAP type. It has a variably higher but narrower peak than Bretschneider/Pierson-Moscowitz spectrum. In Figure 3.4, a typical JONSWAP spectrum with different peak factors and a P-M spectum are shown. All of them have the same

Hs,Tz. The narrower peaks associated with the JONSWAP spectra is due to a frequency dependent term γ^s which multiplies the P-M spectrum.

The form of this spectrum suggested by Hasselmann et al is:

$$S_{\eta\eta}(f)=\frac{\beta g^2}{(2\pi)^4 f^5}\exp(-\frac{5}{4}(\frac{f_p}{f})^4)\gamma^s \tag{3.9}$$

where the values of β, f_p, γ were fitted to the measured wind speed and fetch data (Barltrop, Adams, 1991).

$$f_p=3.5(\frac{g}{U})\bar{X}^{-0.33}\ ,\ \bar{X}=\frac{gF_e}{U^2} \tag{3.10}$$

where F_e is the fetch distance and U is the wind velocity at 19.5 m. above S.W.L. γ is the peak factor ($1<\gamma<6$) and it's exponent is:

$$s=\exp(-\frac{(\frac{f}{f_p}-1)^2}{2\sigma^2})\ ,\quad \begin{matrix}\sigma=0.07 & f<f_p\\ \sigma=0.09 & f>f_p\end{matrix} \tag{3.11}$$

Using wind wave data at several places in the north sea, Homb,Overvick (1976) reported the values of β, γ, f_p in terms of Hs,Tz. Also it was possible to find β in terms of γ, f_p:

$$\beta=603(\frac{Hf_p^2}{g})^{2.036}(1-0.298\ln\gamma) \tag{3.12}$$

The subject of water current-wave interaction is still under intensive research and there is no complete theoretical model to explain the mechanism. When a wave encounters a steady current, it's characteristics generally change. If the current is in the direction of wave propagation, the wave amplitude decreases and the wave length increases and if it opposes the waves, the energy is input to increase the magnitude of the wave spectrum

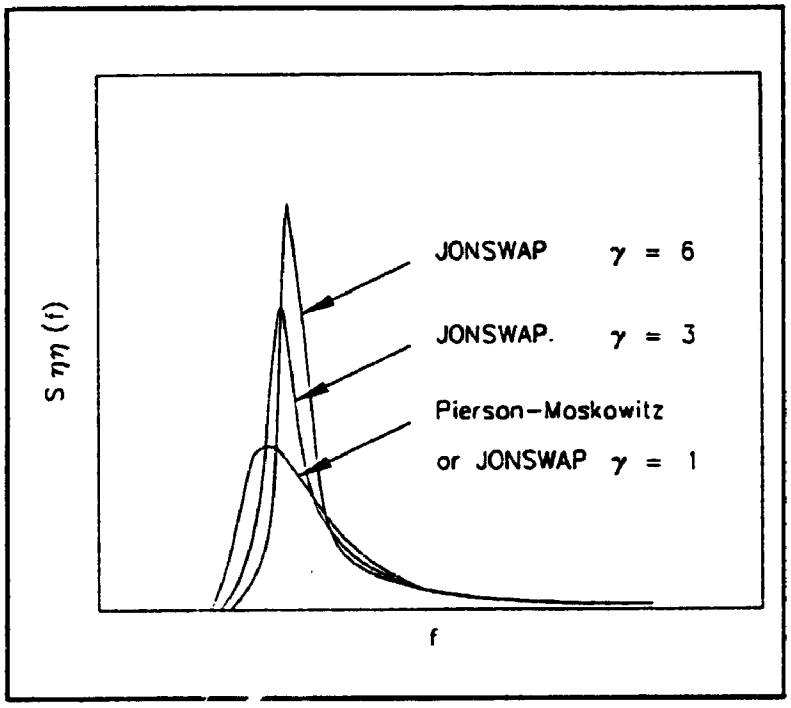

FIGURE 3.4: Comparison of Pierson-Moskowitz and JONSWAP spectra having the same H_s, and mean zero crossing period (from Barltrop, Adams, 1991).

and the waves steepen as well as shorten (Longuet-Higgins, Stewart, 1961).

The modification of the wave spectrum, under the action of the current is given by (Tung, Hung,Wu, 1976):

$$S_{\eta\eta}=\frac{4S^{*}_{\eta\eta}}{(1+(1+\frac{4U_c\omega}{g})^{0.5})^2(1+\frac{4U_c\omega}{g})^{0.5}} \tag{3.13}$$

where U_c is the current velocity in the wave direction and $S_{\eta\eta}$, $S_{\eta\eta}^{*}$ are the wave spectra with and without the current effects. Figure 3.5 shows the effect of water current on the JONSWAP spetrum.

The equations of motion for the N degrees of freedom lumped mass model of the tower are:

$$m\ddot{X}+c\dot{X}+kX=p(t) \tag{3.14}$$

where m is the diagonal mass matrix, c is symmetrical structural damping matrix, k is the structural stiffness matrix, X, $\dot{X}$, $\ddot{X}$ are the structural nodal displacement, velocity and acceleration vectors, p(t) is the hydrodynamic force vector. The relative velocity model which accounts for the wave structure interaction is used to calculate the hydrodynamic force on a nodal point of the compliant tower. The modified Morison equation has the form:

$$p(t)=\frac{1}{2}\rho C_D A_p|u+U_c-\dot{X}|(u+U_c-\dot{X})+(C_M-1)V_p\rho(\dot{u}+\dot{U}_c-\ddot{X}) \tag{3.15}$$

where A_p=Dl, V_p are diagonal matrices of areas and tributary volumes of structural

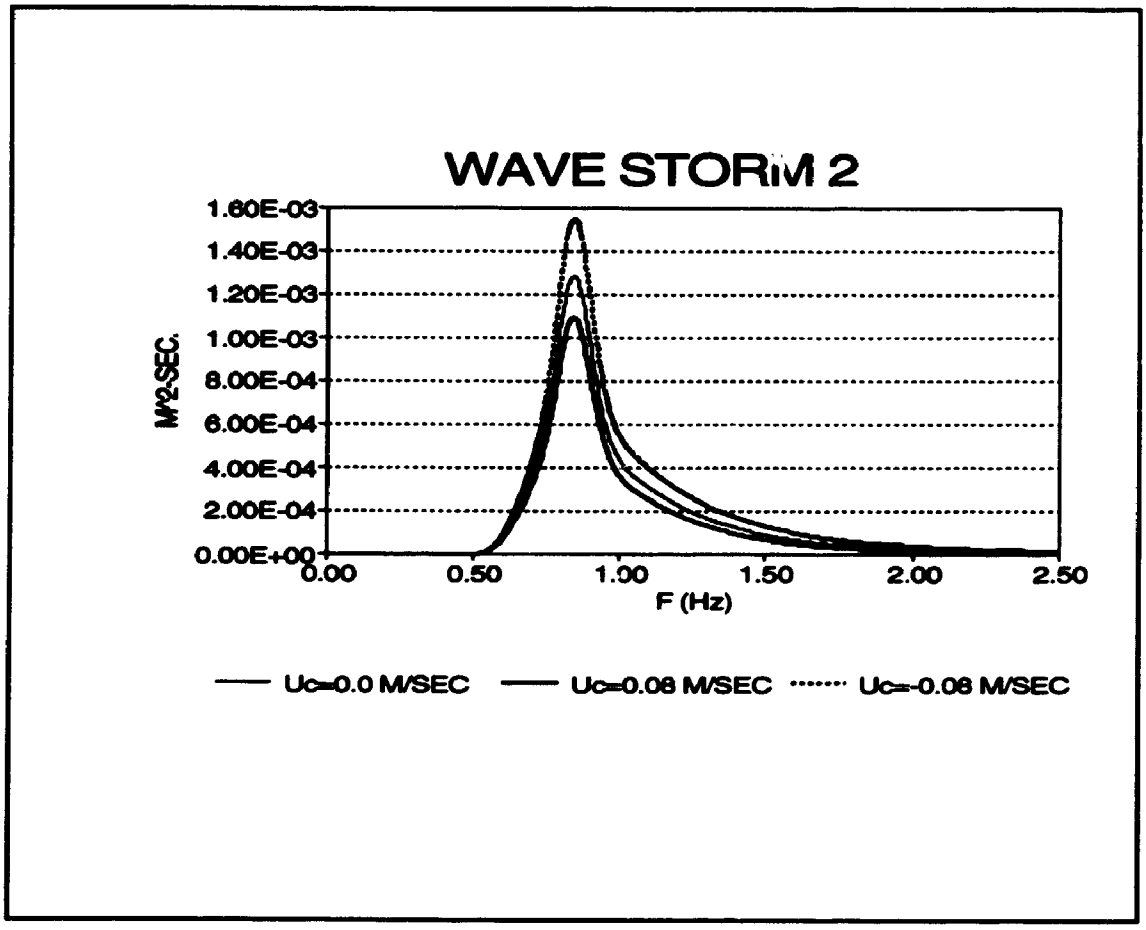

FIGURE 3.5: Effect of water current on a typical wave elevation spectrum.

members lumped at nodal points respectively and U_c is the uniform current velocity. Other parameters are introduced in chapter 2.

Equation 3.14 is a set of nonlinear differential equations and in order to do an spectral analysis the drag term should be linearized. The common techniques are:

1-Equivalent linearization (Malhotra, Penzien 1970; Wu, 1976)

2-Power series expansion of the drag term following the use of Borgman approximation (Gudmestadt,Connor, 1983)

In the second approach the water particle velocity should be much greater than the maximum displacement velocity of the structure:

$$u(t) \gg \dot{X}(t) \tag{3.16}$$

at a given node. Under this condition

$$|u-\dot{X}|(u-\dot{X}) \approx |u|u-2|u|\dot{X} \tag{3.17}$$

The first term can be expanded in to a power series with unknown coefficient and by applying a weighted residual procedure and minimizing the expected value of the weighted error, these coefficient can be found (Gudmestad, Connor, 1984). However in the case of the structure examined in this study it was observed that the maximum velocity response of the structure is not much smaller than the orbital velocity of the water particles and the above decoupling of the drag force would not be suitable any longer and the first method (Equivalent linearization) is used in this study.

The essence of this method, employed by Malhotra and Penzien (Wu, 1976), is to linearize the coupled, nonlinear drag forces by minimizing the mean square of the error function. The differential equation of the motion using $\dot{r}=u-\dot{x}$ can be transformed to:

$$(m+\rho V_p(C_M-1))\ddot{r}+c\dot{r}+kr+\frac{1}{2}\rho C_D A_p \dot{r}|\dot{r}|=m\ddot{u}+c\dot{u}+ku \tag{3.18}$$

In order to linearize the above equation, Malhotra and Penzien introduced the linearized form:

$$(m+\rho V_p(C_M-1))\ddot{r}+\mathbf{C}\dot{r}+kr+E=m\ddot{u}+c\dot{u}+ku \tag{3.19}$$

where $E=(c-\mathbf{C})\dot{r}+(\frac{1}{2}\rho C_D A_p)\dot{r}|\dot{r}|$. In order to determine the optimal values of the coefficients in matrix $\mathbf{C}$ the terms in vector E are minimized in a mean square sense:

$$\frac{\overline{\partial E^2}_i}{\partial \mathbf{C}_{ij}}=0 \tag{3.20}$$

the overline is the time average.

By taking derivative and solving for $\mathbf{C}_{ij}$

$$\mathbf{C}_{ij}=c_{ij}+\frac{1}{2}\rho C_D A_p \frac{\overline{\dot{r}_i^2|\dot{r}_j|}}{\overline{\dot{r}_i^2}} \tag{3.21}$$

Minimizing the error terms given by E, will yield a set of linear differential equations. The response of this linearized model is zero-mean Gaussian and has a probability density function given by:

$$P(\dot{r}_i)=\frac{1}{\sqrt{2\pi}}\frac{1}{\sigma_{\dot{r}_i}}\exp(-\frac{\dot{r}_i^2}{2\sigma_{\dot{r}_i}}) \tag{3.22}$$

where σ_r^2 is the variance of the process. Using this probability density function in equation 3.21, the optimizing equation would be:

$$\mathbf{C}_{ii}=c_{ii}+\frac{1}{2}\rho C_D A_p\sqrt{\frac{8}{\pi}}\sigma_{r_i} \quad i=1,2,..,N \tag{3.23}$$

It is seen that the elements of matrix $\mathbf{C}$ are dependent on σ_{r_i} which can be found when the above equation is solved. As a result, an iterative procedure is necessary to solve the linearized equation of motion. However the convergence is established by the nature of the nonlinear effects (Malhotra, Penzien, 1970). By back substituting the above mentioned transformation, the linearized equation would be:

$$\begin{gathered}(m+\rho V_p(C_M-1))\ddot{X}+\mathbf{C}\dot{X}+kX=\rho V_p C_M\ddot{u}+\bar{c}\dot{u} \\ \bar{c}_{ij}=0 \quad i\neq j \\ -\frac{1}{2}\rho C_D A_p\sqrt{\frac{8}{\pi}}\sigma_{r_i} \quad i=j\end{gathered} \tag{3.24}$$

In the presence of current, Wu and McDermott (1976), using the same technique, have derived the linearized set of equations:

$$(m+\rho V_p(C_M-1))\ddot{X}+\mathbf{C}\dot{X}+kX=\bar{c}\dot{u}+C_M\rho V_p\ddot{u}+\frac{1}{2}\rho C_D A_p b \tag{3.25}$$

$$\begin{gathered}\bar{c}=\mathbf{C}-c \\ \mathbf{C}_{ij}=c_{ij} \quad i\neq j \\ \mathbf{C}_{ii}=c_{ii}+C_D\rho A_p(\sqrt{\frac{2}{\pi}}\sigma_{r_i}+\exp(-\frac{1}{2}(\frac{U_c}{\sigma_{r_i}})^2)+2U_c erf(\frac{U_c}{\sigma_{r_i}})) \\ i=j\end{gathered} \tag{3.26}$$

The erf(f) is given by:

$$erf(u)=\frac{1}{\sqrt{2\pi}}\int_0^u \exp(-\frac{1}{2}u^2)du \tag{3.27}$$

and b is a constant vector given by:

$$b_i=2(\frac{1}{\sqrt{2\pi}}\sigma_{f_i}U_c\exp(-\frac{1}{2}(\frac{U_c}{\sigma_{f_i}})^2)+(\sigma_{f_i}^2+U_c^2)erf(\frac{U_c}{\sigma_{f_i}})) \tag{3.28}$$

where again the elements of matrix $\mathbf{C}$, vector b are dependent on σ_{f_i} and the solution process would be an iterative one.

The normal mode superposition method is used to solve the set of equations 3.25:

$$X=\Phi Y$$

where Y is the generalized modal coordinate vector and Φ is the modal matrix obtained by solving the undamped homogeneous problem:

$$\begin{aligned} M&=\Phi^T(m+\rho V_p(C_M-1))\Phi \\ K&=\Phi^T k\Phi \\ C_0&=\Phi^T C\Phi \\ P&=\Phi^T p \end{aligned} \tag{3.30}$$

The matrices M,K are both diagonal. C_0 is symmetrical but is not a diagonal matrix since the elements of $\mathbf{C}$ are selected successively through optimizing equations 3.26, however it can be diagonalized using an optimization scheme similar to that used to obtain $\mathbf{C}$:

$$C_0\dot{Y}=C\dot{Y}+E_1 \tag{3.31}$$

where C is a diagonal matrix and E_l is the error vector. Upon minimizing this error vector using the mean square approach, the elements of the diagonal matrix C, would be:

$$C_{ii} = \sum_{k=1}^{N} C_{0\,ik} \frac{E(\dot{Y}_i \dot{Y}_k)}{E(\dot{Y}_i^2)} \quad , \qquad \xi_i = \frac{C_{ii}}{2M_i \omega_i} \tag{3.32}$$

Now these set of N uncoupled linear equations can be solved. To solve this problem in the frequency domain, the cross spectral density function of the wave forces for modes j,k can be approximated as:

$$S^{wa}{}_{P_j P_k}(\omega) = \sum_{m=1}^{N} \sum_{n=1}^{N} \phi_{mj} \phi_{nk} ((\rho V_{p_m} C_{M_m})(\rho V_{p_n} C_{M_n}) S_{\ddot{u}_m \ddot{u}_n}(\omega) + \overline{c_m}\ \overline{c_n} S_{\dot{u}_m \dot{u}_n}(\omega) + \rho V_{p_m} C_{M_m} \overline{c_n} S_{\ddot{u}_m \dot{u}_n}(\omega) + \overline{c_m} (\rho V_{p_n} C_{M_n}) S_{\dot{u}_m \ddot{u}_n}(\omega) \tag{3.33}$$

where

$$S_{\ddot{u}_m \ddot{u}_n} = \omega^2 S_\eta(\omega) \frac{\cosh k(z_m + h) \cosh k(z_n + h)}{\sinh^2 kh}$$
$$S_{\dot{u}_m \ddot{u}_n}(\omega) = i\omega S_{\ddot{u}_m \ddot{u}_n} = S^*_{\ddot{u}_m \dot{u}_n}(\omega)$$
$$S_{\ddot{u}_m \ddot{u}_n}(\omega) = \omega^2 S_{\dot{u}_m \dot{u}_n} \tag{3.34}$$

* stands for the complex conjugate Also the response would be:

$$S^{wa}{}_{X_i X_i}(\omega) = \sum_{j=1}^{N} \sum_{k=1}^{N} S_{pp_i}(\omega) H^*{}_j(\omega) H_k(\omega) \phi_{ij} \phi_{ik} \tag{3.35}$$

In order to do the iterative scheme in frequency domain the spectra of the relative velocity at the nodal points are calculated:

$$\begin{aligned} \dot{r}_j(t) &= \dot{u}_j(t) - \dot{X}_j(t) \\ S_{\dot{r}_i\dot{r}_j}(\omega) &= S_{\dot{u}_i\dot{u}_j}(\omega) + S_{\dot{X}_i\dot{X}_j} - S_{\dot{u}_i\dot{X}_j}(\omega) - S_{\dot{X}_i\dot{u}_j}(\omega) \end{aligned} \tag{3.36}$$

By assuming some initial values (it can be zero) for $\sigma_{\dot{r}_i\dot{r}_j}$, $S_{\dot{u}_i\dot{u}_j}(\omega)$ and $S_{\dot{X}_i\dot{X}_j}(\omega)$ can be computed as:

$$\begin{aligned} S_{\dot{u}_i\dot{u}_j}(\omega) &= \omega^2 S_{u_iu_j}(\omega) \\ S_{\dot{X}_i\dot{X}_j}(\omega) &= \omega^2 S_{X_iX_j}(\omega) \end{aligned} \tag{3.37}$$

and

$$\begin{aligned} S_{\dot{X}_i\dot{u}_j}(\omega) &= -i\omega S_{X_iu_j}(\omega) \\ S_{\dot{u}_i\dot{X}_j}(\omega) &= i\omega S_{u_iX_j}(\omega) \end{aligned} \tag{3.38}$$

Note that for real processes:

$$S_{\dot{u}_i\dot{X}_j}(\omega) = S^*_{\dot{X}_i\dot{u}_j}(\omega) \tag{3.39}$$

According to Malhotra and Penzien (1970):

$$S_{\dot{X}_i\dot{u}_j}(\omega) = \sum_{k=1}^{N}\sum_{l=1}^{N} \phi_{jk}\phi_{lk}H^*_k(\omega)(\rho V_{p_i} C_{M_i} S_{\dot{u}_l\dot{u}_j}(\omega) + \bar{c}_i S_{\dot{u}_i\dot{u}_j}(\omega)) \tag{3.40}$$

Upon evaluating $S_{\dot{r}\dot{r}}(\omega)$ the variances $\sigma^2_{\dot{r}_j}$ required for optimization of the damping coefficient would be:

$$\sigma^2_{\dot{r}_j} = \int_0^{\infty} S_{\dot{r}_j\dot{r}_j}(\omega)d\omega \tag{3.41}$$

With these values for $\sigma_{\dot{Y}_j}$, the steps are repeated (damping coefficients C_{ii} are also updated at each iteration step) until convergence is achieved, usually after a few cycles. Calculation of equations 3.32 is performed knowing that:

$$S_{\dot{Y}_i\dot{Y}_k}(\omega)=\omega^2 S_{Y_iY_k}(\omega)=\omega^2 H^*_i(\omega)H_k(\omega)S_{P_iP_k} \tag{3.42}$$

and

$$\overline{(\dot{Y}_i\dot{Y}_k)}=\int_0^{\infty} S_{\dot{Y}_i\dot{Y}_k}(\omega)d\omega \tag{3.43}$$

The wind loading which was adopted from the ESDU data (ESDU parts II,III 1985) was explained in chapter 2. For a 1-D model using the concept of the aerodynamic admittance function, the force spectrum would be:

$$S_{FF}(f)=4\left(\frac{\overline{F_D}}{U}\right)^2 \chi^2(f)S_{uu}(f) \tag{3.44}$$

where $\chi^2(f)$ is given in chapter 2 and U is the mean wind speed at the force center of the super structure. The contribution to the generalized force spectrum for modes j,k due to turbulent wind force is expressed as:

$$S^{wi}_{P_jP_k}(\omega)=S_{FF}(\omega)\phi_j(TN)\phi_k(TN) \tag{3.45}$$

where $\phi_j(TN)$, $\phi_k(TN)$ are the modal coordinates for modes i,j at the deck level (equal to one when normalized at the tip of the stick model).

Using the linear theory for small amplitudes of vibration, the along wind induced aerodynamic damping coefficient for the ith mode, ξ_{ai}, would be:

$$\xi_{ai}=\frac{\rho_a UAC_{Da}\phi_i^2(TN)}{2M_i\omega_i} \tag{3.46}$$

where ρ_a, C_{Da} are air mass density and drag coefficient of super-structure (which is assumed to be unity) respectively.

3.4.2 STRUCTURAL RESPONSE ANALYSIS

The final step in the frequency domain analysis is to calculate the total response due to wind, wave and current.

Due to the lack of information on the wind-wave interaction, they are assumed to be statistically independent and the total response is treated as the linear superposition of responses due to wind and wave-current forces.

$$S_{P_jP_k}(\omega)=S^{wa}_{P_jP_k}(\omega)+S^{wi}_{P_jP_k}(\omega) \tag{3.47}$$

where the first and second terms on the right hand side are the contribution to the total load cross spectral density matrix due to wave-current and turbulent wind. Also the total damping (including structural, hydrodynamic and aerodynamic) is given by:

$$\xi_{ti}=\xi_i+\xi_{ai} \tag{3.48}$$

Finally the response spectrum for displacement (surge), $S_{X_iX_i}(\omega)$, at node i would be:

$$S_{X_iX_i}(\omega)=\sum_{j=1}^{N}\sum_{k=1}^{N}S_{P_jP_k}(\omega)H^*_j(\omega)H_k(\omega)\phi_{ij}\phi_{ik} \tag{3.49}$$

3.5 NONLINEAR STOCHASTIC TIME DOMAIN ANALYSIS

Response prediction of the compliant tower to wind and wave loads in time domain has the advantage of including all nonlinear effects, however it is time consuming and

therefore is expensive. Also the interpretation of the time history response is sometimes difficult.

Significant efforts (Foster, 1970; Malhotra, Penzien, 1970; Vughts et al, 1979) have been made in developing and applying computer based methods for stochastic dynamic analysis of offshore platforms. Nonlinearities of the wave loading are mainly associated with the drag term of the Morison's equation and variation of surface elevation (free surface effects) and they increase with the slenderness of the members.

In this study the modified Morison equation is used to model the coupled nonlinear drag loading and the free surface effects are considered through the use of the modified Airy wave theory (chapter 4). Water particle Velocity and acceleration time histories are simulated by the use of linear wave superposition and random phase method. The same technique is used to simulate the wind load time histories.

3.5.1 SIMULATION OF STOCHASTIC SEA AND WIND FIELDS

To simulate the unidirectional long crested Gaussian sea, the one dimensional spectral density function is defined according to the JONSWAP formulation. The numerical formulation simulate time series for the stochastic fluid field based on the random phase method:

$$\begin{aligned} \eta(x,t) &= \sum_{i=1}^{N} a_i \sin\theta_i \\ \theta_i &= \omega_i t - k_i x + \phi_i \\ a_i &= \sqrt{2 S_{\eta\eta}(f_i)\Delta f} \end{aligned} \qquad (3.50)$$

ϕ_i is a random phase selected from a uniform probability distribution $0<\phi_i<2\pi$,

N is the number of frequencies used in the simulation and k_i is the wave number (calculated from the linear wave dispersion equation).

In this study the number of frequency components used is 532 and the resolution (Δ) is about 0.0028 Hz.

The fluid velocity and acceleration fields are then defined as:

$$u(z,t)=\sum_{i=1}^{N}\omega_i\sqrt{2S_{\eta\eta}(f_i)\Delta f}\,\frac{\cosh k_i(z+h)}{\sinh k_i h}\sin\theta_i \tag{3.51}$$

$$\dot{u}(z,t)=\sum_{i=1}^{N}\omega_i^{\,2}\sqrt{2S_{\eta\eta}(f_i)\Delta f}\,\frac{\cosh k_i(z+h)}{\sinh k_i h}\cos\theta_i \tag{3.52}$$

Using this technique a time history of 16 minutes duration was generated (18 blocks) which the expected coefficient of variation of the resulting observed wave spectrum is approximately 0.23.

The generation of the wind load time history was done by the same approach (random phase method) and again the same number of harmonics was used:

$$P_w(t)=\sum_{i=1}^{N}\sqrt{2S_{FF}(f_i)\Delta f}\,\sin(\omega_i t+\psi_i) \tag{3.53}$$

where $S_{FF}(f)$ is the wind force spectrum.

Having the simulated wave and wind time histories, it was possible to apply them to the lumped mass model of the tower. The time step for the descritized wind and wave records was 0.1 seconds which is a convergence requirement in the solution process.

3.5.2 WAVE KINEMATICS

The stochastic processes given by equations 3.50, 3.51, 3.52, and 3.53 are ergodic in mean value and auto-correlation function and will converge in a mean square sense to an ergodic, Gaussian process as the number of harmonics (N) goes to infinity. Also the generated spectra (wave elevation and wind force) converge to the target spectra in a mean square sense.

A uniform current is included in the fluid field by adding it to the instantaneous horizontal wave velocity.

The linear Airy's wave used in combination with the wave superposition for generation of random seas is only valid for infinitesimal wave heights. As part of this study, the hydrodynamic forces are integrated to the instantaneous water level by using the modified Airy wave theory. In this theory (chapter 2) the fluid field at a point above the mean water level is considered to be identical to the fluid field at the point on the mean water level with the same horizontal coordinates. Also the free surface forcing using the modified Morison equation is given as:

$$F_{fsf}(t) = -\frac{1}{2}\rho C_D D \int_0^{\eta(t)} |u(t,z) + U_c - \dot{X}(t,z)| \, (u(t,z) + U_c - \dot{X}(t,z)) dz \qquad (3.54)$$

Representation of above integral in modal coordinate for the jth mode would be:

$$P_{fsf_j}^{i+1}(t+\tau) = -\frac{1}{2}\rho C_D D \int_0^{\eta(t+\tau)} |u(t+\tau,z) + U_c - \dot{X}^i(t+\tau)|$$
$$(u(t+\tau,z) + U_c - \dot{X}^i(t+\tau))\phi_{(NT-1,j)} dz$$

where i and τ are the iteration number and step size used in the numerical solution explained in the next section. ϕ(NT-1,j) is the value of the jth mode at the mean free surface node. This force is added to the generalized force vector due to wind and wave loading.

3.5.3 NUMERICAL TECHNIQUE FOR THE SOLUTION OF THE EQUILIBRIUM EQUATIONS

Most of the numerical solution methods are step by step methods because the equation is solved at a succession of values of t, t+Δt, t+2Δt, etc. The accuracy of the solution however depends on the length of the step interval Δt. It must be short enough for the load time history, response time history and in many cases the shortest natural period to be well defined.

In this work the Newmark-Wilson Algorithm, which is an implicit method, is used to solve the system of uncoupled equations (Wilson, 1977). This method uses the Newmark method to find the solution at t+θΔt, and then calculates the results at t+Δt (as the initial condition for the next time step), using the linear acceleration method.

In order to obtain an unconditionally stable method with high damping in the higher modes the values of the integration parameters are: δ=1/2, α=1/6, θ=1.4.

In normal mode coordinates the solution is initialized by assuming some initial values for

$$Y_j(0),\ \dot{Y}_j(0),\ \ddot{Y}_j(0)\ .$$

The integration constants are calculated as:

$$\begin{gathered}\tau=\theta\Delta t \quad s_0=\frac{1}{\alpha\tau^2} \quad s_1=\frac{\delta}{\alpha\tau} \quad S_2=\frac{1}{\alpha\tau}\\ s_3=\frac{1}{2\alpha}-1 \quad s_4=\frac{\delta}{\alpha}-1 \quad s_5=\frac{\tau}{2}\left(\frac{\delta}{\alpha}-2\right)\\ s_6=\Delta t(1-\delta) \quad s_7=\Delta t\delta \quad s_8=\Delta t^2\left(\frac{1}{2}-\alpha\right)\\ s_9=\alpha\Delta t^2\end{gathered} \tag{3.56}$$

The loading vector at mode j is given as:

$$\begin{aligned}P^*_j=P^*_j(t+\tau)+M_j(s_0Y_j(t)+s_2\dot{Y}_j(t)+s_3\ddot{Y}_j(t))\\ +C_j(s_1Y_j(t)+s_4\dot{Y}_j(t)+s_5\ddot{Y}_j(t))\end{aligned} \tag{3.57}$$

and the modal displace at time t+τ is given as:

$$Y_j(t+\tau)=\frac{P^*_j}{K^*_j} \tag{3.58}$$

where

$$P_j^*(t+\tau)=\sum_{i=1}^{N} p_i(t+\tau)\phi_{ij} \tag{3.59}$$

and $p_i(t+\tau)$ is the total force vector in geometric coordinate due to wind, wave and current loads at nodal point i. The modal acceleration and velocity at time t+τ, necessary to calculate $P^*_j(t+\tau)$ are given as:

$$\begin{aligned} \ddot{Y}_j(t+\tau)&=s_0(Y_j(t+\tau)-Y_j(t))-s_2\dot{Y}_j(t)-s_3\ddot{Y}_j(t) \\ \dot{Y}_j(t+\tau)&=\dot{Y}_j(t)+s_6\ddot{Y}_j(t)+s_7\ddot{Y}_j(t+\tau) \end{aligned} \tag{3.60}$$

Also, values of the generalized response ($\ddot{Y}_j,\dot{Y}_j,Y_j$) at time t+Δt which are used as initial conditions for the next time step would be:

$$\begin{aligned} \ddot{Y}_j(t+\Delta t)&=\ddot{Y}_j(t)+\frac{1}{\theta}(\ddot{Y}_j(t+\tau)-\ddot{Y}_j(t)) \\ \dot{Y}_j(t+\Delta t)&=\dot{Y}_j(t)+s_6\ddot{Y}_j(t)+s_7\ddot{Y}_j(t+\Delta t) \\ Y_j(t+\Delta t)&=Y_j(t)+\Delta t\dot{Y}_j(t)+s_8\ddot{Y}_j(t)+s_9\ddot{Y}_j(t+\Delta t) \end{aligned} \tag{3.61}$$

Due to the nonlinearity and coupling of the wave loading, some iterations at each time step are necessary (depending on the length of time step). The response variable used for the convergence test was the velocity response at time t+τ:

$$\left|\frac{\dot{Y}_j^{i+1}(t+\tau)-\dot{Y}_j^{i}(t+\tau)}{\dot{Y}_j^{i+1}(t+\tau)}\right|<e \tag{3.62}$$

where i is the iteration number and ε is the convergence criteria.

The displacement response in geometric coordinate at the deck level is given as:

$$X_{TN}(t)=\sum_{j=1}^{N}\phi_{(NTJ)}Y_j(t) \tag{3.63}$$

where TN (top node) stands for the node at the deck level.

The time step used in the calculation was 0.1 sec. and the length of the response record was 16 minutes. In order to compare the time domain results to the frequency domain results the final displacement response was transformed to the frequency domain (spectral density function) using the FFT method.

3.6 RESULTS OF ANALYSIS

Using JONSWAP spectrum and ESDU data, the combination of three wave storms and four wind storms were employed in the analysis which resulted in twelve sea states. These sea states simulate some of the moderate to high seas which exist in a sea.

The significant wave height and peak frequencies for the three wave storms are H_s=4.59 cm, 7.84 cm, 10.82 cm, F_p=0.96 Hz, 0.86 Hz, 0.8 Hz. respectively. Figure 3.6 shows the wave elevation spectra for the three wave storms. Also, Figure 3.7 shows the wind spectra calculated based on equation 2.60, and is plotted in dimensionless form. It can be observed that the energy of the turbulent wind is concentrated in the low frequency range of the spectrum compared to the waves.

The empirical force coefficients C_D,C_M were adopted from the measurements performed in another phase of this study(chapter 4) and are given in Table 3.1.

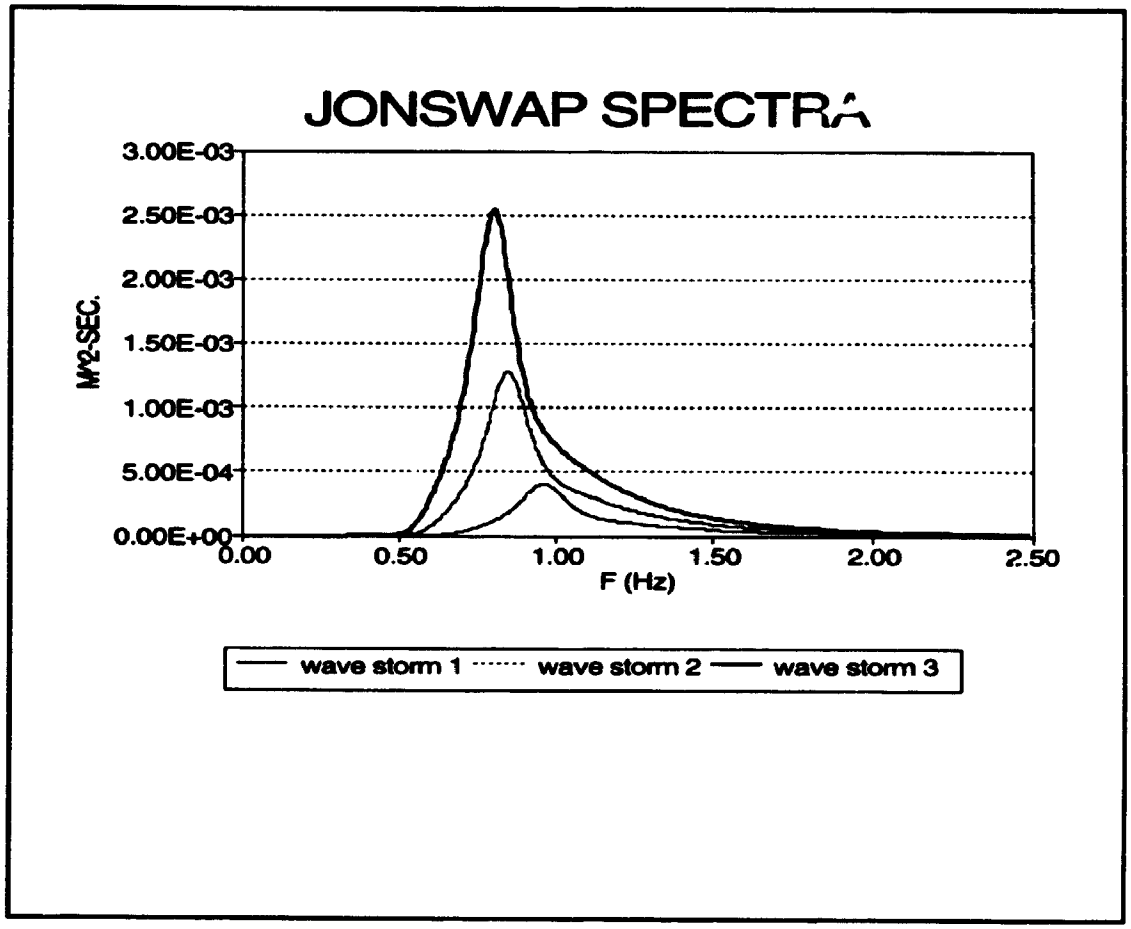

FIGURE 3.6: Sea spectra for the three wave storms

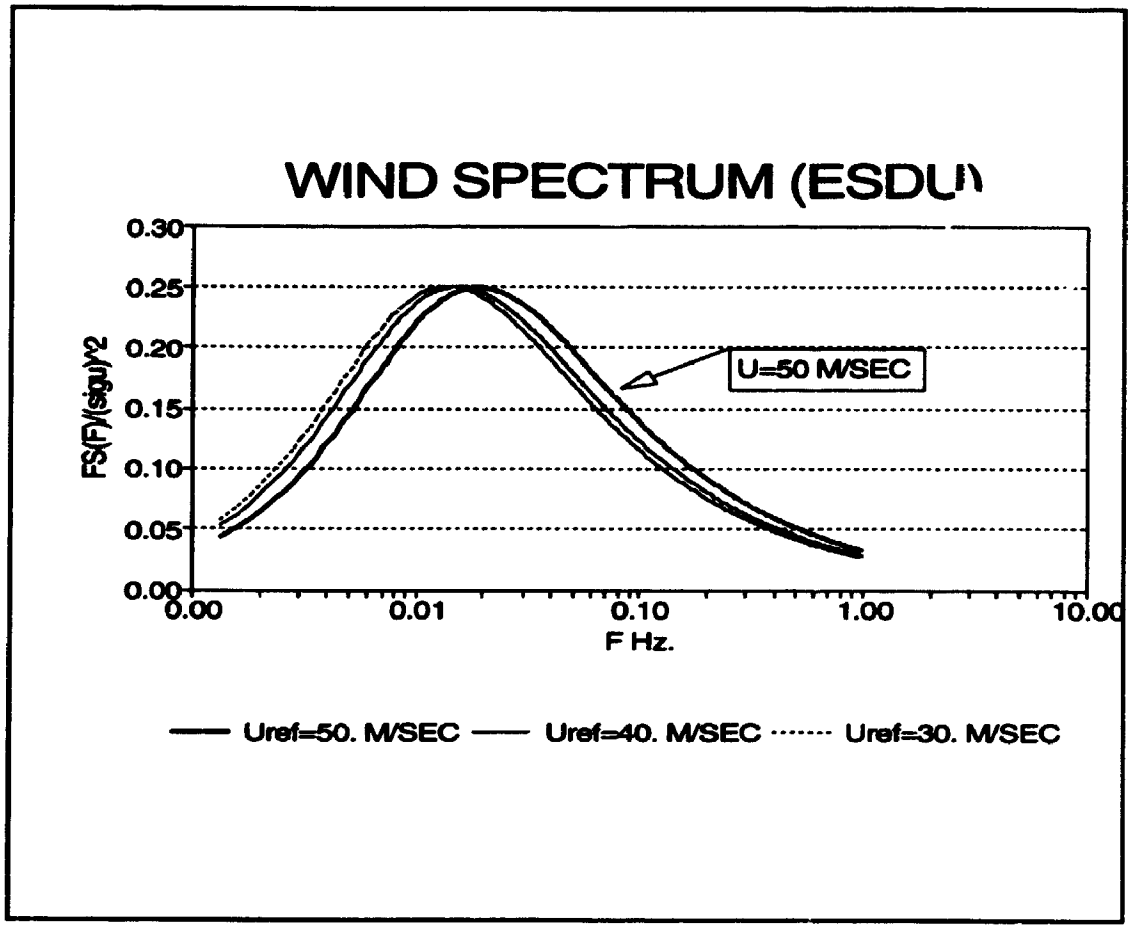

FIGURE 3.7: Wind storms corresponding to 3 wind velocities (full scale)

TABLE 3.1: FORCE COEFFICIENTS		
WAVE STORM	C_D	C_M
1	0.7	2.3
2	0.8	2.3
3	0.9	2.3

3.6.1 TIME DOMAIN VERSUS FREQUENCY DOMAIN RESULTS

In a compliant tower, the structure responds to the excitation by a soft rigid body mode together structural oscillations. The response discussed is the surge response at the lower deck level although bending moment or shear force could have been employed instead.

The results given in this section are for structure B with top side dimensions 8.0 cm (width), 8.0 cm (height), 8.2 cm (depth), described in chapter 4.

The spectra of the surge response for various load cases (sea states) for both frequency and time domain approaches are shown in appendix A. Figures 3.8 to 3.10 show the typical results for sea state 22 (wave storm 2, wind storm 2). In Figure 3.9 the influence of the splash zone (free surface effect using the constant velocity field near the water line) is considered while in Figure 3.8 this effect is neglected in the time domain analysis. Figure 3.10 shows the linearized frequency domain result. As can be seen the free surface forcing mostly contribute to the low frequency response and as the sea becomes rougher (appendix A), this effect becomes more pronounced. This

behaviour is expected since free surface induced forcing is proportional to the cube of the instantaneous wave height (H^3).

Generally the time domain and frequency domain results show similar trends. The wave frequency portion of the response follows the form of the input wave spectrum and the low frequency part of the response is related to the wind gust loading and the interaction of the different wave frequency components resulting from the nonlinear drag force in combination with the free surface effects (in time domain analysis). Figures 3.11 to 3.19 show the rms response versus wind speed for the twelve sea states for the studied structural configuration. For a given wave storm the rms surge response increases as the wind speed increases. For the wave only cases, higher seas (wave storms) result in greater rms responses.

The linearized frequency domain method generally leads to smaller low frequency response compared to the time domain results. This is due to the linearization of the drag loading which mostly accounts for the wave frequency part of the response and the low frequency response is mostly coming from the wind forces in combination with the somewhat underestimated linearized hydrodynamic damping. Also the linearized representation of drag forces produces extreme values of structural response which are generally considerably lower than those predicted by the coupled nonlinear time domain results specially for higher sea states.

The low frequency forces can be important if the system is lightly damped. For the wave storm 1 (mild sea), the response is dominated by the wind forces and as the wind speed increases, the tower responds at a relatively low frequency at its first mode. For higher seas the significance of the wind forces decreases due to the increase in hydrodynamic damping and the larger wave loads.

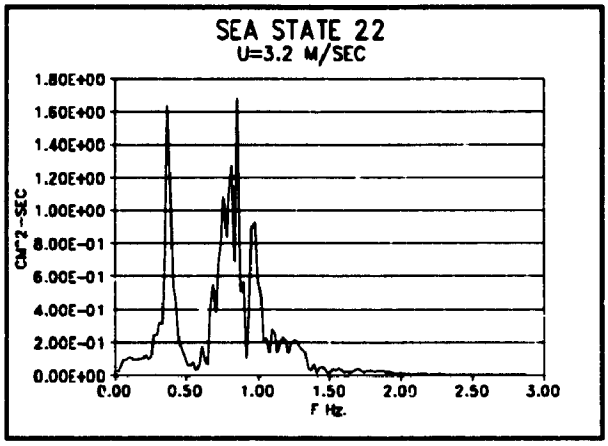

FIGURE 3.8: Surge response spectrum for sea state 22 (time domain analysis)

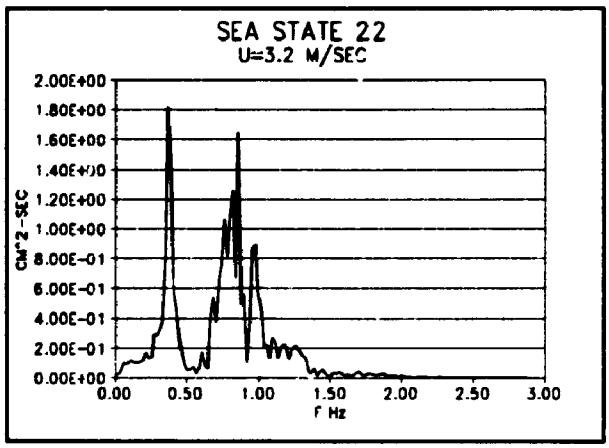

FIGURE 3.9: Surge response spectrum for sea state 22 (time domain analysis including the free surface effect)

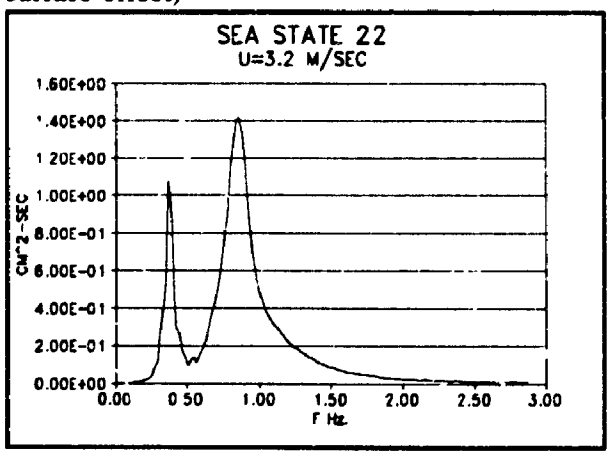

FIGURE 3.10: Surge response spectrum for sea state 22 (frequency domain analysis).

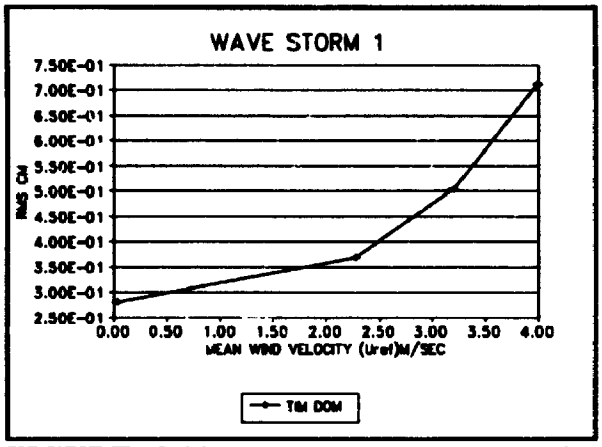

FIGURE 3.11: RMS surge response for structure B (time domain).

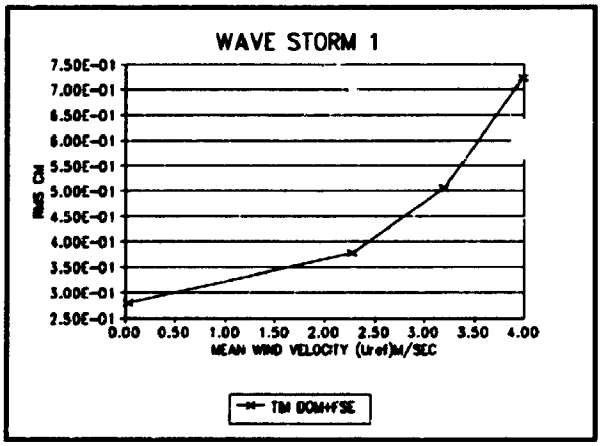

FIGURE 3.12: RMS surge response for structure B (time domain including the free surface effect)

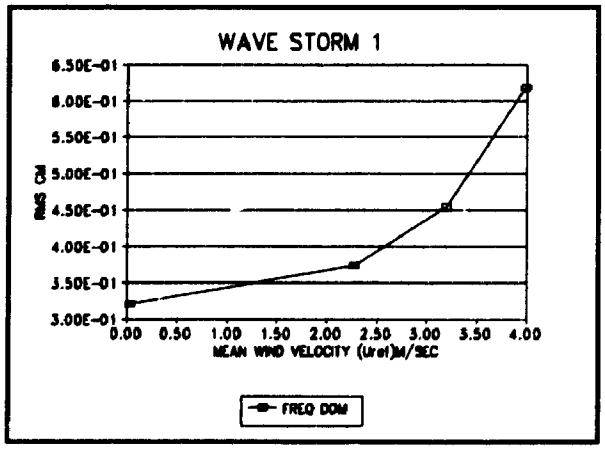

FIGURE 3.13: RMS surge response for structure B (frequency domain)

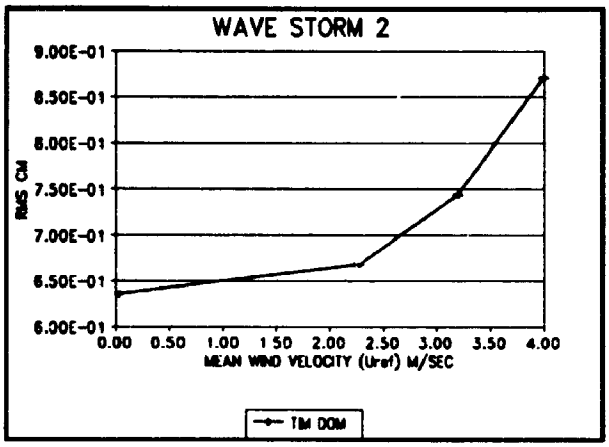

FIGURE 3.14: RMS surge response for structure B (tome domain)

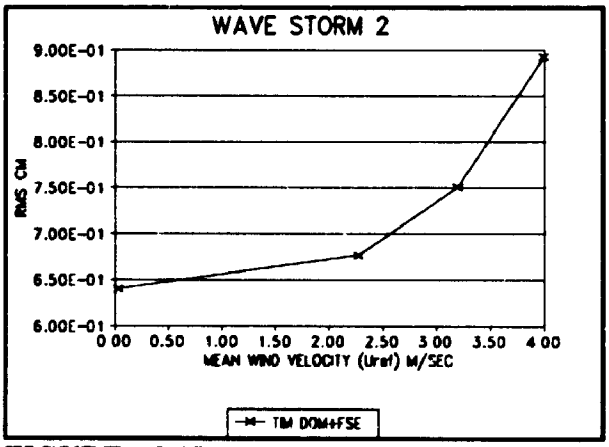

FIGURE 3.15: RMS surge response for structure B (time domain including free surface effect)

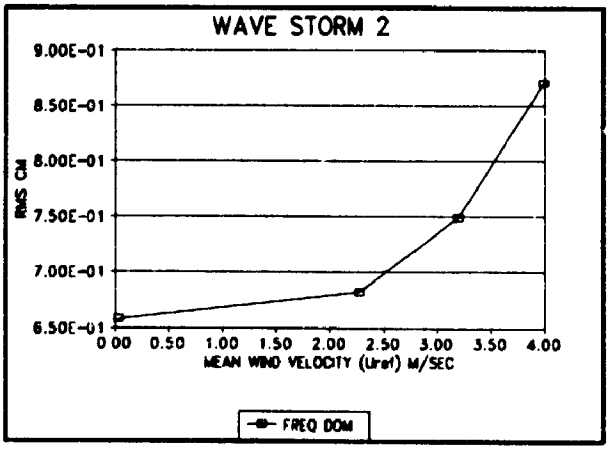

FIGURE 3.16: RMS surge response for structure B (freq. domain)

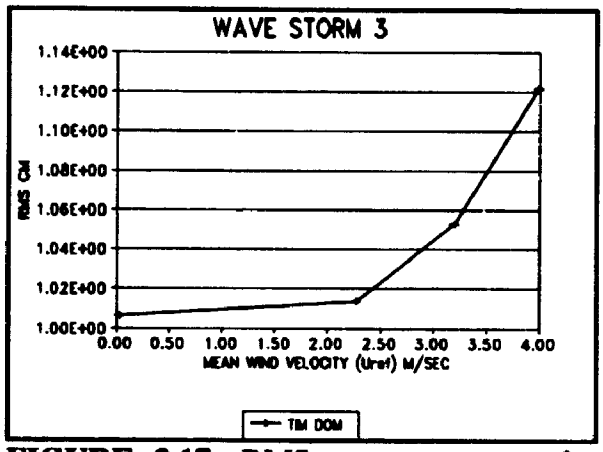

FIGURE 3.17: RMS surge response for structure B (time domain)

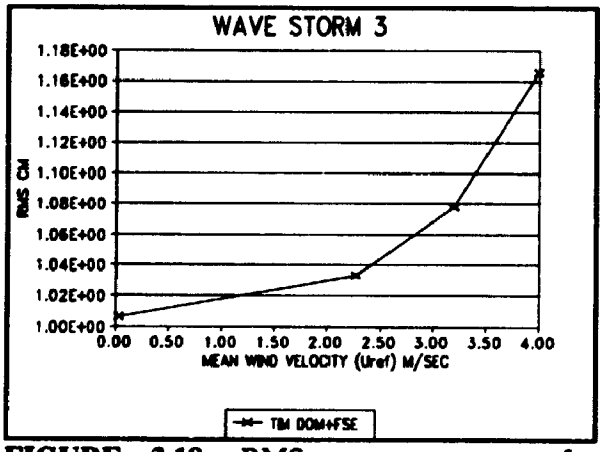

FIGURE 3.18: RMS surge response for structure B (time domain including free surface effect)

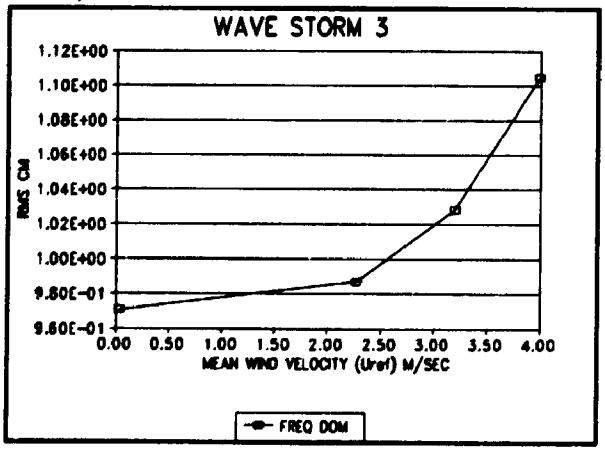

FIGURE 3.19: RMS surge response for structure B (freq. domain)

3.6.2 EFFECT OF CURRENT ON DYNAMIC RESPONSE OF TOWER

In this study the effect of a uniform positive current on the surge response of the tower is reported. The analysis is done in the time domain with the inclusion of free surface effect. The force coefficients used are assumed to be still applicable, due to the limited information available on the wave current interaction.

The effect of current on the lower deck level displacement response for structure B is presented in appendix B. The main contribution of the an increasing current is to change the response in the low frequency region of the spectrum in combination with increase in hydrodynamic damping.

Figures 3.20 to 3.22 show the response of the wave-only cases for different water current velocities. It was observed that the increased hydrodynamic damping due to increasing current velocity leads to more or less the same rate of increase of rms response.

In a series of tests performed in the present wind-wave facility at the Boundary Layer Wind Tunnel Laboratory the wind induced current was on the order of 3.0 cm/sec.

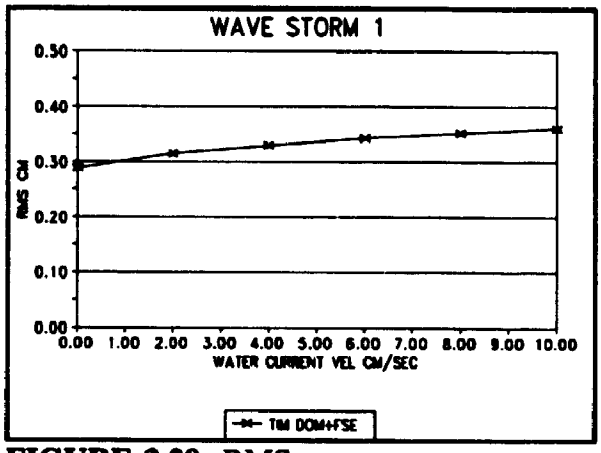

FIGURE 3.20: RMS surge response versus water current velocity

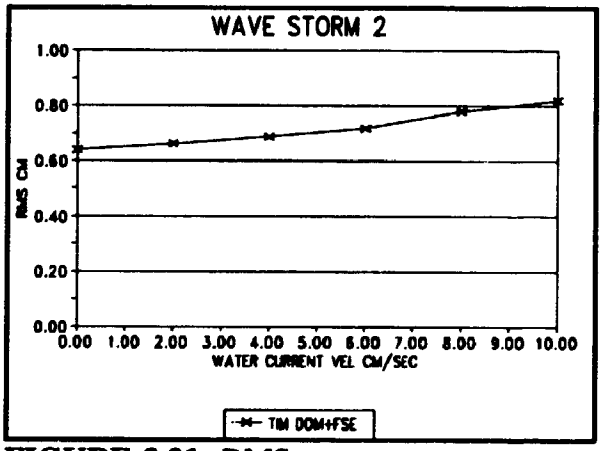

FIGURE 3.21: RMS surge response versus water current velocity

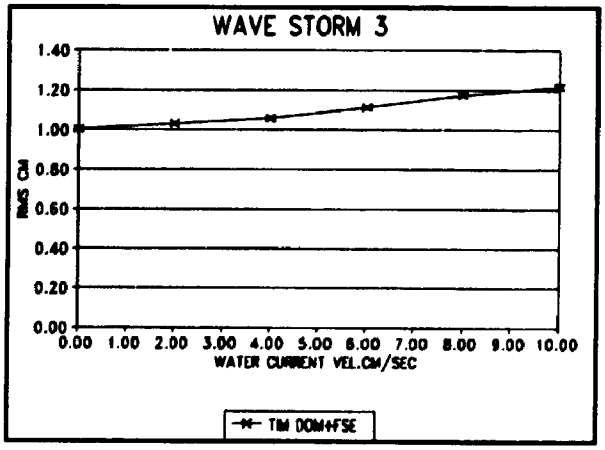

FIGURE 3.22: RMS surge response versus water current velocity

CHAPTER 4

EXPERIMENT DESIGN, ANALYSIS AND COMPARISON OF THEORETICAL AND EXPERIMENTAL RESULTS

4.1 INTRODUCTION

Numerical simulation of the response of slender structures to waves are available, however experimental investigation is an important part of the work. Morison's equation and its modified forms (when allowing for motion) are semi-empirical by nature, and the hydrodynamic force coefficients (C_D,C_M) need to be verified experimentally. The analysis also involves some approximation, especially when modelling forces up to the instantaneous water level, and demands for the verification of theory. Restrictions on Reynolds number scaling and some of other limits on the wave height prevent the direct use of the experimental force coefficients, nevertheless they can be used to estimate the input parameters in a preliminary design case.

The objective of this chapter is to predict the surge response of scaled simple cantilever model of a typical compliant tower to the combined action of wind and waves, and verify the numerical results by comparing them with the experimental responses obtained in the wind/wave facility at the BLWTL at the University of Western Ontario. In this chapter, the test program and physical modelling of the experimental part of this work is described. It consists of:

1- The calibration of the wave tank to measure the frequency response of the tank at different frequencies and amplitudes, and to obtain the reflection characteristics of the tank as well as breaking pattern of the waves. Generation of the random waves was done based on the JONSWAP spectrum, using the measured frequency response of the tank.

2- Design of a set up to measure damping, drag and inertia coefficients for a typical scaled stick model of the compliant tower for a variety of sea states (regular and random waves) and motion KC numbers (Kc_m). This information were then used in the final model analysis.

3- Design of a set up to measure the low frequency forces (including free surface drift and bounded long waves) in bichromatic and random waves. These results were then compared with those obtained by employing the theory given in Chapter 2 to see how good the correlation was. An approximate analysis was performed to evaluate the long wave activity in the tank and its contribution to the total low frequency forces on the member.

4- Design of a stick model which is scaled model of the leg of a typical compliant tower and measurement of the surge response of such structure to the combined action of random wave and wind storms. The results were compared with those obtained by employing the measured wave and wind records in dynamic modal analysis.

Over the wave tank section of the wind tunnel wind speeds of up to 5 m/sec are possible and the test consisted of three different wave storms, with each of them being repeated for four different wind speeds. These combinations will cover some of the probable average to rough wind-wave conditions encountered by a compliant tower.

4.2 CALIBRATION OF THE WAVE TANK

4.2.1 DESCRIPTION OF THE WAVE TANK

The wave tank in BLWTLII at the University of Western Ontario is shown in Figure 4.1. This is a facility for testing offshore structure models under the combined action of the wind and wave loads.

The tank is 52 meters long by 5 meters wide and has a depth of 1.6 meters for most of its length. At the test section (pit) the depth is increased to 3.2 meters to allow for installation of deep water offshore platform models. At one end of the tank is a computer controlled wave paddle which is used to generate both regular and random long crested waves. Further detail on paddle control and geometry of the beach may be found in Slezak (1986), and Thomas (1987). At the other end of the tank is a bilinear beach and is designed to minimize the reflection of the incident wave fields. Further detail about the beach and it's design may be found in Thomas (1987).

4.2.2 WAVE TRAINS OF INTEREST

Regular (monochromatic) incident wave trains were used for calibration of the wave tank. By changing the frequency and amplitude independently a series of tests were performed to measure the reflection and performance (frequency response) characteristics of the wave tank.

4.2.3 REFLECTION MEASUREMENTS

If plane waves are incident on a beach, the beach will absorb some of the wave energy and the amplitude of the reflected waves are reduced. In a two dimensional case, with the incident wave $\eta_I(x,t) = A\cos(kx-\omega t)$ travelling from $-\infty$, the surface elevation due to the superposition of the incident and reflected waves is:

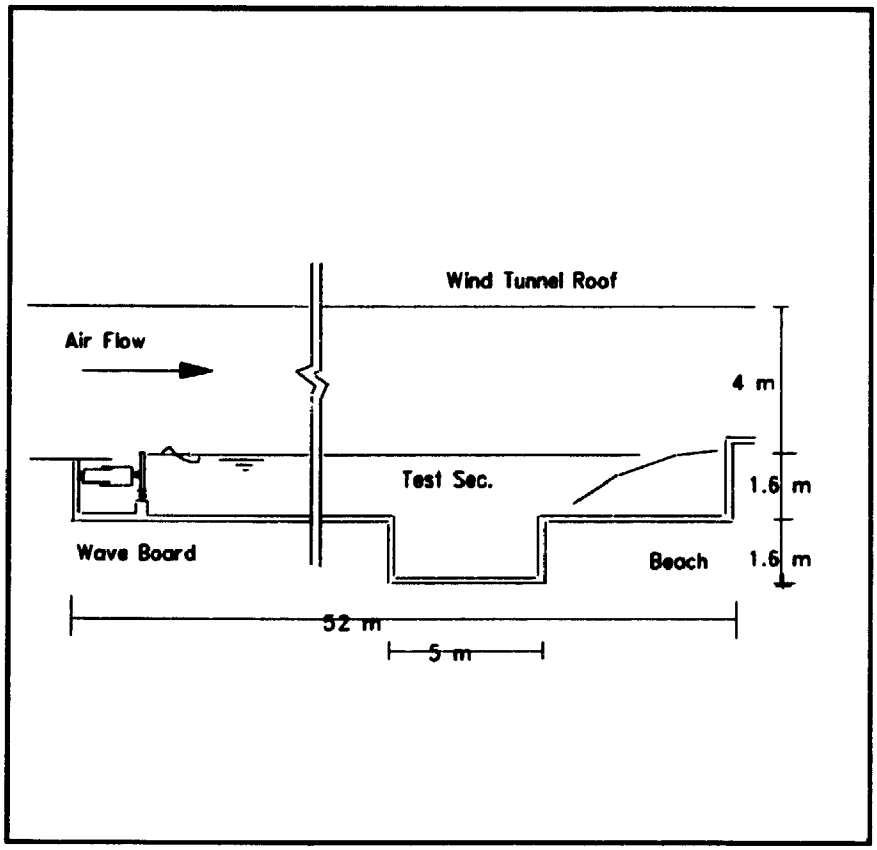

FIGURE 4.1: Wind/Wave facility at BLWTL at UWO.

$$\eta = A\,Rea(\exp(-ikx+i\omega t)+R\exp(ikx+i\omega t)) \qquad (4.1)$$

where 'Rea' is the real part of the expression. The complex notation considers the effect of the phase of the reflected wave with the corresponding coefficient R being complex. For a beach, the magnitude of the reflection coefficient R, is generally small. Equation (L1) can be written in the form of

$$\eta = A\,Rea(\exp(-ikx+i\omega t)\,[1+R\exp(2ikx)]) \qquad (4.2)$$

The factor inside the bracket is the amplitude variation which varies in x with half of the wavelength. This can be observed by following the change in the amplitude of a typical wave crest in a wave tank.

In this study the reflection coefficient is measured by two different techniques:

1-Method of two stationary probes

2-Method of moving probe

4.2.3.1 METHOD OF TWO STATIONARY PROBES

In this method two stationary probes measured the time histories of the resultant wave field at two separate locations along the longitudinal axis of the tank (Goda, Suzuki; 1976). The probes for measuring the water elevation were capacitive probes, and they consisted of an insulated sensing wire which is submerged in the free surface of the water. The capacitance of the wire changes linearly with the depth of the submergence of the water and is described in detail by Thomas (1987).

The resultant surface elevation due to incident and reflected waves at the two locations (x_1,x_2) are:

$$\eta_1=\eta_I+\eta_R=a_I\cos(\omega t-kx_1+\delta_I)+a_R\cos(\omega t+kx_1+\delta_R) \qquad (4.3)$$

$$\eta_2=\eta_I+\eta_R=a_I\cos(\omega t-kx_2+\delta_I)+a_R\cos(\omega t+kx_2+\delta_R) \qquad (4.4)$$

where a_I and a_R are the amplitudes of the incident and reflected waves, δ_I, δ_R are their phases and x_1, x_2 are the coordinates of the probes in the x direction (direction of wave propagation). For convenience, one of them can be set equal to zero, so the distance between the probes is x. The wave elevation measured by each probe can be given as:

$$\eta_1=A_1\cos(\omega t) \qquad (4.5)$$

$$\eta_2=A_2\cos(\omega t+\delta) \qquad (4.6)$$

where

$$R=\frac{a_R}{a_I}$$

note that $kx=|\delta|$.

Expanding these equations and solving the four equations in four unknowns yields:

$$\delta_R=\arctan\left(\frac{\cos kx}{\sin kx}\right)=\arctan(\cot kx) \qquad (4.8)$$

$$R=\frac{-A_1+A_2}{4\tan kx\,\sin\delta_R} \qquad (4.9)$$

$$\delta_I=\arctan\left(\frac{A_1-A_2}{A_1+A_2}\cot kx\right) \qquad (4.10)$$

$$a_I = \frac{A_1 - A_2}{4 \tan kx \sin\delta_I} \qquad (4.11)$$

This method is sensitive to the distance between probes and this distance should not be equal to a multiple of a half a wavelength to avoid singularity in the solution of the equations.

Two typical wave trace with f = 0.8 Hz., measured by the two probes, are shown in Figure 4.2 from which the above mentioned quantities can be computed. In this experiment the probes were located above the pit with x=0.4 meter, and the reflection coefficients measured are shown in Figures 4.4 to 4.7 for comparison with the other method .

4.2.3.2 METHOD OF MOVING PROBE

In this method only one wave probe is required. The probe was installed on the mid span of a trolley which was able to traverse along the tank by a motor with a constant velocity of V=0.62 ft/sec. Using this approach, the apparent frequency of the incident waves (c+v)/L and reflected waves (c-v)/L would be different.

The measured time history of the moving probe was used to find the reflection coefficient for each of the monochromatic waves. This time history was fitted to a bichromatic wave system of the form:

$$\eta = a_0 + a_I \sin(\omega_1 t + \phi_1) + a_R \sin(\omega_2 t + \phi_2) \qquad (4.12)$$

In which all of the coefficients a_0, a_I, a_R, ω_1, ω_2, ϕ_1, ϕ_2 were considered as

unknowns and were found by using a nonlinear least square scheme (Gauss-Newton search method). Figure 4.3 shows the typical fitted wave trace for f=0.8 Hz when the paddle voltage is V=2.4 volts. The measured values of coefficient of reflection by this method compared relatively well with the results found by the stationary probes method (Figures 4.4 to 4.7). As can be seen in the curves the reflection coefficients of the tank are in the range of 3% to about 10%, depending on the wave frequency and steepness. For the range of frequencies and steepnesses used in this study the reflection coefficient is on the order of 8%.

During this experiment the motion of the trolley and vibration of the motor connected to it, introduced some low frequency phenomenon in the time history of the measured waves which made it difficult to enhance the quality of fitting (Figure 4.3), although frequency and phase wise the fitting was reasonable.

Using a moving probe, another method was tried to find the reflection coefficient by transforming the measured time history in to the frequency domain and finding the area under the two peaks corresponding to the incident and reflected waves. It was clear that the peaks corresponding to the reflected waves are small but the resolution was not good enough to get a reliable value for that peak. The results from this method were not conclusive.

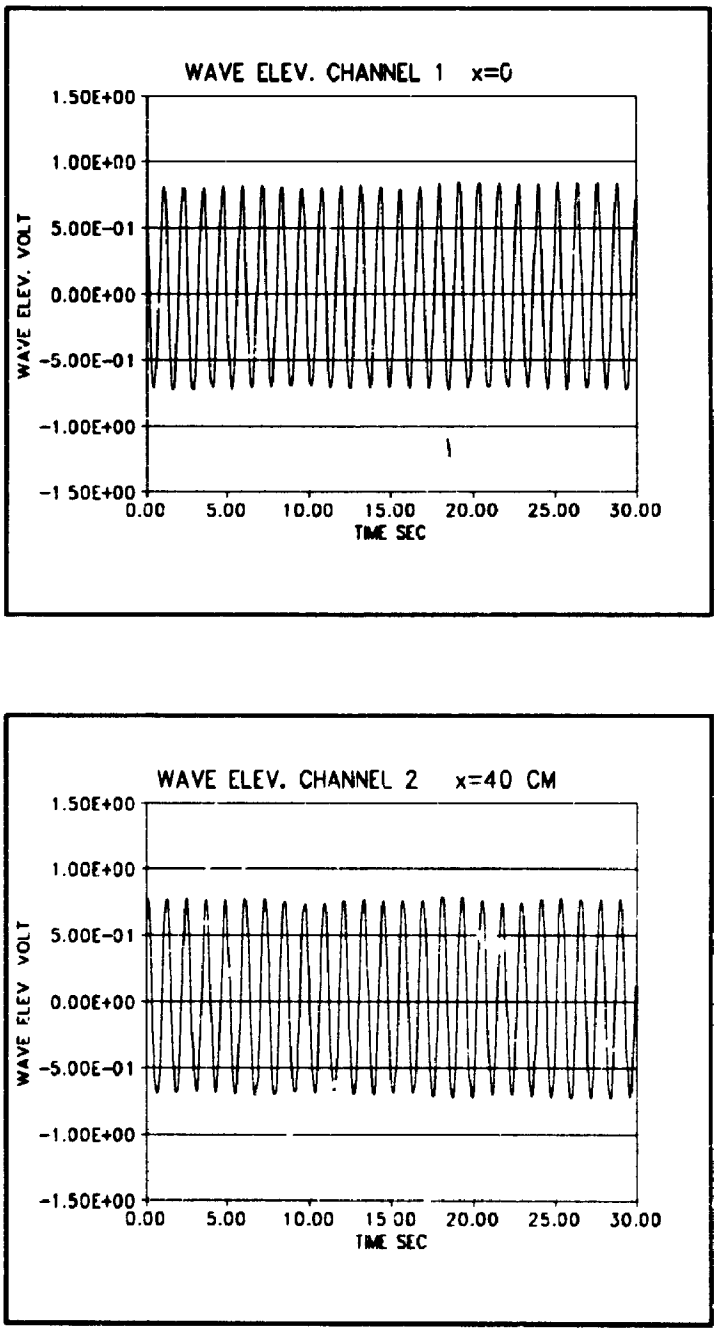

FIGURE 4.2: Typical wave elevation time history in volt. RE2480

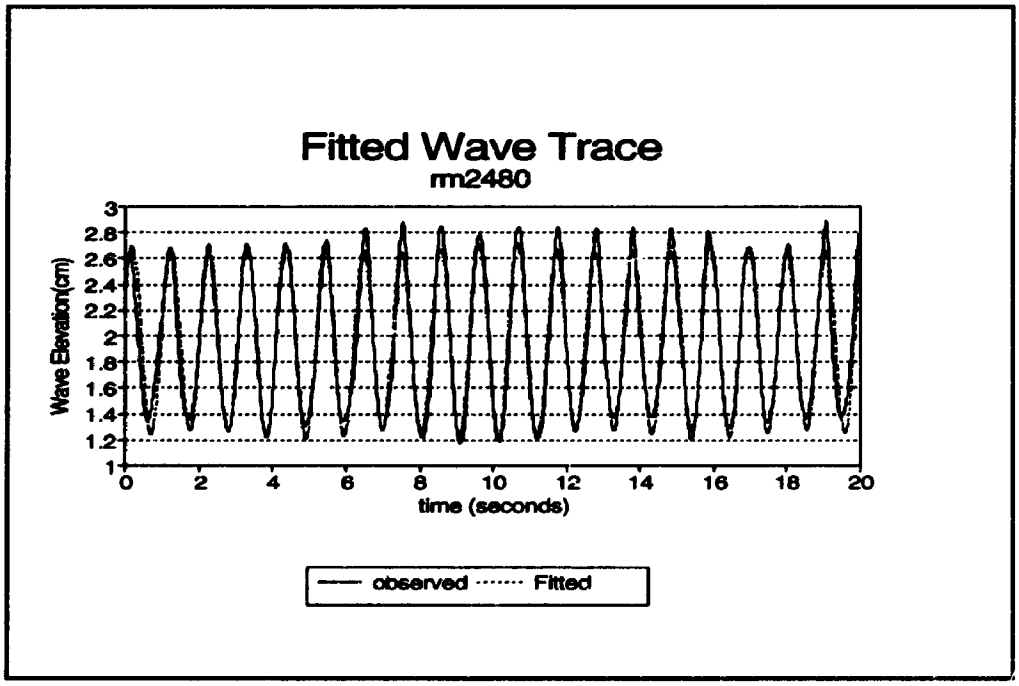

FIGURE 4.3: Fitted wave trace to the time history measured by the moving probe. f=0.8 Hz,V=2.4 Volts.

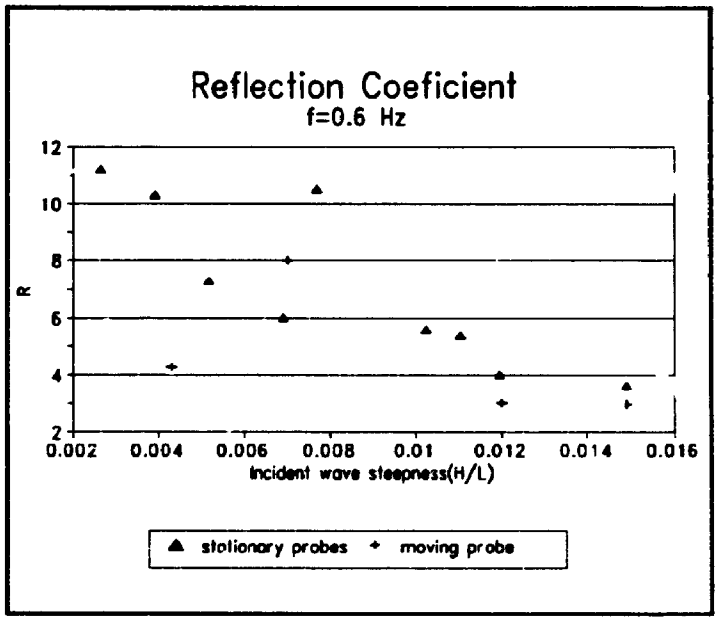

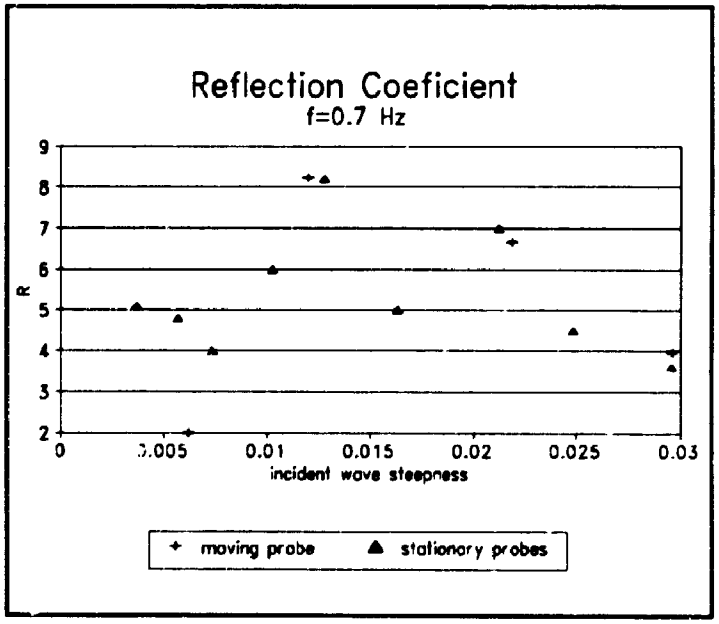

FIGURE 4.4: Measured reflection coefficient (%) vs. wave steepness

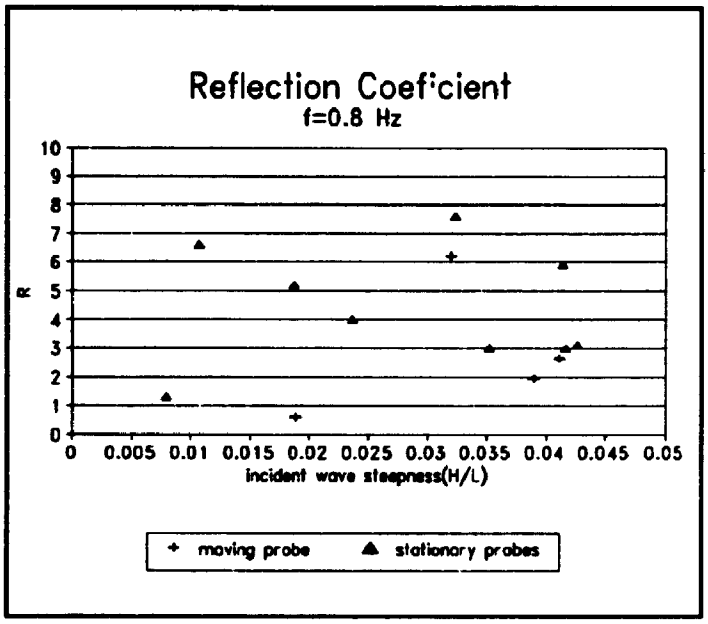

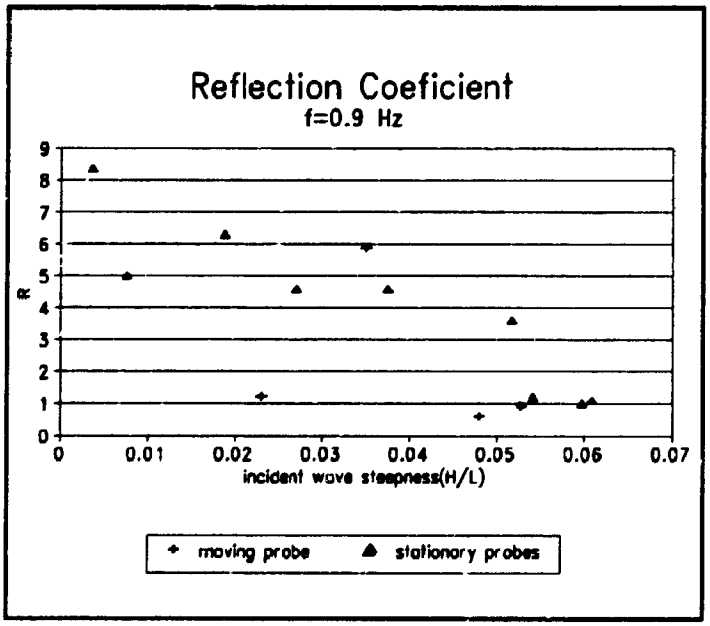

FIGURE 4.5: Measured coefficient of reflection (%) vs. wave steepness.

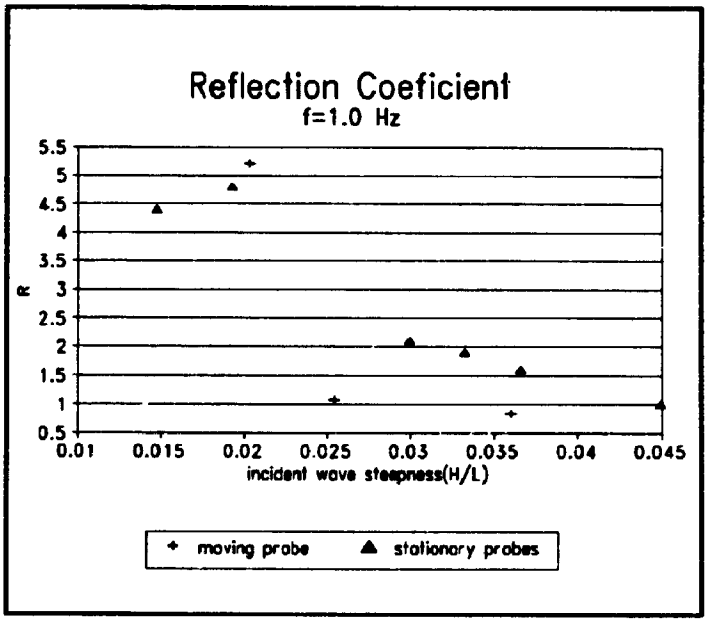

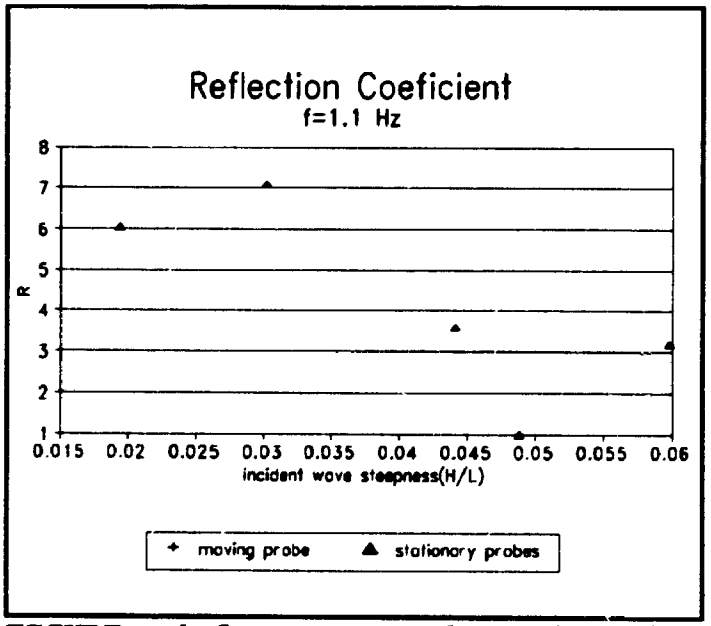

FIGURE 4.6: Measured reflection oefficient (%) vs. wave steepness

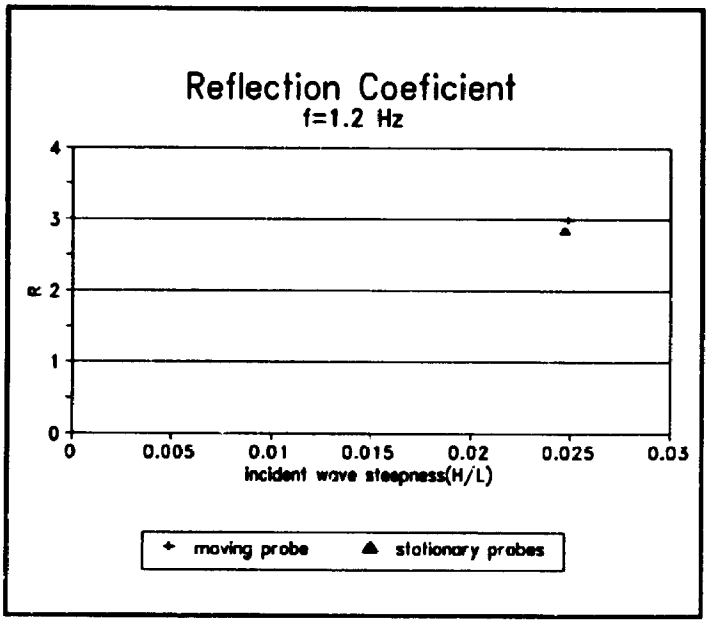

FIGURE 4.7: Measure.. reflection coefficient (%) vs. wave steepness.

4.2.4 PERFORMANCE CHARACTERISTIC OF THE WAVE TANK

After calculating the value of the incident wave amplitude, the curves showing the variation of wave amplitude versus paddle voltage for each frequency were plotted for the two different methods (Figures 4.8 to 4.11), and as it is shown the results are in good agreement.

Increasing the amplitude of the waves at a constant frequency causes them to becomes steeper until at some amplitude they start breaking. Wave breaking occurs as the waves reach a critical limit in steepness which can no longer maintain their trochoidal geometry. The critical ratio of wave amplitude to wave length at which this phenomenon begins is about 1/7 (H/L=0.14tanh(2d/L)). For frequencies above 1.0 Hz., breaking was observed at an amplitude of about 4 cm. During the experiment no transverse standing wave was observed.

4.3 RANDOM WAVES AND WIND

4.3.1 RANDOM WAVES

Three different wave storms were used and their short term description (peak frequency and significant wave heigth) are, F_p=1.05 Hz, H_s=5.3 cm; F_p=0.86 Hz, H_s=7.8 cm; F_p=0.81 Hz, H_s=10.9 cm.

The random waves were generated considering the frequency response of the tank, H(f). It was calculated using a polynomial fit, based on linearity of the characteristic curves represented in Figures 4.8 to 4.11. Wave elevation time history was calculated based on the input target wave spectra (JONSWAP, γ=2.5) using the random phase and frequency method. This time history was then transfered to a PC which was connected to the wave

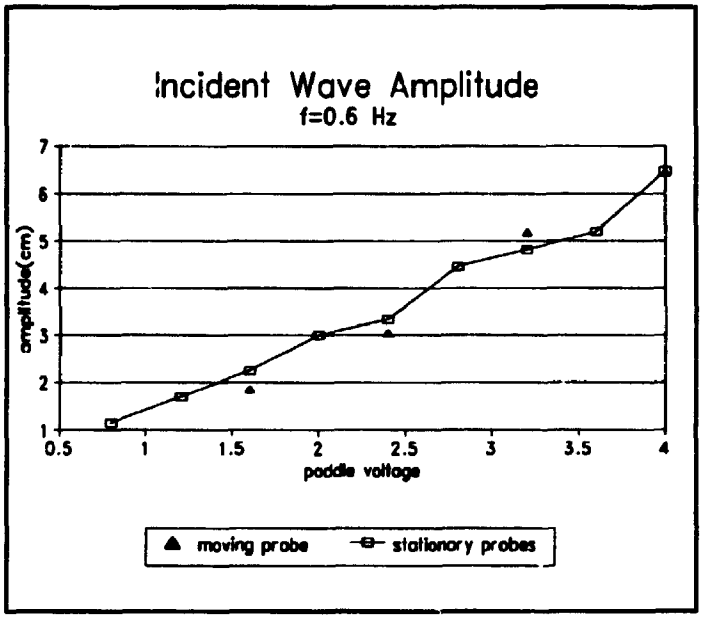

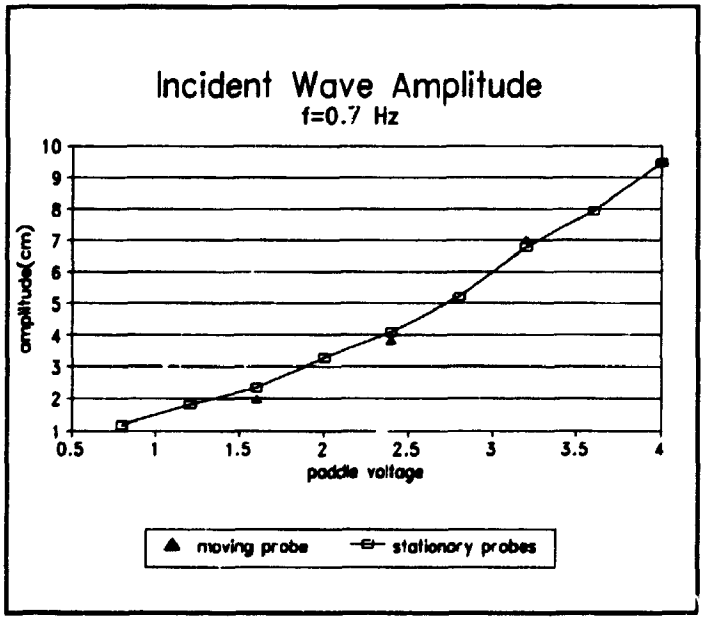

FIGURE 4.8: Wave tank calibration

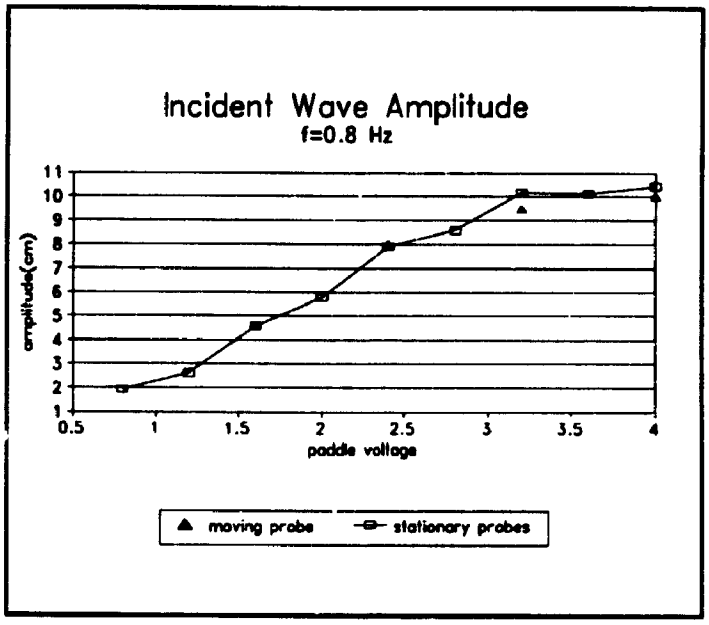

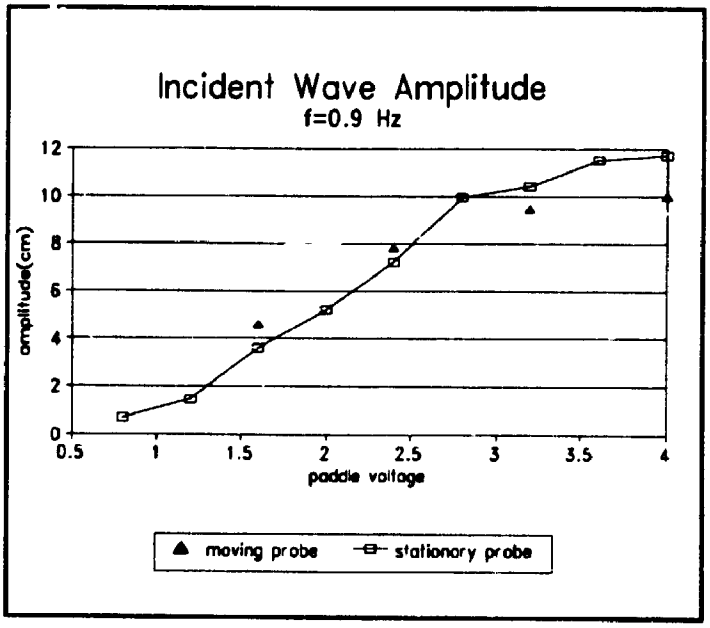

FIGURE 4.9: Wave tank calibration

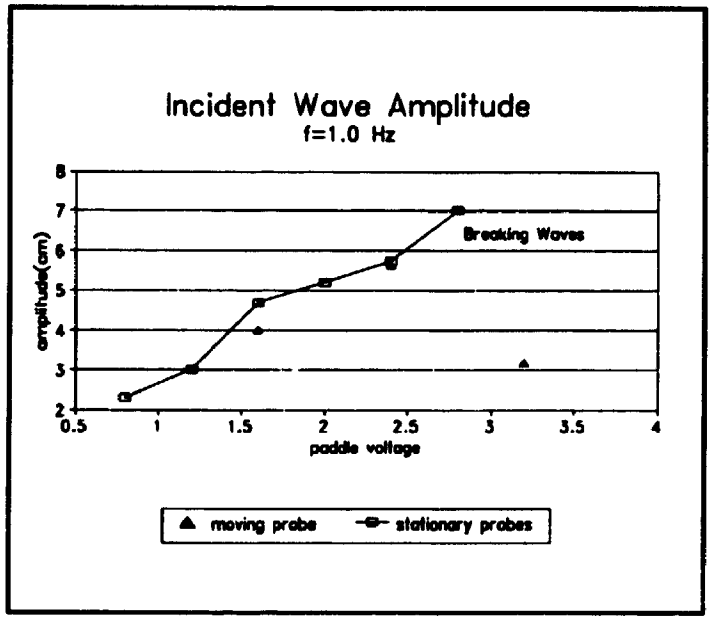

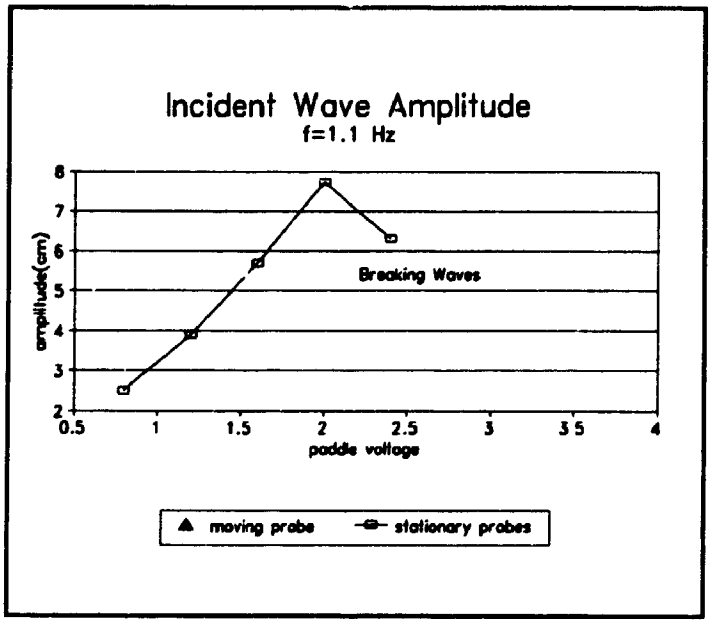

FIGURE 4.10: Calibration of the wave tank

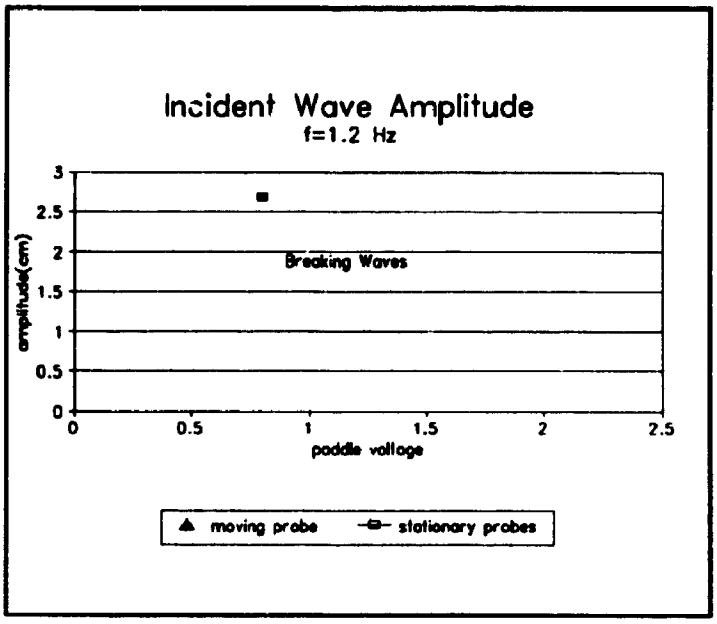

FIGURE 4.11: Calibration of the wave tank

paddle.

A program, using a delay, was written to send the digitized signal to the paddle. By calibrating the delay using time histories of the same spectum with different Δt, it was possible to achieve a reasonable spectrum at the test section. The wave elevation spectrum observed at the site (model section) by the wave probe was monitored by the HP structural dynamic analyzer. The whole process was an iterative process until the wave spectrum observed at the site more or less matched the required spectrum.

The observed wave spectra are shown in the following sections.

4.3.2 SIMULATION OF WIND

Wind profile and intensity measurements were carried out at the center line of the tunnel at a model scale speed of 4.0 and 4.9 m/sec. The 4.9 m/sec velocity was attempted for the 'wind only' case, and the 4.0 m/sec was attempted in combination with the three wave storms 1,2,3. The tunnel was scanned vertically using a hot wire anemometer. Figures I.1 to I.4 (Appendix I), show the measured wind velocity and intensity profiles.

In the caes of strong wind over the sea, only a limited full scale tests indicating the structure of the turbulence exist, and most of them contain to some extent scatter and are not very reliable , specifically at low frequencies. Ng (1988) carried out some measurements on the wave tank to obtain the wind velocity profile and spectra. These measurements were done at a height of 8 inches above the mean water level and were compared with the ESDU data (1974.1985). He concluded that both the velocity profile and spectra were in agreement with the simulated data.

4.4 VERIFICATION OF HYDRODYNAMIC DAMPING, DRAG AND INERTIA COEFFICIENT (EXPERIMENT AND ANALYSIS)

4.4.1 INTRODUCTION

The present study investigates the interaction between wave and structural motion in a variety of free vibration damping tests in still water, monochromatic waves and in random seas. The drag coefficients based on the relative velocity model (RVM) and independent flow fields model (IFFM) were evaluated both from the damping traces and by matching of the measured and computed force time histories. The results from the two models were compared. The inertia coefficients (C_M) based on the RVM was also derived using the matching method, both for still water and regualar waves.

4.4.2 EXPERIMENTAL PROCEDURE

The model is shown in Figure 4.12 and is a 1:150 scaled model of the leg of a compliant tower. It is a hollow aluminum cylinder with a diameter of 1.9 cm and was submerged 50 cm and 80 cm in the water. The water depth at the model site was 3.2 meters which with the above-mentioned scaling implies a deep water condition for the range of frequencies (0.6 to 1.2 Hz.) used. The model was clamped to a force balance attached to the bottom plate assembly. This plate was suspended by three vertical steel straps with the length of 2.4 m. The force balance was instrumented with two unbonded

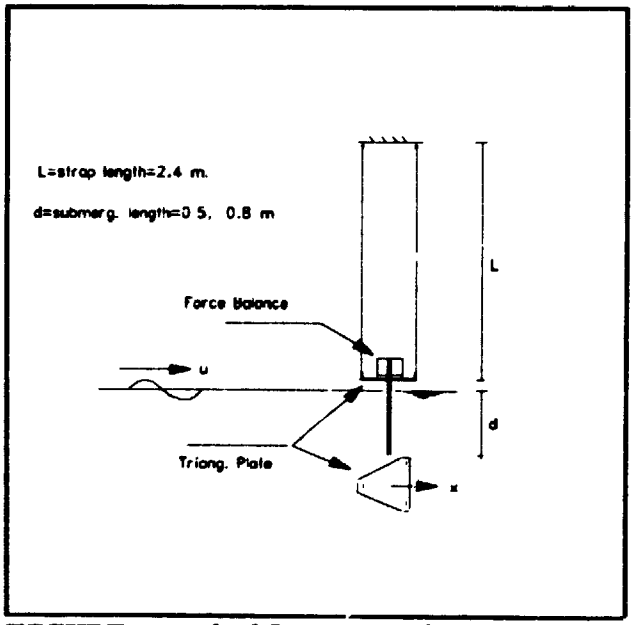

FIGURE 4.12: Scheme of experimental set up for measurement of damping, and Morison force coefficients.

load cells, one to measure the force in the surge direction and the other to measure the force in the sway direction.

The natural period of the system was 2.61 seconds. The weight of the bottom part of the pendulum including force balance and the triangular plate was 32 kg which produced an effective mass parameter ($m/\rho D^2$, where m is the equivalent mass per unit length of the cylinder) of about 160 and resulted in a slow decay of the induced motion. A strain gauge was connected to the top of the one of the strap bars to monitor the motion of the model. Wave elevation was monitored by using three capacitive type wave probes (two were located approximately 40. cm from the centerline of the model on each side and the other one was 1. meter behind). The wave probe, the force balance and the motion detector were sampled at a rate of 20 Hz.

The test consisted of four different phases:

1- Model fixed in regular waves.

2- Pendulum motion in still water (simple surging test).

3- Pendulum motion in regular waves.

4- Pendulum motion in random waves.

In order to determine the nonhydrodynamic (structural) damping some extinction tests in air were also performed.

The sea states examined included regular waves with an average wave height of H=2, 5.5, 7.5, 11, 14, 19 cm, T (wave period)=0.6, 0.7, 0.8, 0.9, 1.0 and three random seas with Hs=5.4 cm., Tp=0.96 sec.; Hs=7.9 cm., Tp=1.16 sec.; Hs=10.9 cm., Tp=1.25 sec. (Hs and Tp are the significant wave height and peak period respectively). The wave elevation spectra for the three random wave storms are shown in Figure 4.1?

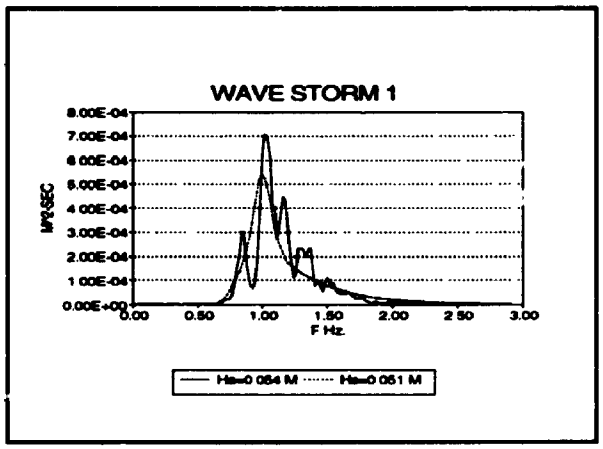

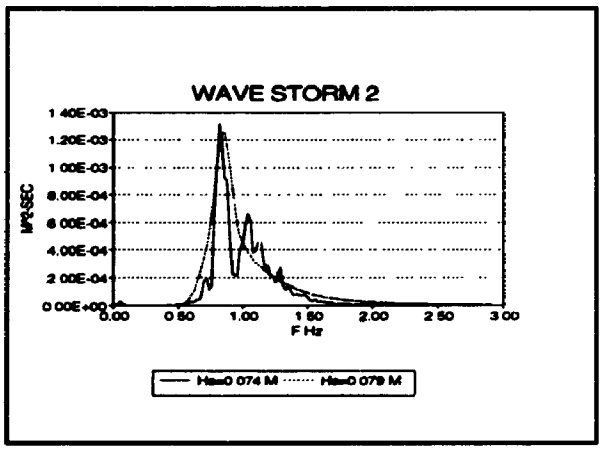

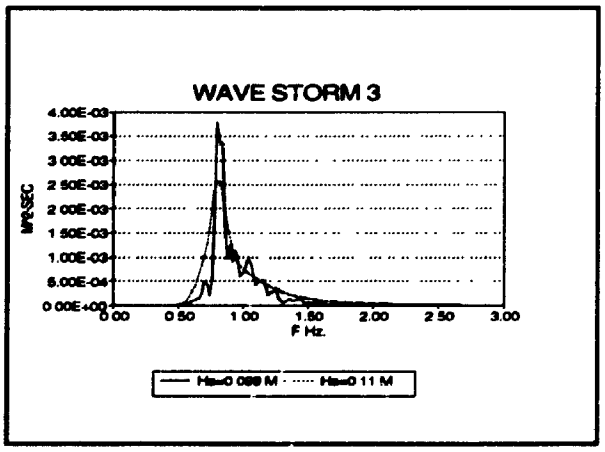

FIGURE 4.13: Sea storm 1-3 used in the experiment (target and observed spectra)

4.4.2.1 FIXED CYLINDER IN WAVES

Drag and inertia coefficients were derived from force time histories measured on a fixed cylinder in monochromatic seas. If the observed wave elevation trace ($\eta(t)$) is fitted $\eta = \frac{H}{2}\cos(\omega t+\phi)$ (x=0 is the axis of the cylinder), the total hydrodynamic force after integration is:

$$F(t) = \frac{1}{8}K_D g H^2 (1-e^{-2kd})|\cos(\omega t+\phi)|\cos(\omega t+\phi) - \frac{\pi}{8}\rho D^2 C_M H g (1-e^{-kd})\sin(\omega t+\phi) \qquad (4.13)$$

where d=submergence length of the model and $K_D=1/2\rho C_D D$.

In deriving this equation, the deep water dispersion relation has been used $(\omega^2=kg)$.

Values of C_M, C_D were evaluated by a least square method in which the measured trace was fitted by a relationship of the form defined by equation 4.13.

4.4.2.2 PENDULUM MOTION IN STILL WATER AND REGULAR WAVES

If x_0 is the envelope of a decaying damping trace, then the damping, $\beta(x_0)$, as a function of critical can be expressed as:

$$\beta(x_0) = -\frac{1}{2\pi}\frac{dln(x_0(t))}{dN} = -\frac{1}{\omega_0}\frac{dln(x_0(t))}{dt} \qquad (4.14)$$

where $\omega_0 t=2\pi N$, $x_0(t)$=decaying motion amplitude, ω_0=natural radian frequency of motion, and N=cycle number.

The measured decaying motion was fitted by a relationship of the form:

$$x(t) = x_0 e^{A_1 t + A_2 t^2 + A_3 t^3} \cos(\omega_0 t + \delta) = X_0(t) \cos(\omega_0 t + \delta) \qquad (4.15)$$

where x_0, Ai=1,2,3, δ are unknown parameters.

The fitting procedure used a nonlinear optimization scheme (steepest descent method). Upon finding this envelope, damping ratio was obtained using equation 4.14. The same procedure was used in a dry condition (model in air) to find the structural damping (β_{st}). Damping due to hydrodynamic effects was then given by:

$$\beta_{hyd} = \beta_{tot} - \beta_{st} \qquad (4.16)$$

A drag coefficient can be obtained by equating the work done by the drag force over one cycle to the loss of energy assuming a constant C_D per cycle (Moe and Verley, 1980; Demirbilek et al., 1986).

The dynamic equation for the pendulum system is:

$$(M + \frac{mL}{3})\ddot{x} + C_s\dot{x} + (\frac{1.2Mg}{L} + 0.6mg + \frac{12EI}{L^3})x = F(t) + \frac{Bx}{L} \qquad (4.17)$$

where M is the lumped mass at the bottom part including model force balance and triangular plate, ml is the mass of the straps. The buoyancy force, $B = \frac{1}{4}\pi\rho D^2 gd$, is assumed to be constant and the change of the submergence due to wave action is neglected. Also the change of submergence due to pendulum motion is quite small since the maximum horizontal displacement is about 8 cm which on a 2.4 m length pendulum corresponds to 1.9 degrees.

4.4.2.2.1 RELATIVE VELOCITY MODEL

Assuming the horizontal structural motion with respect to the equilibrium position of the centreline of the leg,x(t), and the corresponding wave velocity, u, to be respectively:

$$x(t) = x_0 \cos(\omega_0 t + \theta) \tag{4.18}$$

$$u = \frac{H\omega}{2} e^{kz} \cos\omega t \tag{4.19}$$

The phase lag θ can be calculated from previous stages of the work (θ=δ-ϕ)
The horizontal force f(t,z) per unit length using the relative velocity model then would be:

$$f(t,z) = K_D \left| \frac{H\omega}{2} e^{kz} \cos\omega t + x_0\omega_0 \sin(\omega_0 t+\theta) \right| \left(\frac{H\omega}{2} e^{kz} \cos\omega t + x_0\omega_0 \sin(\omega_0 t+\theta) \right) + K_I(\dot{u}-\ddot{x}) + \frac{\pi}{4}\rho D^2 \dot{u} \tag{4.20}$$

where,

$$K_I = \frac{\pi}{4}\rho D^2 C_A \quad , \quad K_D = \frac{1}{2}\rho D C_D \tag{4.21}$$

The dissipated energy per cycle due to the drag force would be:

$$E_{dis} = \int_0^{T_0} \int_{-d}^{0} f_D \dot{x}\, dt\, dz \tag{4.22}$$

where f_D is the drag part of f(t). This equation can be written as:

$$E_{dis} = -\frac{1}{2} \frac{\rho C_D D^3 x_0 \omega_0^2}{(2\pi)^2} \int_0^{2\pi} \int_{-d}^{0} \left| V_r e^{kz} \cos\omega_r\Theta + KC_m \sin(\Theta+\theta) \right| \left(V_r e^{kz} \cos\omega_r\Theta + KC_m \sin(\Theta+\theta) \right) \sin(\Theta+\theta)\, d\Theta\, dz \tag{4.23}$$

where V_r is the reduced velocity at the still water level, KCm is the motion KC number, $\Theta=\omega_0 t$ and $\omega_r=\omega/\omega_0$

$$V_r=\frac{\frac{H\omega}{2}T_0}{D}=\frac{u_0 T_0}{D} \quad , \quad KC_m=\frac{2\pi x_0}{D} \tag{4.24}$$

Equating this work to the work associated with the hydrodynamic damping force per cycle (equivalent linear damping) leads to the hydrodynamic drag coefficient as a function of

β_{hyd} , V_r , KC_m

$$C_d=\frac{8\pi^2\beta_{hyd}KC_m M^*}{\rho D^2\int_0^{2\pi}\int_{-d}^{0}\cdot\cdot} \tag{4.25}$$

where the double integral is the same as that in equation 4.23.

Since ω/ω_0 is generally more than 2. The effect of phase lag between wave and motion decreases as one integrates over more than one cycle and in general the smaller the natural frequency (compared to wave frequency), the smaller the effect of this phase would be. The errors induced by ignoring the phase effect were examined and, for the cases studied, found to be less than 10% for integration over one cycle.

4.4.2.2.2 INDEPENDENT FLOW FIELDS MODEL

For this model, the drag force per unit length assuming one drag coefficient is:

$$f_D=\frac{1}{2}\rho C_D D(|u|u-|\dot{x}|\dot{x}) \tag{4.26}$$

According to this model the two fields are independent and the first term (far field wave) produces a high frequency excitation (Demirbilek et al.,1987) which does not have much effect on the response (this is valid when the response is mostly dominated by the resonance part and frequency ratio is more than 3.) hence the free vibration of the model in waves is still like a decay motion in still water. Damping can be derived as in the case of the still water surge test.

Using the approach given before, the value of C_D required to match the damping trace is:

$$C_D = \frac{3}{2}\frac{\pi M^* \beta_{hyd}}{\rho D X_0 d} \qquad (4.27)$$

4.4.2.3 RANDOM WAVES

In the case of random waves using the same approach as given before for the regular waves in RVM but using:

$$u(t,z) = \sum_{i=1}^{N} \frac{H_i \omega_i}{2} \exp(k_i z) \cos(\omega_i t + \phi_i) \qquad (4.28)$$

which was generated on the basis of the achieved spectrum for the 3 sea states and using the related motion envelope function $x_0(t)$ for each sea states a drag coefficient was found corresponding to each motion KC_m number.

For the IFFM the method is the same as for regular waves and the drag coefficient as a function of KC_m for each case can be obtained.

4.4.2.4 FORCE MEASUREMENT

As a check of the drag coefficient derived based on the damping trace, estimates were also obtained from an analysis of the force time histories for motion in both still water and in regular waves. Although there were some difficulties associated with this phase of the work specially with steep waves which do not follow the frame of the linear theory (higher peaks and shallower troughs) and problems at very small KC_m due to lateral motion of the model and vortex shedding, this method resulted in good matching of the force time histories.

The inertia coefficient, C_M, was also derived using the matching of the measured force time history with the RVM.

The decaying motion time history x(t) and wave elevation $\eta(t)$ were obtained during the previous sections using the RVM the inline force exerted on the member (prediction of the measured force) would be:

$$F_m(t) = \int_0^d -\frac{\pi}{4}\rho D^2 C_M \frac{H\omega^2}{2} e^{-kz}\sin(\omega t+\phi)\,dz - K_I\ddot{x} - mL\ddot{x} + \frac{Bx}{L} + \int_0^d K_D\left|\frac{H\omega}{2}e^{-kz}\cos(\omega t+\phi) - \dot{x}\right|\left(\frac{H\omega}{2}e^{-kz}\cos(\omega t+\phi) - \dot{x}\right)dz \qquad (4.29)$$

Using numerical integration for drag force (in case of waves) and correlating this force to the measured inline force it was possible to obtain the force coefficients C_D, C_M. In the case of still water surging test the exponential terms in the above equation would be zero. The measured drag coefficient was mostly in good agreement with those obtained by damping trace method except for very small KC_m number. During the analysis, it was observed that the value of added mass coefficient (C_A=CM-1) was mostly bigger than one in the range of KC_m numbers studied.

The force prediction using the IFFM was also examined. The drag coefficients were bigger than those due to RVM especially for KC_m<20.

4.4.3 EXPERIMENTAL RESULTS

The drag coefficients determined for decaying motion in still water and force measurements in regular waves are shown in Figure 4.14. The continious line is the result obtained from the damping trace while the individual

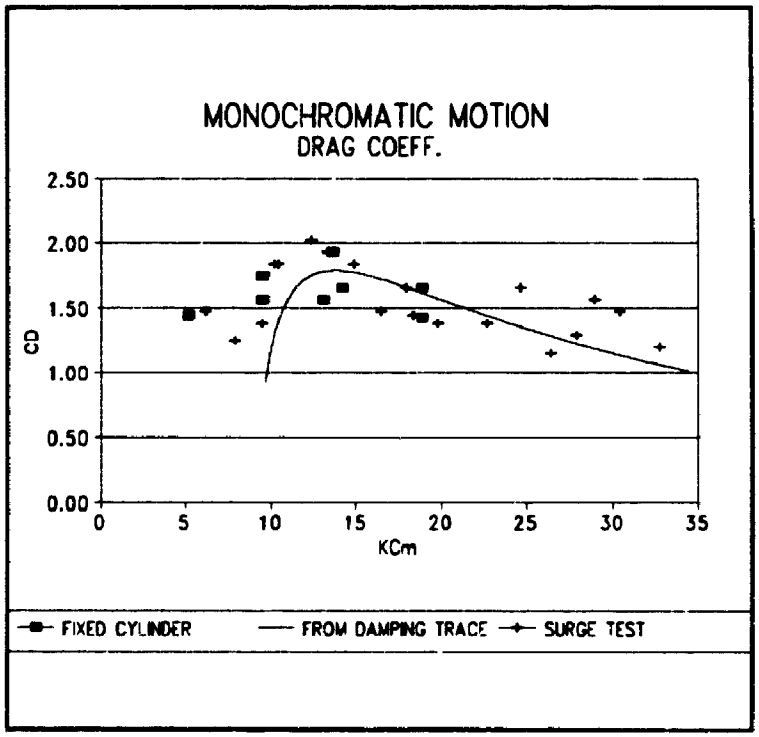

FIGURE 4.14: C_D vs KC_m for surge and fixed cylinder tests.

points have been derived from force time histories. An example of a fitted force time history is shown in Figure 4.15. In this example KC_f=7.3 and the value of C_D is 1.45. The results in the case of fixed cylinder in waves for some other wave amplitudes and frequencies are presented in appendix C. The damping trace for decaying motion in still water is shown in Figure 4.16 together with the envelope function. The damping ratio (% of critical) derived from Figure 4.16 is shown in Figure 4.17. The inertia coefficients derived from the force time histories in still water and fixed cylinder in regular waves are

shown in Figure 4.18. A typical damping trace for decaying motion in regular waves is shown in Figure 4.19 together with the envelope function. The damping ratio (% of critical) derived from Figure 4.19 is shown in Figure 4.20 while Figure 4.21 shows the deduced values of C_D assuming the independent flow fields model (IFFM) and the relative velocity model (RVM). Also shown in Figure 4.21 (as individual points) are the values of CD derived from the force time history matching. The results for other wave amplitudes and frequencies are presented in appendix D.

Typical time histories from which CD was determined by force matching is shown in Figures 4.22 to 4.25 together with the simulated trace, for both simple surge and oscillation in wave tests.

Figure 4.28 shows the drag coefficients obtained from both models for a variety of frequencies and regular seas using the damping method. The heavy line represents the still water test. The vertical arrows in this figure indicate increasing wave height and frequency for both models. In Figure 4.26, the inertia coefficients derived based on the measured force time histories in the case of motion in regular waves using RVM, are shown. The results corresponding to the still water test are also presented in the same figure. The envelope, damping and drag coefficients derived from damping tests in random seas (three wave storms) are presented in appendix D. The result for the third wave storm is shown in Figure 4.27. The significant wave height and central frequency for the third wave storm are nearly equal to the wave height and frequency of the regular wave train used to derive the data in Figure 4.21.

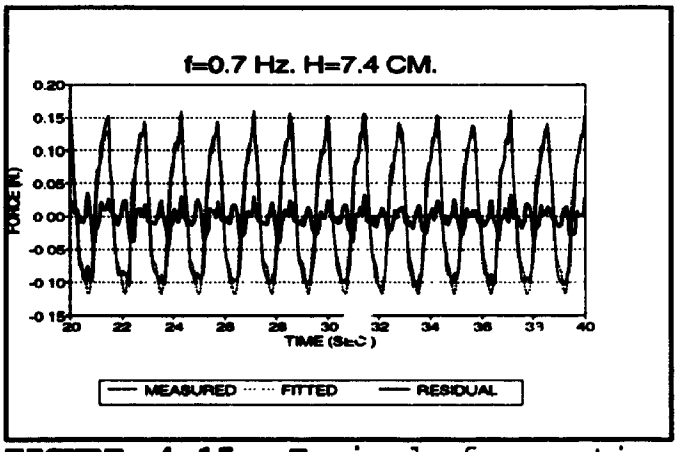

FIGURE 4.15: Typical force time history for the fixed cylinder in regular waves, measured and predicted (f=0.7 Hz, H=7.4 cm).

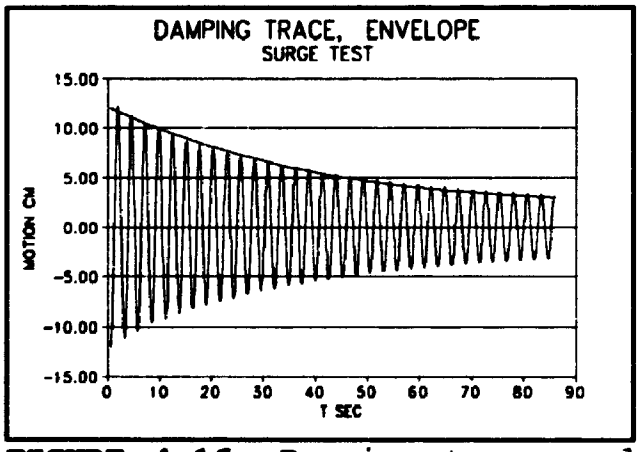

FIGURE 4.16: Damping trace and corresponding envelope in simple surge test.

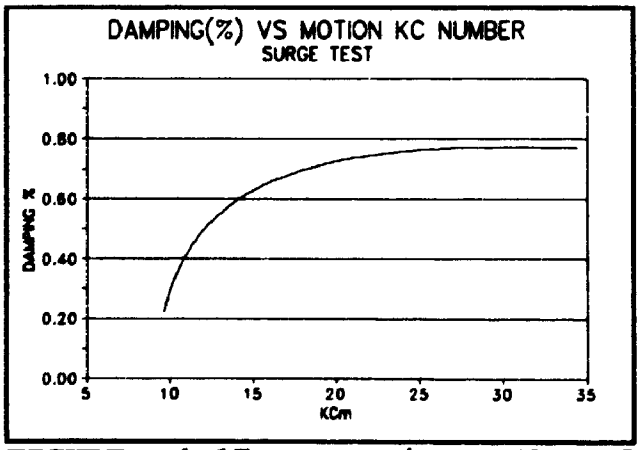

FIGURE 4.17: Damping (% of critical) in surge test.

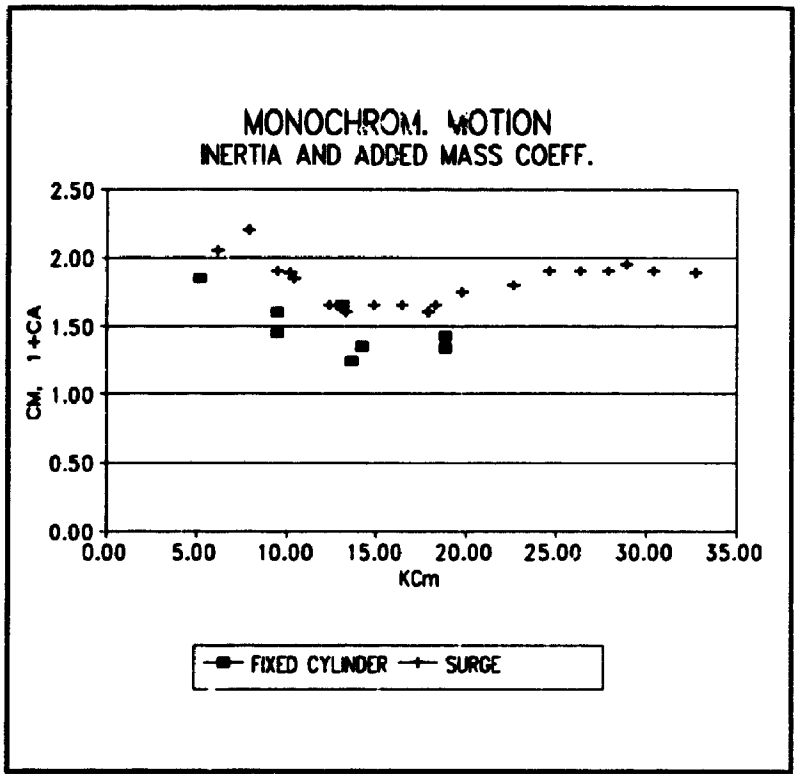

FIGURE 4.18: C_M and C_A vs KC_m for surge and fixed cylinder tests.

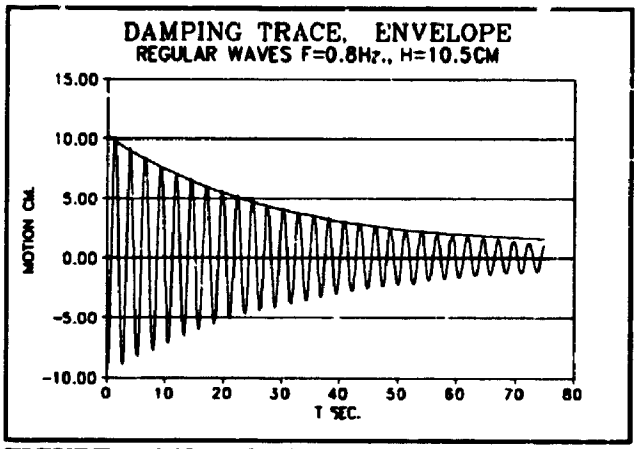

FIGURE 4.19: Typical damping trace and corresponding envelope in regular waves f=0.8 Hz, H=10.5 cm.

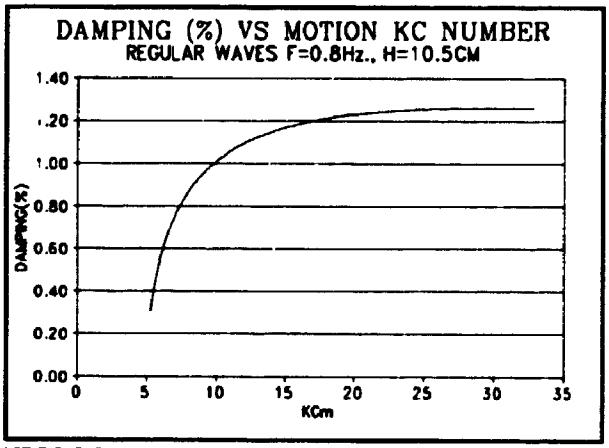

FIGURE 4.20: Typical damping (% of critical) in regular waves f=0.8 Hz, H=10.5 cm.

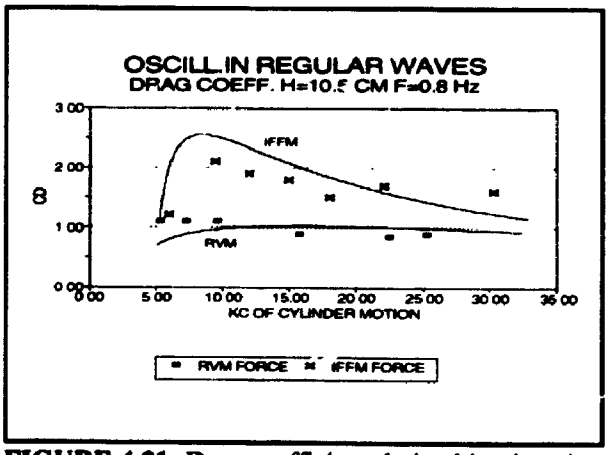

FIGURE 4.21: Drag coefficient derived by damping and force measurements using RVM and IFFM in regular waves f=0.8 Hz, H=10.5 cm.

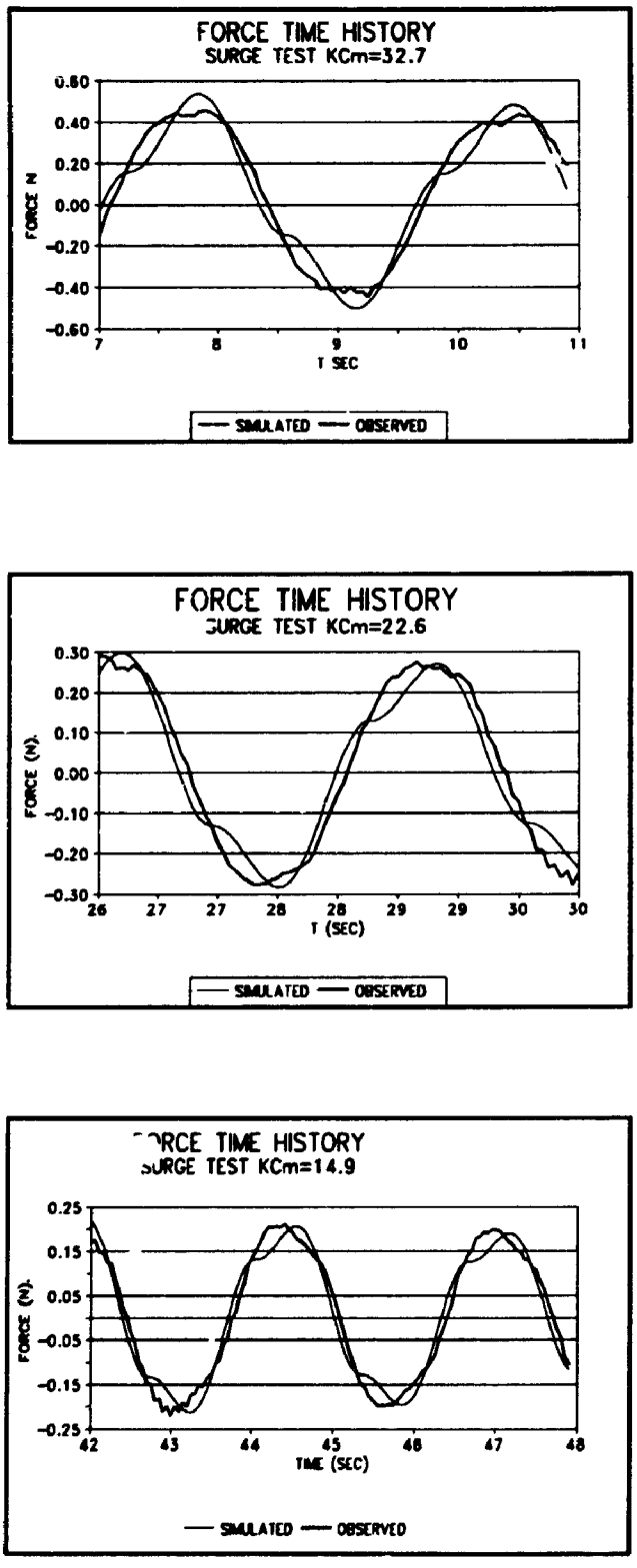

FIGURE 4.22: Typical force time histories for the simple surge test, measured and predicted.

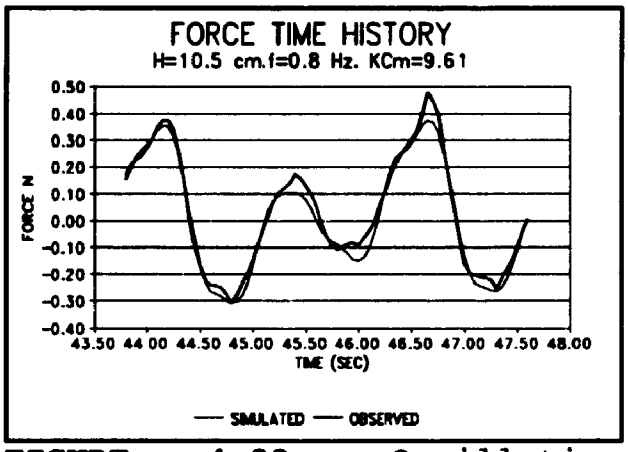

FIGURE 4.23: Oscillating cylinder in regular waves (f=0.8 Hz, H=10.5 cm)

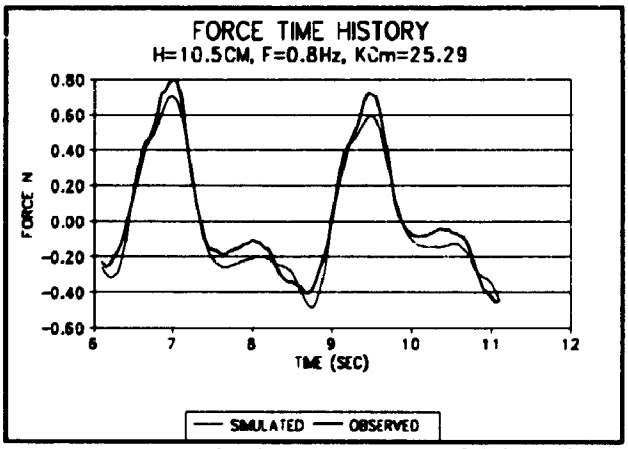

FIGURE 4.24: Oscillating cylinder inregular waves (f=0.8 Hz, H=10.5 cm).

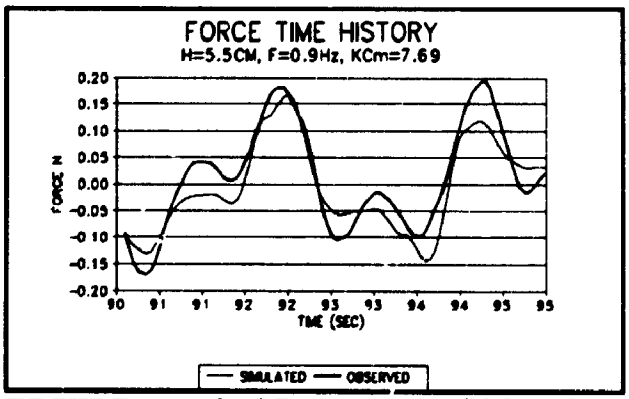

FIGURE 4.25: Oscillating cylinder in regular waves (f=0.9 Hz, H=5.5 cm). Good correlation was not observed.

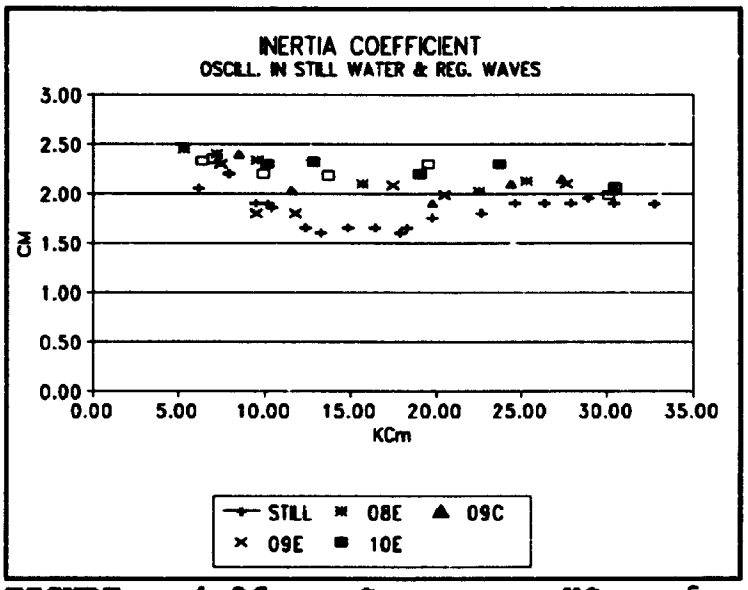

FIGURE 4.26: C_M vs KC_m for monochromatic motion tests and oscillation in wave tests.

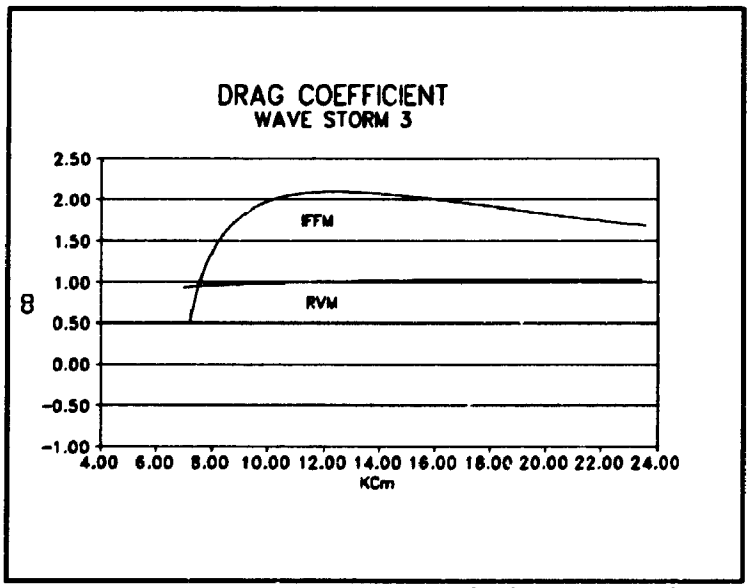

FIGURE 4.27: Drag coefficient derived by damping measurements using RVM and IFFM in random waves (wave storm 3).

4.4.4 DISCUSSION OF RESULTS

The results of Figure 4.14 show considerable scatter but there is generally good agreement among the three methods used to evaluate the drag coefficient for monochromatic motion. Figure 4.19 is a typical damping trace and it can be seen that the envelope is well fitted by the empirical relationship employed for amplitudes down to 20 mm, or values of KC_m of about 6. At lower amplitudes ($KC_m<5$), particularly in random seas, the fitting process is not as successfull since the disturbances created by the waves are relatively more significant.

The envelope, $x_0(t)$, was a cubic function and was sensitive to the value of the coefficients A_1, A_2, and A_3. This sensitivity was more pronounced for small KC_m regarding the A_2 and A_3 coefficients and was reflected in the damping ratio (which is proportional to derivative of the envelope) and C_D. This behaviour was more observed in the IFFM for $KC_m<10$ and small changes in the parameters A_2, and A3 could lead to large variation in C_D and sometimes it was necessary to derive a second envelope for this range of KC_m to get more reliable results, on the other hand, the RVM was more stable from this point of view. For very small KC_m the drag force is small and the change in hydrodynamic force between various cycles was quite small in addition to the fact that for small displacements $x_0<1$ cm. cross motion of the leg made it difficult to get accurate results in this range for both models.

The difference between the two models is shown in Figure 4.21. It is seen that the C_D coefficient predicted by the IFFM is greater than that of the RVM especially for smaller KC_m numbers. As KC_m increases they get closer together. The difference between the two models is even more pronounced for longer wave amplitudes. In Figure 4.28, the same result is shown for different seas. It was observed that as the wave height or frequency

increases the results given by the two models slowly diverge. Figure 4.29 shows the same results plotted versus KC_{com}. KC_{com} is a rough indication of the resultant amplitude in the case of motion in presence of waves and for simplicity was defined as:

$$KC_{rel} = \frac{2\pi\left(\left(\frac{H}{2}\exp(-k\zeta)\right)^2 + (x_0)^2\right)^{\frac{1}{2}}}{D} \qquad (4.30)$$

Both figures 4.28, 4.29 show scatter and even plotting the data versus KC_{com} (Figure 4.29) does not show a conclusive trend.

Figure 4.27 also shows the drag coefficient for the case of random waves. Again the same trend regarding the two models was observed. The results by the RVM in this case were made possible by the simulation of the observed wave spectrum using the random phase method. This approach was assumed valid due to the random nature of the wave field (although there may be some deviation in the C_D coefficient since the phasing of the waves are different from those observed).

Figure 4.21 shows the C_D coefficients derived from matching of the inline force trace to the RVM. Generally the force prediction using this method is in good agreement with the damping method. Again for very small KC_m the error increases due to vortex shedding and member lateral motion. Figures 4.22 to 4.25 show the correlation of the force time histories obtained from the R.M. For most of the cases the prediction was of good quality although some phase variation can be observed and in case of steep waves the effect of nonlinearity (Figure 4.23) can be distinguished (higher crest and shallower trough). Also, as shown in Figure 4.25 for f=0.9 Hz.and H=5.5 cm at KC_m=7.69 the resonance response due to vortex shedding made the prediction unsatisfactory. The same procedure was applied to the IFFM in figure 4.19. In the range of $8<KC_m<15$, the C_D values derived from the correlation of the forces were mostly smaller than those predicted

by the damping method (approximately 15 percent) and for higher KCm numbers the results were closer. This over-prediction may be due to the sensitivity associated with the envelope function and it's effect on C_D in this model. The force correlation by using this model had more or less the same quality as those due to the RVM except for higher waves and very small KC_m numbers.

The added mass coefficient, $C_A=C_M-1$, obtained by using the IFFM and the RVM in waves was more than those obtained during the surging test in still water for the KC_m numbers examined (Figure 4.21). This effect was observed in particular for higher waves. This increase will have some effect on the calculation of the natural frequency in the case of structural motion in waves.

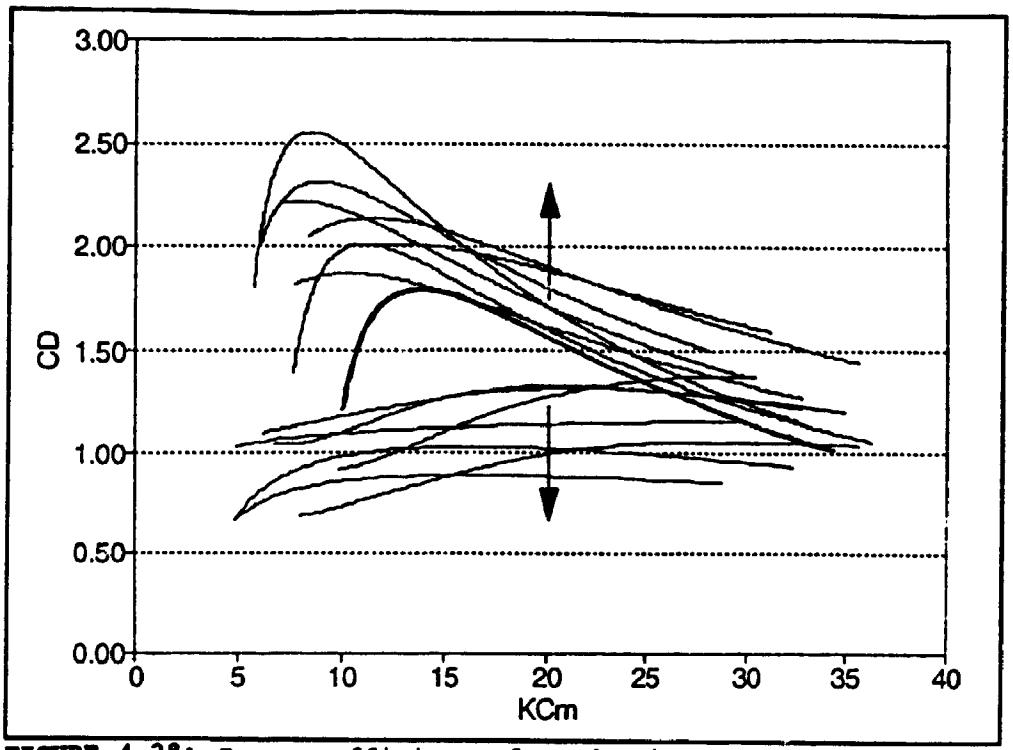

FIGURE 4.28: Drag coefficients from damping measurements vs KC_m compared, for a variety of frequencies and sea states. The heavy line represents measured still water damping test.

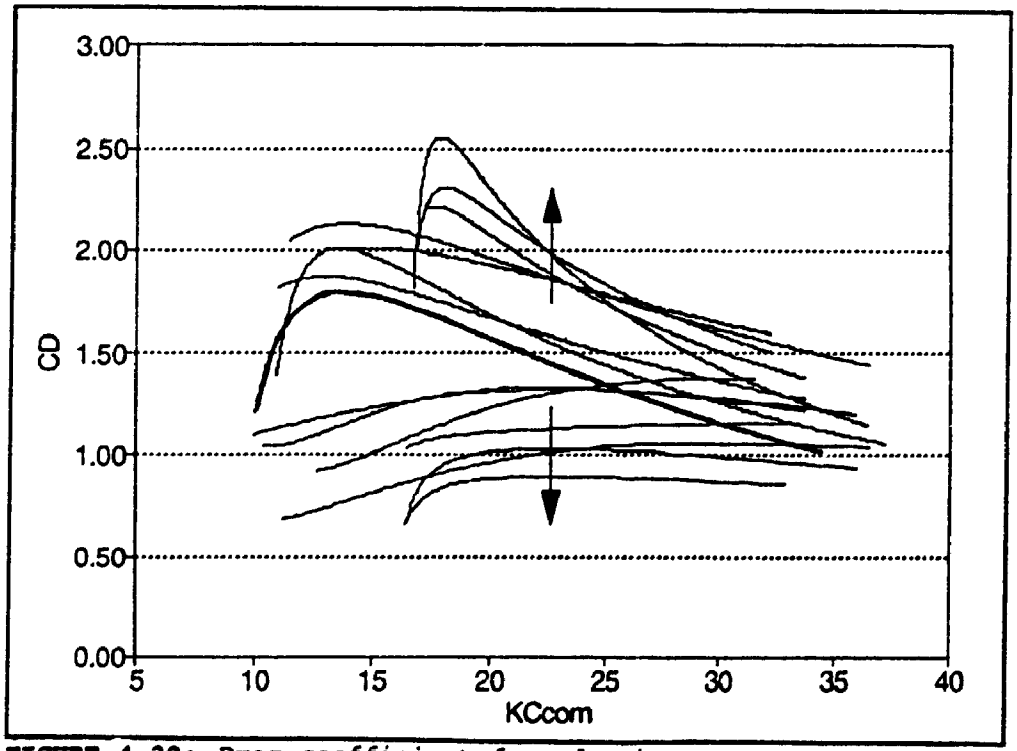

FIGURE 4.29: Drag coefficient from damping measurements vs KC_{com} compared, for a variety of frequencies and sea states. The heavy line represents the measured still water damping test.

4.5 LOW FREQUENCY FORCING (EXPERIMENT AND THEORY)

4.5.1 INTRODUCTION

As mentioned in Chapter 2, the nonlinear nature of the waves results in a crest velocity which is greater than that of trough. This information combined with the change of submergence when a wave passes a surface piercing cylinder, results in an average positive horizontal force on the member. This idea when extended to the case of a narrow banded irregular wave will result in a slowly varying horizontal force which as explained before is proportional to the cube of the associated envelope.

This experiment was designed to measure these forces on a slender surface piercing cylinder and the measured forces are compared with the results predicted by the theory given in Chapter 2. The objective was to examine the quality of the predicted results based on the Gudmestad's second order model and the constant velocity field model in bichromatic and random waves. Through such an evaluation, it would be possible to employ a model to represent the free surface low frequency forcing as part of a general stochastic time domain analysis to predict the response of a typical compliant type structure to the combined action of wind and wave.

4.5.2 EXPERIMENT SET UP AND PROCEDURE FOR MEASURING LOW FREQUENCY FORCING

The set up for measuring the low frequency forcing due to the bichromatic and irregular waves are the same as that used during the force measurement on fixed cylinder in monochromatic waves for drag and inertia force measurement. Two different submergence

lengths were examined consisting of d=30 cm, and d=50 cm.

The wave generation in this case was done by feeding the required simulated time history to the computer controlled paddle, considering the tank admittance function and regulating the suitable time delay.

For the bichromatic waves (group waves), eleven different cases were examined, seven of them with a submergence length of d=30 cm and the rest with d=50 cm. In Table 4.1 the wave heights (H_1,H_2,H_3) achieved at the site for the three main frequencies, f_1=0.8 Hz, f_2=0.88 Hz, f_3=0.96 Hz, are given.

For random waves, three wave storms, (no wind), were tried with the peak frequencies, fp_1=0.92 Hz, fp_2=0.86 Hz, and fp_3=0.80 Hz, and the significant wave heights were Hs_1=5.3 cm, Hs_2=7.8 cm, and Hs_3=10.3 cm respectively.

Probes number 3, number 4 measured the surface elevation with a distance of 20 cm on either side of the model across the tank, and care was taken to have a good alignment between the probes and model. Skewness due to the phase difference between wave probes and force measurements (in time domain) was less than 0.1 second and negligible. The wave elevation and force spectra for the bichromatic groups and the three random waves are given in Appendix E.

In the case of the groups, the spikes are associated mainly with frequencies of f=0.8 Hz, 0.8^9 Hz , and 0.96 Hz. Notice that there are super and subharmonics due to the nonlinear interaction of the main frequencies. In the force spectra (Figure 4.37) related to low frequency force measuremens, the peaks associated with Δf=0.08 Hz and its higher harmonics, can be observed. The significance of these peaks has been already discussed in Chapter 2. Theoretically, the spikes should be like the Dirac delta function but because of spectral resolution and some energy spilling inherent in the fourier analysis they appear as triangles.

As the wave height in a bichromatic group increases, the spread of energy in to

TABLE 4.1

GROUPED WAVE CONDITION

Dimensions Cm, Hz, Ra, d(m).

Group	A1	A2	A3	A4	f1	f2	f3	f4	ϕ1	ϕ2	ϕ3	ϕ4	d
1	1.66	1.09	0.43		0.80	0.88	0.96		-0.39	4.03	-3.04		0.3
2	-1.6	-2.05	-0.65		0.80	0.87	0.96		1.25	1.32	1.08		0.3
3	1.96	1.94	-0.90	0.45	0.80	0.88	0.96	1.04	2.37	-0.07	2.28	-1.00	0.3
4	1.41	1.73	-0.44		0.80	0.88	0.96		-0.98	-1.59	2.17		0.3
5	-1.62	1.53	0.5		0.80	0.88	0.96		2.87	-1.28	-1.02		0.3
6	1.92	1.84	-0.71		0.80	0.88	0.965		-0.33	-0.99	2.82		0.3
7	-1.6	-1.73	0.66		0.80	0.88	0.966		-0.31	-0.95	2.25		0.3
8	0.06	0.32	-1.68	-0.43	0.81	0.90	0.98	1.08	0.02	-2.4	-0.76	-0.14	0.5
9	0.01	-0.22	1.66	-0.72	0.79	0.89	0.99	1.07	-0.33	-2.5	-0.53	-1.30	0.5
10	0.02	0.45	1.22	0.35	0.86	0.90	0.99	1.07	-0.33	-0.97	-0.15	-0.06	0.5
11	-0.07	-0.27	1.58	0.42	0.80	0.90	0.99	1.07	-0.33	-2.48	-0.21	-0.60	0.5

subharmonics and superharmonics also increases until breaking starts which causes the dissipation of the energy from the system and reduces the second order higher harmonics.

In random waves, the presence of the superharmonics can be observed as the waves get bigger and the bounded superharmonic changes the shape of the first order waves to have higher crests and shorter troughs.

The length of the test for groups were 5 minutes and in the case of irregular waves it was 18 minutes. Due to the sensitivity of the force measurements and electrical and mechanical drifts and hysteresis effects in the load cells, the vishays (amplifiers) were set to zero at the beginning of each test and the zero values measured for 150 seconds before and after each test.

The measured wave elevation and force spectra for all of the group waves and random waves are shown in Appendix E. The corresponding measured quantities in time domain for a period of 50 seconds are also shown in the same appendix. Figure 4.30 shows the typical wave elevation and force spectra for groups 5,7, also Figures 4.31, 4.32 show the wave elevation and force spectra for the three random waves. For the random waves, the force spectra is broader than the wave elevation spectra. This is an indication of the nonlinear interaction present in the transfer function between the wave elevation and the force. Furthermore, the magnitude of the first order wave force in the case of groups is a function of the submergence length and for greater submergence length the force will be larger. However regarding the low frequency water line forces the dependency in the submergence length is quite weak but still exists. When looking at this problem using the second order Chakrabari-Gudmestad model (Chapter 2), the dependency in this case can be observed and well justified.

4.5.2.1 MEASUREMENT OF THE LOW FREQUENCY FORCING

The low frequency portion of the measured force time history in frequency domain was obtained using a fourier analysis on the record and low pass filtering with a suitable cut-off frequency. By doing an inverse fourier transform, the time history of the low frequency forcing was obtained. The cut-off frequency regarding the groups was not constant and depending on the amount of interaction between the main frequencies and their energy, there existed harmonics at Δf=0.08 Hz, 0.16 Hz, 0.24 Hz, 0.32 Hz. The maximum cut-off frequency used was 0.32 Hz. In random waves the cut-off frequency was not well defined so an upper bound of about 0.5 Hz. was used in that case.

In appendix E the time history of the measured total and low frequency forces for groups and for the three random waves are shown. These force time histories include the long wave effects, tank reflection and resonance. The effect of the bounded long waves on the drag forcing in natural wave trains has been discussed in Chapter 2. The contribution of the observed long waves will be discussed in the next section.

The reflection coefficient in the tank for the range of the frequencies examined was about 5 to 6 percent and since the low frequency forcing due to the free surface intermittency is proportional to the cube of the wave height (H^3), this reflection coefficient can contribute up to about 20 percent to the force measurement depending on the position of the force measurement (due to the increased intermittency). On the other hand, the horizontal velocity field is greater when the position of measurement is close to the minimum of the envelope of the resultant incident and reflected wave system and is smaller when the position is closer to the maximum of this envelope. However the contribution of the increased intermittency seems to be dominant due to its proportionality to H^3.

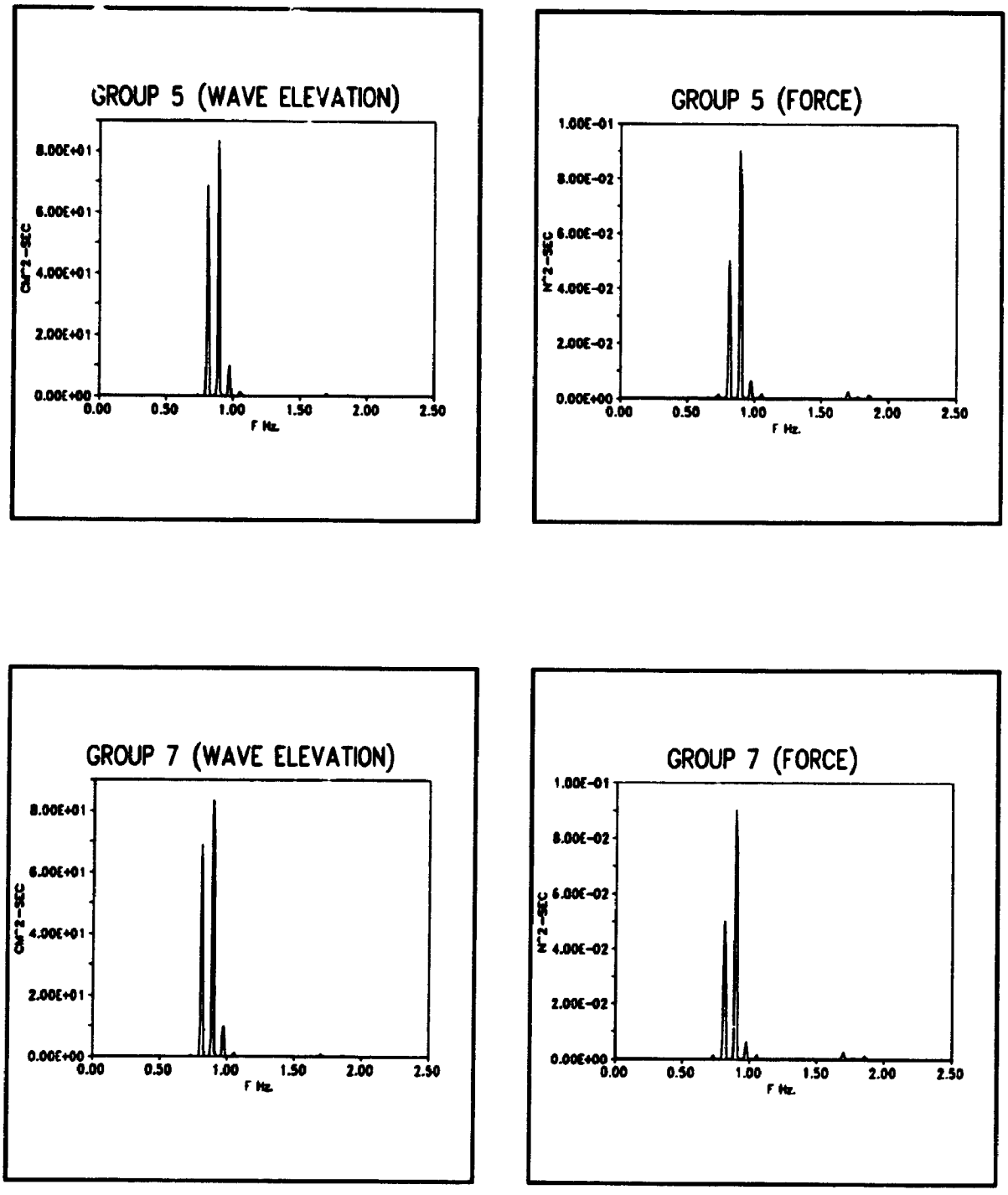

FIGURE 4.30: Typical measured elevation and force spectra (Groups 5,7)

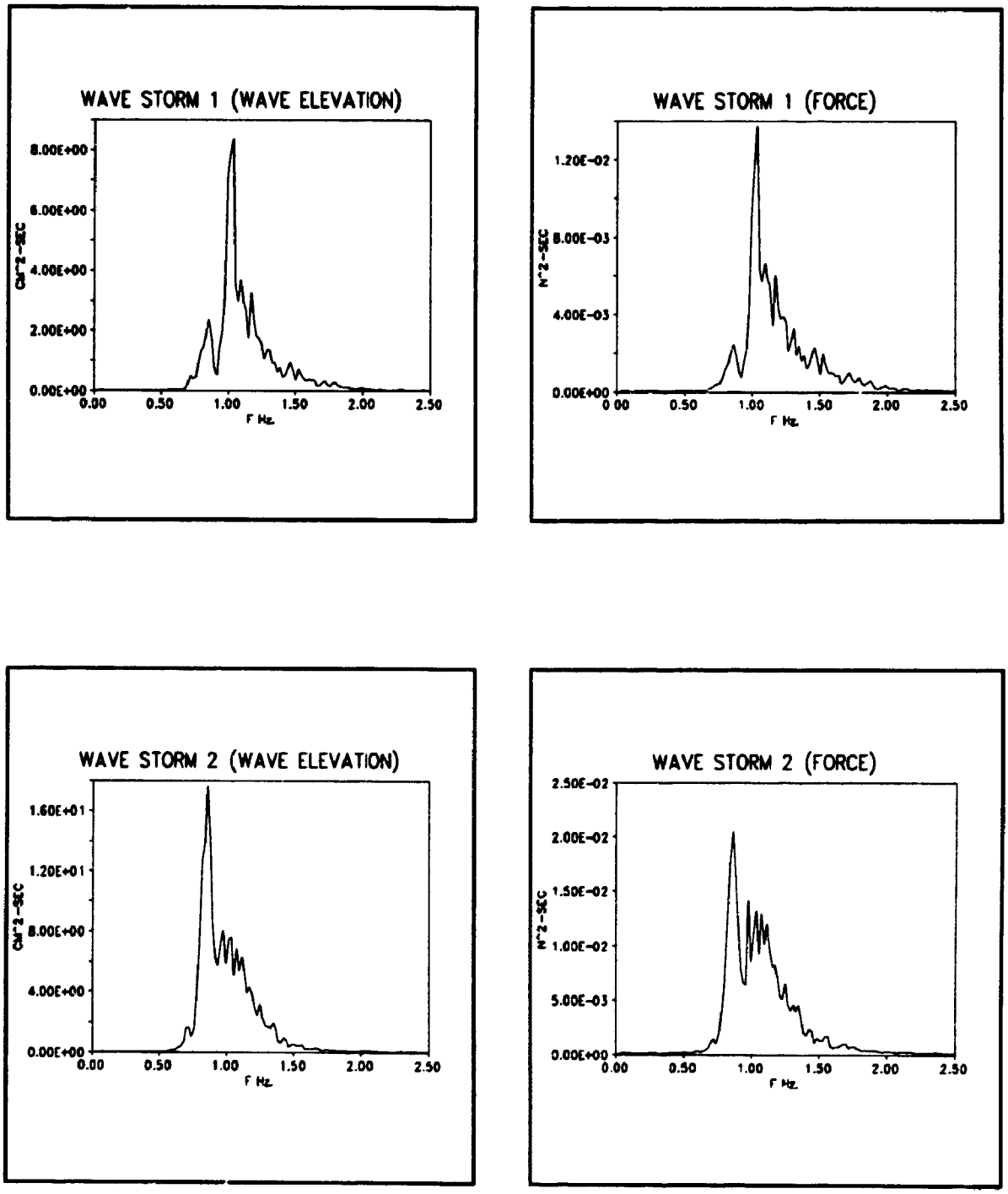

FIGURE 4.31: Measured wave elevation and force spectra for wave storms 1,2.

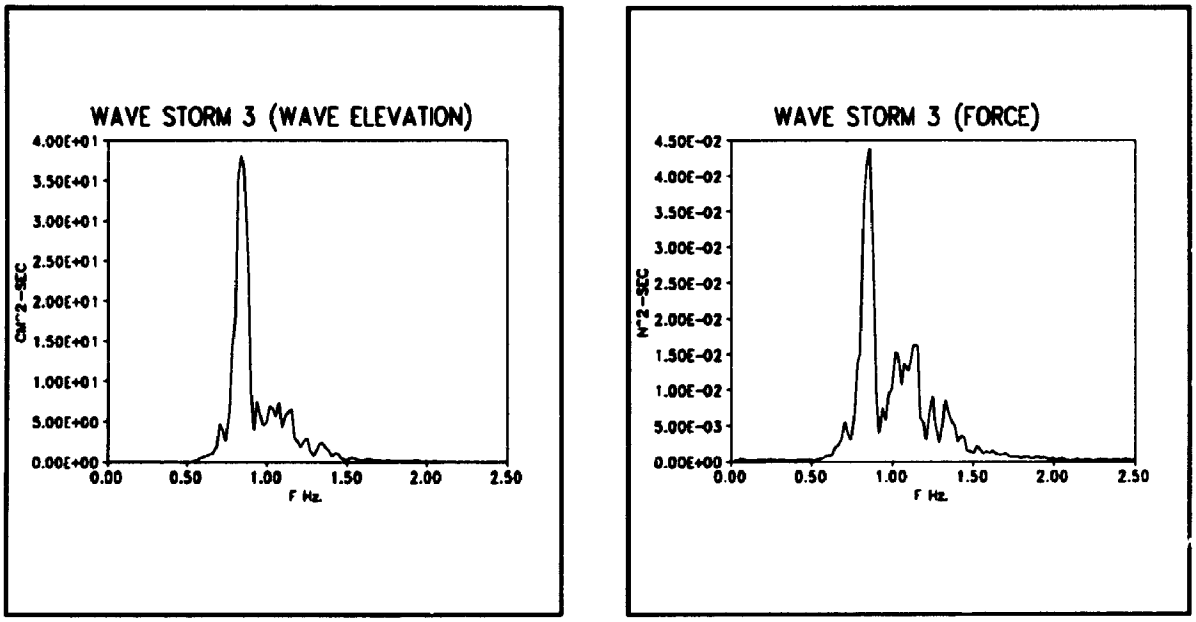

FIGURE 4.32: Measured elevation and force spectra for wave storm 3.

4.5.3 LONG WAVES

Considering the reflection of the long waves, the tank can be considered as a closed basin and using the nominal depth of the wave tank as d=1.8m, the natural period of the n^{th} sloshing mode would be:

$$T_n = \frac{2l}{n(gd)^{0.5}} \qquad (4.31)$$

where l is the length of the tank, and n is the sloshing mode number. Using l=50 m, the period of the first and second mode would be 0.04 Hz., and 0.08 Hz.
The second mode frequency is the same as the difference frequency, Δf=0.08 Hz. This brings about the possibility of existence of some kind of standing wave at this frequency. As is shown in Figure 4.33, using harmonic analysis on the wave elevation time history for group number seven, the long wave associated with frequency of 0.08 Hz, is extracted and has an amplitude of about 0.28 mm. Using an analysis based on Sand (1982), the expected bounded long wave would be about 0.10 mm. In the same reference it was demonstrated that for deep water waves, (first order wave frequency f=0.8 Hz., where $(\frac{h}{g})^{0.5} f > 0.2$), the long waves bound to the first order wave groups is relatively small compared to a shallow water condition (about one tenth).
It was also reported that in deep water waves, the amplitude of the free displacement waves (Chapter 2) is dominating and is about 5 times that of the bounded long waves, and the contribution due to the local disturbance free waves (chapter

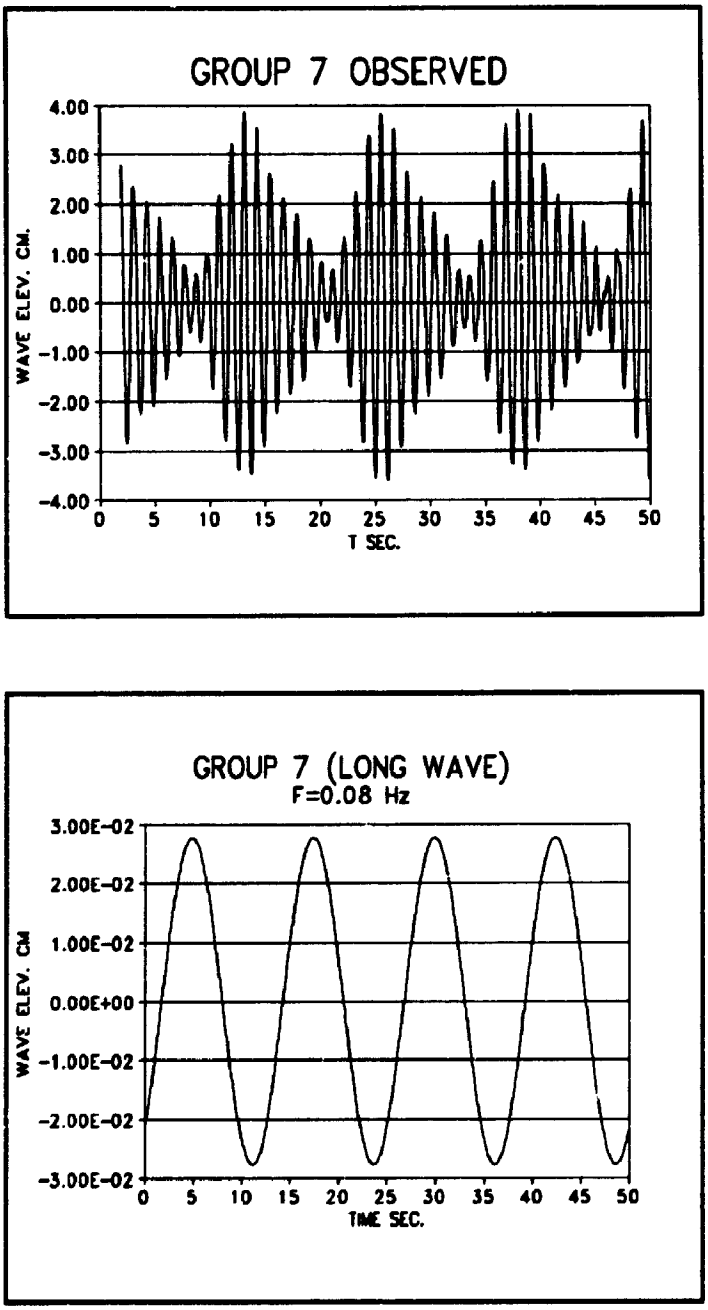

FIGURE 4.33: Time history of the measured wave elevation and the associated long wave at f=0.08 Hz (Group 7).

2) is negligible. Using this reasoning and graphs provided in the above mentioned reference, the long wave amplitude produced by the generation of the first order group waves would be about 0.55 mm. The free displacement wave, which is the dominant contributor, has a phase lag of 180 degree relative to the group bounded long waves at the paddle position, and due to the phase difference between the phase velocity and group velocity, their relative phase lag will vary with distance from the paddle.

As mentioned before the observed long wave from wave elevation of group seven is about 0.28 mm., and the expected one is about 0.55 mm. The difference is attributed to the tank reflection because at this frequency (f=0.08 Hz), the wave absorption ability of the tank is small and the reflection coefficient would be high. In the following, an analysis will be carried out in order to investigate the low frequency force time history associated with the observed long wave.

Group number seven is shown in Figure 4.33. For this group a_1=1.663 cm, a_2=1.884 cm, a_3=0.660cm, ϕ_1=-0.312 rad, ϕ_2=-0.950 rad, ϕ_3=2.254 rad, f_1=0.08 Hz, f_2=0.883 Hz, f_3=0.966 Hz. For the long wave a=0.028 mm., f=0.08 Hz, ϕ=3.650 rad. Using the linear theory, and constant velocity on the free surface zone (explained in Chapter 2), the total second order free surface wave forcing would be:

$$F_{fsf}(t) = \frac{1}{2}\rho C_D D V_{fs}(t)|V_{fs}(t)|\eta(t)$$

where

$$\eta(t) = a_1\cos(\omega_1 t+\phi_1) + a_2\cos(\omega_2 t+\phi_2) + a_3\cos(\omega_3 t+\phi_3) \qquad (4.33)$$

and

$$V_{fs} = a_1\omega_1\cos(\omega_1 t+\phi_1) + a_2\omega_2\cos(\omega_2 t+\phi_2) + a_3\omega_3\cos(\omega_3 t+\phi_3) \quad on \quad z=0. \qquad (4.34)$$

Also, using the Borgman approximation the force due to the observed long wave would be (chapter 2, long waves):

$$F_{LW}(t) = \frac{1}{2}\rho C_D D\int_0^{0.3} 2V_{LW}(z,t)|V(z,t)|dz \qquad (4.35)$$

where V(z,t) is the linear velocity field on the submerged part of the member (d=0.3 m.). The long wave velocity field due to the bichromatic waves would be (chapter 2):

$$V_{LW}(z,t) = a\omega\frac{\cosh(\Delta k(z+h))}{\sinh(\Delta kh)}\cos(\omega t+\phi) \qquad (4.36)$$

where $\Delta k=k_2-k1$ and k_1,k_2 are wave numbers corresponding to f_1, and f_2, and h=3.0 m. The observed long wave is assumed to be due to the first two harmonics. In reality the 2nd and 3rd harmonics can contribute to this wave but then the problem would be indeterminate. Several analyses have been done by the author using components associated with (a_1,a_2), and (a_2,a_3) assuming two amplitudes and two phases.

$$V_{LW}(z,t) = \overline{a_1}\omega\frac{\cosh(\Delta k_{12}(z+h))}{\sinh(\Delta k_{12}h)}\cos(\omega t+\overline{\phi_1}) + \overline{a_2}\omega\frac{\cosh(\Delta k_{23}(z+h))}{\sinh(\Delta k_{23}h)}$$
$$\cos(\omega t+\overline{\phi_2})$$

This velocity field was matched to the observed long wave (a=0.28 mm., ϕ=3.65 rad.) using the least square method. However, the force analysis was not sensitive to this decoupling and it was decided to use only one component corresponding to a_1, and a_2 as given in equation 4.36.

Doing the integration given above, the forces corresponding to the total free surface effect, $F_{fsf}(t)$ and long waves, $F_{LW}(t)$ are shown in Figure 4.34. Upon using a low pass

filter (Fourier analysis), the low frequency portion of the above mentioned forces are also shown in the same figure. It is seen that the force due to the long wave is about 1 percent of the free surface forcing. If the total expected long wave (a=0.55 mm.) was used in the analysis the percentage of the force would increase up to about 2 percent. This analysis can clarify that in a nearly deep water laboratory situation where

$f_1(\frac{h}{g})^{0.5}>0.2$, although the long waves are exaggerated by about 5 times

compared to real bounded long waves, they are not a threat to the free surface low frequency force measurement.

4.5.4 ANALYSIS AND COMPARISON OF EXPERIMENTAL RESULTS WITH THEORY

The method described in chapter 2 is used to define the concept of the envelope function. The complex analytic signal $\tilde{\eta}(t)$ was defined based on the observed wave elevation $\eta(t)$ and was given as

$$\tilde{\eta}(t)=\eta(t)+i\eta_H(t) \qquad (4.38)$$

where $\eta_H(t)$ is the Hilbert transform of $\eta(t)$. The modulus of this analytical signal, $|\tilde{\eta}(t)|$, defines the envelope of the process.

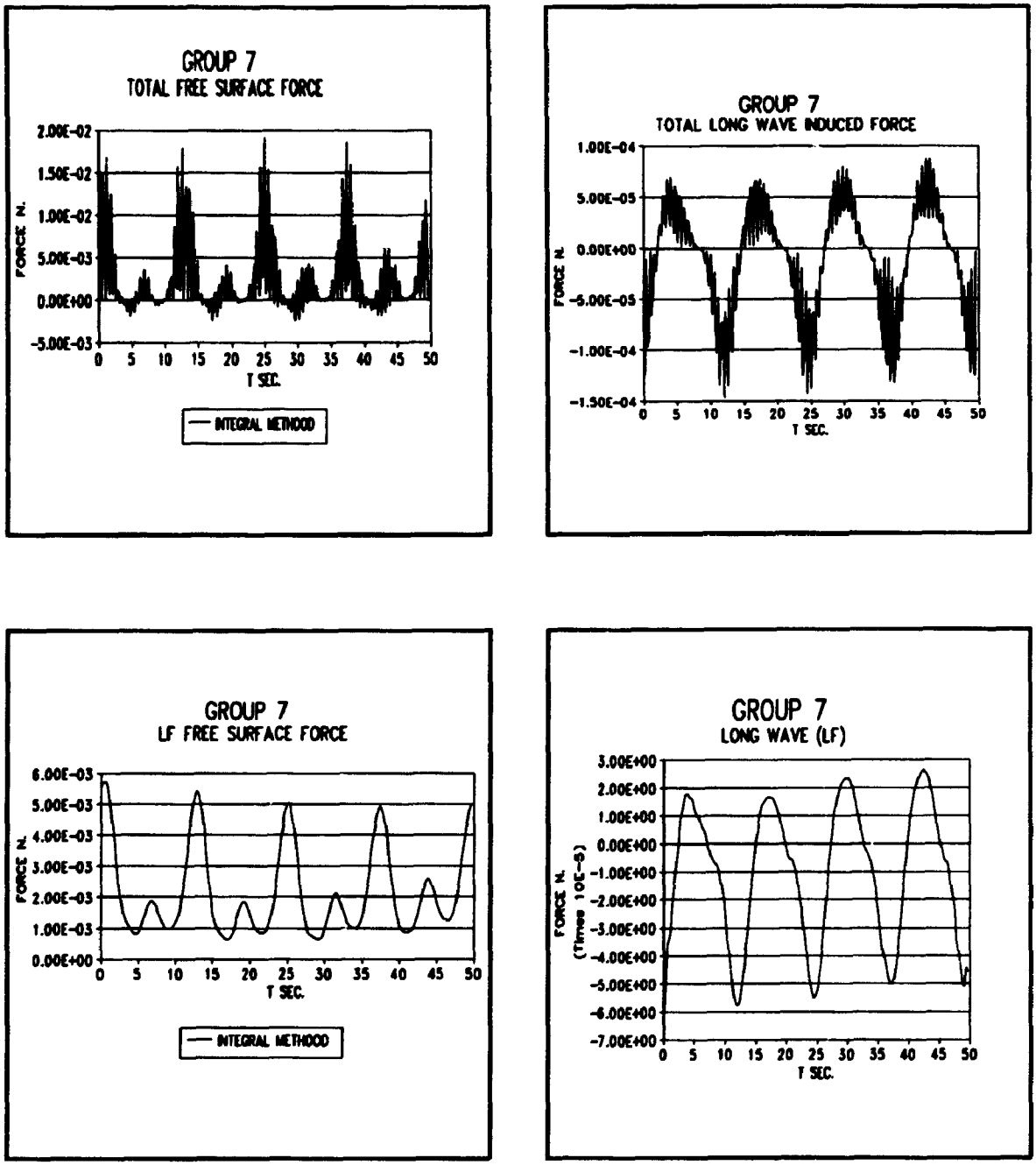

FIGURE 4.34: Force time history (Group 7). Total calculated free surface force (top left). Total calculated long wave induced force (top right). Free surface drift force (bottom left). Drift force induced by long waves (bottom right).

4.5.4.1 GROUP WAVES

In the case of group waves using Fourier analysis, the amplitudes, frequencies, and phases of the contributing harmonics in the wave elevation time history were obtained and optimized using a nonlinear least square scheme. The general fitted wave elevation has the linear form:

$$\eta(t) = a_1\cos(\omega_1 t+\phi_1) + a_2\cos(\omega_2 t+\phi_2) + a_3\cos(\omega_3 t+\phi_3) + a_4\cos(\omega_4 t+\phi_4) \tag{4.39}$$

And knowing that:

$$HI[\sin(\theta)] = \cos\theta \ , \quad HI[\cos(\theta)] = \sin(\theta) \tag{4.40}$$

where HI is Hilbert transform operator, the modulus of the analytical signal would be:

$$|\tilde{\eta}(t)| = \left(\sum_{i=1}^{4} (a_i)^2 + \sum_{i=1}^{4}\sum_{j=i+1}^{4} 2a_i a_j\cos(\Delta\omega_{ij}+\Delta\phi_{ij})\right)^{0.5} \tag{4.41}$$

Using this envelope as input to equation 2.153, 2.154 (Chakrabarti's nonlinear wave model) in Chapter 2:

$$\begin{aligned} F(t) = {} & \frac{1}{12\pi}\rho C_D D\tilde{\omega}^2 H^3(t)\left(1-\frac{3}{4}(kH(t))^2\right) + \frac{0.212}{8}\rho C_D D\tilde{\omega}^2 H^3(t) \\ & \left(-\frac{1}{5}+\frac{1}{2}\exp(-2kd)-\frac{1}{2}\exp(-3kd)+\frac{1}{5}\exp(-5kd)\right) \end{aligned} \tag{4.42}$$

where

$$H(t) = 2|\tilde{\eta}(t)| \quad , \tag{4.43}$$

$$\bar{\omega}^2 = \frac{\sum_{i=1}^{3} (a_i)^2 (\omega_i)^2}{\sum_{i=1}^{3} (a_i)^2} \tag{4.44}$$

it was possible to predict the intermittent low frequency forcing. In regular waves and a submergence length of d=30 cm, the force predicted by this model is about 16 percent smaller than the force predicted by the constant velocity field model (envelope approach). Figures 4.35 and 4.36 show the time histiory and envelope of the measured wave elevation together with the time history of the total force for groups 5, and 7. In the same figures, the comparison of the observed and predicted drift force in time domain is presented. In Figure 4.37, the measured and predicted free surface drift forces in the frequency domain (power spectrum) for groups 5, and 7 are given. The results for all groups are presented in appendix E.

As can be seen, the results considering the phase agreement between the predicted and observed force are quite good but an overprediction of about 20-30 percent exists. The reason is believed to be partly due to the tank reflection at the nominal first order wave frequencies and partly due to the mathematical model. The KC_f in the experiment was between 4 to 8.5 and the C_D values used were between 1 to 1.4 (based on the C_D measurements from the fixed cylinder test).

Theoretically, the model works when the process is narrow-banded and has a slowly varying envelope. It takes account of the fact that during the passage of each single wave in the group only, a mean force is exerted to the member and each wave is considered to have a constant amplitude. However, each wave is the superposition of the several harmonics (equation 4.39) and the envelope may not be a slowly varying

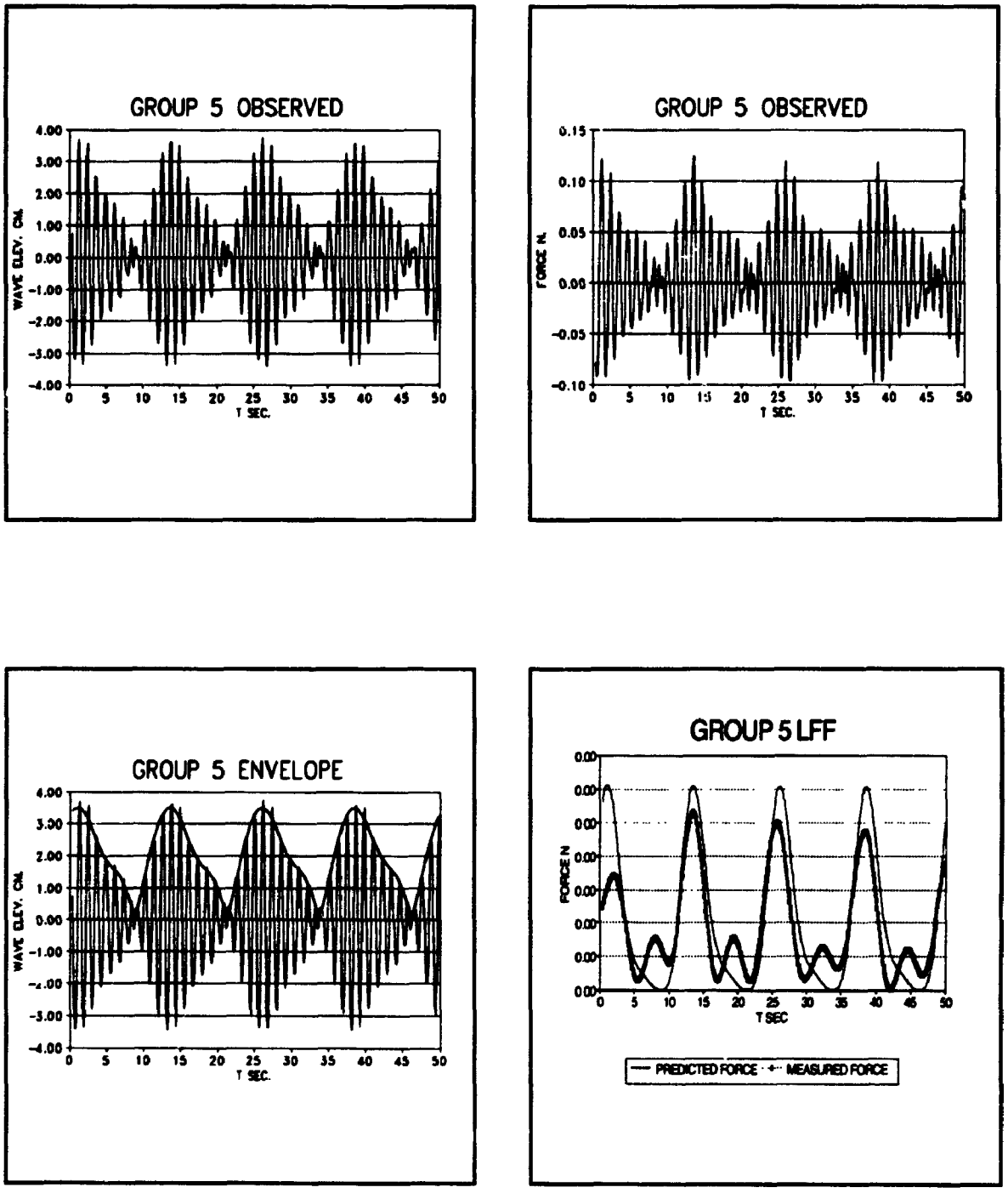

FIGURE 4.35: Measured wave elevation and force together with the computed envelope. The comparison of the measured and predicted drift force is shown in bottom right (Group 5).

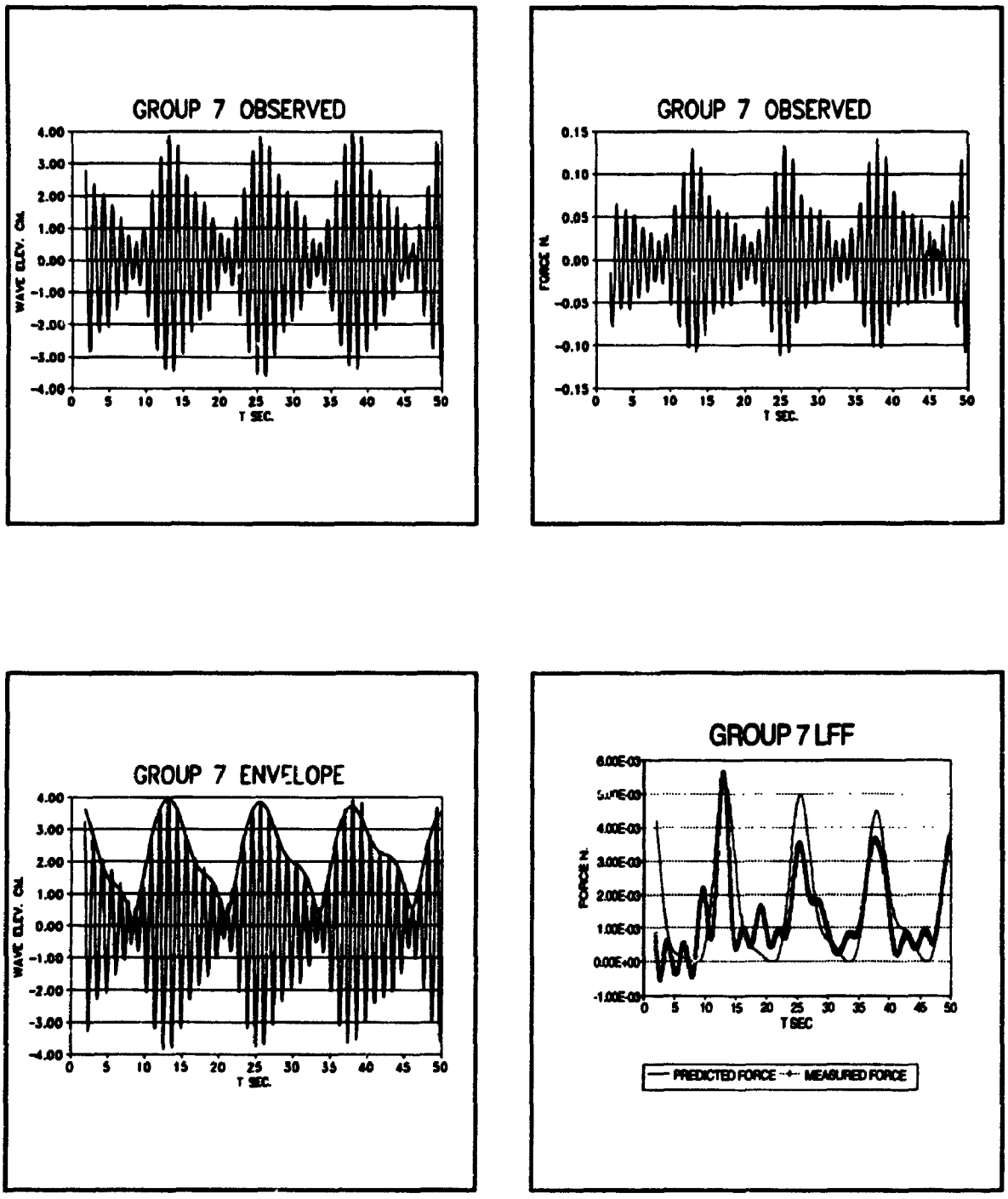

FIGURE 4.36: Measured wave elevation and force together with the computed envelope. The comparison of the measured and predicted drift force is shown in bottom right (Group 7).

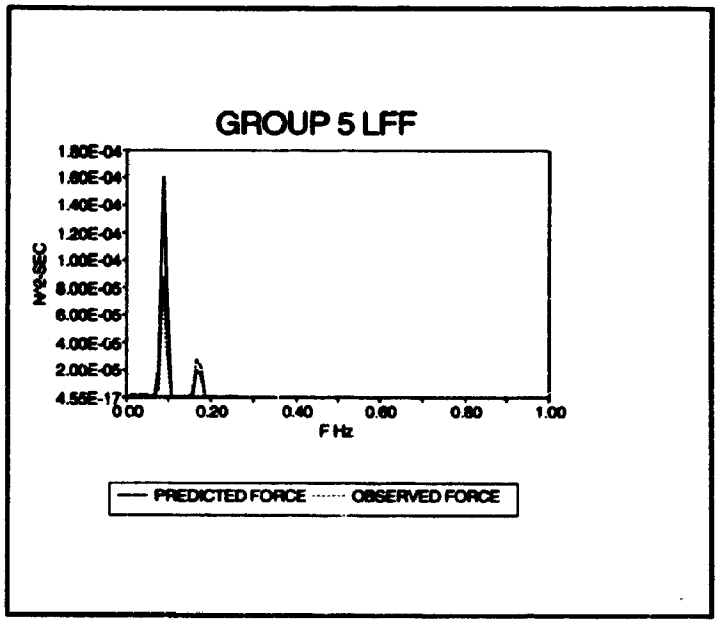

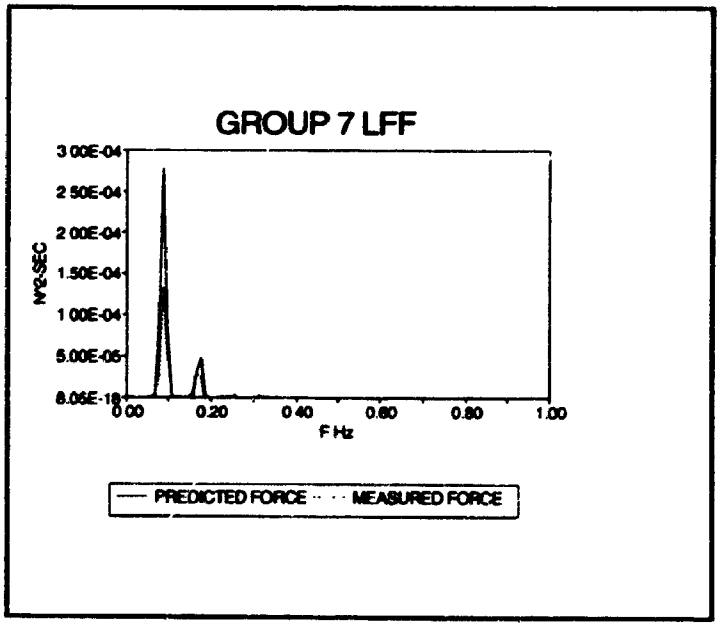

FIGURE 4.37: Comparison of the measured and predicted drift forces in frequency domain (Groups 5,7).

function of time (in case of random waves). Another way of defining the force due to the free surface effects in bichromatic and irregular waves would be using the model:

$$F_{fsf}=\frac{1}{2}\rho C_D D\int_0^{\eta}|w|v\,dz \qquad (4.45)$$

which by using a constant velocity field model (at z=0) for the water line zone will lead to:

$$F_{fsf}=|v(t)|v(t)\eta(t) \qquad (4.46)$$

Using Fourier analysis and taking the low frequency portion of this force has improved the results and reduces the overprediction to about 20 percent (for most of the bichromatic sea states). The comparison for group 7 is given in Figure 4.38.
Also, the tank reflection, as explained before, depending on the position of the measurement, can have a contribution up to about 20 percent since the force is proportional to H^3.
In the final phase of this work, prediction of the response of the hydroelastic model to random waves in the time domain, has been done with the second model, first because its results are 5 to 10 percent smaller than the envelope approach, and secondly because it does not need the calculation of the envelope. The linear velocity field used in the analysis, is computed from the simulated time history based on the observed wave spectrum.

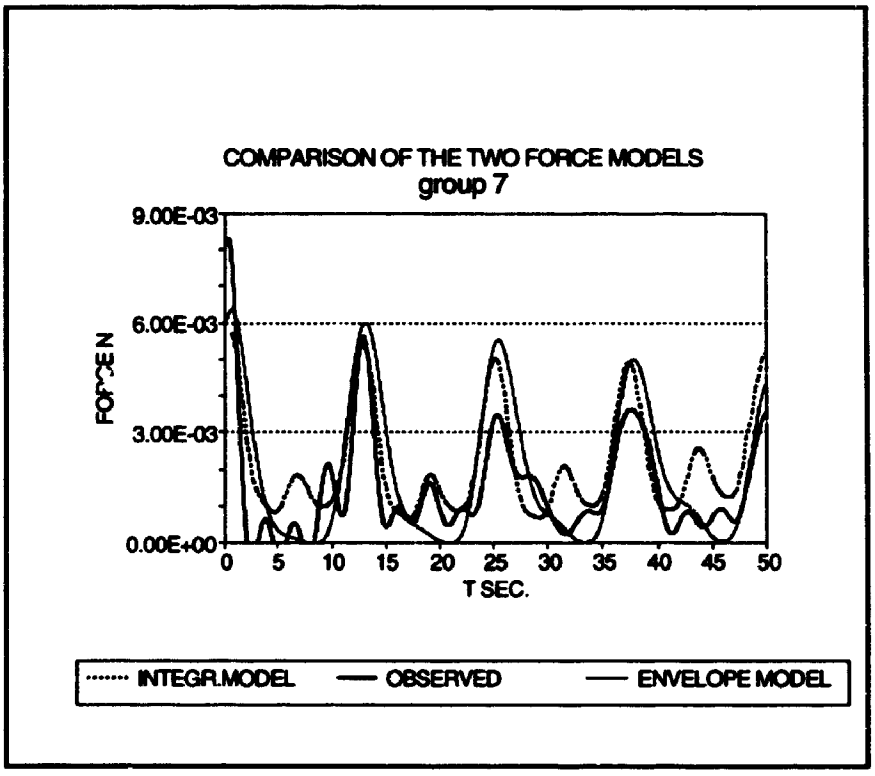

FIGURE 4.38: Comparison of the results, measured drift, free surface drift calculated from the envelope, free surface drift calculated by the integral (based on constant velocity field on the water line zone).

4.5.4.2 RANDOM WAVES

In the case of random waves, three wave storms were examined. Again the envelope of the wave elevation was calculated using the Hilbert transform technique. However, in this case it was inaccurate to extract the amplitude and phases of the contributing harmonics to the random process by a standard Fourier analysis. The transform of the wave elevation in time domain given by equation:

$$\eta_H(t) = \int_{-\infty}^{\infty} \frac{\eta(s)}{\pi(t-s)} ds \qquad (4.47)$$

was also tried but there was a problem with its numerical calculation due to the singularity that was observed whenever s is close or equal to t. The practical way of finding the envelope of a given time history when the process is random, is to use Fourier analysis. In the following, the technique is explained. By definition the Hilbert transform is the convolution of the wave elevation time series with the function $1/(\pi t)$:

$$\eta_H(t) = \eta(t) * \frac{1}{\pi t} \qquad (4.48)$$

As a result its Fourier transform would be:

$$\eta_H(f) = \eta(f)\left(-i\frac{|f|}{f}\right) \qquad (4.49)$$

where $-i\frac{|f|}{f}$ is the fourier transform of $1/\pi t$ (Bandet, Piersol, 1986). Using the

definition of the analytical signal:

$$\tilde{\eta}(t) = \eta(t) + i\eta_H(t) \qquad (4.38)$$

its Fourier transform would be:

$$\tilde{\eta}(f) = \eta(f) + i\eta_H(f) = \eta(f)\left(1 + \frac{|f|}{f}\right) \qquad (4.50)$$

which for positive f would be $2\eta(f)$ and for negative f would be zero.

In order to find the time history of the analytic signal, it is only necessary to find the imaginary part of the inverse Fourier transform of $\tilde{\eta}(f)$:

$$\eta_H(t) = Im\left[2\int_0^{\infty}\eta(f)\,e^{i2\pi ft}df\right] \qquad (4.51)$$

where its digital form would be:

$$\eta_H(j\Delta t) = \frac{2}{N\Delta t}\,Im\left[\sum_{k=0}^{N/2}\eta(f_k)\,e^{i\frac{2\pi kj}{N}}\right] \qquad (4.52)$$

and

$$\eta(f_k) = \Delta t\sum_{j=0}^{N-1}\eta(t_j)\,e^{-i\frac{2\pi kj}{N}} \qquad (4.53)$$

where $f_k = k/(N\Delta t)$, $t_j = j\Delta t$.

The envelope would be the modulus of the complex signal $\tilde{\eta}(t) = \eta(t) + i\eta_H(t)$.

In Figures 4.39 to 4.41, the time histories of the measured wave elevation and force together with the calculated envelope for the three wave storms are presented. It is tangent to every peak in the group. Due to the nature of the random process and the associated sudden excursions which is a result of paddle strokes and also breaking

waves (for higher sea states) there are sometimes sudden jumps in the envelope because it is trying to follow the peaks of the wave elevation trace. This effect will be magnified in the force prediction because again the forces are proportional to H^3. This behaviour was observed mostly in the third sea storm. In low to intermediate sea storms it was less pronounced. Figures 4.39 to 4.41 also show the low frequency free surface forces, both measured and predicted, in the time domain, and Figure 4.42 shows the corresponding results in the frequency domain. It is seen that in the first and second wave storms the results compare relatively well. In the third wave storm due to the phenomena explained above less agreement was observed. Table 4.2 shows the rms of the measured and predicted results.

TABLE 4.2: RMS OF MEASURED AND PREDICTED DRIFT FORCES (RANDOM WAVES)

	WAVE STORM 1	WAVE STORM 2	WAVE STORM 3
MEASURED	2.05E-3 N	5.48E-3 N	9.87E-3 N
PREDICTED	2.35E-3 N	7.60E-3 N	1.49E-2 N

The force model given by the integral method equation 4.46 (using the linear wave theory up to mean water level and a constant velocity field in the water line zone), seems to be better since it does not need the computation of the envelope signal, and it is somewhat less conservative.

In the analysis of the hydroelastic model the inclusion of the free surface effects would be through the use of the integral model. Practically, there is no need for low pass filtering since the high frequency components of the force are small, (Fig. 4.34),

and their effect on the structural response of a compliant tower would be even smaller because they are away from resonance.

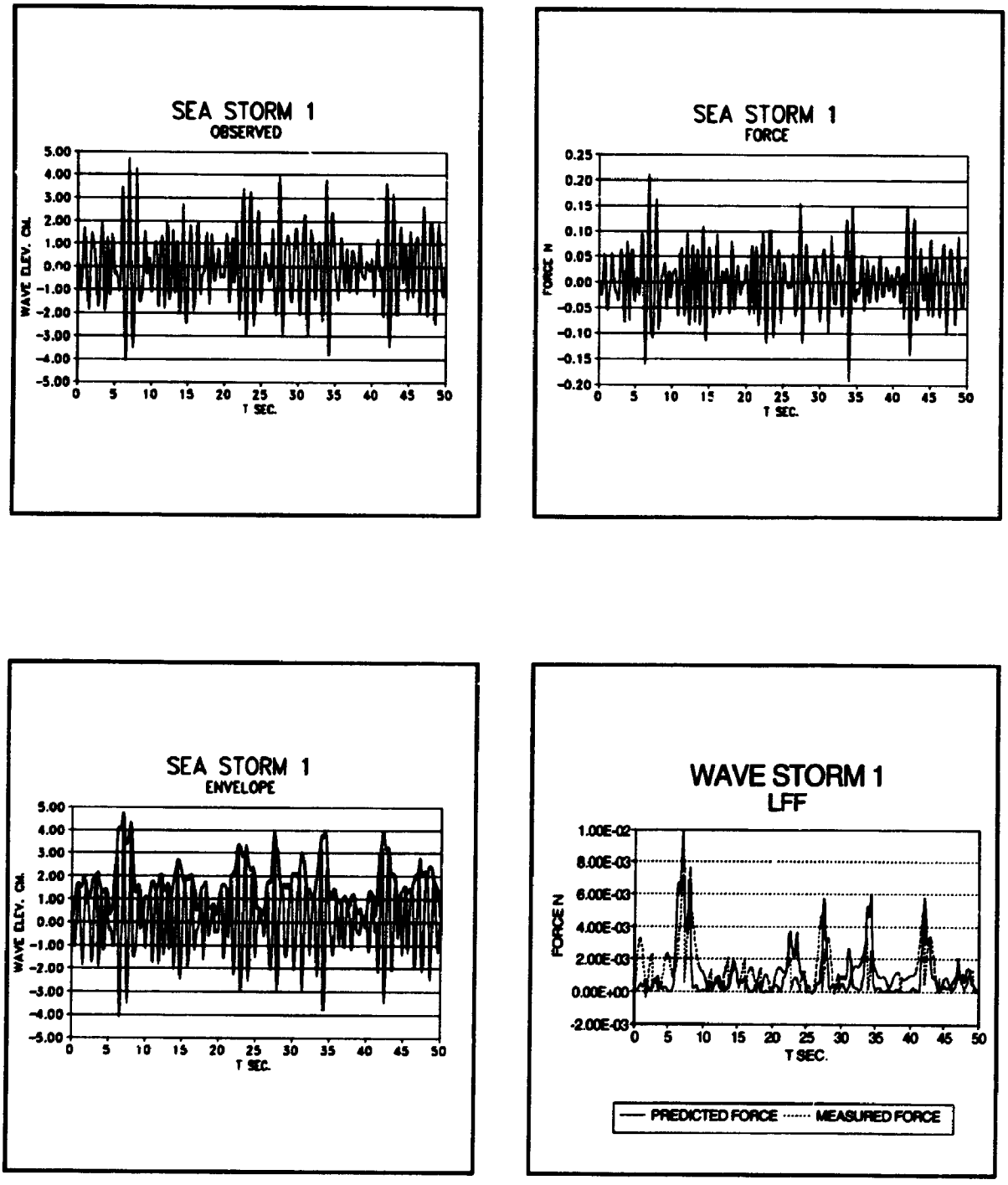

FIGURE 4.39: Time domain results for wave storm 1. Measured wave elevation, measured force, calculated envelope, comparison of measured and predicted drift force.

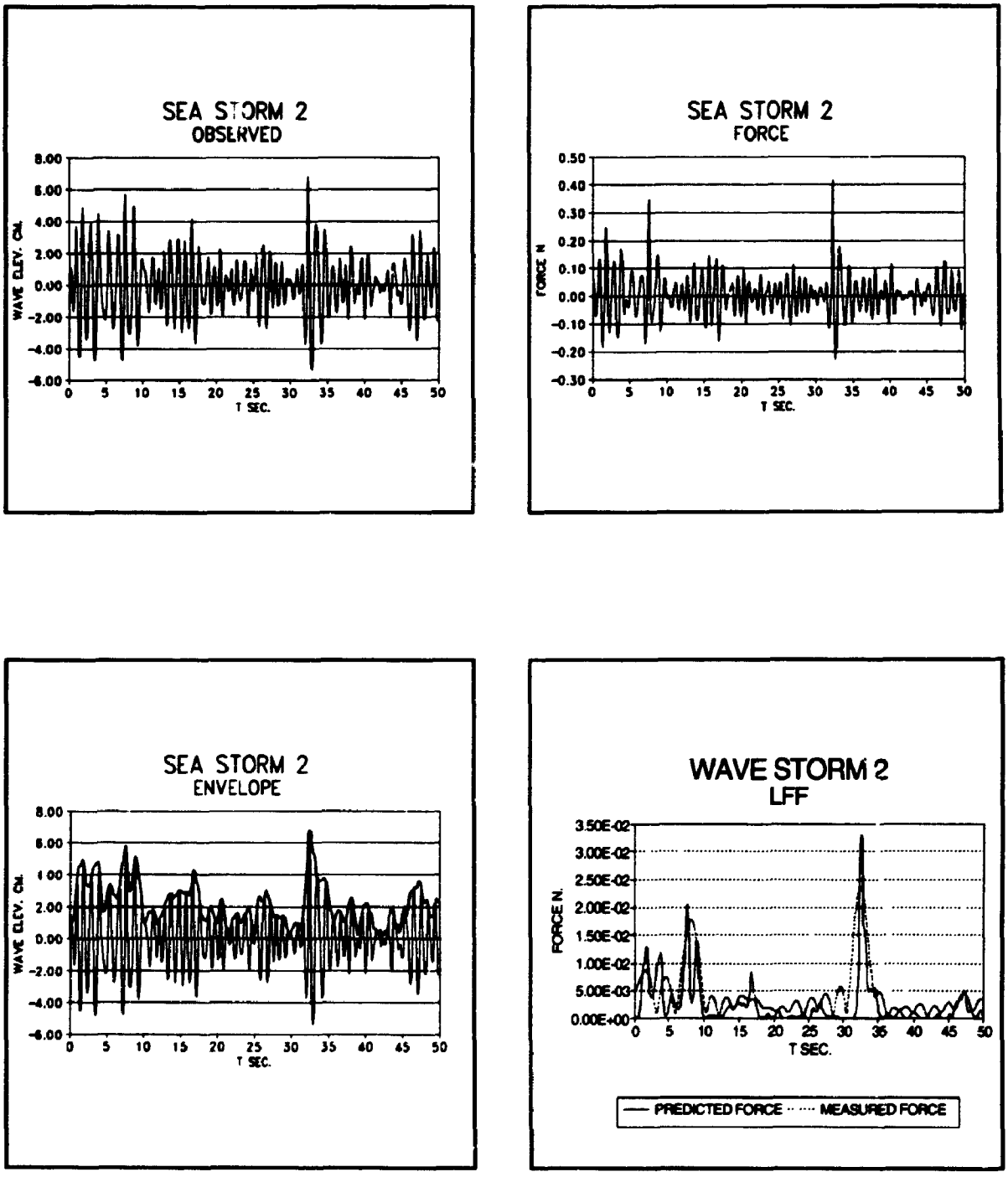

FIGURE 4.40: Time domain results for wave storm 2. Measured wave elevation, measured force, calculated envelope, comparison of measured and predicted drift force.

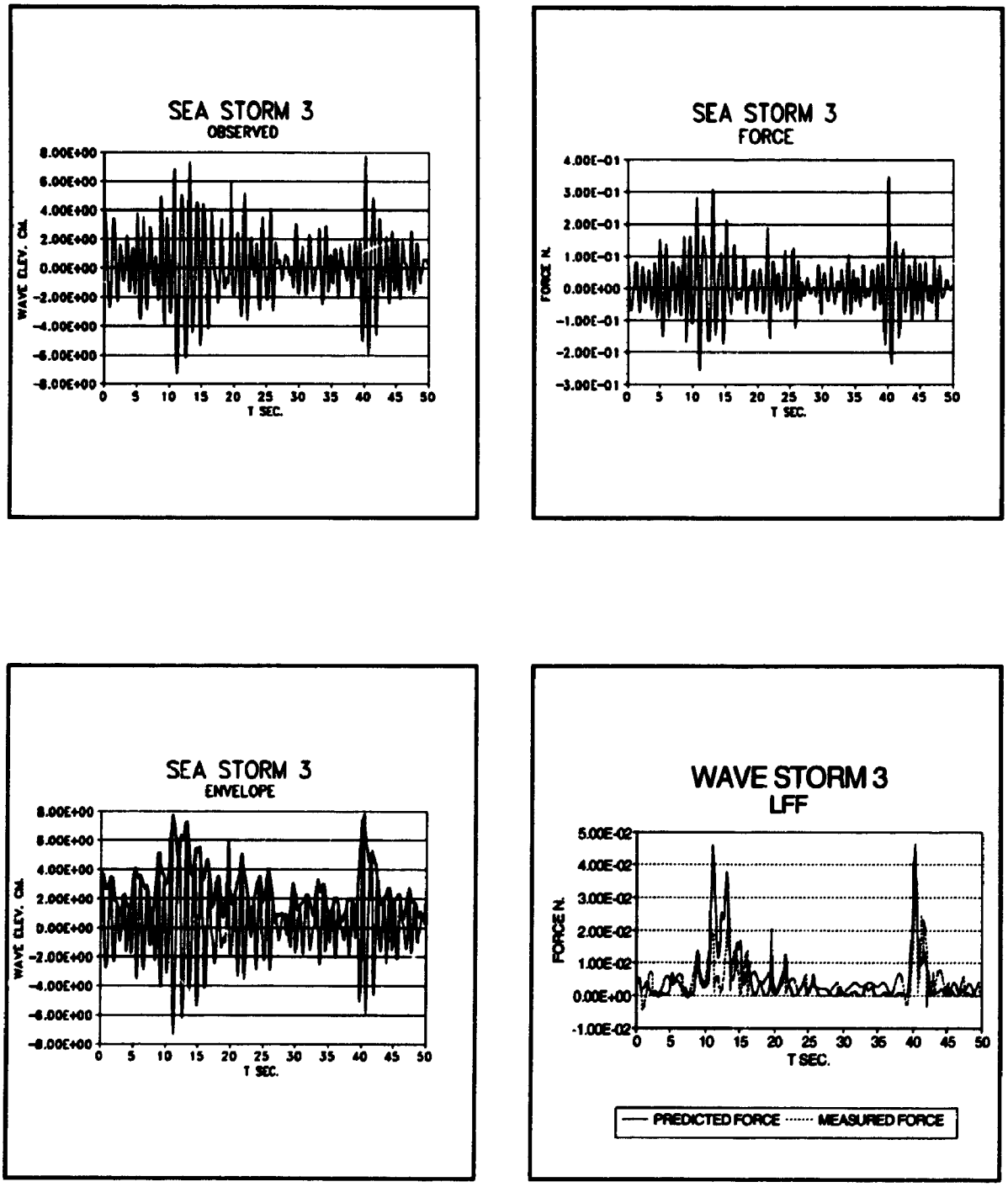

FIGURE 4.41: Time domain results for wave storm 3. Measured wave elevation, measured force, calculated envelope, comparison of measured and predicted drift force.

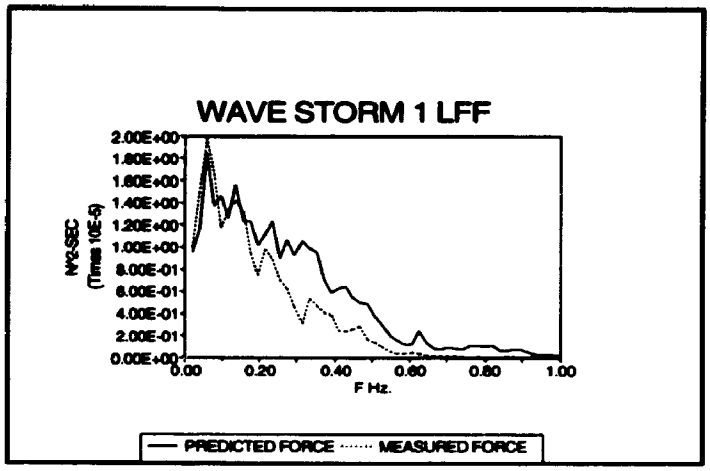

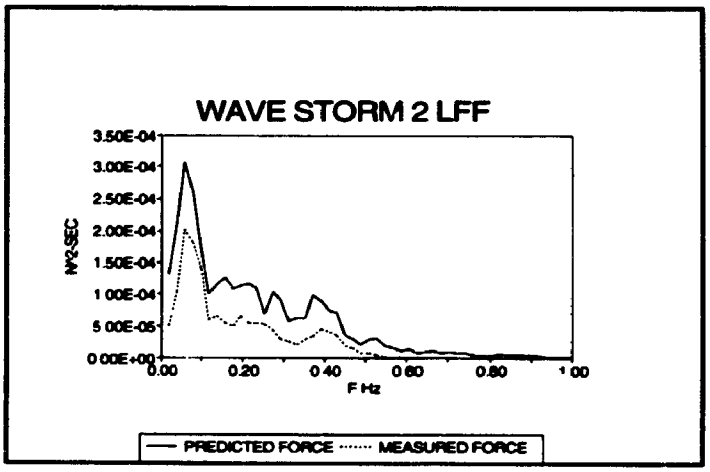

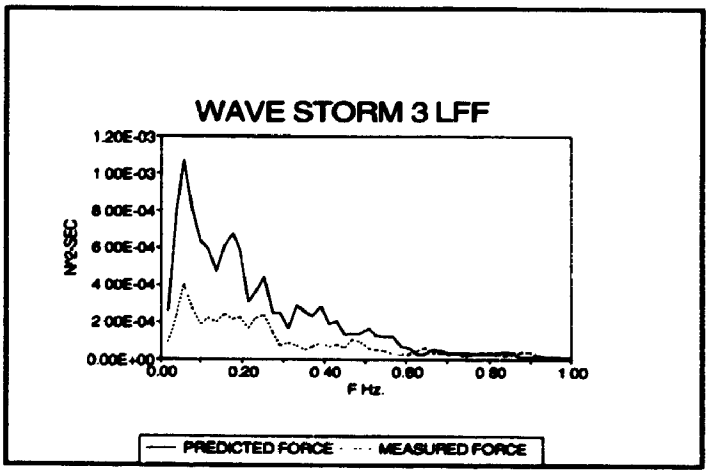

FIGURE 4.42: Frequency domain results for wave storms 1,2,3. Comparison of measured and predicted drift force.

4.6 DYNAMIC RESPONSE OF THE MODEL (EXPERIMENT VS. THEORY)

4.6.1 INTRODUCTION

In order to investigate the response of the simple cantilever model of the compliant tower to the combined action of wind and waves, model tests were carried out in the wind/wave facility in BLWTL II.

The model test program consisted of three platforms (heads) with the same cantilever structure. The difference among the heads was only in their volume but their mass was the same. The idea was to examine the effectiveness and perhaps improve the dynamic characteristics of the response, by changing the aerodynamic properties of the model while keeping the hydrodynamic properties constant.

Three wave storm in combination with four wind storms where used to generate fifteen different sea states. These sea states covered the likely range of wind-wave combinations for which a compliant tower would be expected to be exposed to.

The response of the models obtained in the above mentioned tests were compared to the results obtained by the numerical models described in chapter 3. The objective was to evaluate the suitability of the numerical modelling (time domain and frequency domain methods) for prediction of the response of the compliant tower to the combined action of wind and wave and investigate the contribution of the free surface effect (time domain analysis) to the total and low frequency responses.

4.6.2 MODEL DESCRIPTION AND INSTRUMENTATION

As was explained in chapter 3, a cantilever model was used. It was designed to simulate

the instantaneous tangent to the tip of the tower.

Figure 3.2, (Chapter 3), shows the model and Table 4.3 shows the three superstructures used (A, B , and C). The superstructures were made of a high quality foam and their mass was calibrated by placing the required mass inside them. A pair of strain gauges was mounted near the base of the structure (on the thin section at the bottom) to measure the surge response at the lower deck level. Calibration was carried out to obtain the linear relationship between the output voltage from the gauge and the lower deck level surge response.

Two wave probes measured the surface elevation at a distance of 35 cm on either side of the model across the tank and were aligned with the centerline of the model. The data acquisition was handled by the 11/23 vax at a sampling rate of 20 Hz.

A static pitot tube was placed near the middle of the deck level (22.8 cm above the mean water level) to measure the reference mean wind speed.

Wind profile measurements (velocity and intensity) were obtained at the center line of the tunnel for wave storms 1,2,3 with one high reference wind speed (Uref=4 m/sec.), and for the wind only case with Uref=4.8 m/sec. The profiles are shown in appendix I. Measurements of the wind velocity spectral density function were made at a height of 22.5 cm above the MWL. A typical wind spectrum (sea state 33) is shown in Appendix I. The measured spectrum is compared with ESDU 1975 and ESDU 1985 wind spectra. It can be seen that the results given by ESDU 1975 fit the experimental wind spectrum better than ESDU 1985.

4.6.3 RANDOM WAVE AND WIND TESTS

The parameters of the three wave storms used in the tests are shown in Table 4.4 . Figure 4.13 shows the target and observed wave storms. The addition of the wind storms

introduces slight change in the wave spectra. Measurements of the wind velocity time history and calculation of wind spectra were made at a height of 23 cm above the mean water level for all 15 sea states.

The wave elevation and turbulent wind velocity records (wind/wave data), obtained during the course of experiment, were used as input to the numerical models. The length of the time series used in the numerical analysis were 16 minutes. Experiments were performed for the zero wave heading only.

The aerodynamic drag coefficient (C_D for the super-structure) was calculated based on a series of experiments carried out on the 2 pound force balance in tunnel 1. The model consisted of the top side and the stem and had the same geometry as used during the wind wave tests. It was connected to the balance and the forces at the base were measured for the same range of wind speeds used in the wind/wave tests.

The experiment was performed using two types of terrains (bare floor and carpet). In the case of the bare floor, the effect of a relatively uniform flow on the drag coefficient was studied while in the second terrain the effect of tubulence was considered. A pitot tube was used to measure the wind speed at the height of 23 cm as was used during the wind/wave tests. Based on the measured mean forces, the C_D values were obtained. Figure 4.43 shows the values of drag coefficient vs wind speed (the area of the stem was included in the calculation of C_D).

Based on the experiments carried out in the wind/wave facility, the wind induced current were approximately measured by a submerged ping pong ball connected to small piece of foam by a varying length of string. On the basis of these data, the current was modelled (in the theoretical analysis) as being constant with depth and equal to the values shown in Table 4.5.

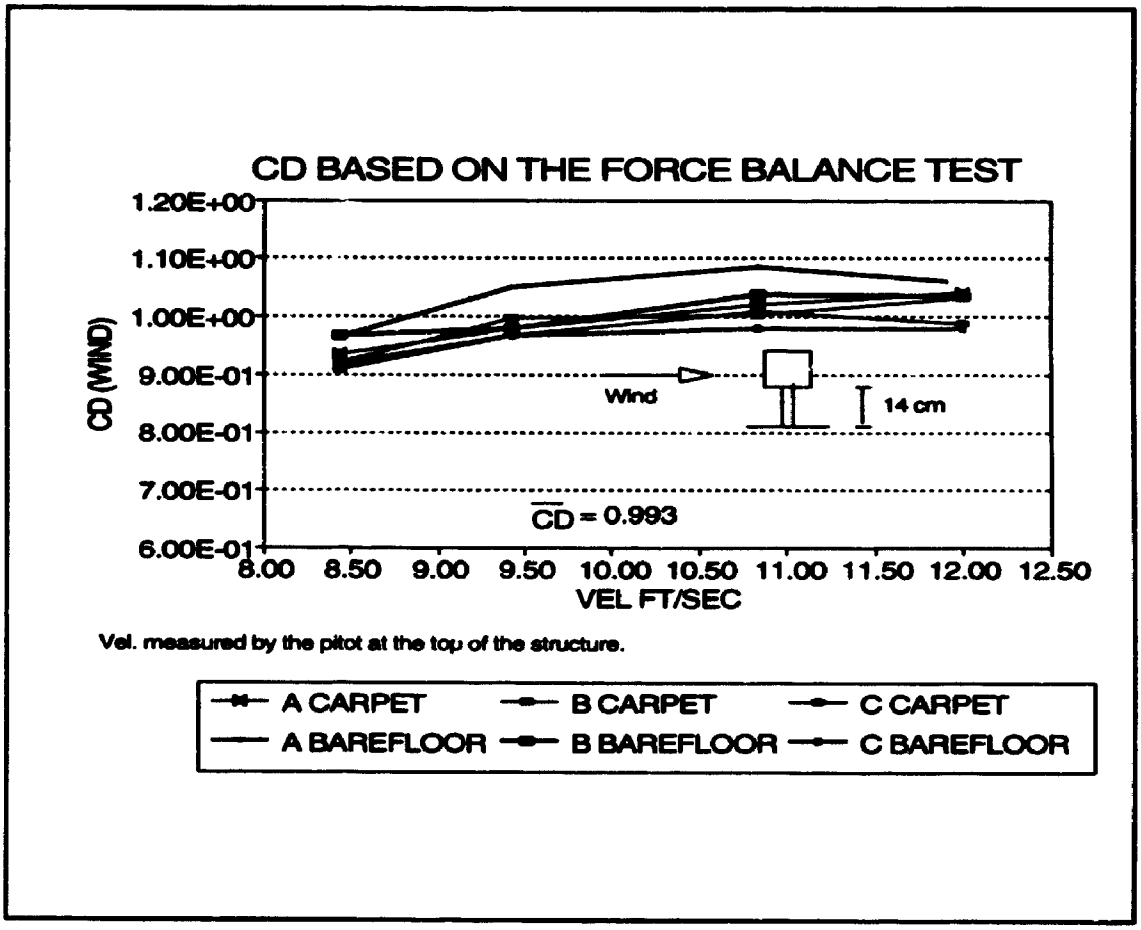

FIGURE 4.43: Aerodynamic drag coefficient

TABLE 4.3: STRUCTURAL CONFIGURATIONS			
	W	H	D
Structure A	6.3	8.5	6.3
Structure B	8.0	8.5	8.2
Structure C	10.	8.5	10.2

TABLE 4.4: WAVE STORM PARAMETERS		
	F_p Hz	$H_{s\ Cm}$
SEA STORM 1	1.05	5.1
SEA STORM 2	0.86	7.9
SEA STORM 3	0.81	11

TABLE 4.5: MEASURED EQUIV. UNIFORM CURRENT VELOCITY	
wind speed Uref m/sec	U_c cm/sec
0.	0.
2.25	2.5
3.2	3.
4.0	3.5

4.6.4 EXPERIMENTAL RESULTS

The recorded time histories of the surge response at the lower deck level for structures A,B,C were analyzed to find the mean, rms and the surge response spectra. The surge response spectrum due to the combined action of wind and waves, can be divided into two parts. The first part comes from the resonant response of the fundamental mode of the structure(f=0.375 Hz.), and it is excited by the nonlinear nature of the drag force including second order free surface effect as well as the wind gust. The second part is due to the first order wave forces and it follows the shape of the wave elevation spectrum. The measured surge response spectra are presented in appendix F. The resonant part of the response is sensitive to the total damping while the wave frequency part is relatively independent from the damping.

For a given sea state, the rms surge response increases as the mean wind speed increases, and in a mild sea the low frequency response due to wind load exceeds the wave frequency response as the wind grows. At higher wind speed, (typically more than 30 m/sec full scale), for the loading cases 'wind only' and 'wind and wave', the low frequency part of the surge response of the former was higher than the latter (for equal wind speed). Figure 4.44 shows a typical surge response spectrum for sea state 32 (structure A). Also Figures 4.45 to 4.47 present the rms surge response as a function of mean wind speed at the deck level (Uref) for structures A,B, and C. Figures 4.48 to 4.50 present the mean response of the lower deck level as a function of the mean wind speed. The mean response is caused by the mean wind forces, wind induced current and mean wave drift forces (second order free surface forces). For a given wave storm, the mean response increases as the wind speed increases.

Figure 4.51 shows the measured rms surge response as a function of mean wind speed for structures A,B, and C for the 'wind-only' case. The values of the

rms response for structure C falls between structures A and B. As the ratio of the projected area for the three structures are 80.2:94.6:111.6 (A:B:C), it is expected that the value of rms response for structure C, under nearly equal wind/wave conditions (Table 4.6), would be greater than that of structure B. This behaviour is not observed in the experimental results (Figure 4.51). Although the aerodynamic drag coefficient for structure C is about 7% smaller than those of structures A and B, it is not small enough to explain the behaviour. The response characteristics of the three structures were compared by plotting the coefficient of variation (CoV) vs wind speed (Figure 4.52). In this way, the differences caused by the small change in aerodynamic drag coefficient is removed. It is observed that the CoV for structure C is clearly smaller than those of structures B and C. The reason for this reduction in rms response is not clear, but it is thought to be related to hydrodynamic damping. During the course of the experiment it was observed that there was a slow leak in the wave tank, and although great care was taken to ensure that the water level did not change by more than approximately 5 mm, there are instances where changes in the water level exceeded 5 mm.

TABLE 4.6: Typical Mean Wind Speed (at tip of Structure) and associated H_s WIND ONLY

	Mean Wind Vel. (M/S)	H_s (CM)
Structure A	4.05	2.79
Structure B	4.048	2.55
Structure C	4.092	2.58

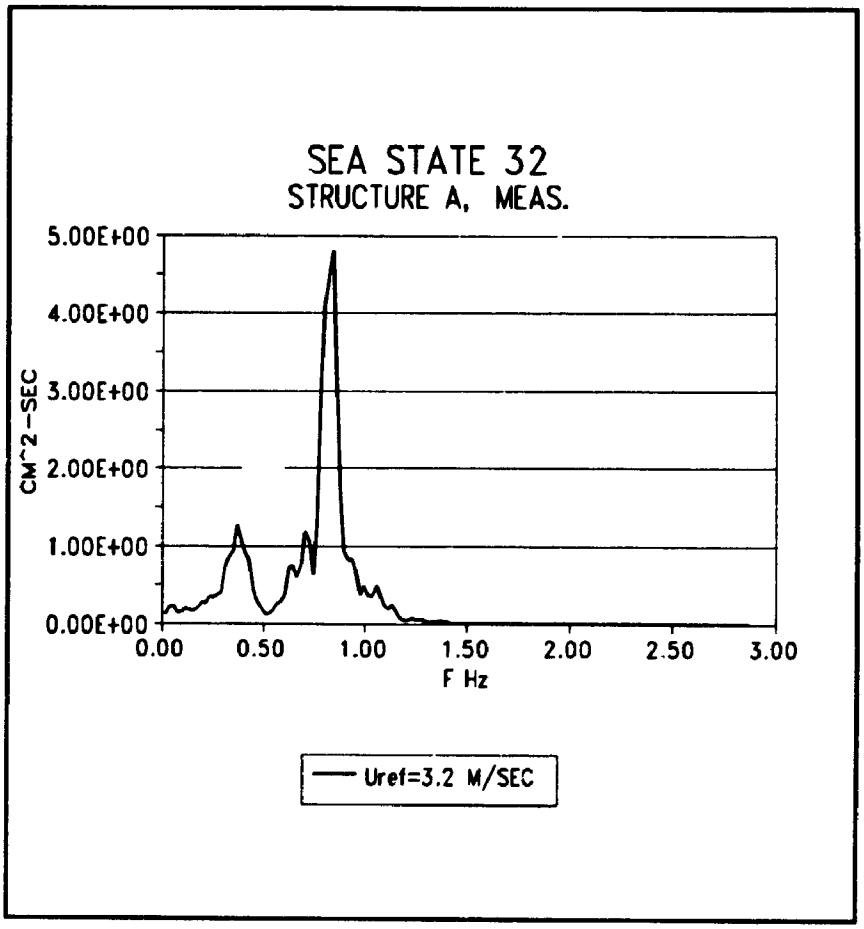

FIGURE 4.44: Measured surge response spectrum for structure A, sea state 32.

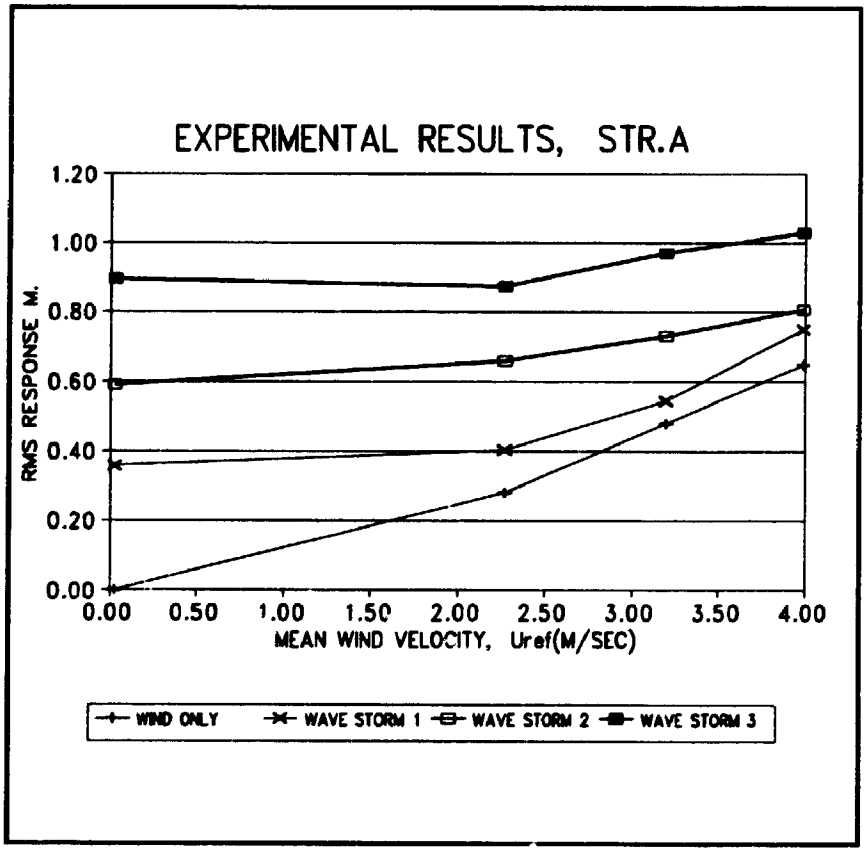

FIGURE 4.45: Comparison of the measured rms surge response vs wind speed (structure A)

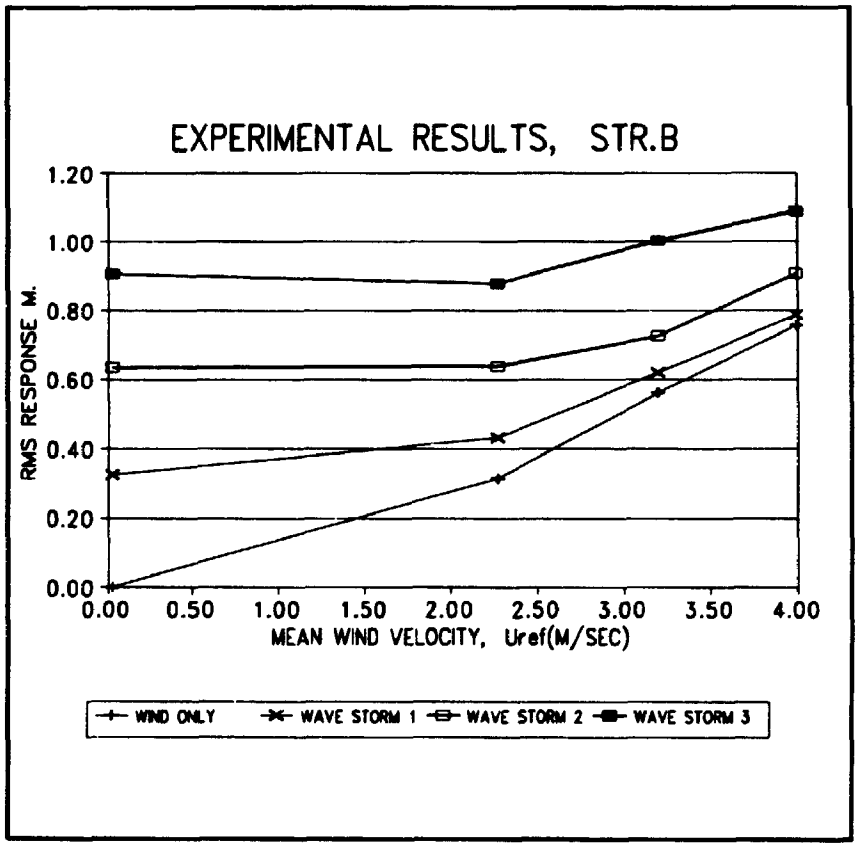

FIGURE 4.46: Comparison of the measured rms surge response vs wind speed (structure B).

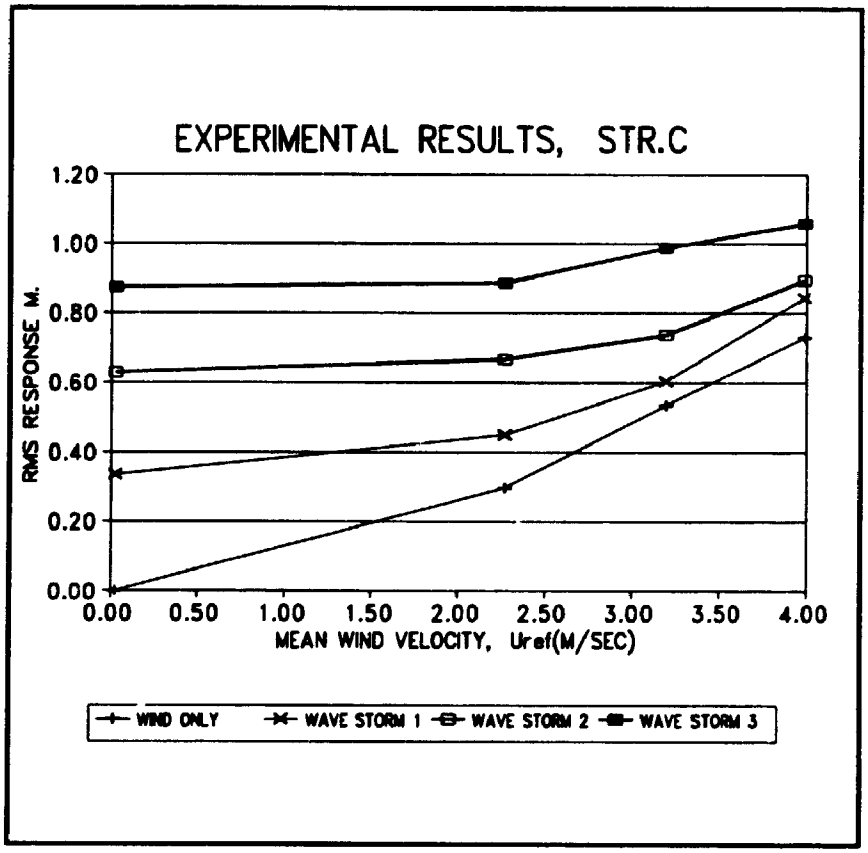

FIGURE 4.47: Comparison of the measured rms surge response vs wind speed (structure C)

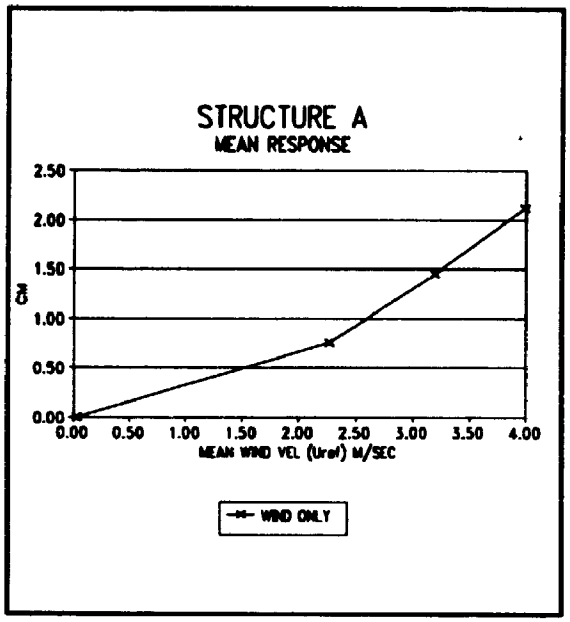

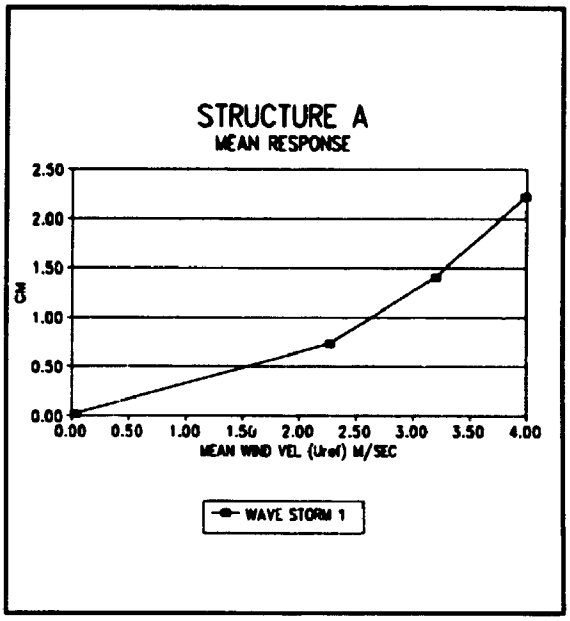

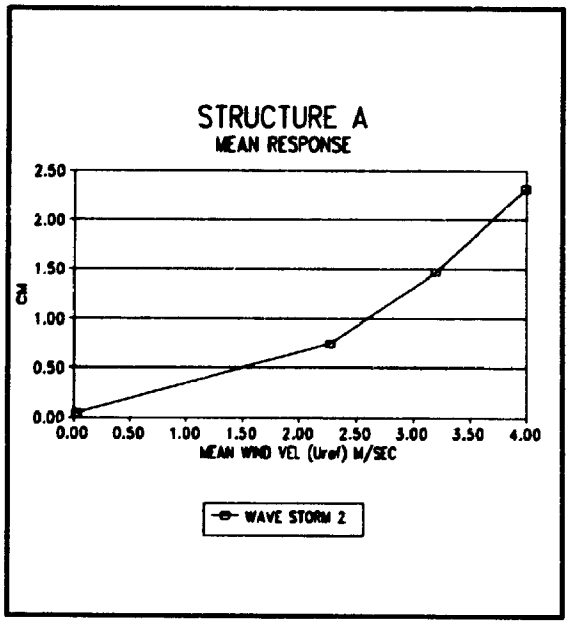

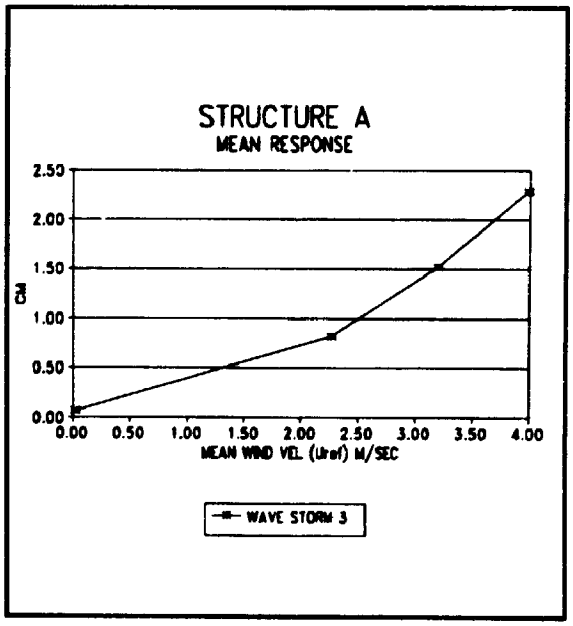

FIGURE 4.48: Mean response vs. wind velocity (A)

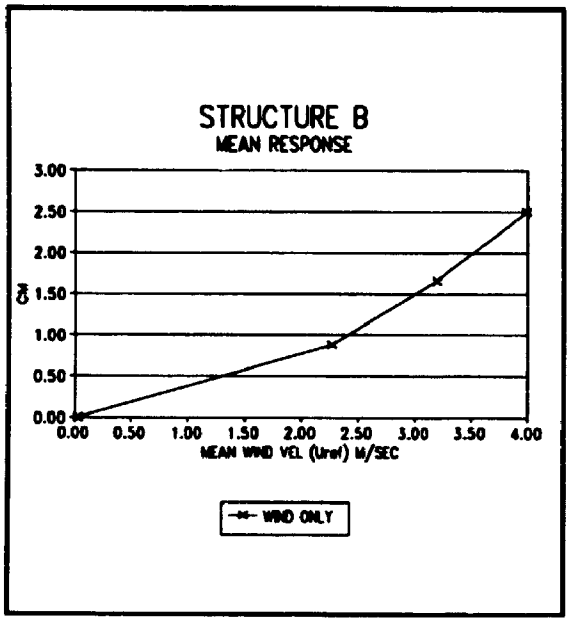

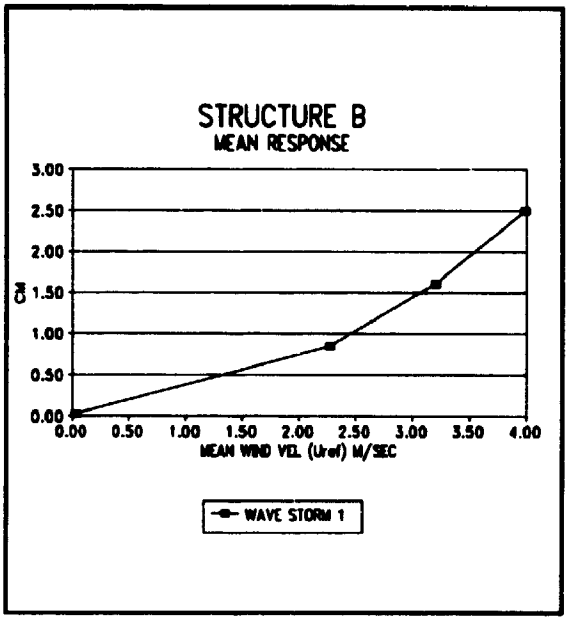

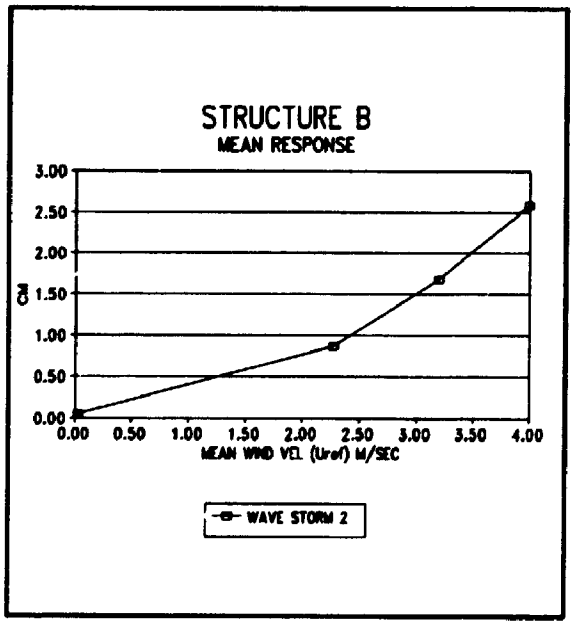

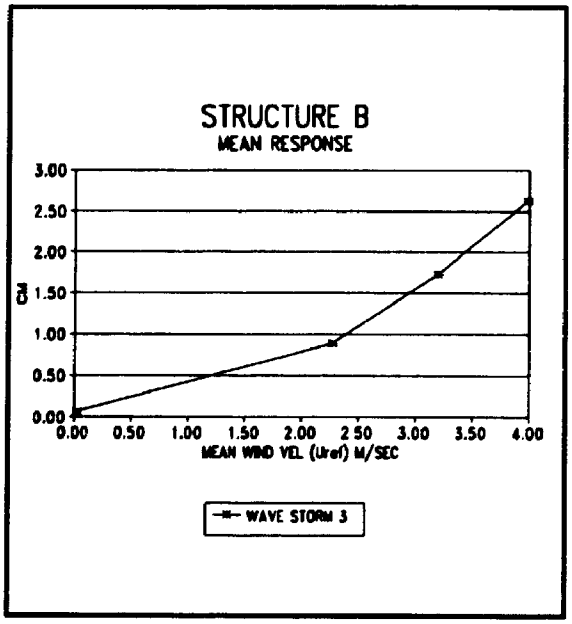

FIGURE 4.49: Mean response vs wind velocity (B)

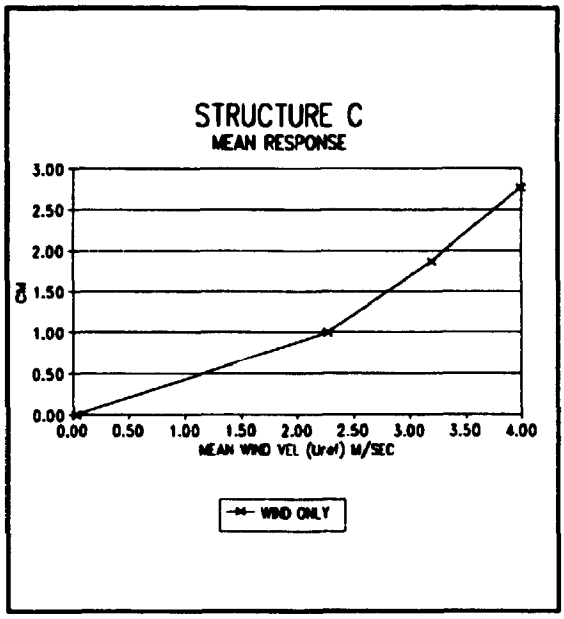

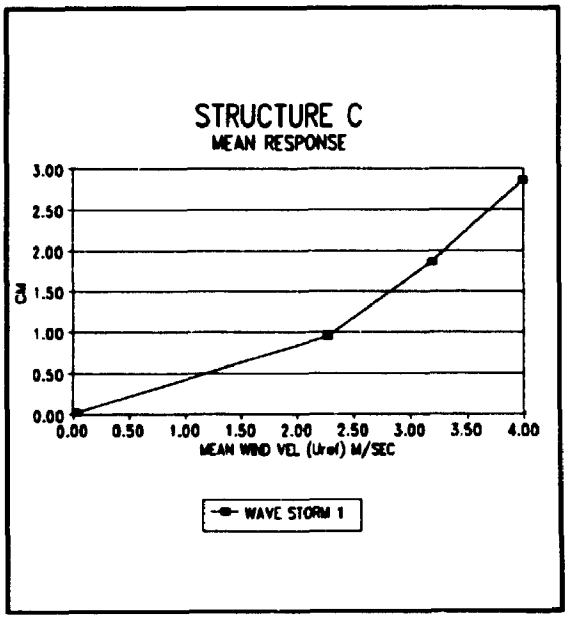

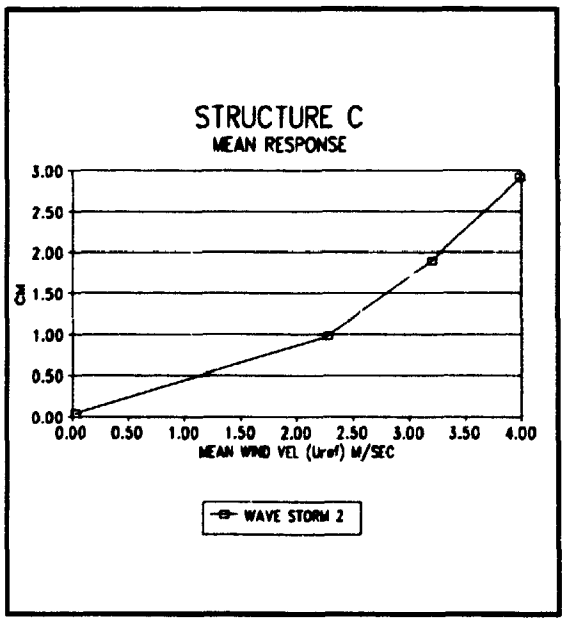

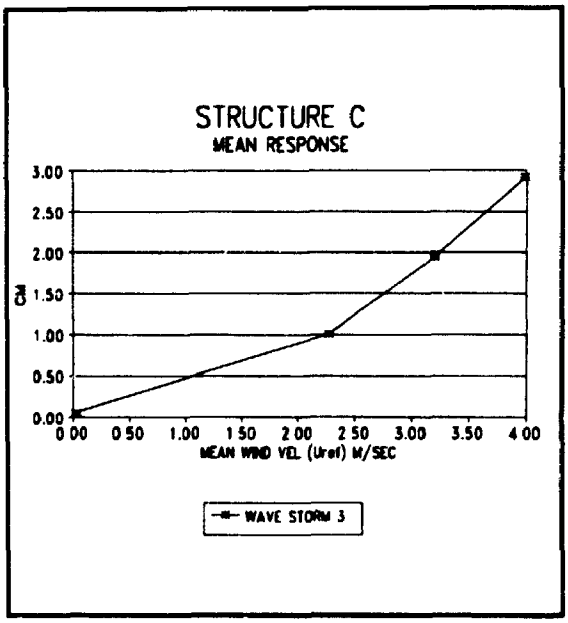

FIGURE 4.50: Mean response vs wind velocity

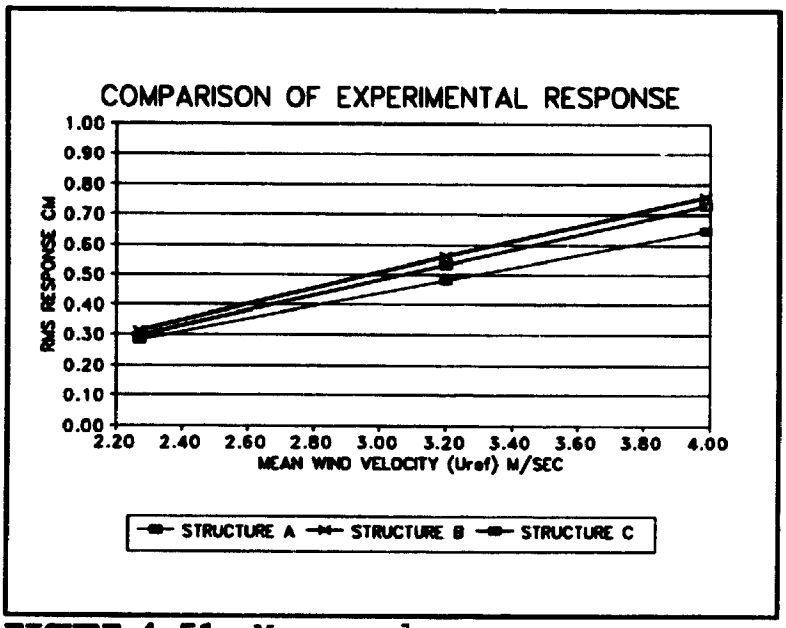

FIGURE 4.51: Measured rms surge response vs wind speed for structures A,B and C (WIND ONLY)

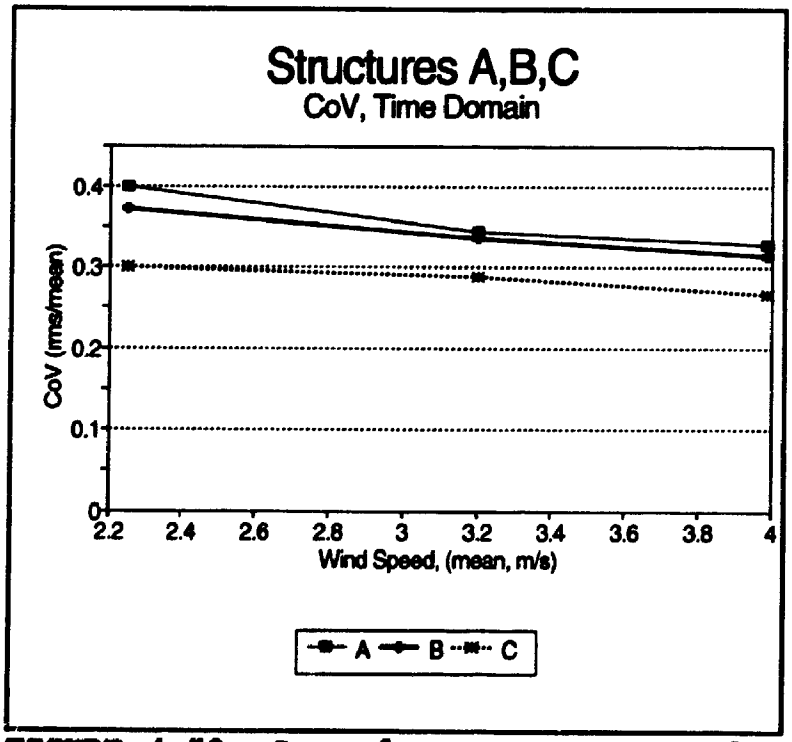

FIGURE 4.52: Cov of surge response for structures A,B and C (measured).

4.6.5 COMPARISON OF THEORETICAL AND EXPERIMENTAL RESULTS

In order to investigate the reliability of the numerical model, the experimentally obtained surge response is compared with the corresponding numerical results. Both time domain analysis and frequency domain analysis were performed for the three structural configurations.

The member was not filled (no water allowed in the member) and the structural lumped masses were calculated based on this condition.

As is shown in figure 4.43, the scatter in the aerodynamic drag coefficient is small and it has a mean value of 0.99. A value of C_D=1 was used in the numerical calculations. Based on the KC_m numbers observed in the experimental results for the surge response ($1< KC_m <4$), the values of C_D,C_M were selected from the measurements reported in section 4-4 (Daneshvaran, Vickery, 1994). Table 4.7 shows the values of CD,CM used in the numerical models.

TABLE 4.7: DRAG AND INERTIA COEFFICIENTS

	C_D	C_M
WIND ONLY	0.7	2.3
WAVE STORM 1	0.7	2.3
WAVE STORM 2	0.8	2.3
WAVE STORM 3	0.9	2.3

The C_D values were determined based on the damping tests in random waves and the C_M values were determined based on the force measurements of the oscillating body in regular waves. The process of selection is somewhat judgemental. In this range of

KC_m, the envelope fitted to the decaying trace, was not reliable for the purpose of measurement of damping (Daneshvaran, Vickery, 1994), and the C_D values will have an error margin of about ±0.2. The values of C_M, however, seemed to have a more stable trend.

The uncertainty associated with the selection of these coefficient is reflected in the comparison of the experimental and theoretical results.

4.6.5.1 TIME DOMAIN RESULTS VS. EXPERIMENTAL RESULTS

Stochastic time domain solution based on the Morison relative velocity model, both including the free surface effect and not including the free surface effect, are compared with the experimental results.

The model used to integrate the nonlinear drag forces up to the current water level was based on the constant velocity field above the mean water level as it was explained in chapters 2,3, and 4. The length of the time history in each simulation was 16 minutes and the results were transformed in to the frequency domain using 18 blocks.

Appendix G presents the spectra of the surge response based on the time domain results for the three structures. Figure 4.53 shows comparison of the surge response spectra for sea state 32, structure A. Also Figures 4.54 to 4.56 show the comparison of the measured and theoretical response vs. wind speed for the three structural configurations. Overall, the rms response predictions compared well with the experimental results for the three structural configurations. However, there are cases of underprediction which originate from the low frequency part of the response. Figures 4.57 to 4.59 present the rms of low frequency and wave frequency parts of the response for the time domain as well as the experimental results. The dividing frequency was 0.5 Hz. For a given wave storm, increasing the wind speed from 0 to

about 3 m/s, decreases the wave frequency part of the rms response. This is due to a small reduction in the significant wave height in the wave elevation spectrum in the presence of wind.

In sea states 13, and 14, the theory underpredicts the response by approximately 15% for structure A. For structure B, this happens in sea states 13. For the 'wind only' case and for structures A, and B, there is approximately 9% underprediction in the response. These underpredictions are related, partly to the selection of the drag coefficient, and partly to the constant wind induced current used in the relative velocity model. As was explained the drag coefficients for the three sea storms were somewhat selected by judgement, since the envelope fitted to the decay trace at small KC_m numbers, in the measurement of damping was not quite satisfactory. As such, the C_D values employed in the range of KC_m numbers encountered in the current experiment may have introduced some underestimation in the low frequency part of the response. The other source of the underprediction might be related to the magnitude of the constant current used in the relative velocity model. The current velocities measured are subject to error because of the device employed. Modelling the wave current interaction by the relative velocity equation might not be completely appropriate and the subject is still under research.

The inclusion of the free surface effect increases the low frequency part of the response and the wave frequency part is not sensitive to this effect. In most of the cases its inclusion improves the agreement between the experimental and time domain results. In sea states 31, and 32, a difference of about 40% in the prediction of low frequency response between the two time domain models was observed which is due to the proportionality of the second order drift forces to H^3, and in higher seas, this effect would be more pronounced.

For a given wave storm, increasing the wind speed will increase the low frequency

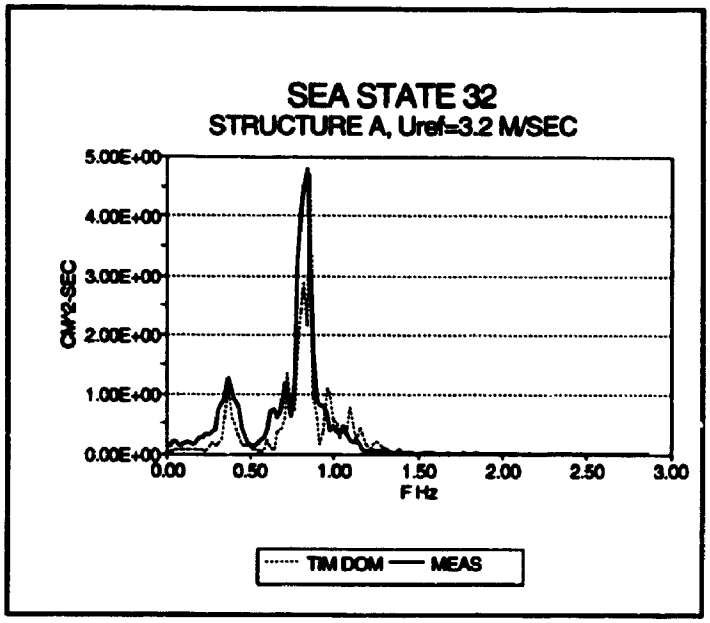

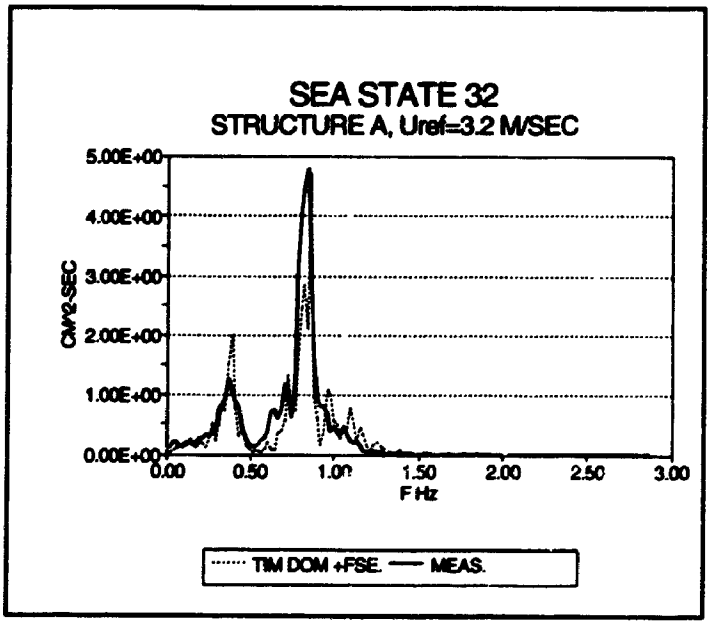

FIGURE 4.53: Comparison of the time domain results (without and with inclusion of free surface effects), with the measured results for sea state 32, structure A.

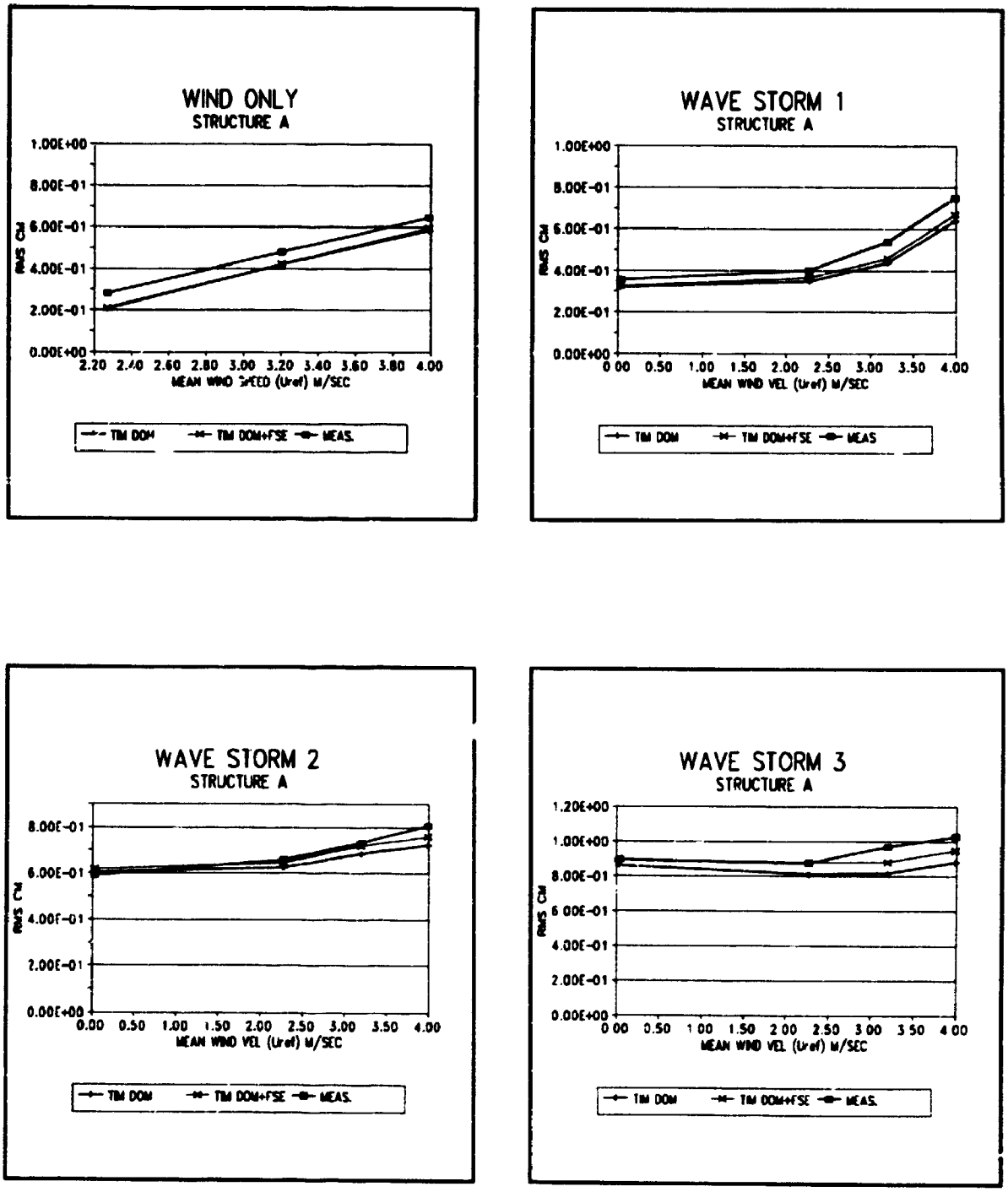

FIGURE 4.54: Comparison of the time domain results with measured results (structure A)

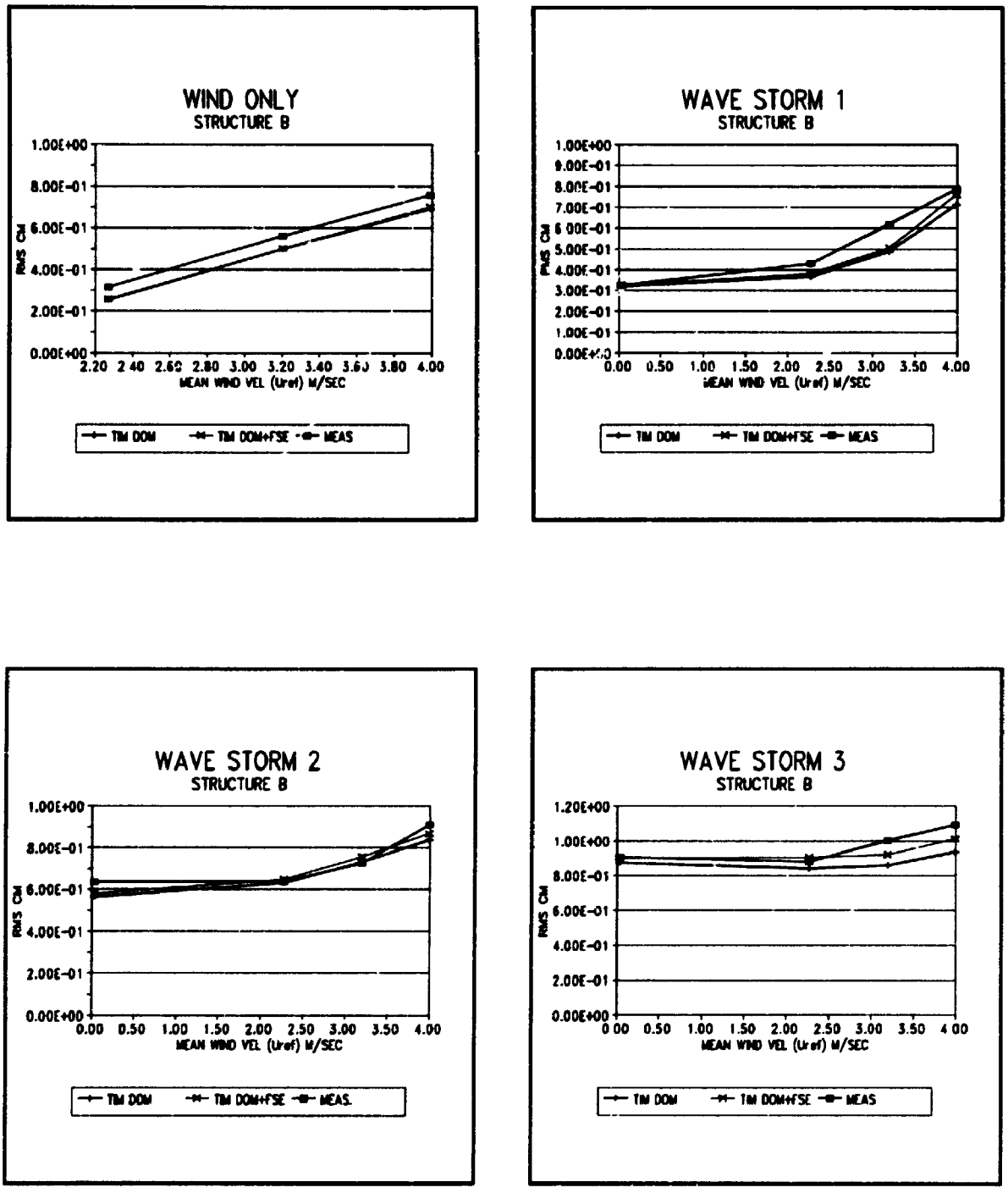

FIGURE 4.55: Comparison of the time domain results with the measured results (structure B)

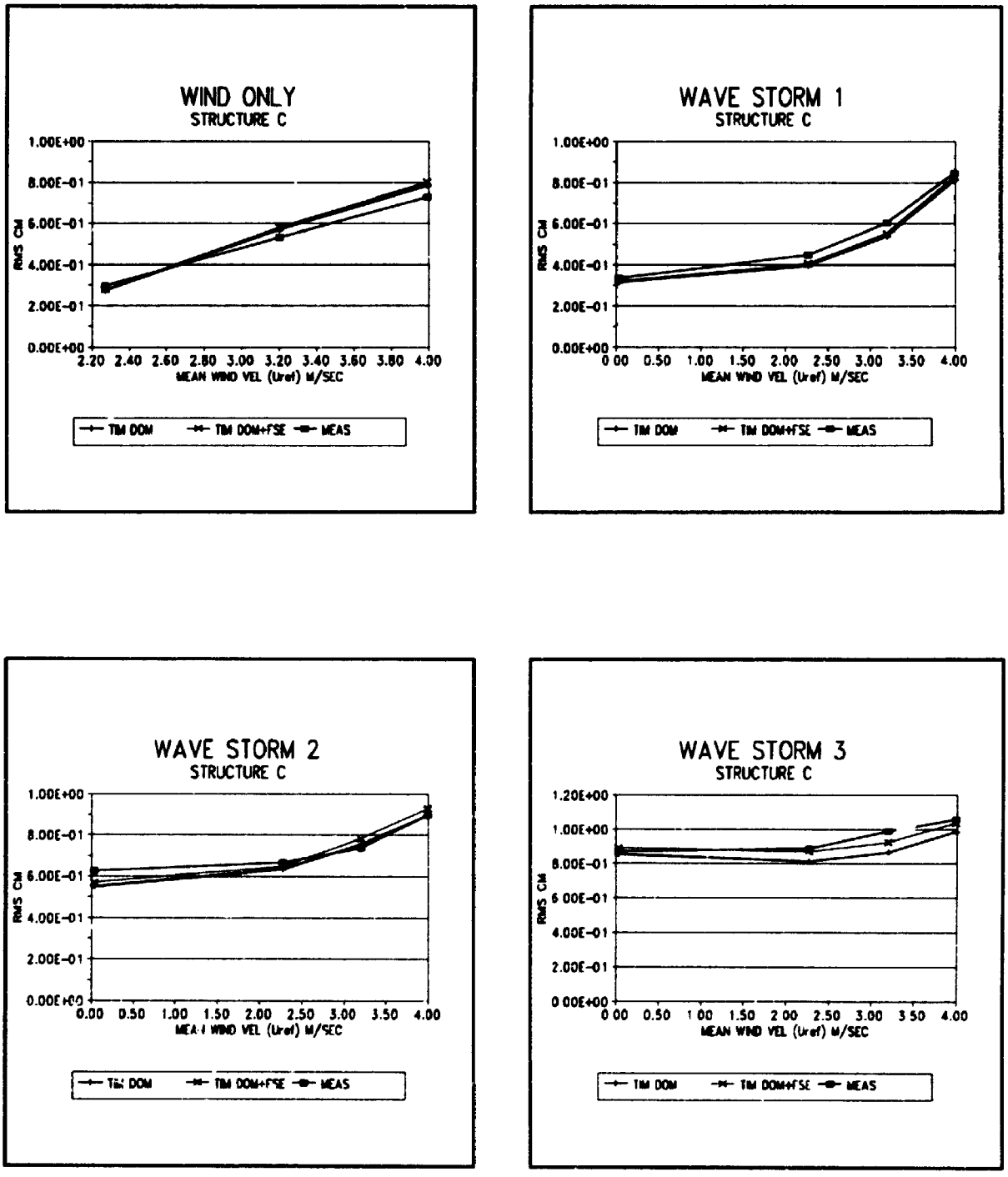

FIGURE 4.56: Comparison of the time domain results with the measured results (structure C)

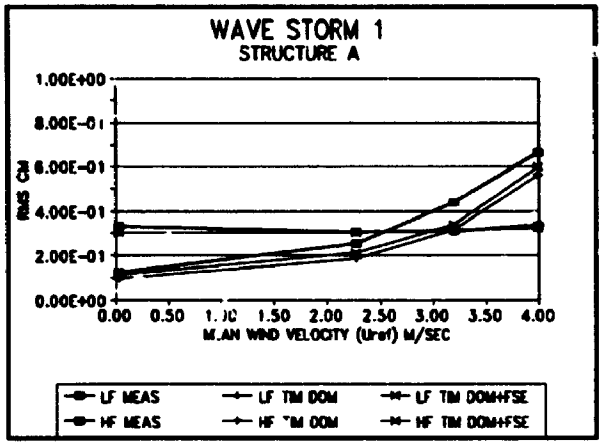

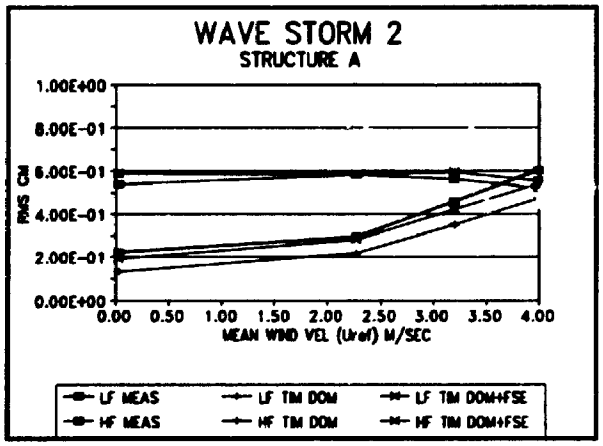

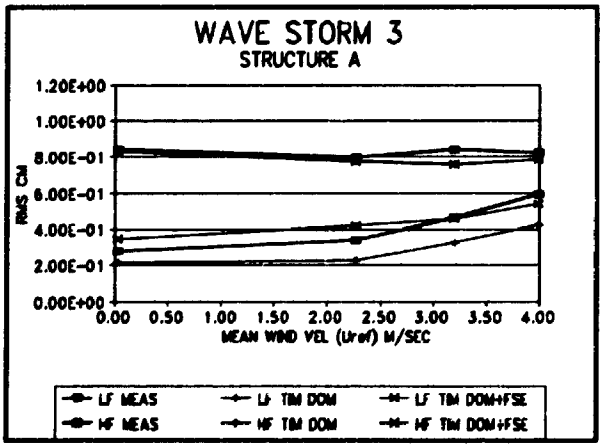

FIGURE 4.57: Low and wave frequency parts of the response (comparison of the time domain results with the measured results for structure A)

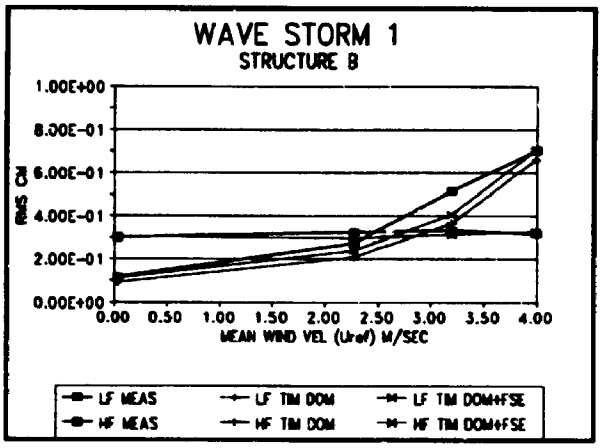

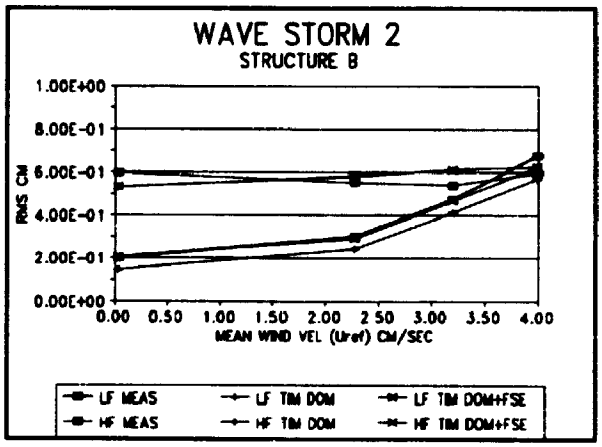

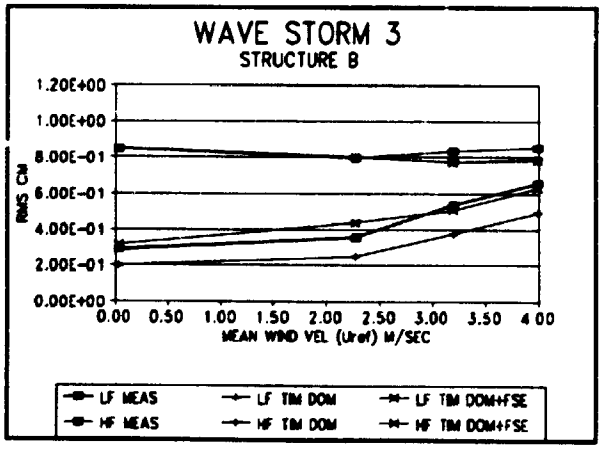

FIGURE 4.58: Low and wave frequency parts of the response (comparison of the time domain results with the measured results for structure B)

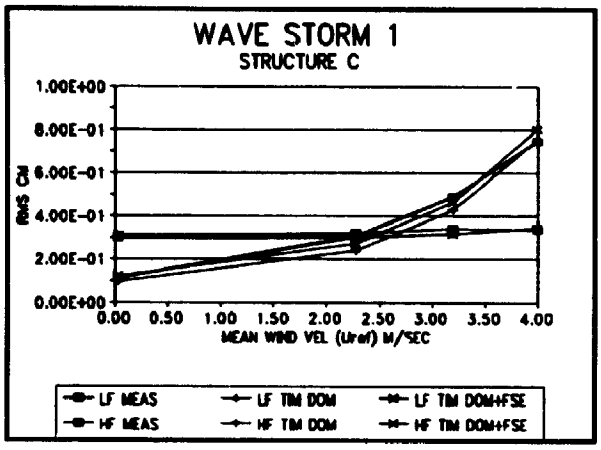

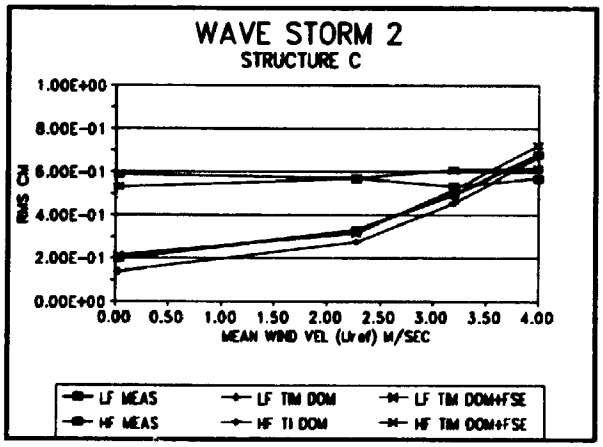

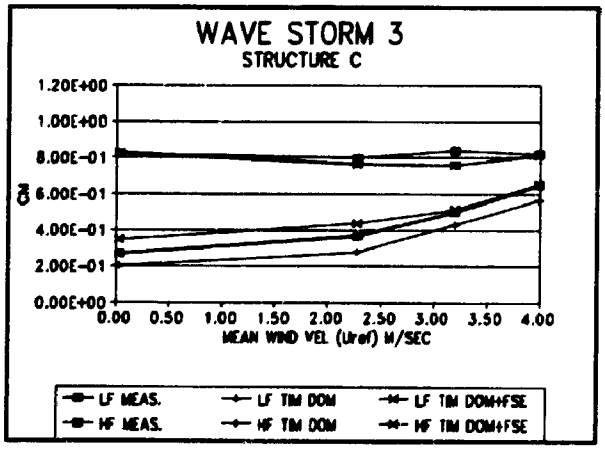

FIGURE 4.59: Low and wave frequency parts of the response (comparison of the time domain results with the measured results for structure C)

response, but the response due to the first order waves remains relatively uniform. For the 'wind only' cases, the response is governed by the low frequency responsepart and it increases as the reference mean wind speed increases. For the 'wave only' cases, the more severe the sea states, the greater the structural response becomes. In higher seas, the relative significance of the drift wind and wave forces are reduced. These trends can also be observed in the time domain results.

4.6.5.2 FREQUENCY DOMAIN RESULTS VS. EXPERIMENTAL RESULTS

Frequency domain solutions based on the linearized Morison's relative velocity model are compared with the experimental results.

The surge response spectra obtained from the frequency domain results are presented in Appendix H. Figure 4.60 shows the comparison of the surge response spectrum obtained for sea state 32, structure A.

The general features of the response observed in the time domain results are also observed in the frequency domain results.

Figures 4.61 to 4.63 show the rms surge response vs. wind speed for the frequency domain and experimental results. Note that the frequency domain analysis gives smaller rms response than the experimental results.

Due to the stochastic linearization of the drag loading, it leads to smaller drift response as compared to the time domain results. The use of this approach can save a lot of time and economically it is more attractive.

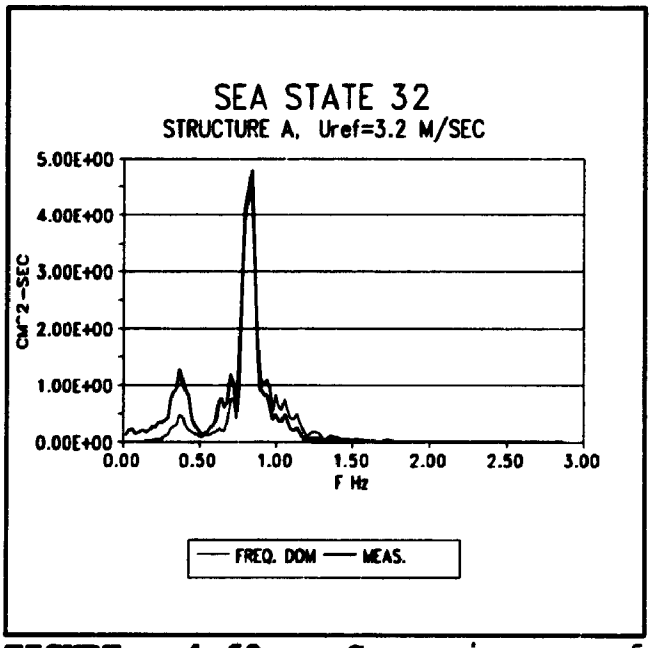

FIGURE 4.60: Comparison of measured result with frequency domain result for sea state 32, staructure A.

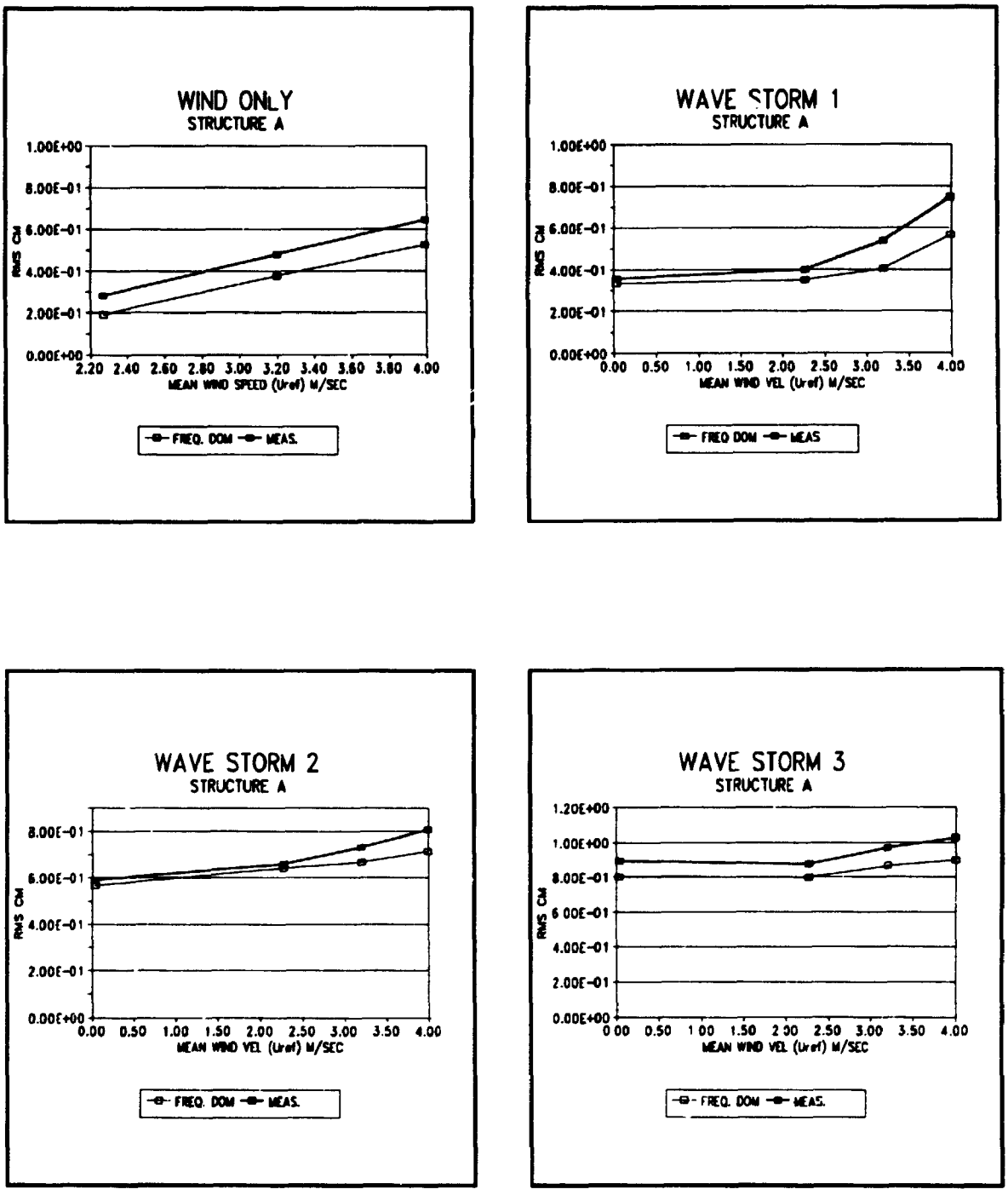

FIGURE 4.61: Comparison of the frequency domain results with the measured results (structure A)

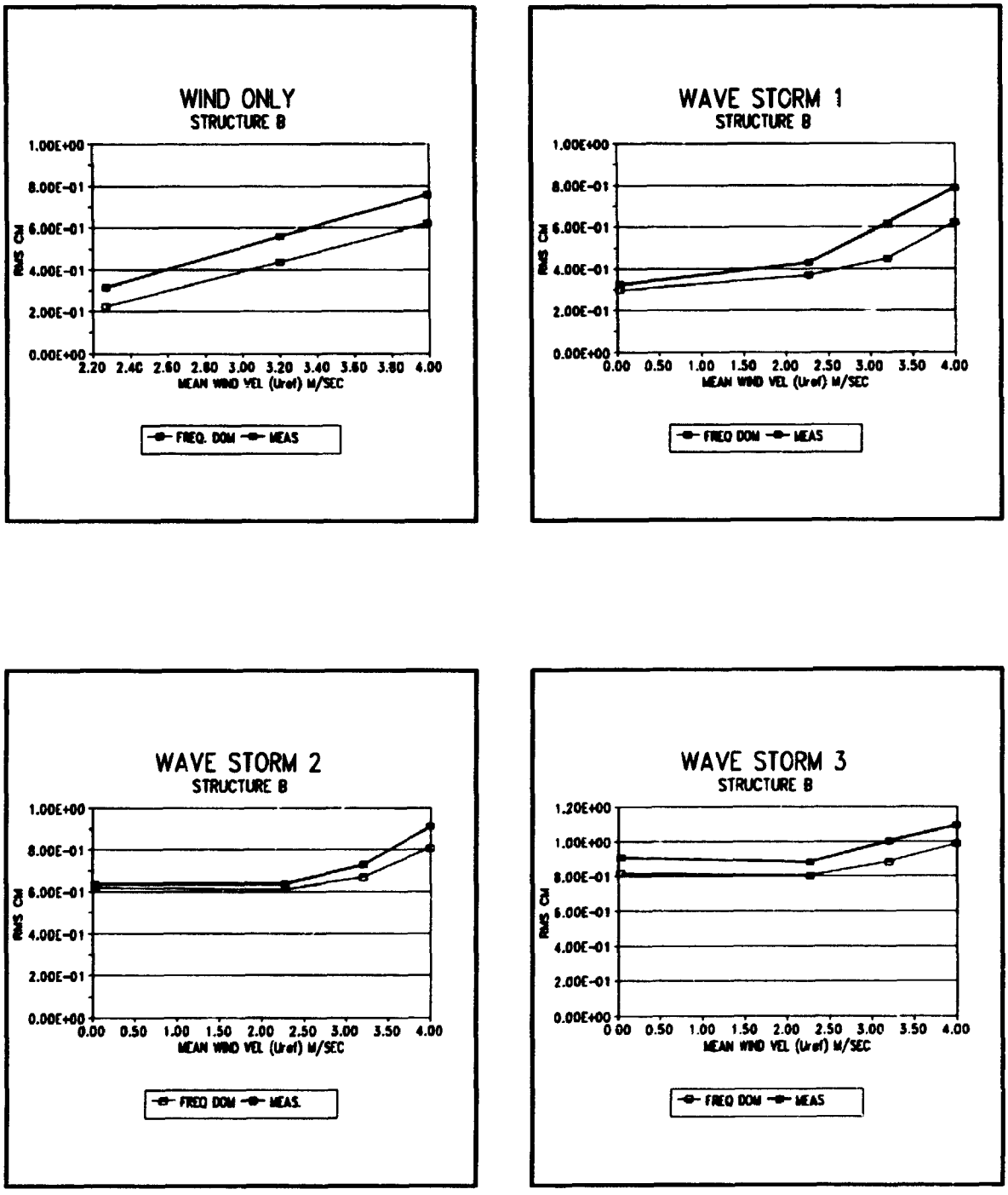

FIGURE 4.62: Comparison of the frequency domain results with the measured results (structure B)

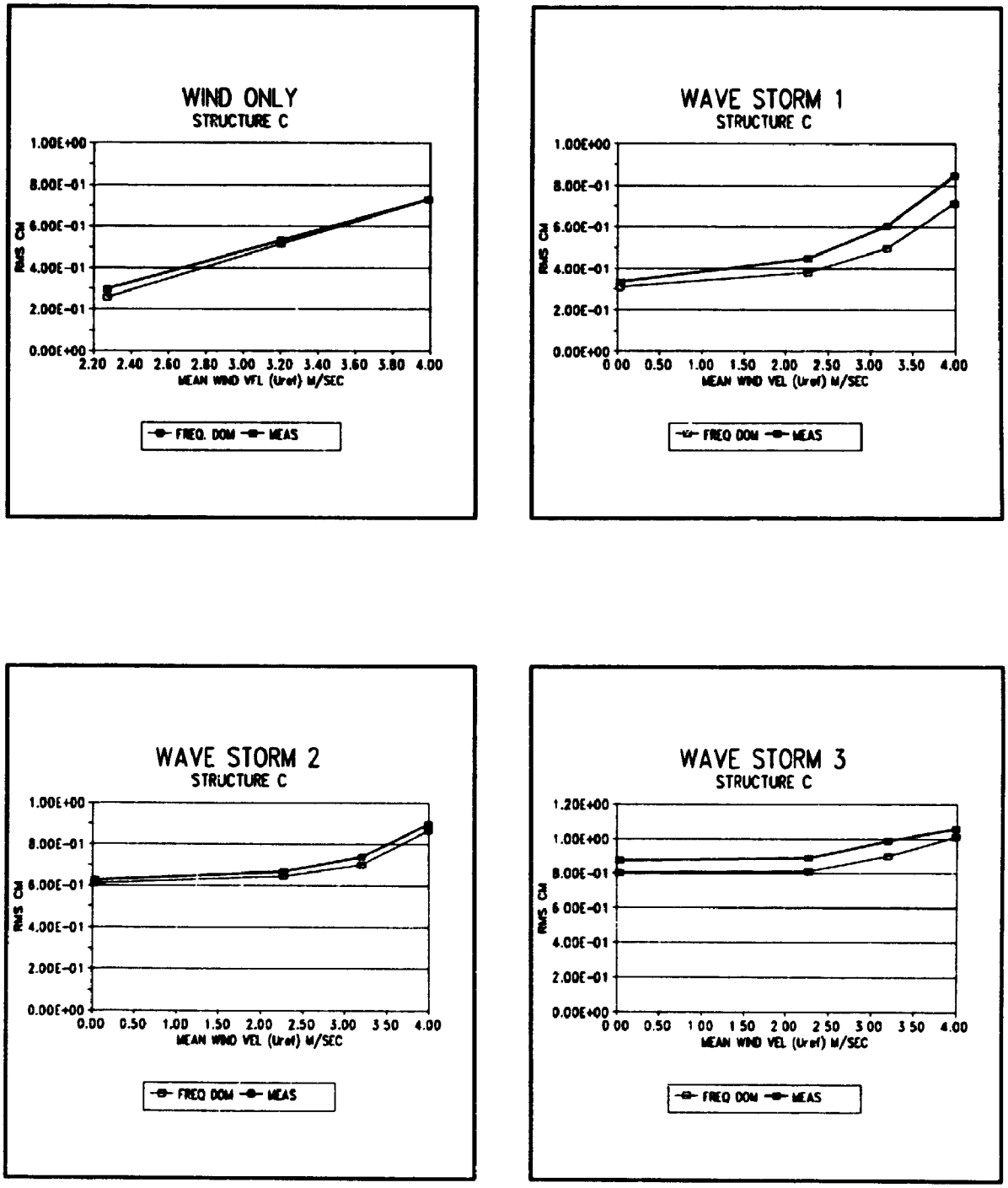

FIGURE 4.63: Comparison of frequency domain results with the measured results (structure C)

4.6.6 COMPARISON OF THE EXPERIMENTAL RESULTS FOR THE THREE STRUCTURAL CONFIGURATIONS

The three structural configurations used are only different in their aerodynamic properties (topsides), i.e., the platform volume/area is different among them. Their volume and windward area are respectively, A(337.36 cm^3,53.55 cm^2), B(557.6 cm^3, 68. cm^2), and C(867.0 cm^3, 85.0 cm^2).

Figure 4.64 to 4.67 show the variation of rms response vs. wind speed for the three structural configurations. As can be observed, structure A has generally smaller rms response compared to structures B, and C. In higher seas the difference in response is smaller (about 3%) which is related to the increased hydrodynamic damping. However, in smaller seas the difference is more pronounced. Overall, optimizing (i.e. reducing) the platform size in order to reduce the response, might not be so beneficial in higher sea states. Since the structure is designed to withstand the extreme wind and wave loads based on a return period of 50 years or so, the cost of streamlining the platform to reduce drag, might make the process of optimization uneconomical.

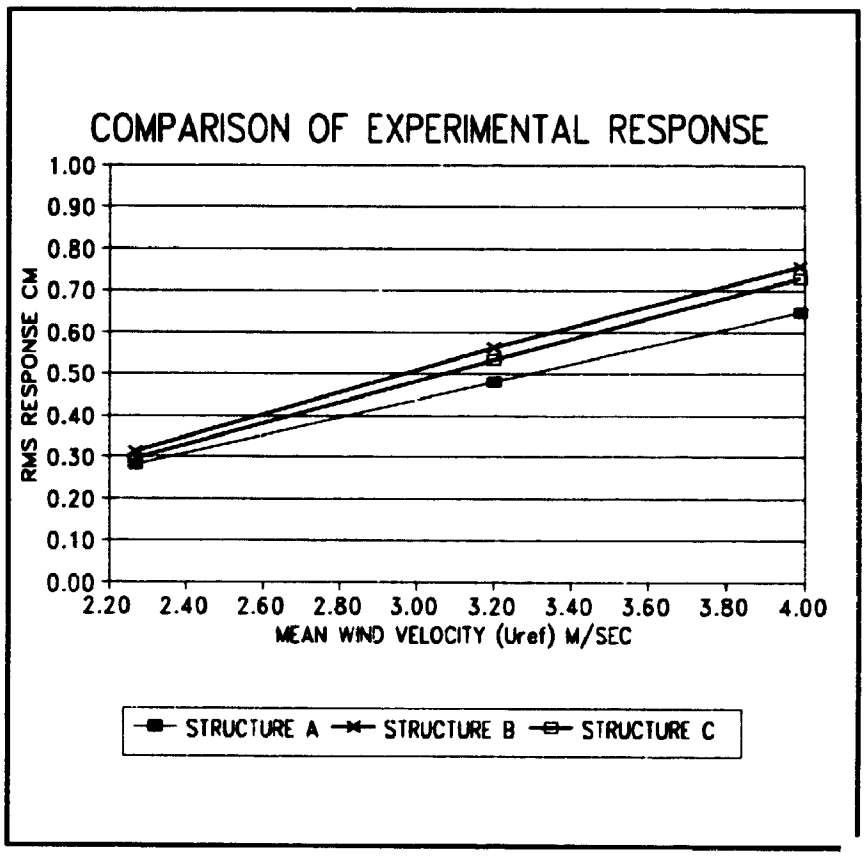

FIGURE 4.64: Measure rms surge response vs wind speed for structures A,B,C (WIND ONLY).

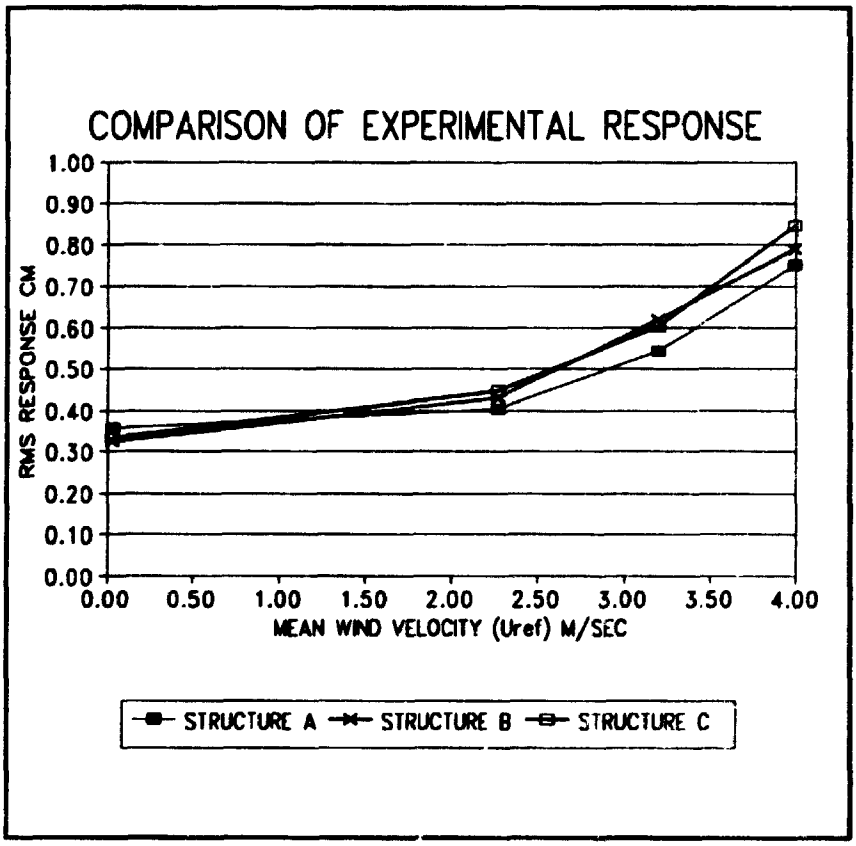

FIGURE 4.65: Measured rms surge response vs wind speed for structures A,B,C (WAVE STORM 1).

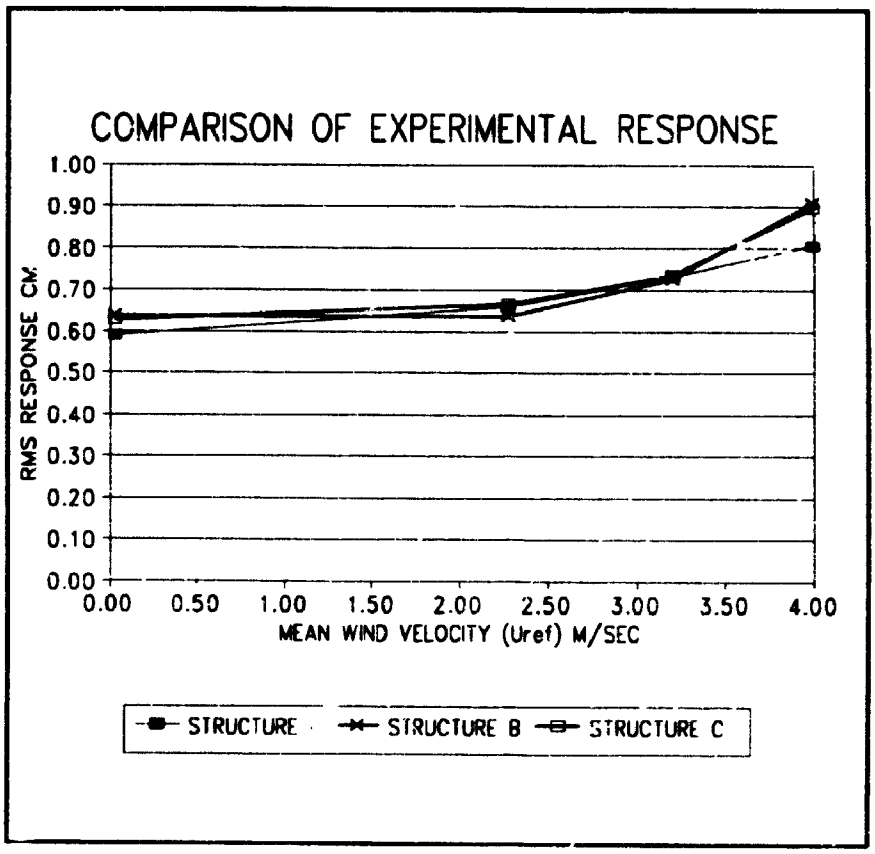

FIGURE 4.66: Measured rms surge response vs wind speed for structures A,B and C (wave storm 2).

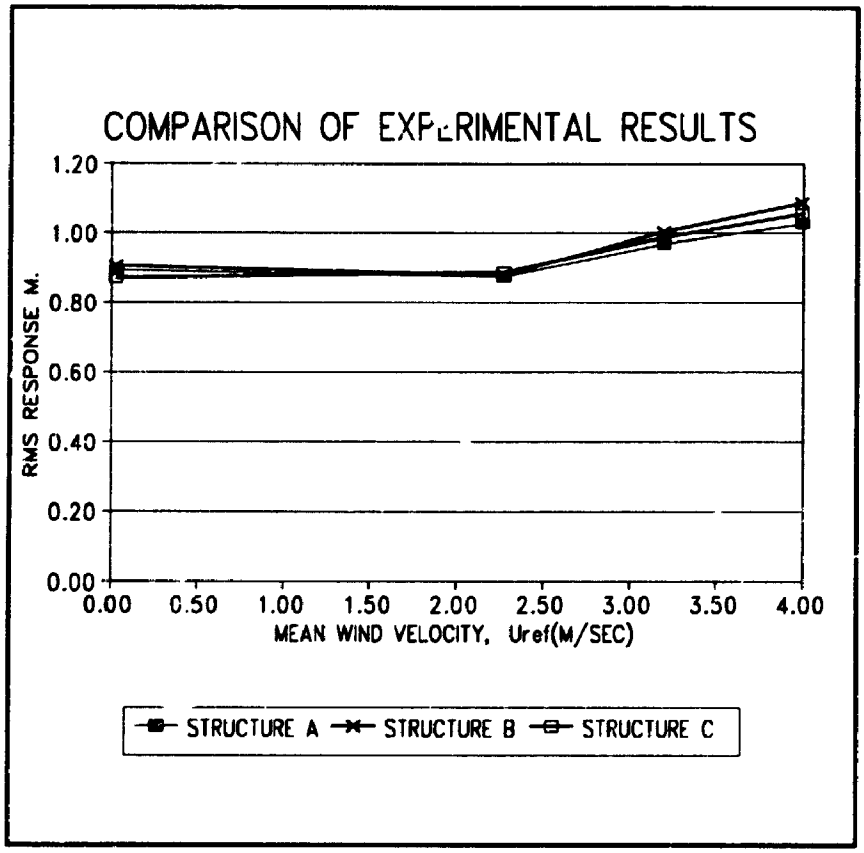

FIGURE 4.67: Comparison of rms surge response vs wind speed fcr structures A,B,C (WAVE STORM 3)

4.6.7 EFFECT OF REDUCING THE FUNDAMENTAL FREQUENCY

The model response was numerically predicted for four different fundamental structural frequencies. The idea was to observe the relative importance of the wave, wind, and free surface drift forces in the response as the fundamental structural frequency is reduced. The structural configuration B and sea state 32 (wave storm 3, wind storm 2) were typically used in the analysis.

In order to increase the natural period, only the mass was increased (near the nodal position of the second mode, node number 8 in Figure 3.2) and the stiffness was kept constant. The achieved natural periods are T_1=2.65 Sec (original model), T_1=3.10 Sec, T_1=3.59 Sec, and T_1=4.08 S. Figure 4.68 shows the predicted surge response spectra. With the decrease of the natural frequency, the low frequency part of the response exceeds the wave frequency part of the response. Also, the lower the natural frequency, the more pronounced the contribution of the free surface forces would be. Figure 4.69 shows the rms surge response vs the natural period. It is observed that the total response decreases as the natural frequency decreases. This behaviour is mostly related to the variation of structural admittance function. In Figure 4.70, the low frequency and wave frequency parts of the response vs natural period is presented. Again, it is observed that the wave frequency response is decreasing with increasing of the natural periods. Also, the effect of the free surface forces becomes more pronounced as the natural period increases. The same C_D and C_M were used in these analyses, and the change in C_D due to the relative importance of resonance and wave parts of the response has not been considered.

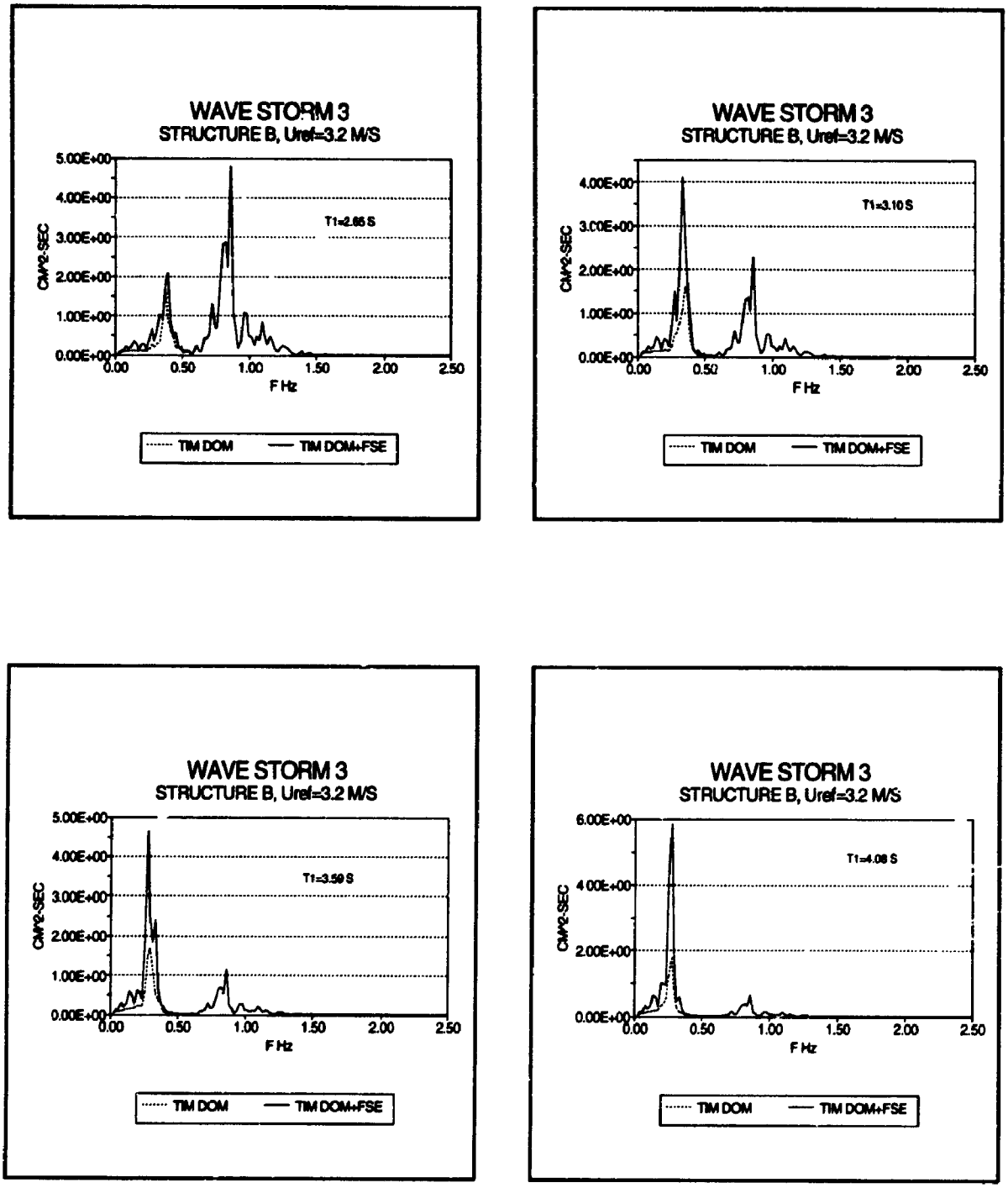

FIGURE 4.68: Predicted rms surge response for sea state 32 and structural configuration B (time domain analysis with and without the inclustion of free surface effect). T_1 is the fundamental period of model.

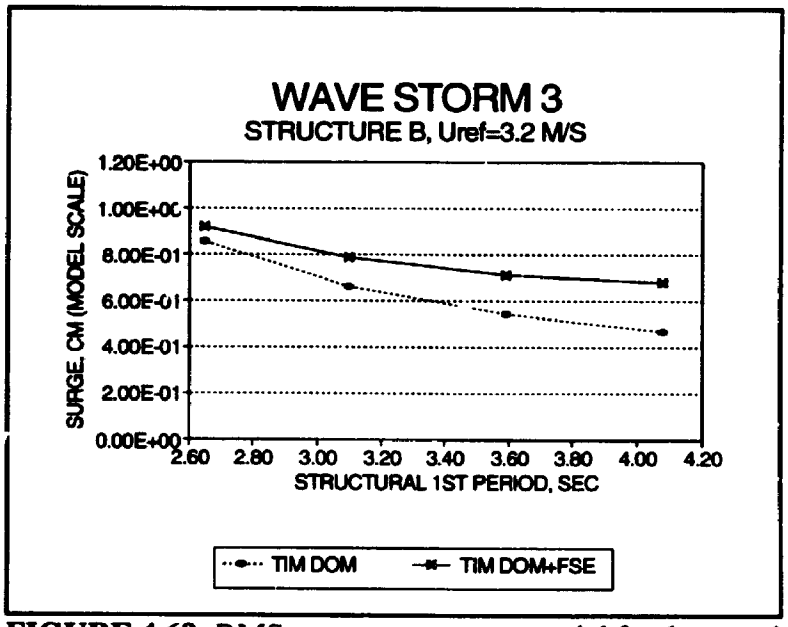

FIGURE 4.69: RMS surge response vs model fundamental period.

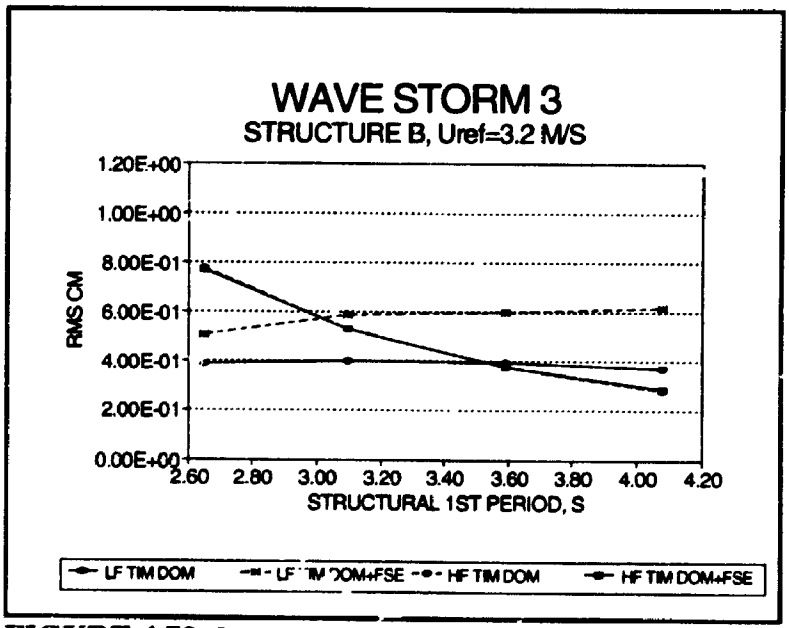

FIGURE 4.70: Low (resonance) and wave frequency parts of the response vs model fundamental period

CHAPTER 5
CONCLUSIONS AND RECOMMENDATIONS

Although Compliant Towers have been studied extensively over the past decade, this study represents an attempt to consider the response due to both wind and wave loads. In this work the contribution of the group induced drift free surface forces was included in the analytical model.

The study included three types of analytical models to predict the surge response (frequency domain, time domain without inclusion of free surface effect, time domain with inclusion of free surface effect), and the results of these models were compared to experimental results obtained in the wind/wave facility at the BLWTL, University of Western Ontario.

5.1 SUMMARY

The study consists of three main parts:

1. Analysis of damping was made using a surface piercing cylinder supported from a heavy three point pendulum moving just above the water surface. The force and displacement time histories (free vibration) were recorded for a variety of both regular and random waves and the amplitude dependent damping forces evaluated. The experimental values are compared with those predicted using a Morison type equation applied to both the relative and the independent flow fields associated with the wave and the cylinder motions. The force coefficients in the Morison equation in monochromatic motion, i.e. surge test and fixed cylinder test were also measured for the range of KC_m and Re numbers encountered in the damping test. The force

coefficients obtained are used to predict the force and displacement response of the model.

2. The study of drag induced drift forces was made using the same instrumentation described in step 1. The forces on the surface piercing cylinder were measured for a variety of bichromatic waves (11 groups) and 3 different wave storms. The results were compared to the prediction made based on Chakrabarti's second order wave kinematic model as well as the modified Airy's wave theory (constant velocity field in the waterline zone). The comparison was made both in time and frequency domains.

Also, using an approximate analysis the contribution of the natural bounded long waves to the drag induced drift forces was investigated.

3. Using the relative velocity form of the Morison's equation, the results obtained from the above steps were then employed to predict the response of the scaled model (1:150) of a simple cantilever compliant tower to different wind/wave states in both frequency (linearized load) and stochastic time domain. The nonlinear drag force was considered in combination with the dynamic wind and free surface drift effects. Finally, the theoretical response is compared with the experimental results obtained in the wind/wave facility where the model was subjected to the combined action of the scaled random wave and wind loadings. The model test program consisted of three platforms (sizes) with the same cantilever structure. The difference among the heads was only in their volume but their mass was the same. The idea was to examine the effectiveness and perhaps improve the dynamic characteristics of the response, by changing the aerodynamic properties of the model while keeping the hydrodynamic properties constant.

5.2 CONCLUSIONS

▸ Using the independent flow fields model reduces the hydrodynamic damping ratio compared to the relative velocity model (for the same C_D) and this by itself increases the resonance part of the response. This effect is more pronounced in higher sea states. The relative velocity model drag coefficient although more difficult in calculation, was found to be a better way of demonstrating the force traces and it was more uniform in the range of the KC_m numbers examined.

▸ Observations of the comparison of the predicted and measured drag induced drift forces show that, these forces are in-phase with the wave groups. It can be concluded that the change in submergence length with the passage of an individual wave is the main contributor in generating the low frequency forces on a slender cylinder (free surface effect).

▸ The comparison of the measured and predicted results based on the Chakrabarti's second order model were performed for both groups and random waves (both in time domain and in frequency domain). The predicted results indicated about 20 to 30 percent overprediction, which is believed to be partly (up to 20%) due to tank reflection at the nominal first order wave frequencies and partly due to the mathematical model (including the uncertainty in the C_D values used).

▸ The activity of parasitic long waves in the wave tank, caused by the first order wave signal, is an experimental difficulty. In a deep water laboratory situation the free displacement waves may be exaggerated by about 5 times compared to the real bounded long waves, but are not a threat to the free surface force measurement.

▸ Using an approximate analysis, in natural sea, the magnitude of the low frequency forcing due to bounded long waves was compared to that of the free surface effect. The results showed that the contribution of the bounded long waves is small (about 10% of free surface effects).

▸ Overall, the rms surge response predictions in both frequency domain and time domain compared well with the experimental results. For a given sea state, the rms surge response increases as the mean wind speed increases and in a mild sea the low frequency response due to wind load exceeds the wave frequency response as the wind grows.

▸For a constant wind, the low frequency part of the response generally decreases with increasing wave heights. In higher seas due to the increased drag induced hydrodynamic damping the significance of the low frequency wind and wave forces are reduced.

▸The low frequency force due to the free surface effect increases the low frequency part of the response and its inclusion improves the agreement between the experimental and analytical (time domain) results in most cases.

▸ The study of the rms response for the three structural configurations A,B, and C showed that reducing the drag force (by streamlining, shrouding or by other means) in order to reduce the response may not be beneficial at higher sea states.

▸ With the decrease of the natural frequency of the tower, the low frequency part of the response exceeds the wave frequency part of the response. Also, the lower the natural frequency, the greater the contribution of the free surface drift forces to the surge response.

5.3 RECOMMENDATIONS FOR FUTURE WORK

Detailed measurement of the velocity profile using Doppler Velocimeter in regular waves in the tank and comparison of the results with linear wave theory and second order Chakrabarti's model, is recommended. This comparison will help to understand the contribution of the tank reflection to the drift forces. Also, the discrepancies between the measured and predicted drift forces can be related since the forces in the model are proportional to H^3.

To improve the quality of experimental results, a complete (first and second order) paddle signal is recommended to remove the parasitic waves.

During the dynamic analyses performed in chapter 3, it was realized that the wind induced current would influence the surge response to some extent. A detailed laboratory measurement is recommended to study the magnitude and distribution of water current in order to determine its significance in the surge response.

APPENDIX A
DYNAMIC ANALYSIS BASED ON GIVEN ANALYTICAL WIND AND WAVE SPECTRA

This appendix presents the lower deck level surge response spectra calculated from time domain and frequency domain analysis methods. The input spectra for simulation of wind and wave loads were adopted from JONSWAP and ESDU. The time domain analysis are performed twice, with and without inclusion of free surface effect.

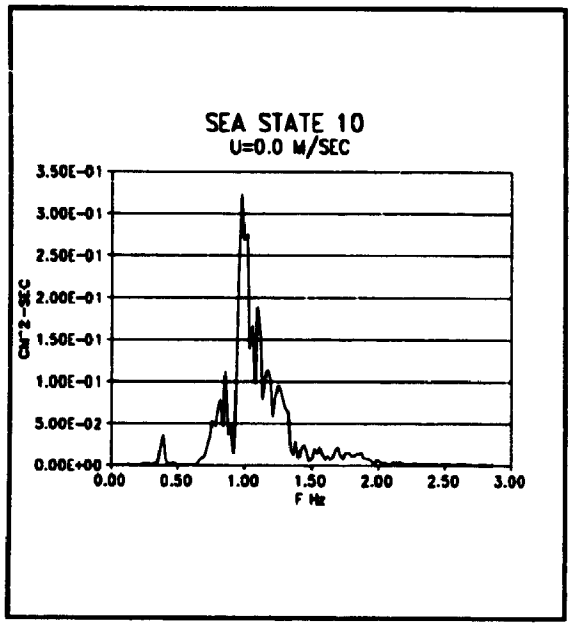

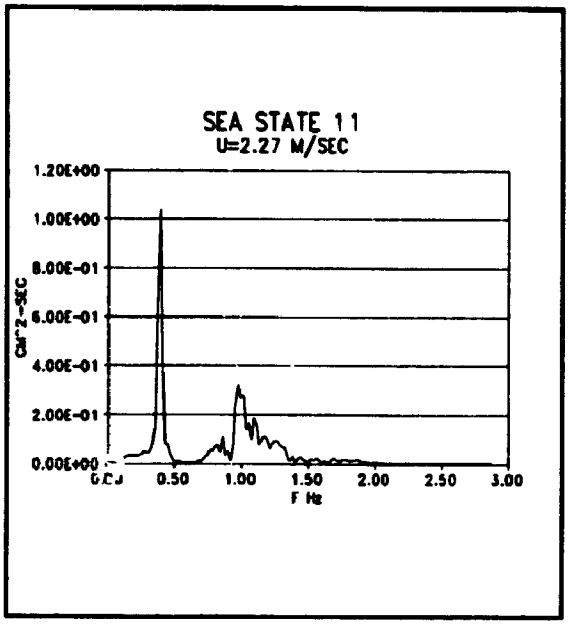

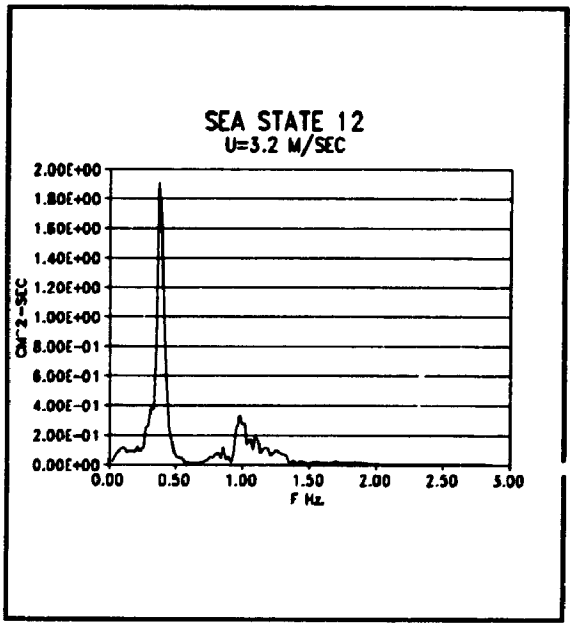

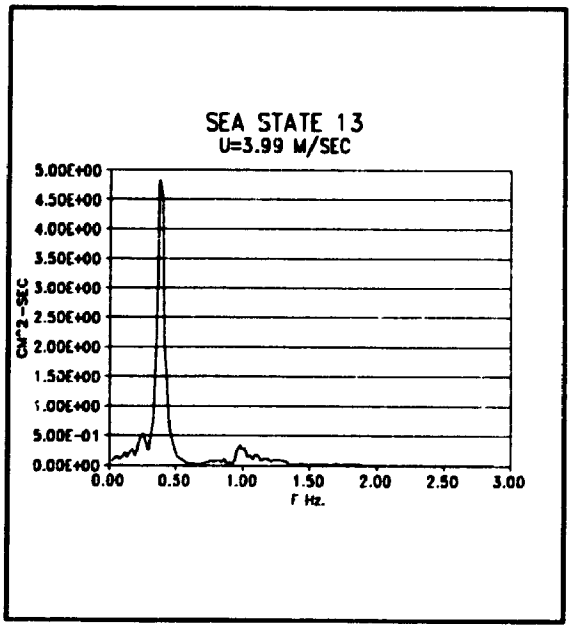

Figure A-1: Surge response spectra for structure B (time domain)

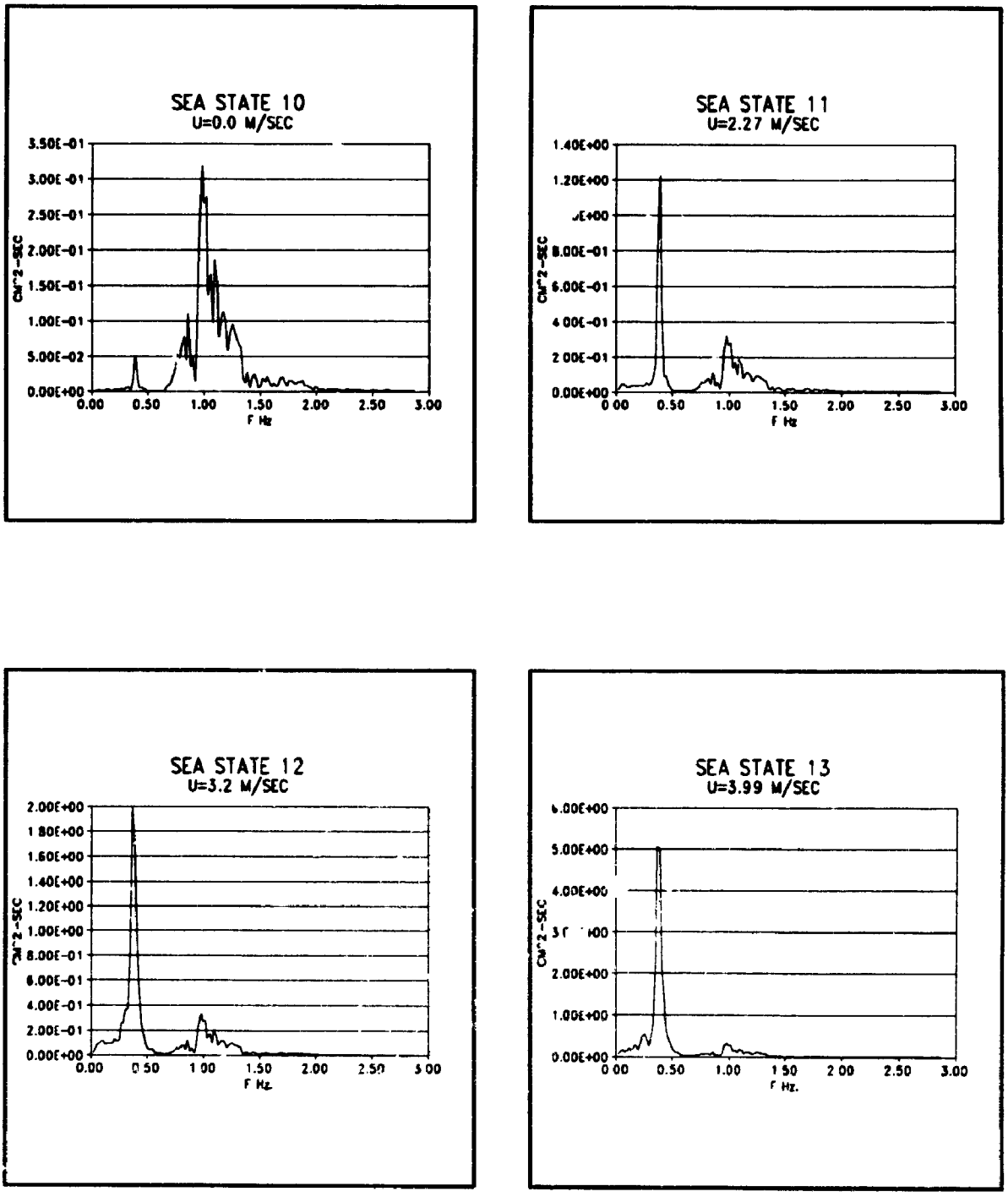

Figure A-2: Surge response spectra for structure B (time domain including surface effect)

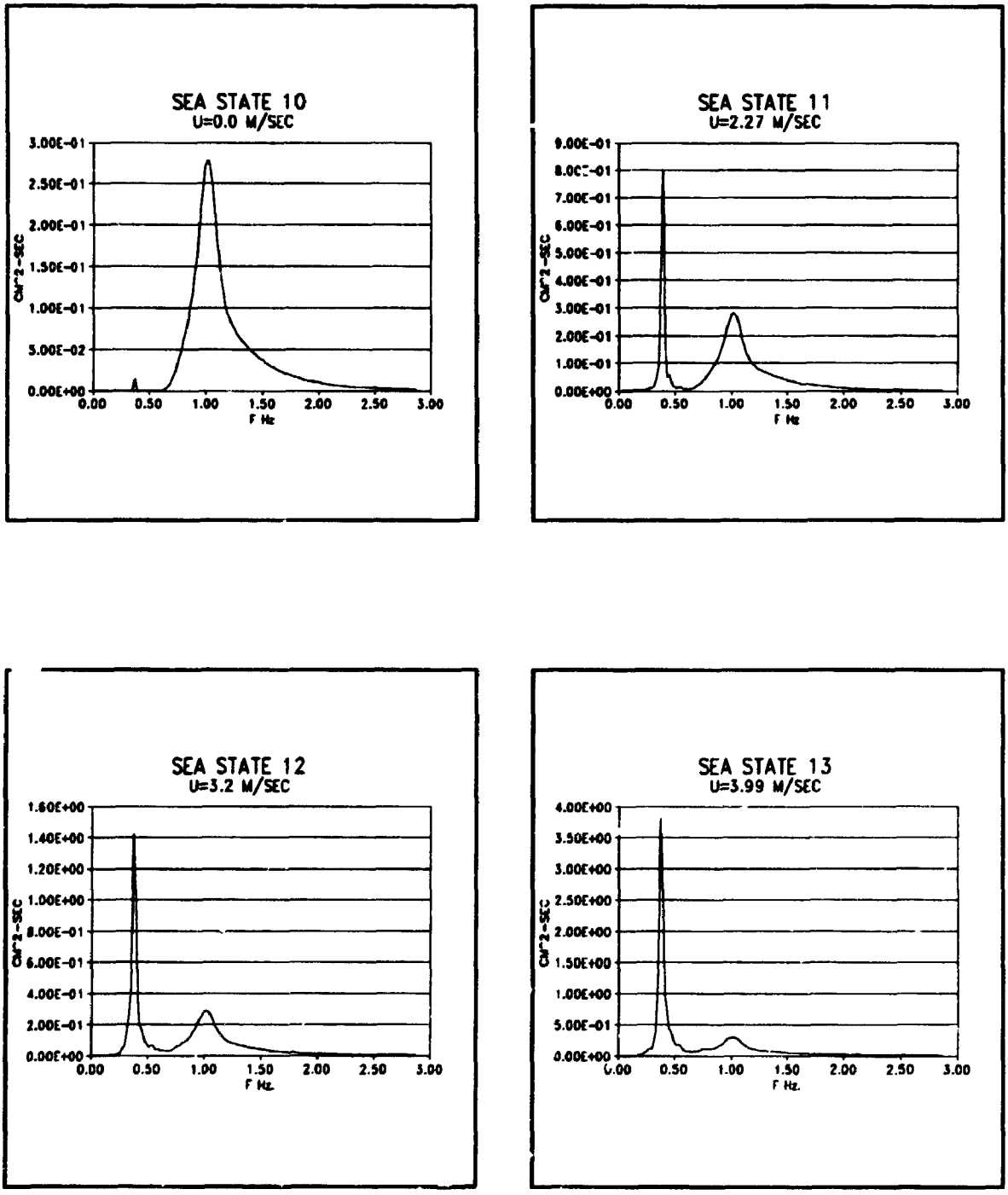

Figure A-3: Surge response spectra for structure B (frequency domain)

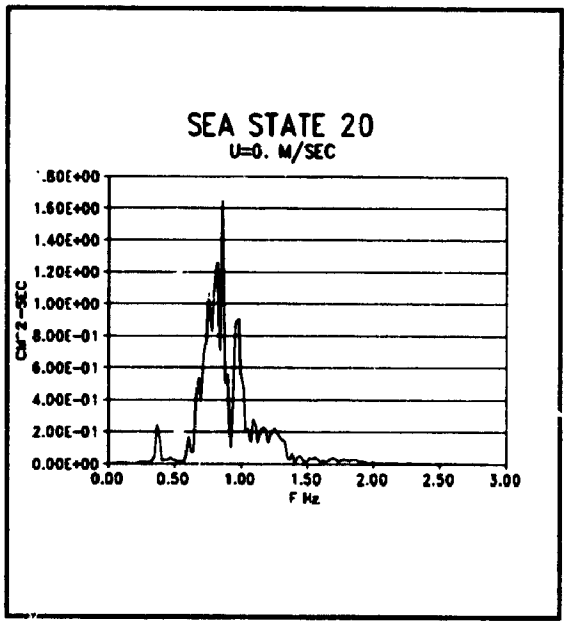

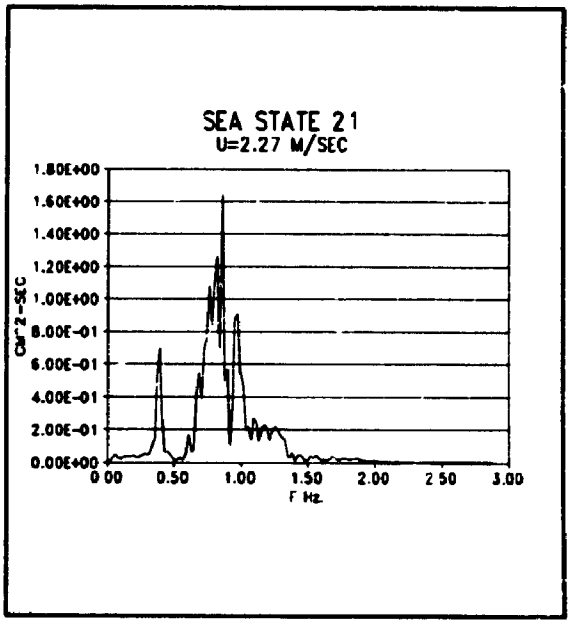

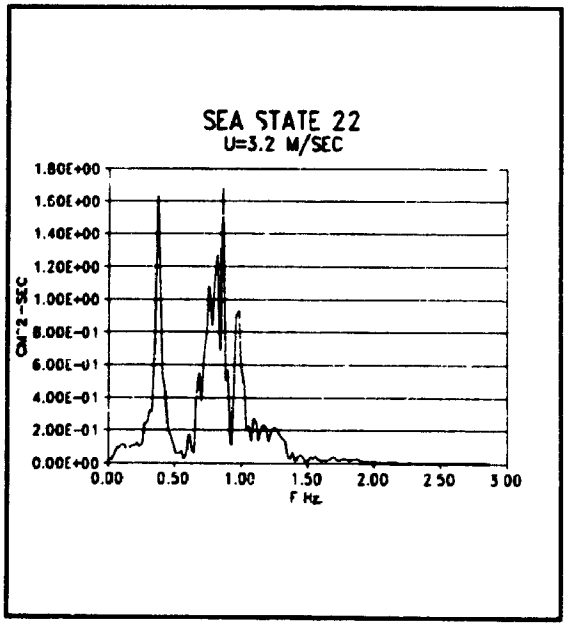

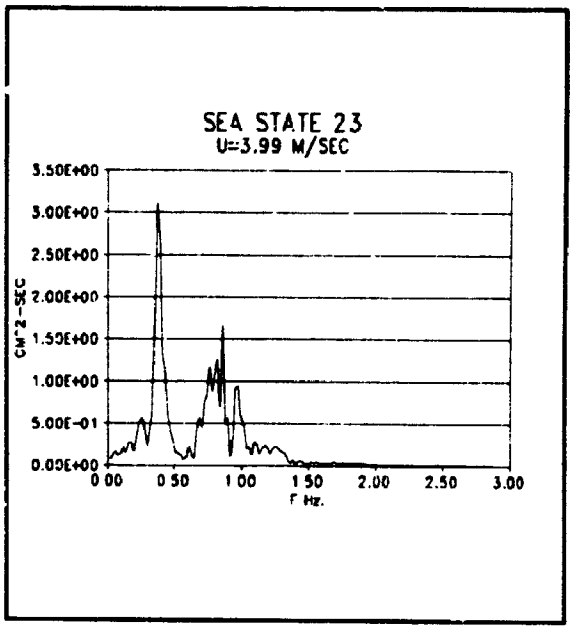

Figure A-4: Surge response spectra for structure B (time domain)

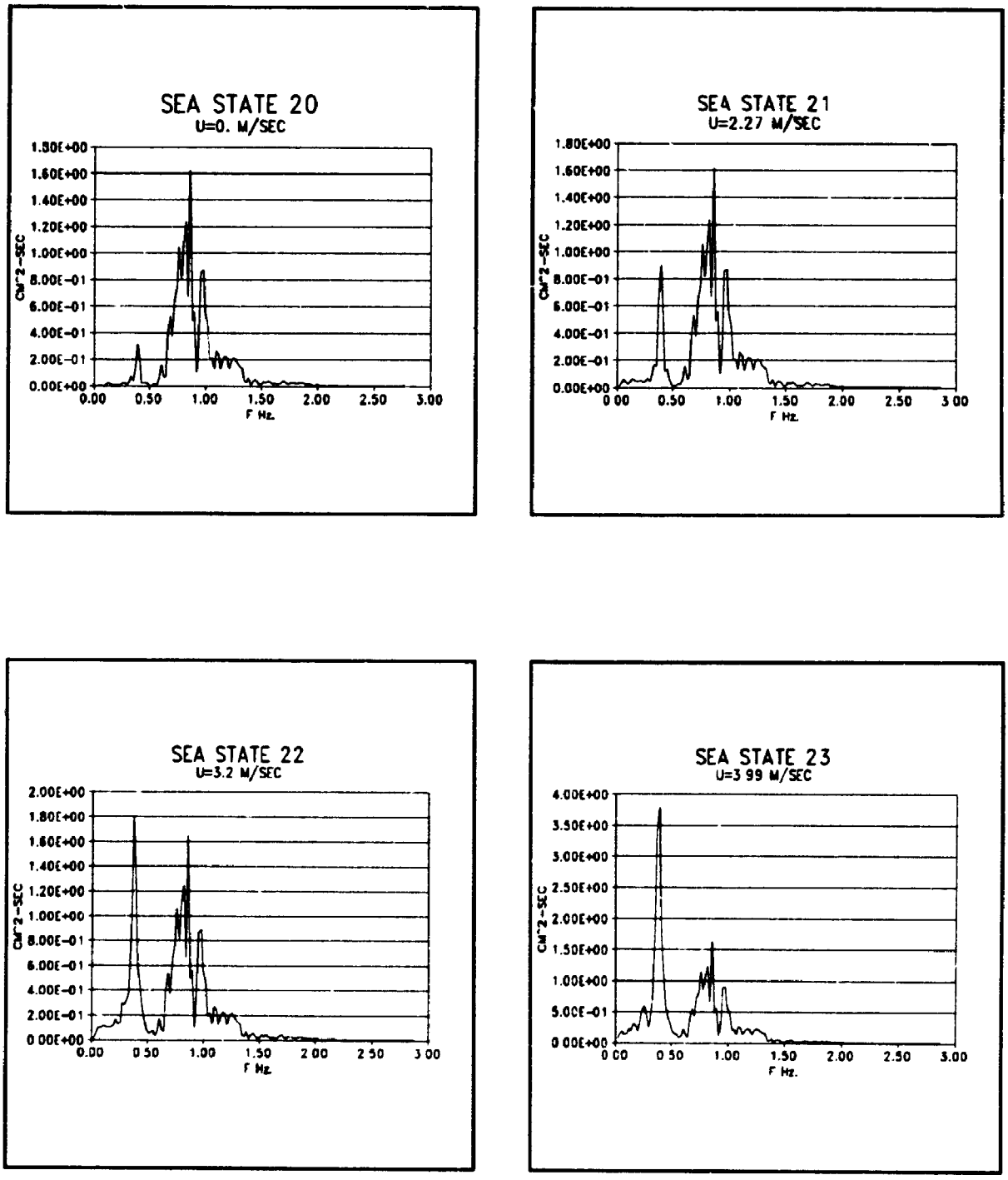

Figure A-5: Surge response spectra for structure B (time domain including surface effect)

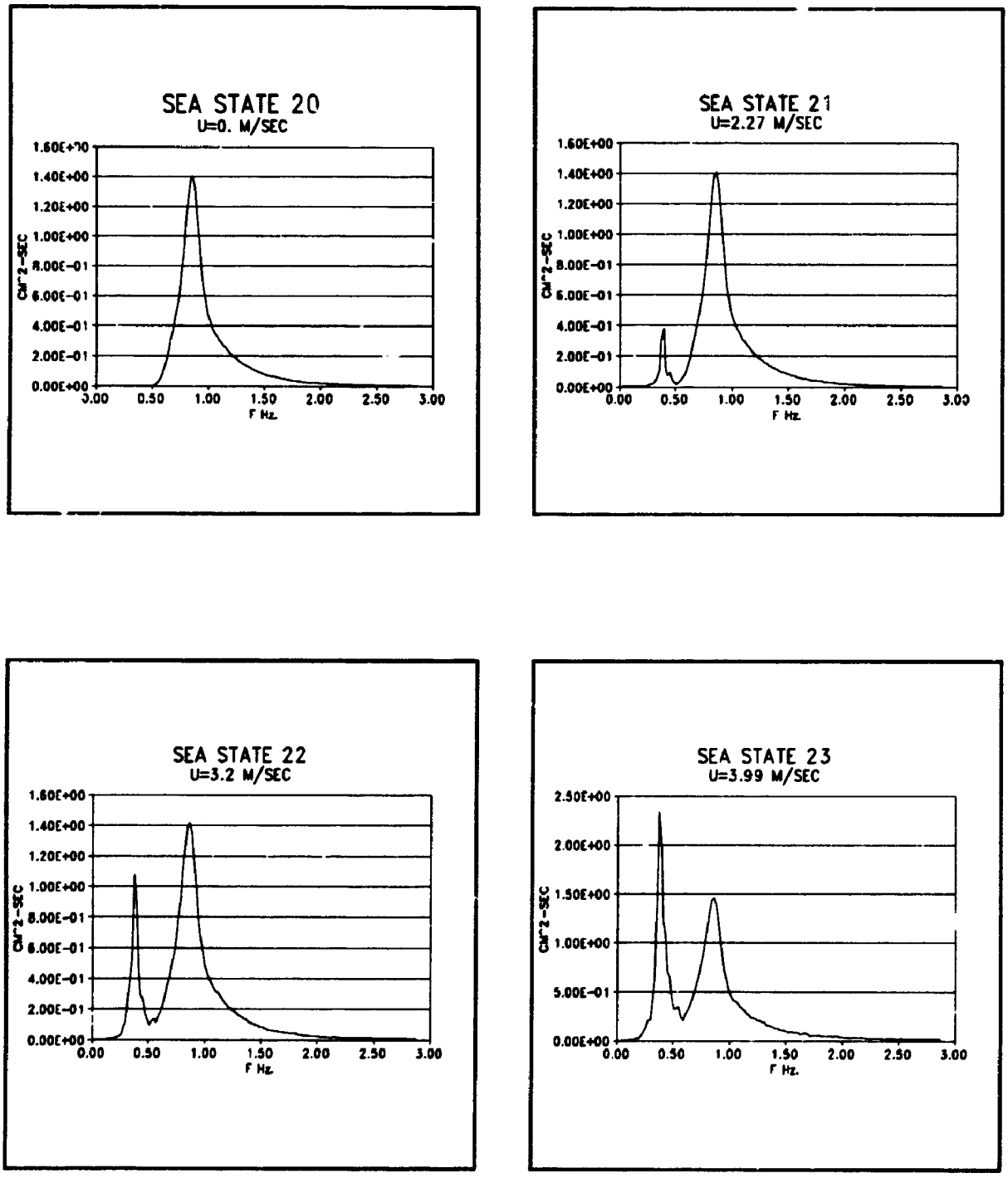

Figure A-6: Surge response spectra for structure B (frequency domain)

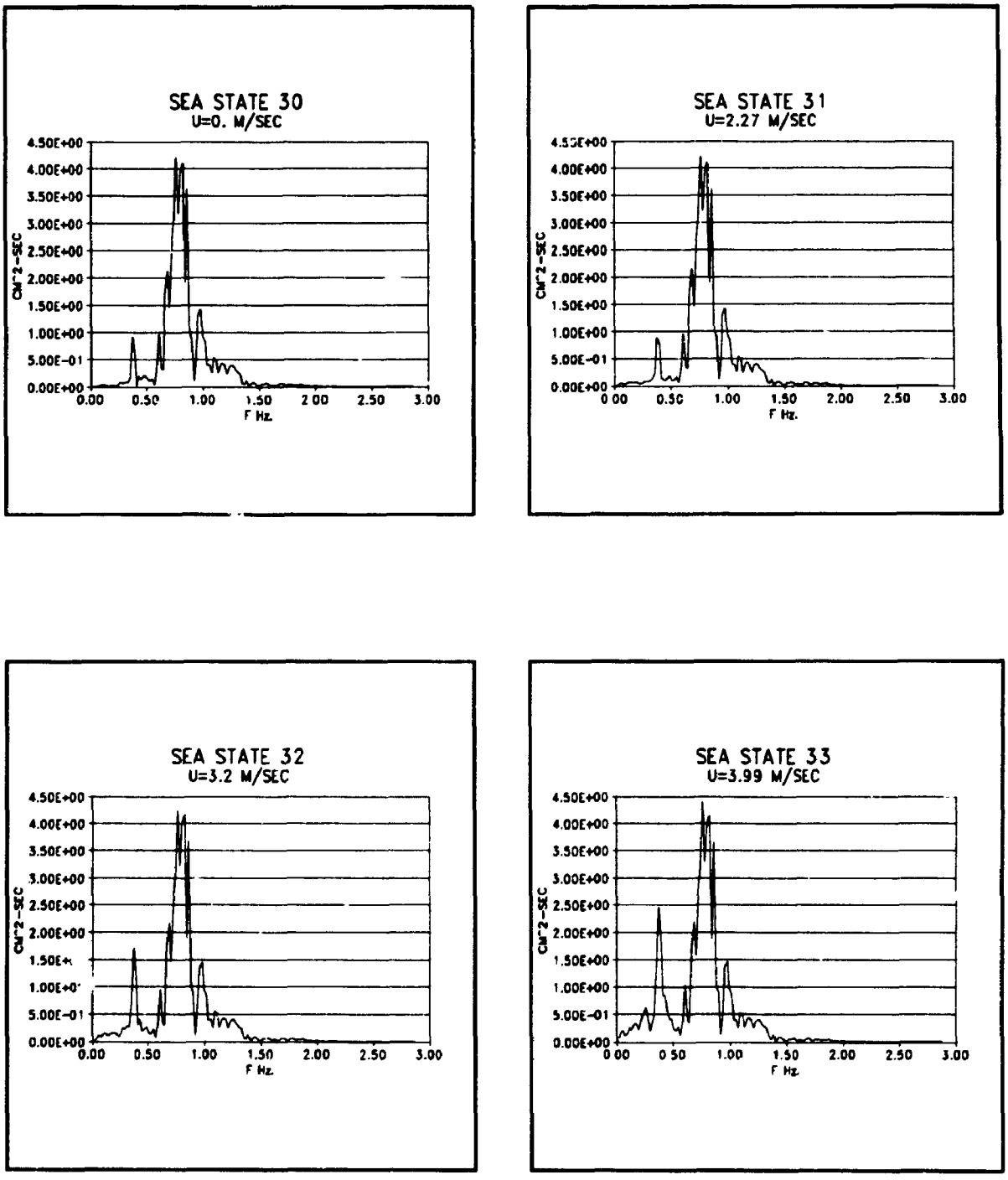

Figure A-7: Surge response spectra for structure B (time domain)

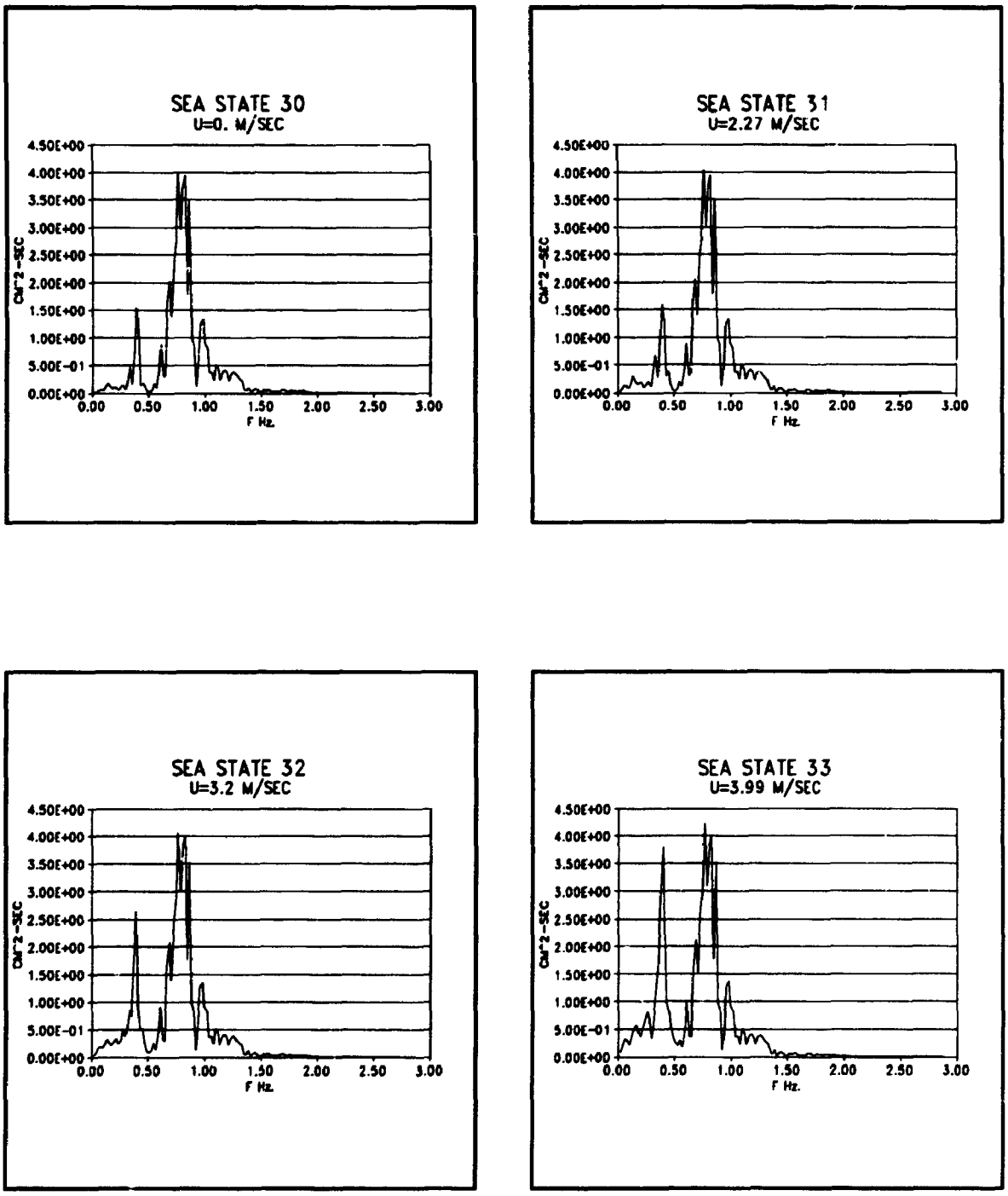

Figure A-8: Surge response spectra for structure B (time domain including surface effect)

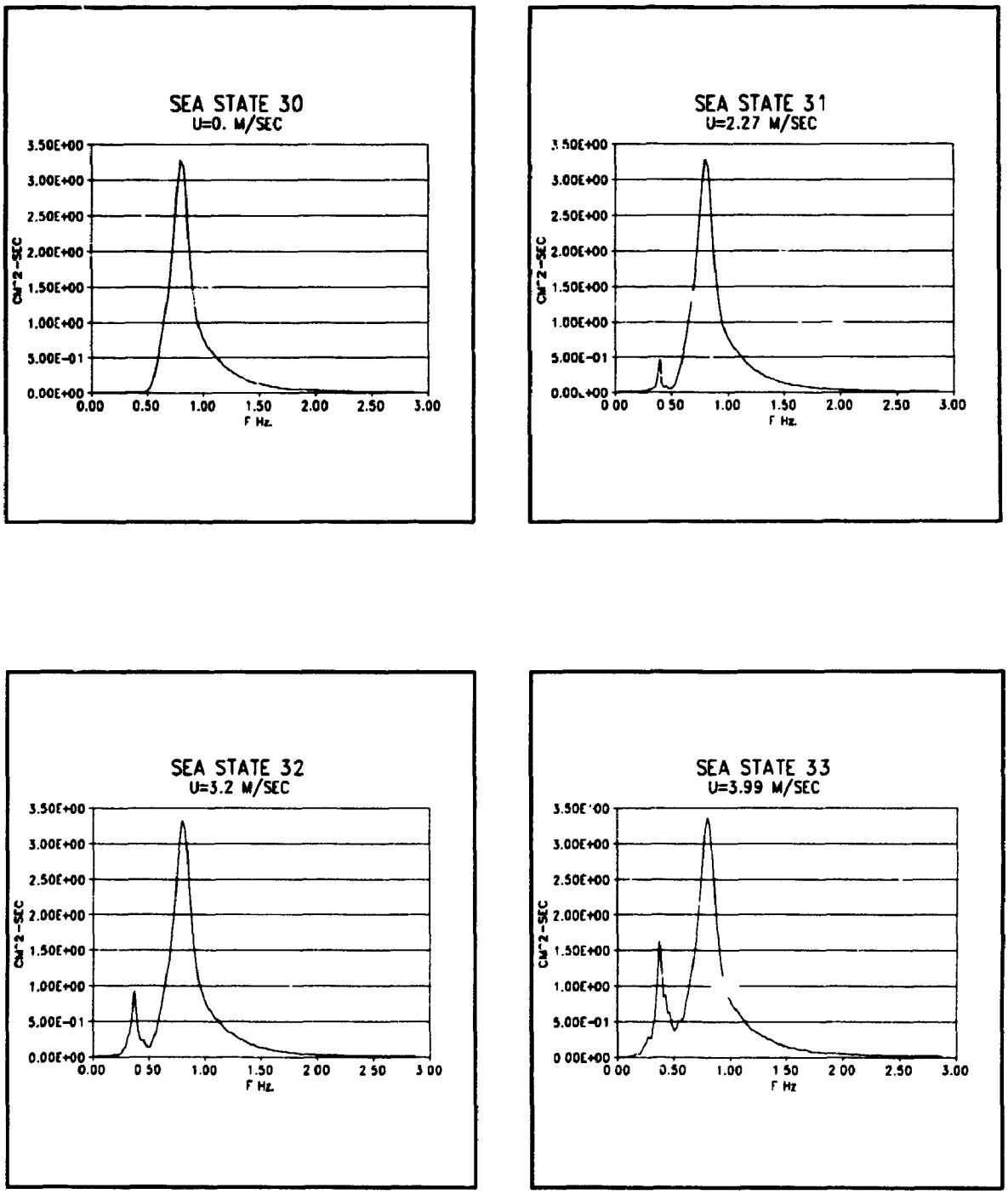

Figure A-9: Surge response spectra for structure B (frequency domain)

APPENDIX B
EFFECT OF UNIFORM CURRENT ON THE WAVE SPECTRA

This appendix presents the lower deck level surge response spectra calculated from time domain analysis. The effect of growing current for different wave storms is shown. The contribution of the drift free surface forces are included.

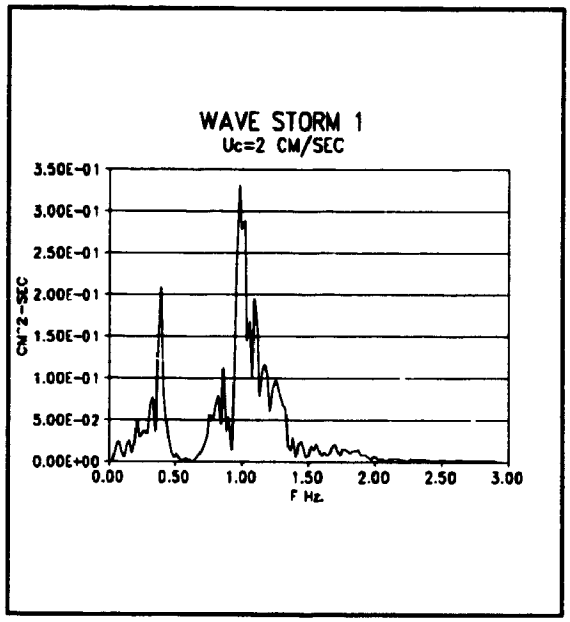

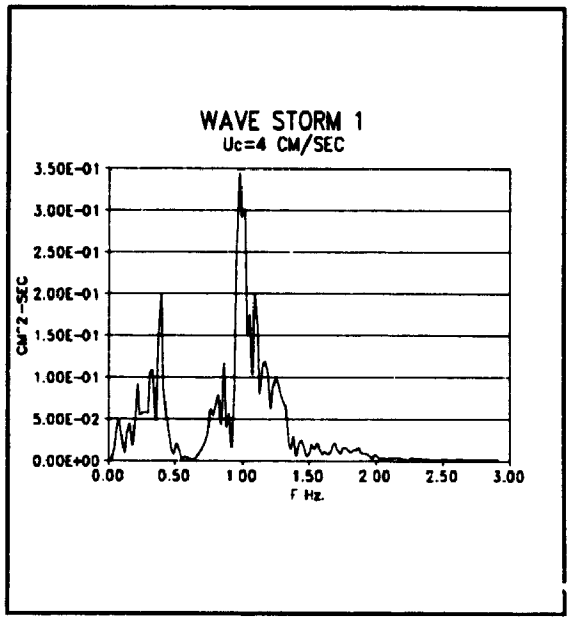

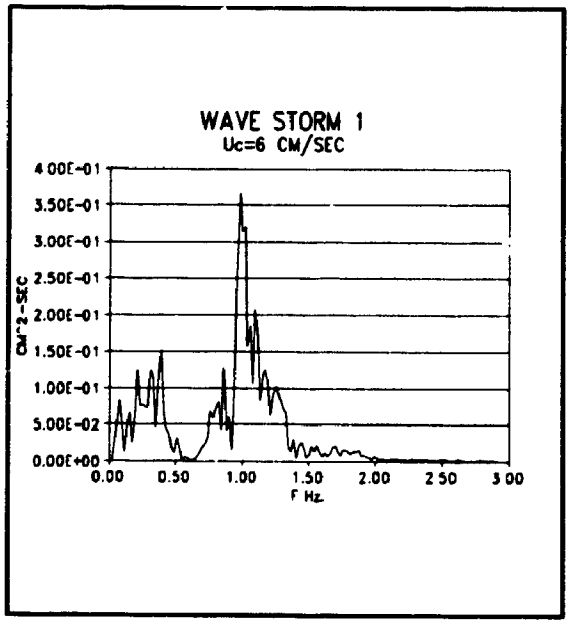

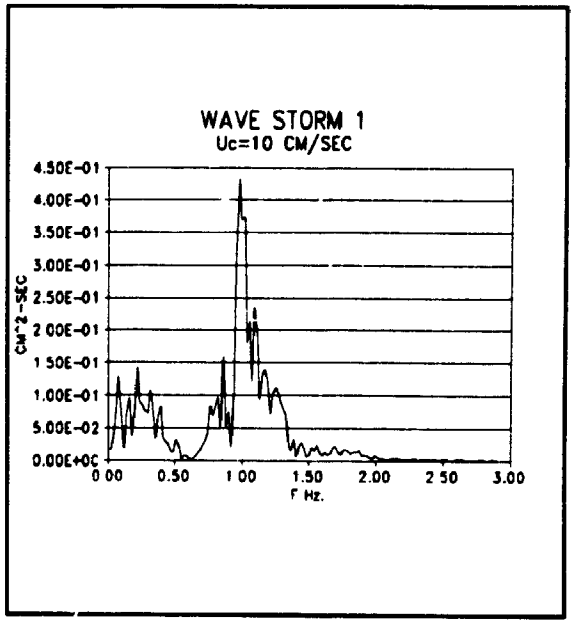

Figure B-1: Surge response spectra for structure B

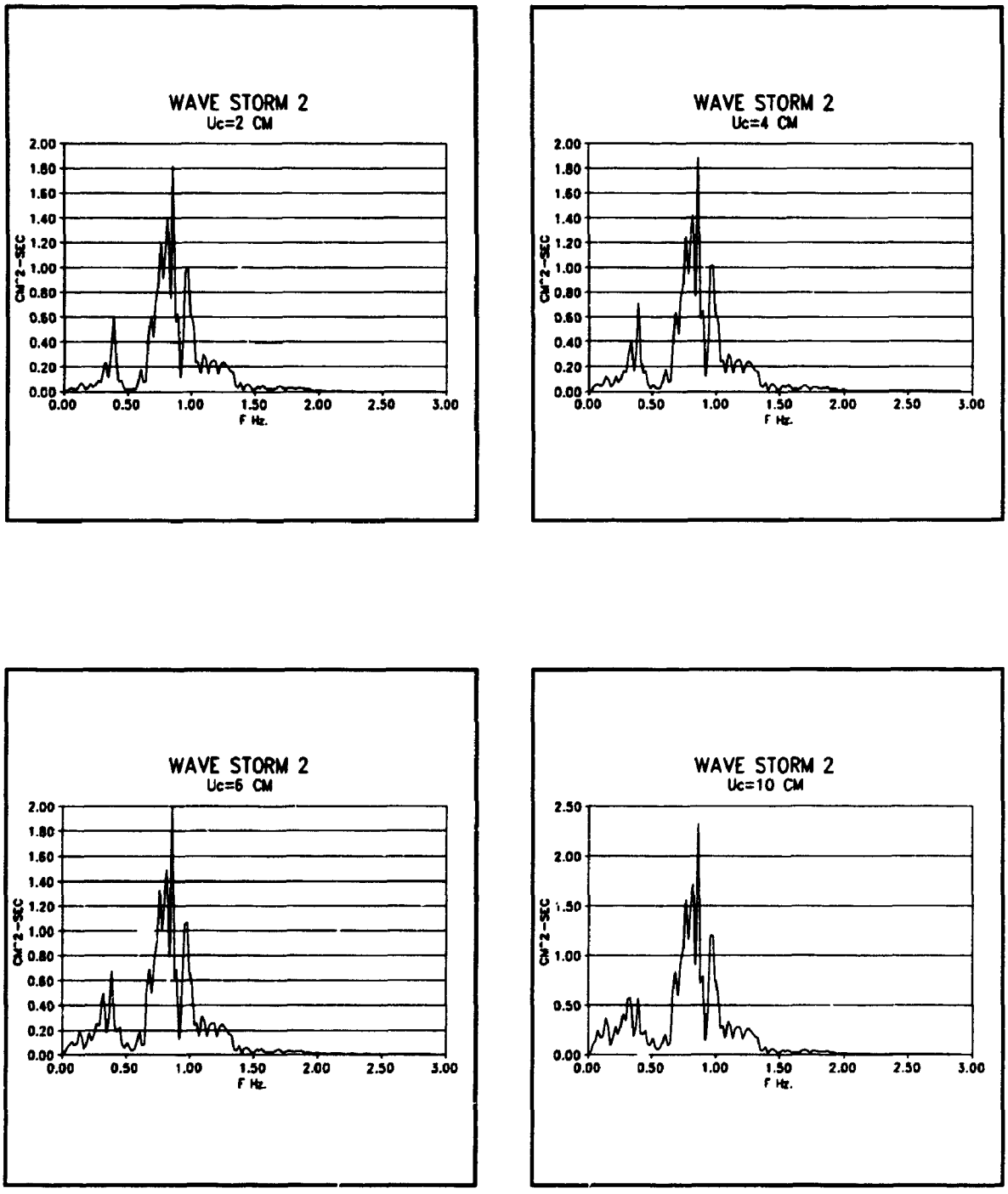

Figure B-2: Surge response spectra for structure B

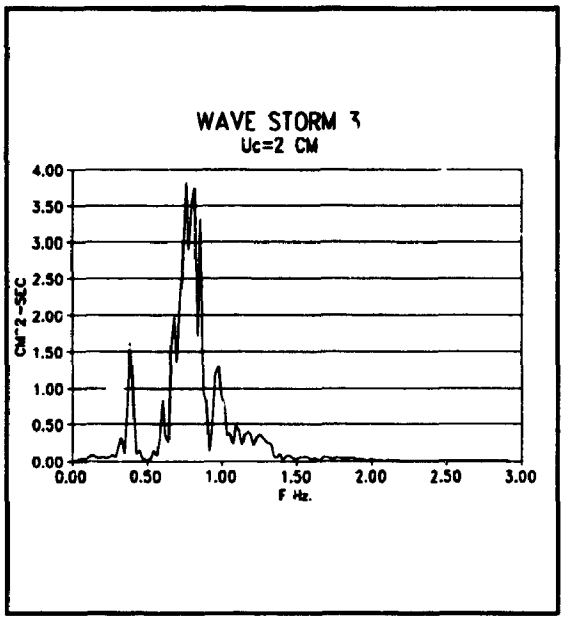

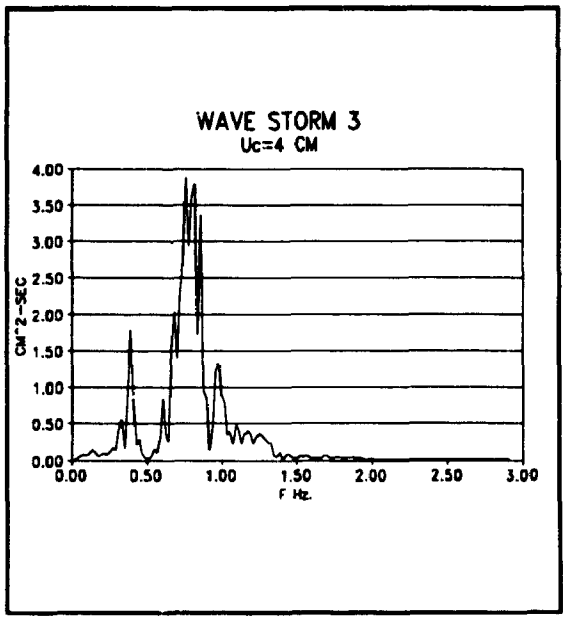

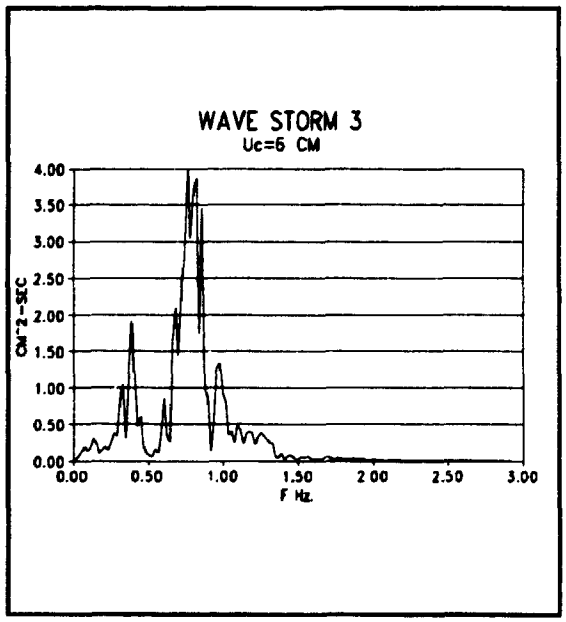

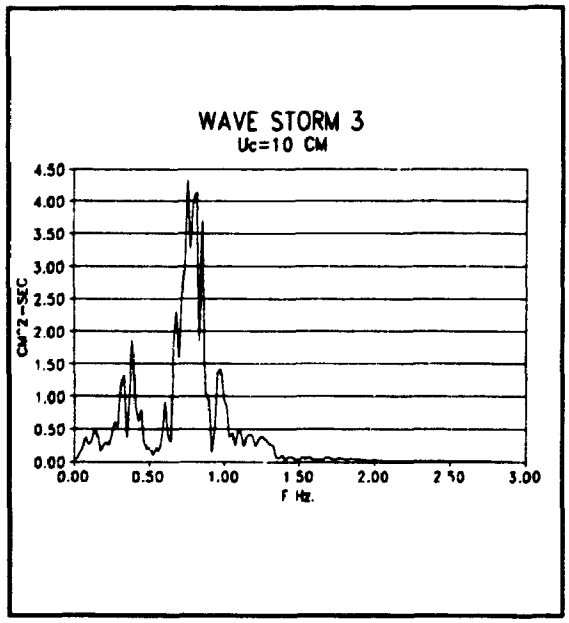

Figure B-3: Surge response spectra for structure B

APPENDIX C

FORCE TIME HISTORY, FIXED CYLINDER IN WAVES

This appendix presents typical time histories of the measured and simulated forces in the case of fixed cylinder in regular waves. The simulation was done using the Morison equation.

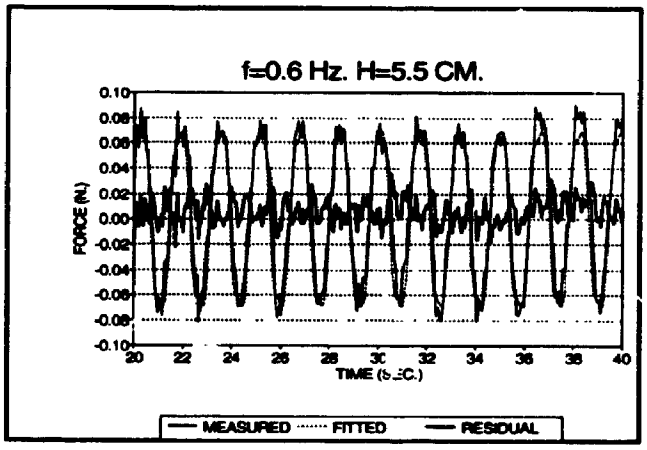

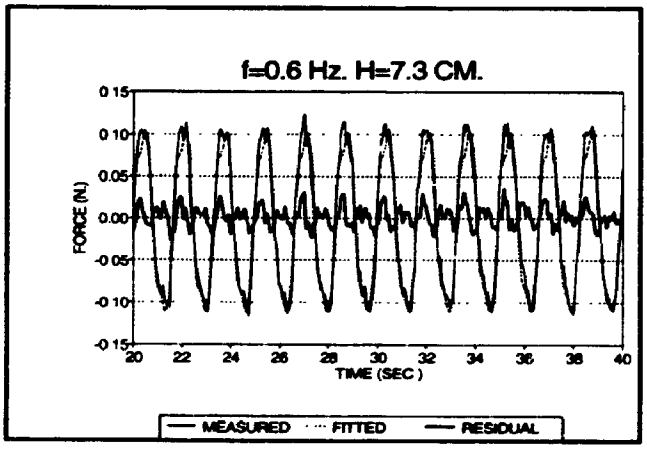

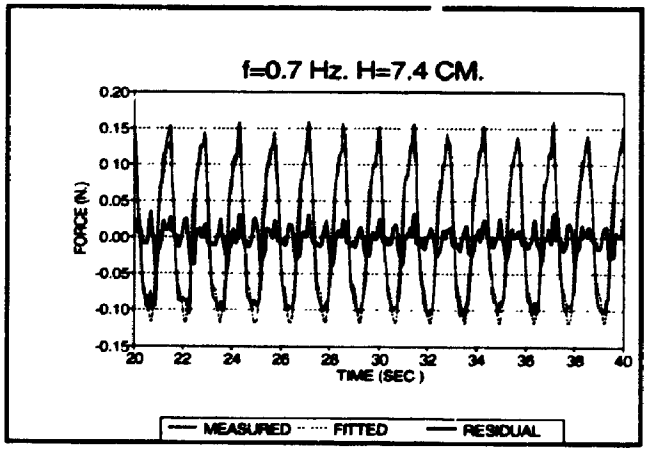

FIGURE C.1: Typical force time histories for the fixed cylinder in waves

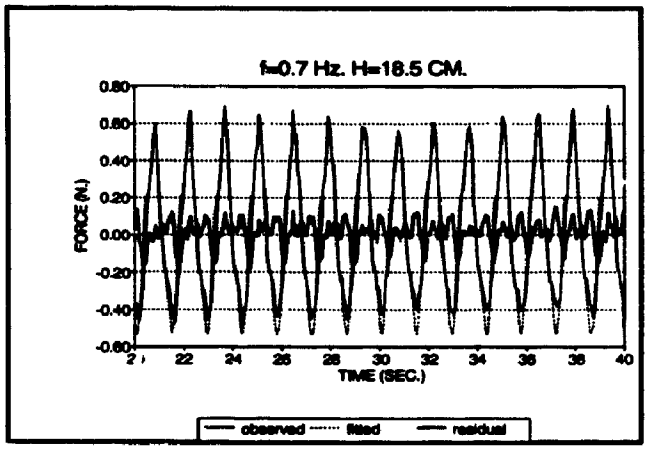

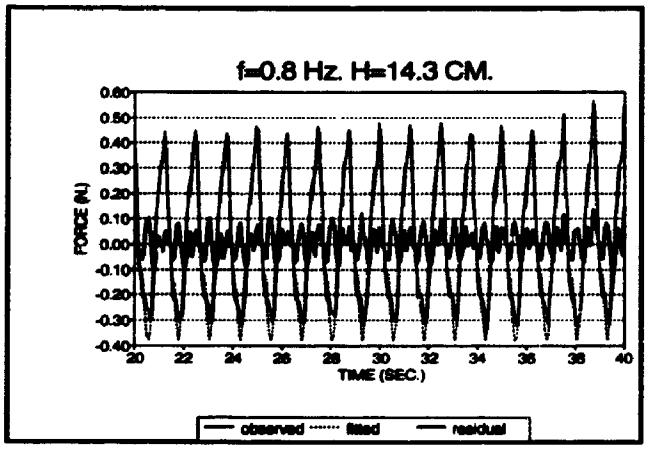

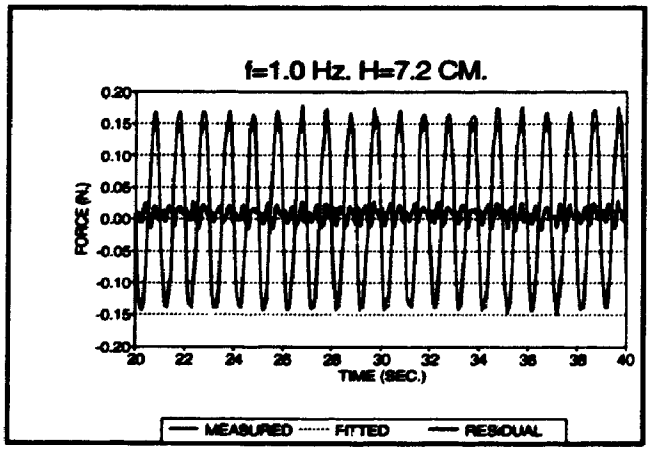

FIGURE C.2: Typical force time histories for the fixed cylinder in regular waves.

APPENDIX D
OSCILLATING CYLINDER IN REGULAR AND RANDOM WAVES

This appendix presents typical measured damping traces, hydrodynamic damping, and drag coefficients derived in the case of oscillating cylinder in regular and random waves. The drag coefficients were derived by using the damping trace as well as by match of the measured force time histories. Results for both relative velocity model as well as independent flow field model are shown.

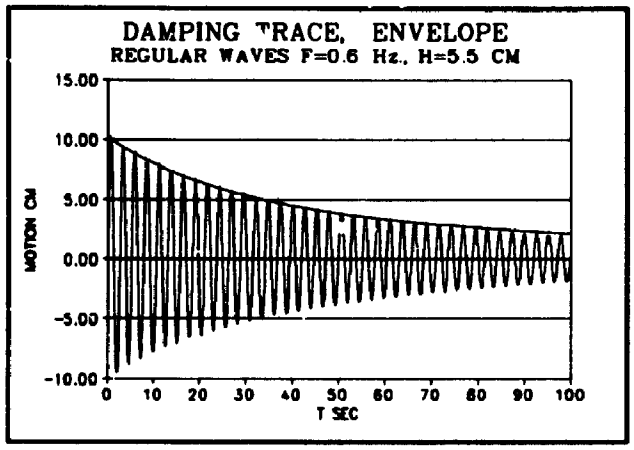

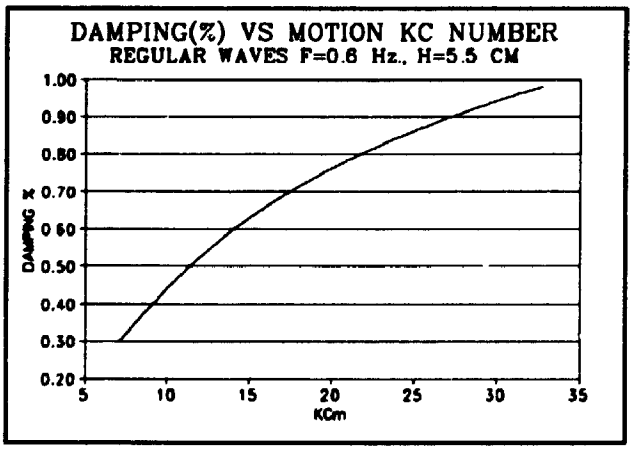

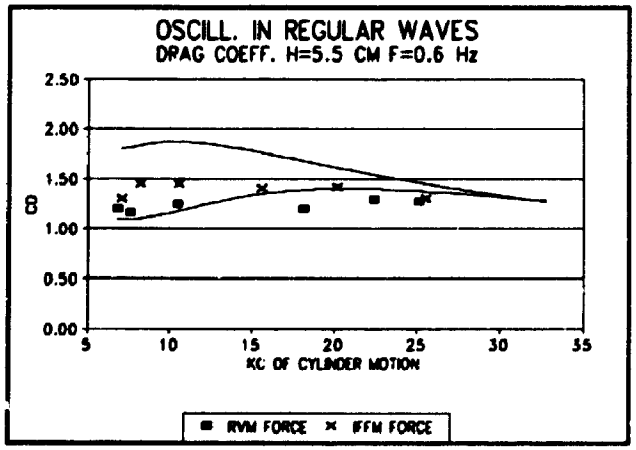

FIGURE D.1: Damping trace, Damping ratio (% of critical), and drag coefficient derived by damping and force measurements using RVM, IFFM in regular waves.

[1] In the bottom Fig. the curves show drag coeff. derived from damping trace. The upper and lower curves represent the results from IFFM, RVM respectively.

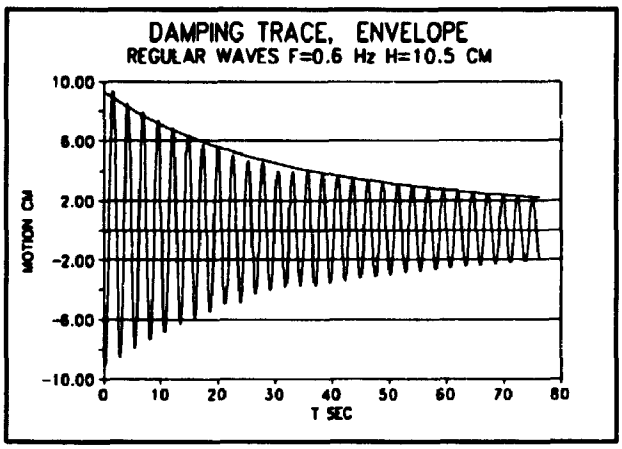

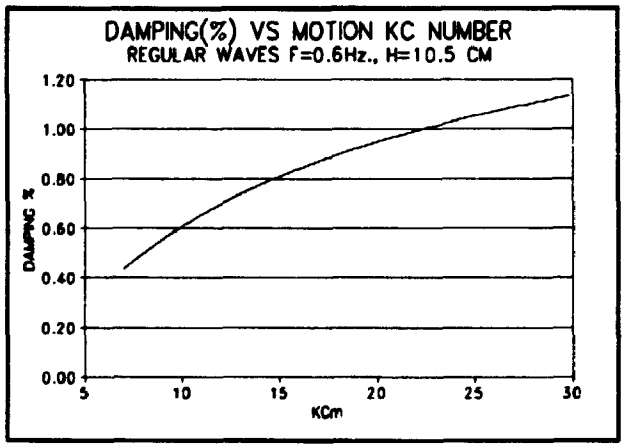

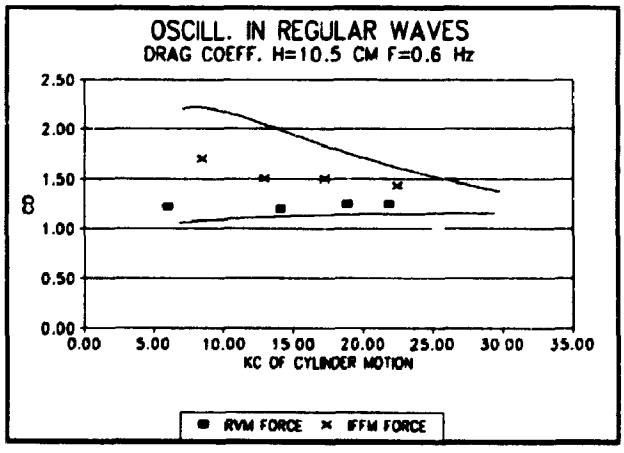

FIGURE D.2: Damping trace, Damping (% of critical), and drag coefficient derived by damping and force measurements using RVM, IFFM in regular waves.

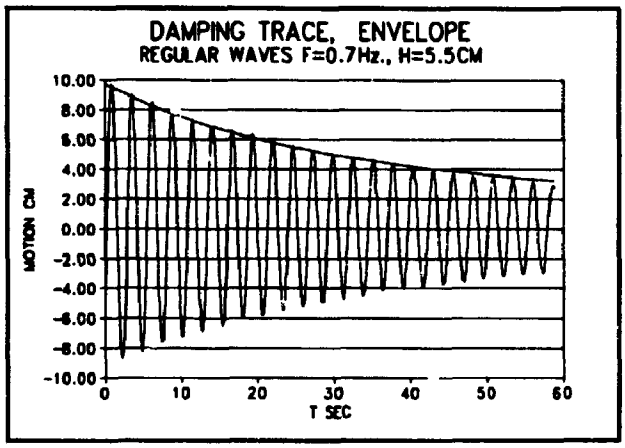

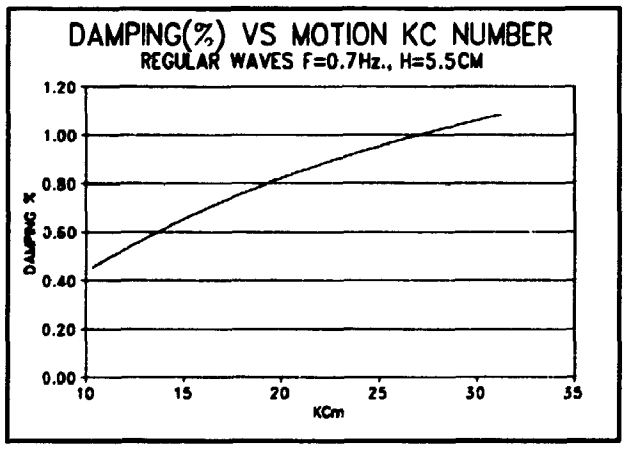

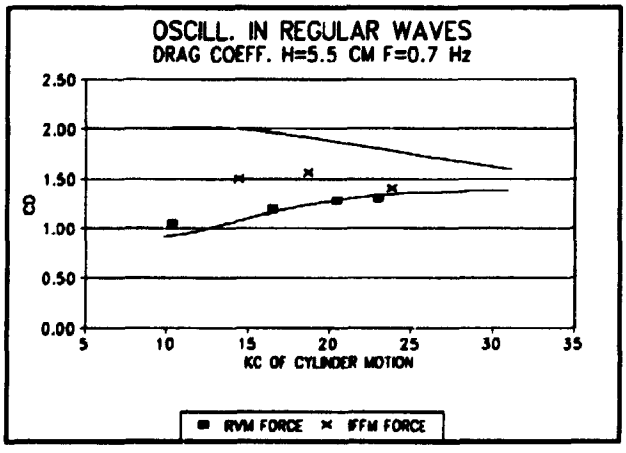

FIGURE D.3: Damping trace, Damping (% of critical), and drag coefficient derived by damping and force measurements using RVM, IFFM in regular waves.

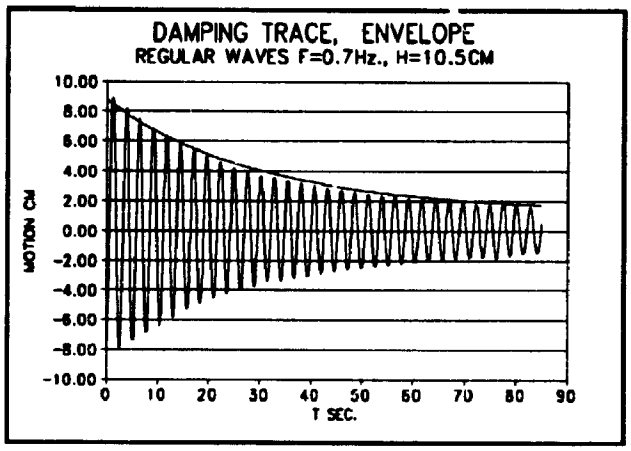

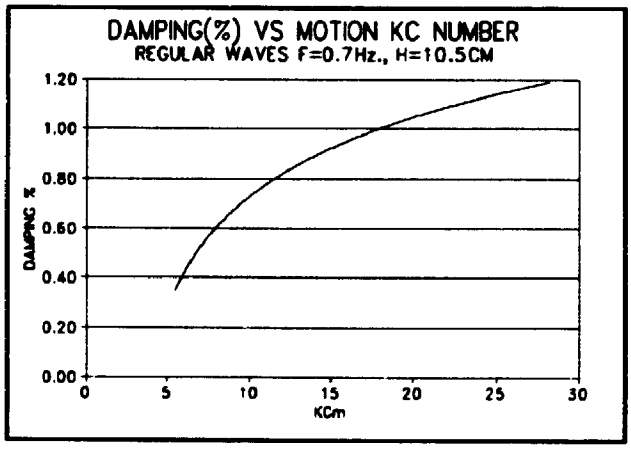

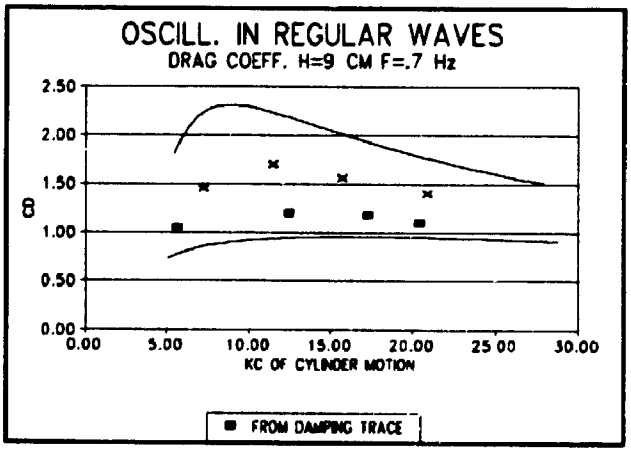

FIGURE D.4: Damping trace, Damping (% of critical), and drag coefficient derived by damping and force measurements using RVM, IFFM in regular waves.

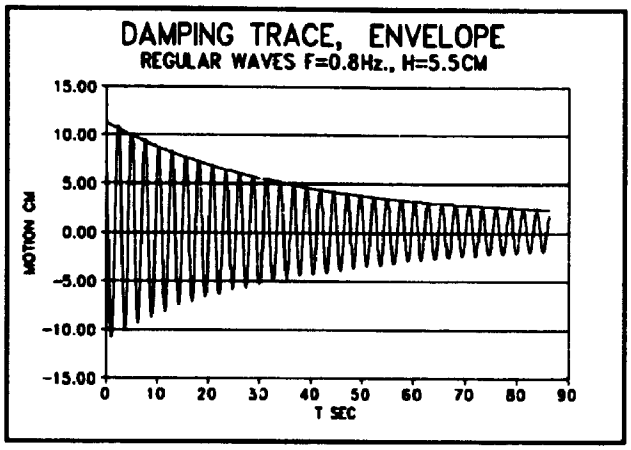

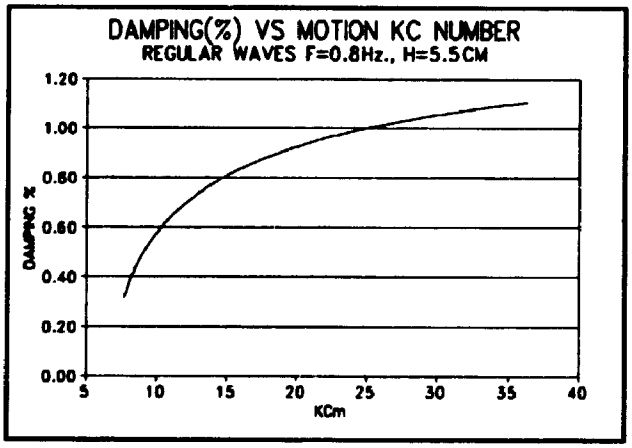

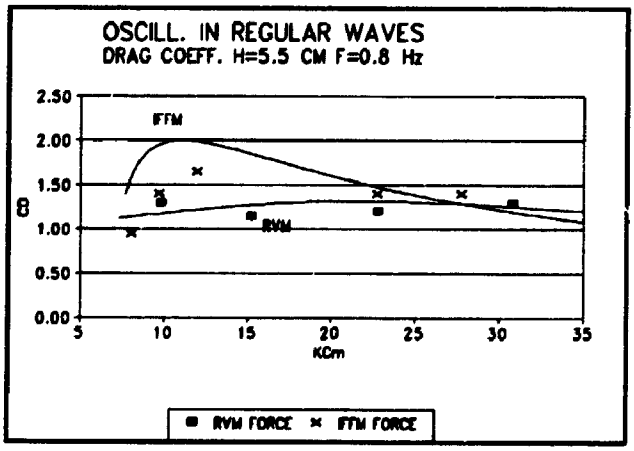

FIGURE D.5: Damping trace, Damping (% of critical), and drag coefficient derived by damping and force measurements using RVM, IFFM in regular waves.

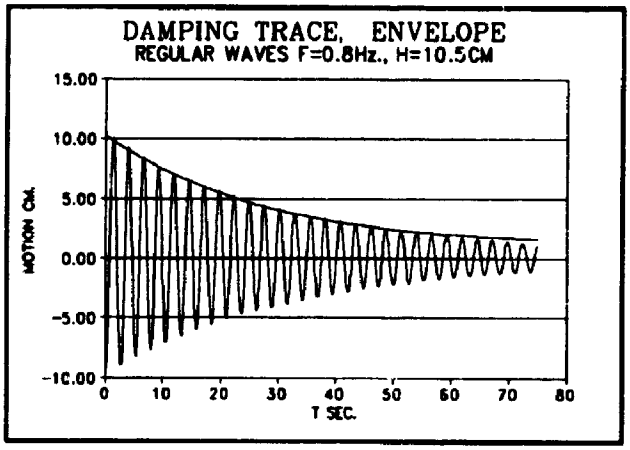

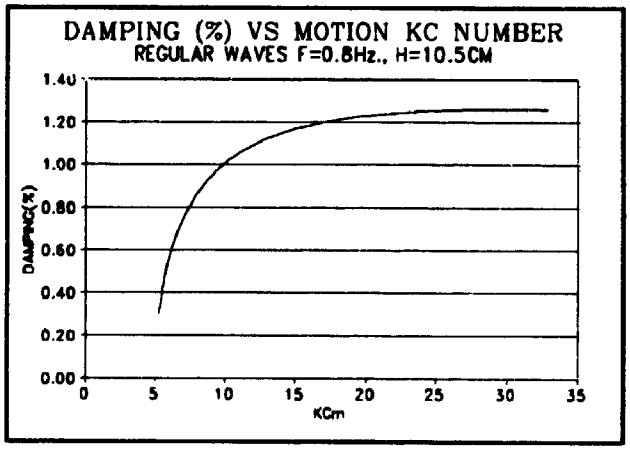

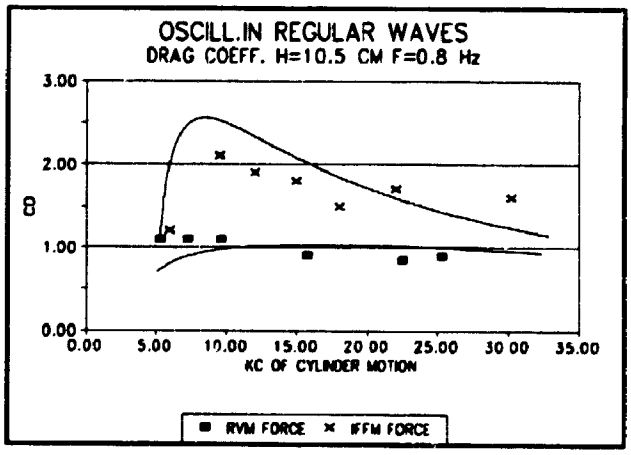

FIGURE D.6: Damping trace, Damping (% of critical), and drag coefficient derived by damping and force measurements using RVM, IFFM in regular waves.

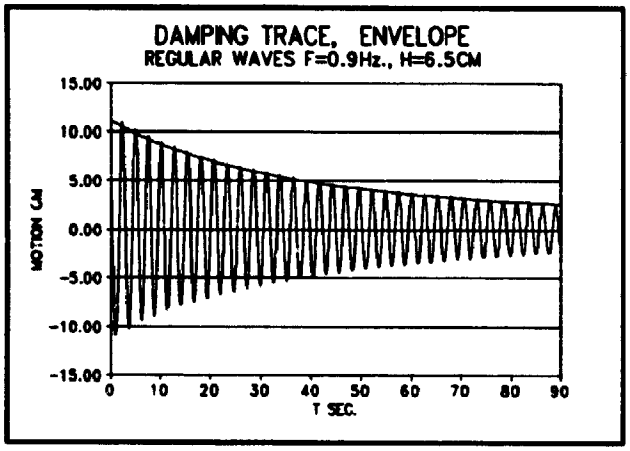

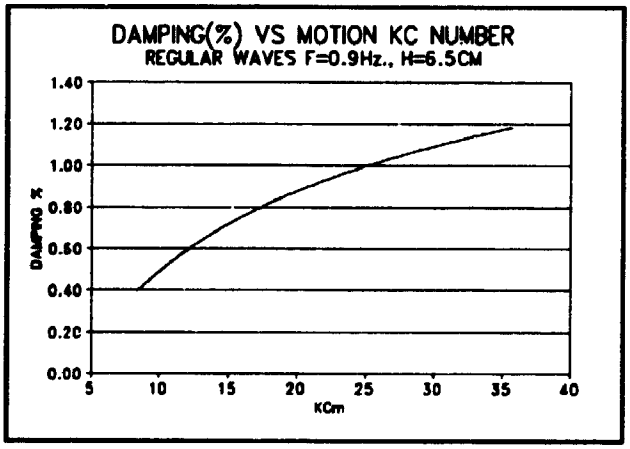

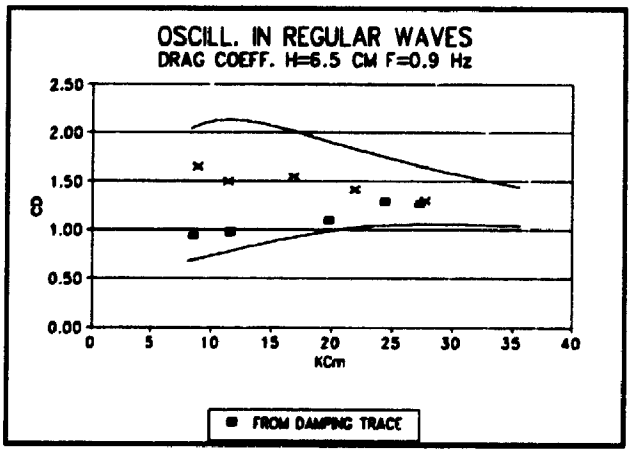

FIGURE D.7: Damping trace, Damping (% of critical), and drag coefficient derived by damping and force measurements using RVM, IFFM in regular waves.

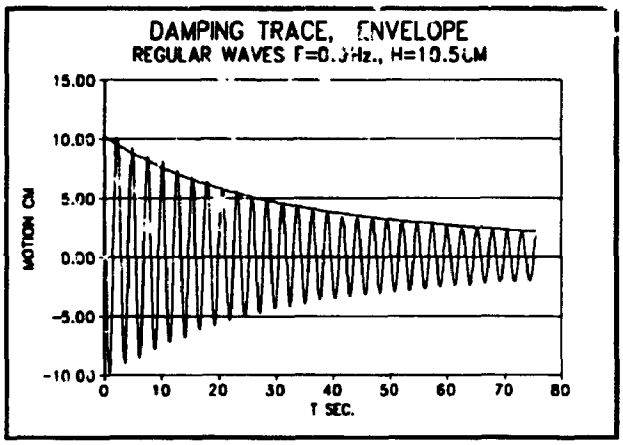

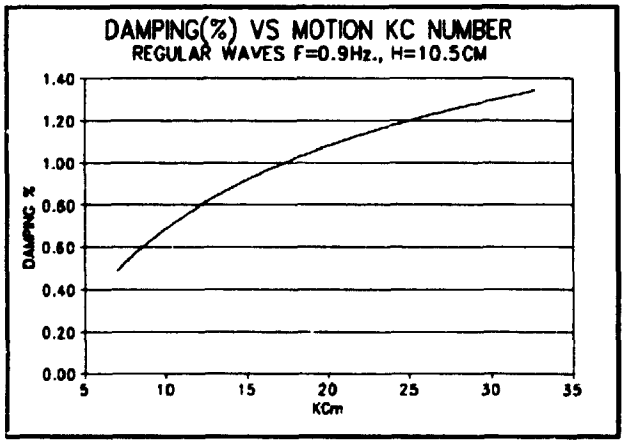

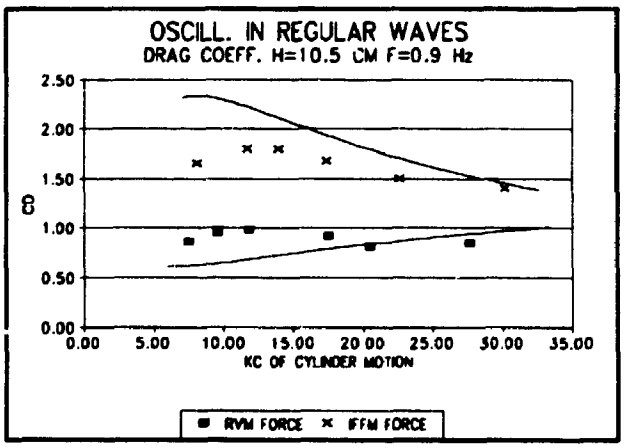

FIGURE D.8: Damping trace, Damping (% of critical), and drag coefficient derived by damping and force measurements using RVM, IFFM in regular waves.

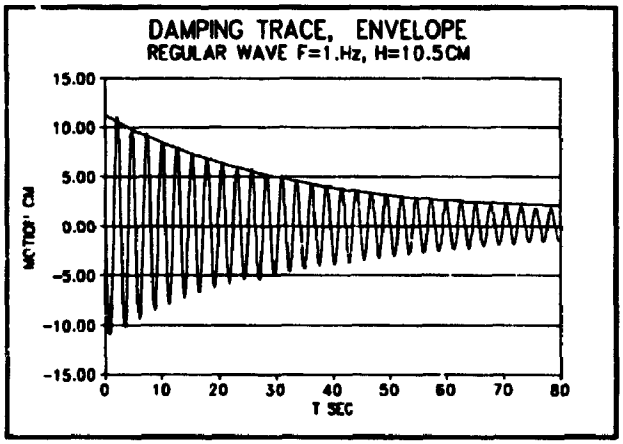

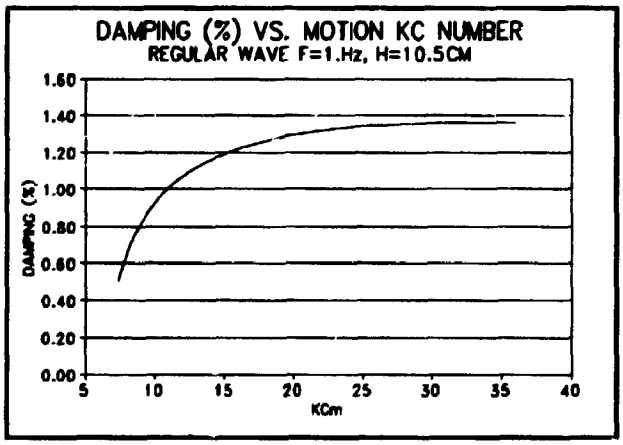

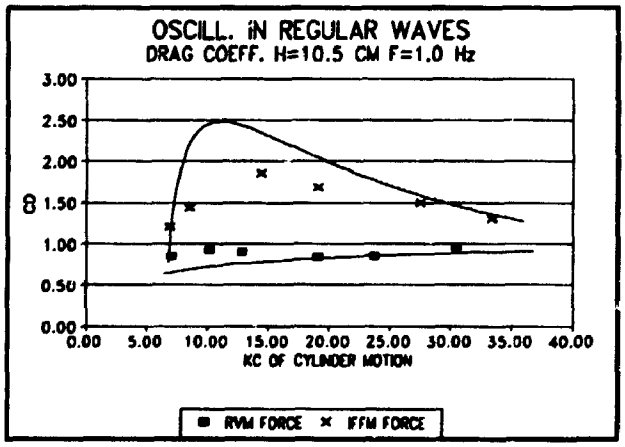

FIGURE D.9: Damping trace, Damping (% of critical), and drag coefficient derived by damping and force measurements using RVM, IFFM in regular waves.

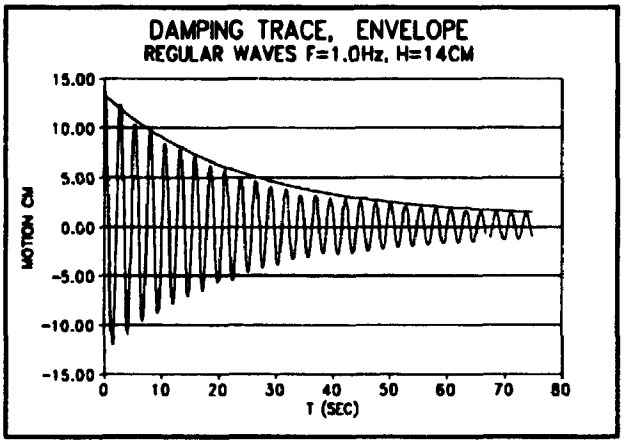

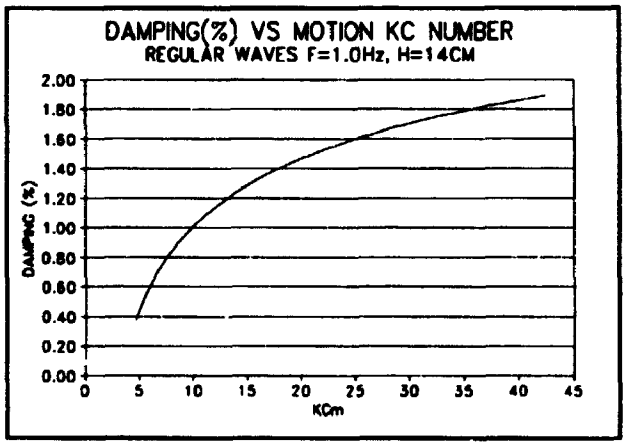

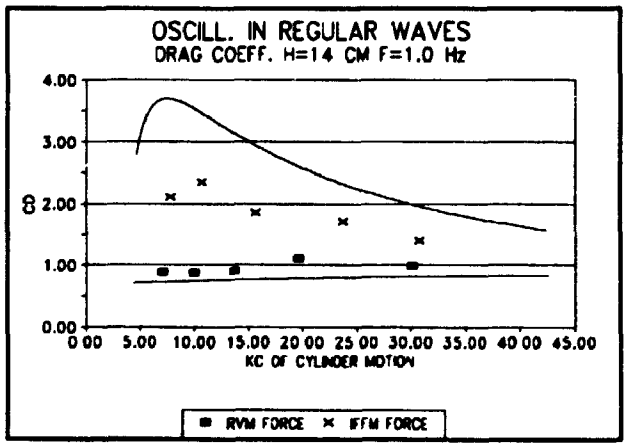

FIGURE D.10: Damping trace, Damping (% of critical), and drag coefficient derived by damping and force measurements using RVM, IFFM in regular waves.

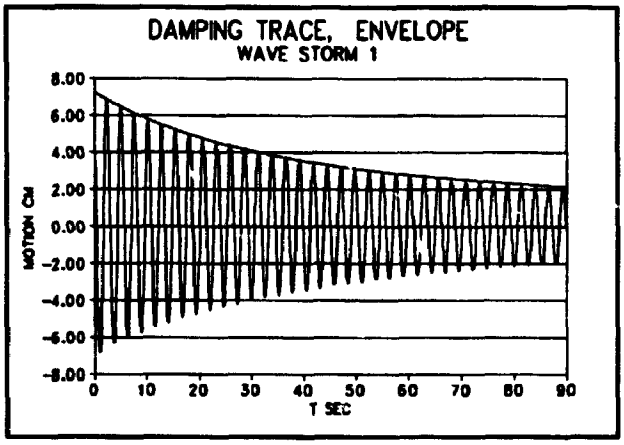

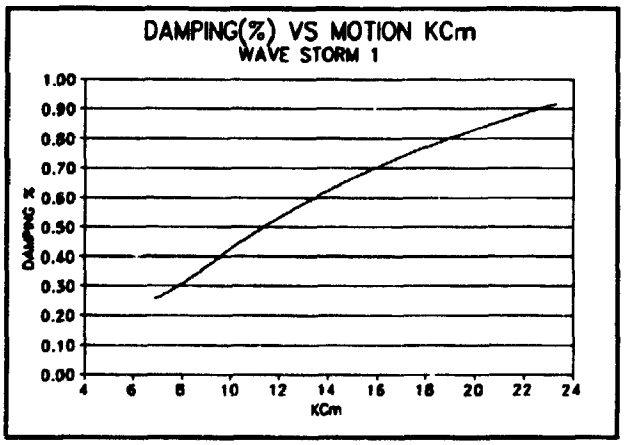

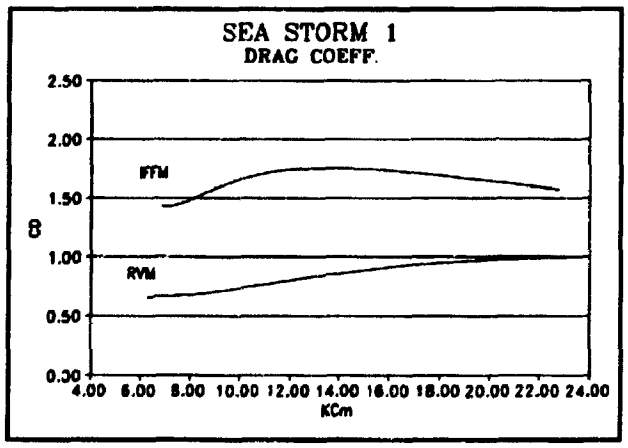

FIGURE D.11: Damping trace, Damping (% of critical), and drag coefficient derived by damping using RVM, IFFM in wave storm 1.

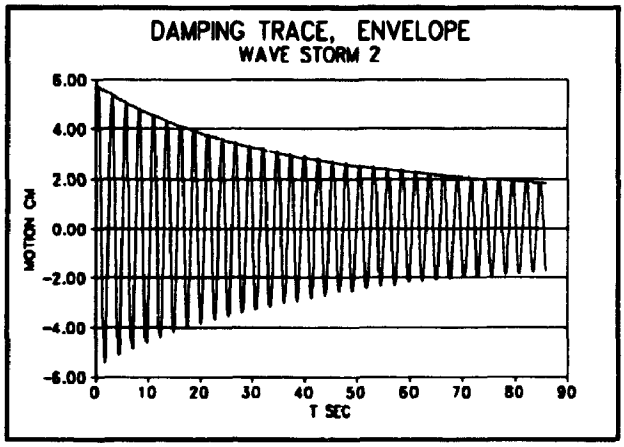

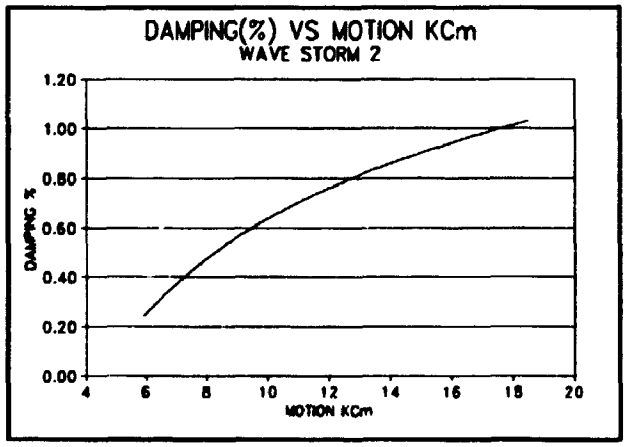

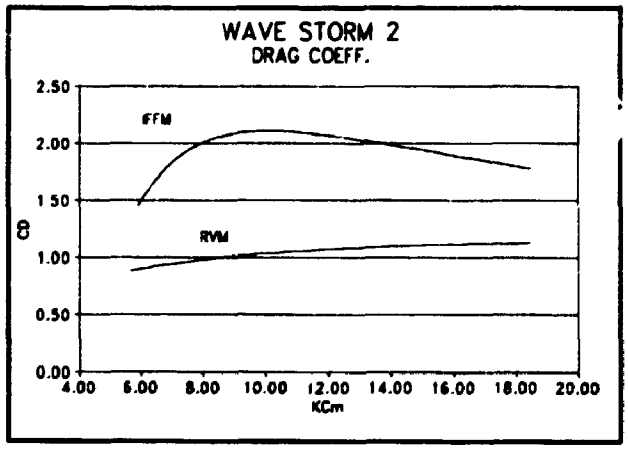

FIGURE D.12: Damping trace, Damping (% of critical), and drag coefficient derived by damping and using RVM, IFFM in wave storm 2.

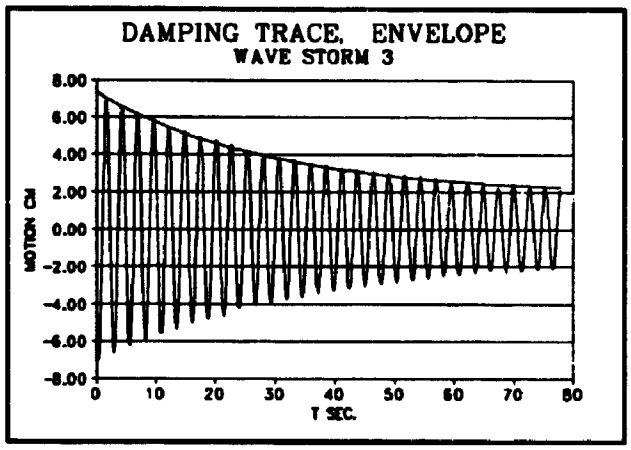

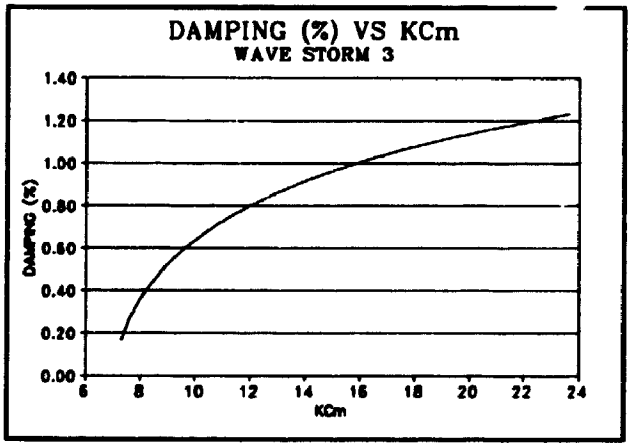

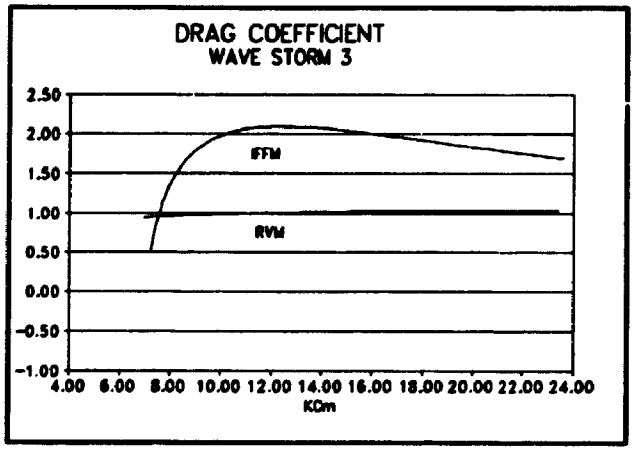

FIGURE D.13: Damping trace, Damping (% of critical), and drag coefficient derived by damping using RVM, IFFM in wave storm 3.

APPENDIX E

FREE SURFACE DRIFT FORCES (PREDICTED AND MEASURED RESULTS)

This appendix presents the measured and predicted free surface drift forces in the case of bichromatic and random waves. The first part is the measured wave elevation and force spectra for groups. The second part shows the time histories of the measured and predicted drift forces for bichromatic waves (the random wave results are given in chapter 4). The third part presents the comparison of measured and predicted drift force spectra in the case of groups and random waves.

MEASURED WAVE ELEVATION AND WAVE FORCE SPECTRA (BICHROMATIC WAVES)

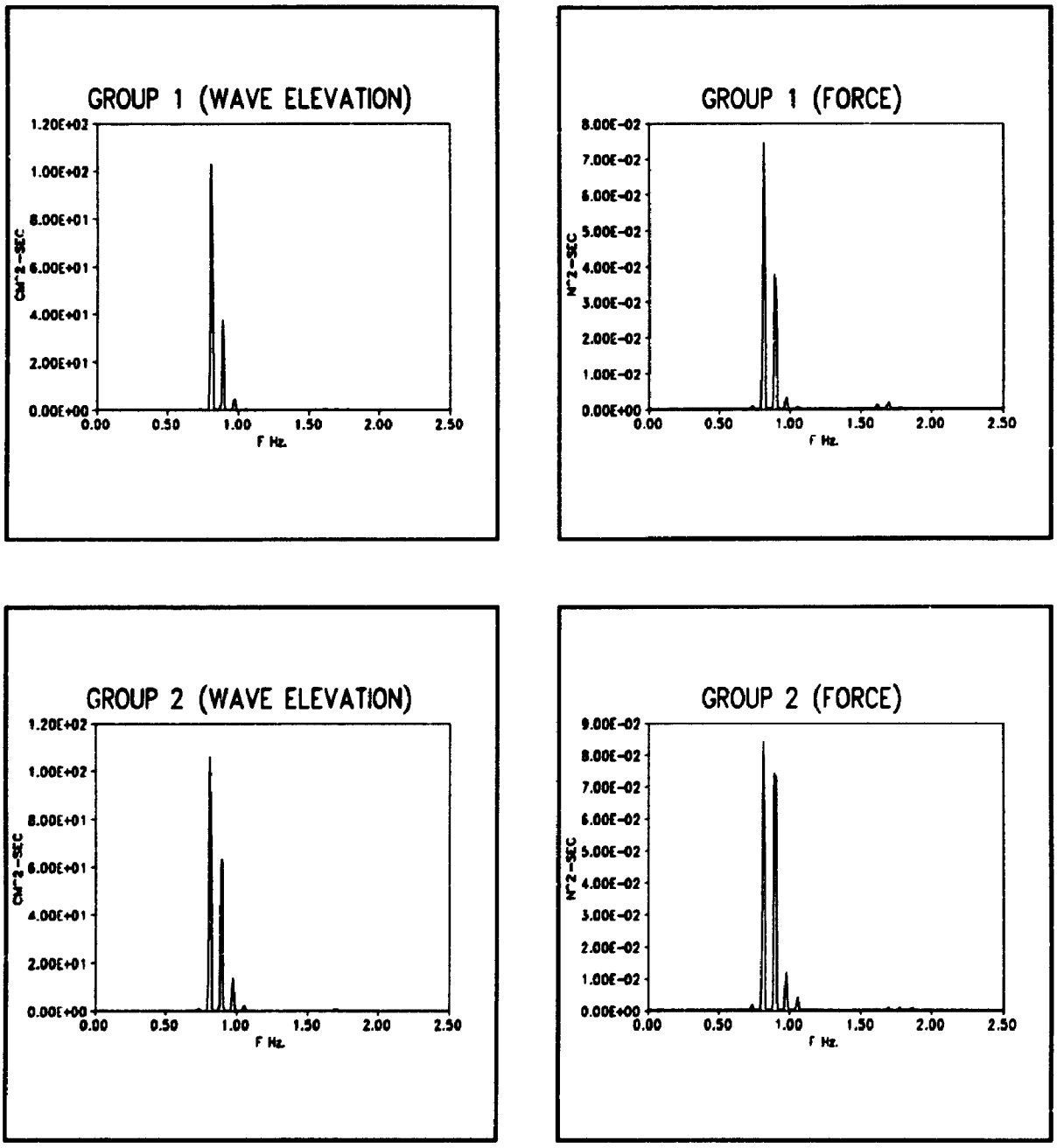

FIGURE E.1: Measured wave elevation and wave force spectra (bichromatic waves).

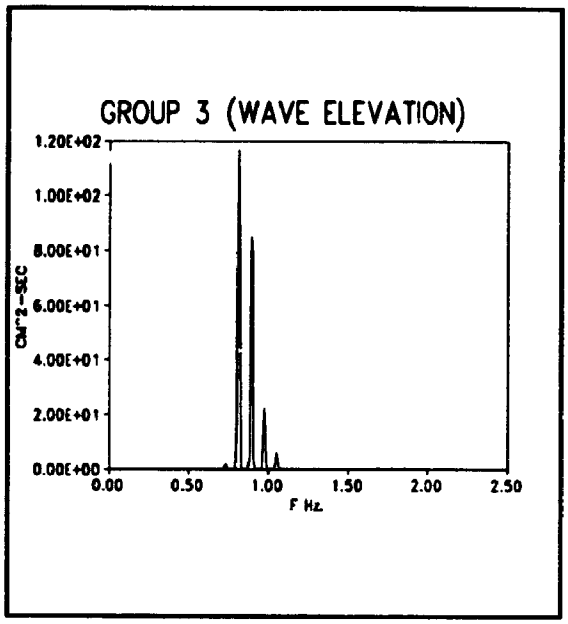

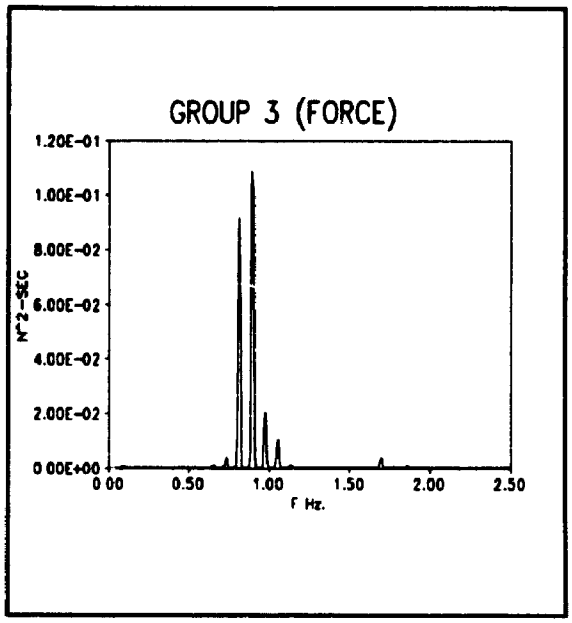

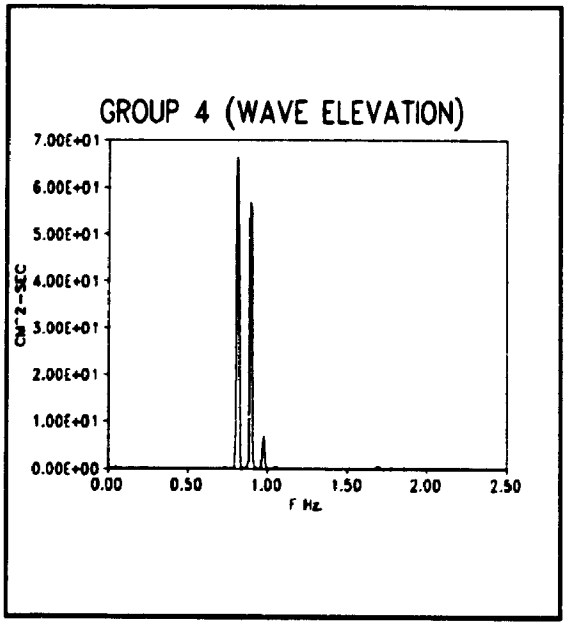

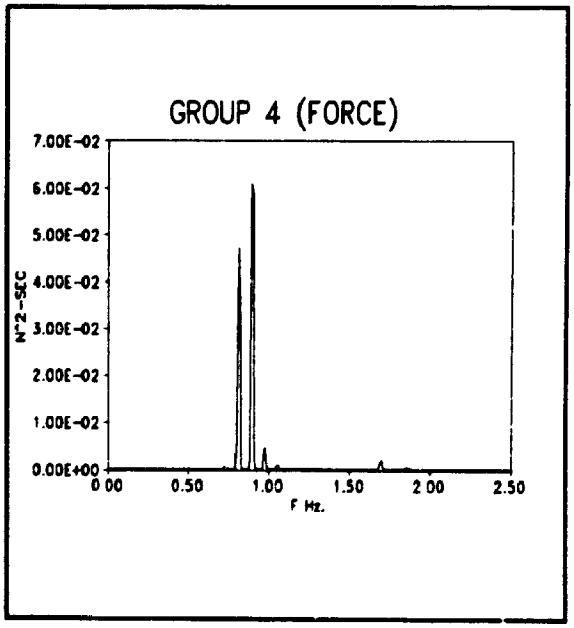

FIGURE E.2 Measured wave elevation and wave force spectra (bichromatic waves).

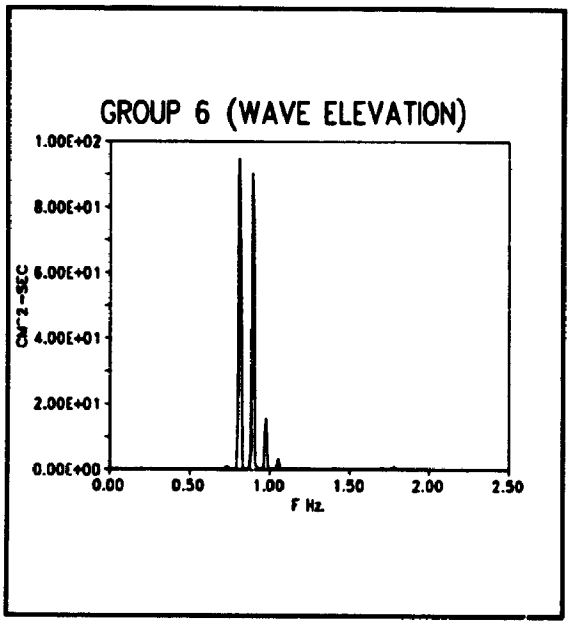

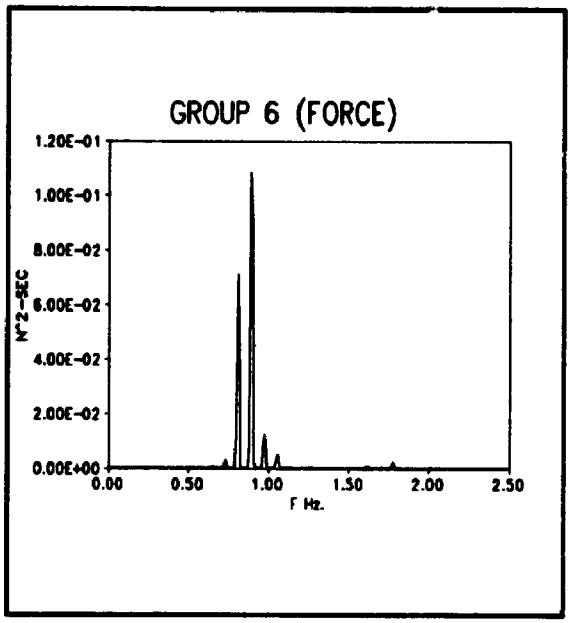

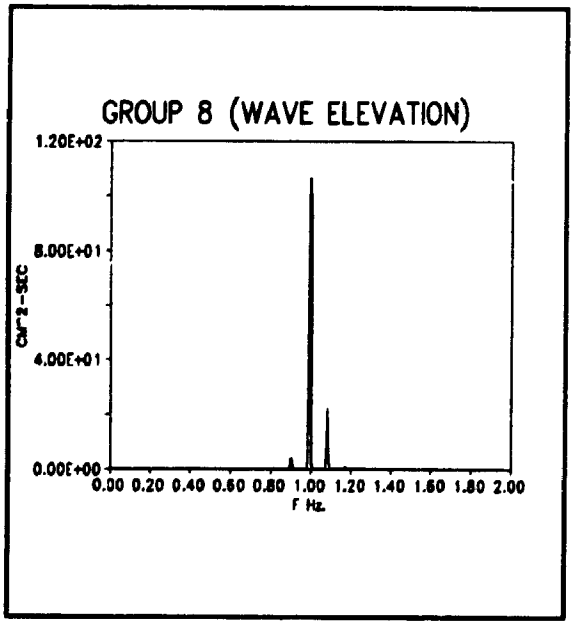

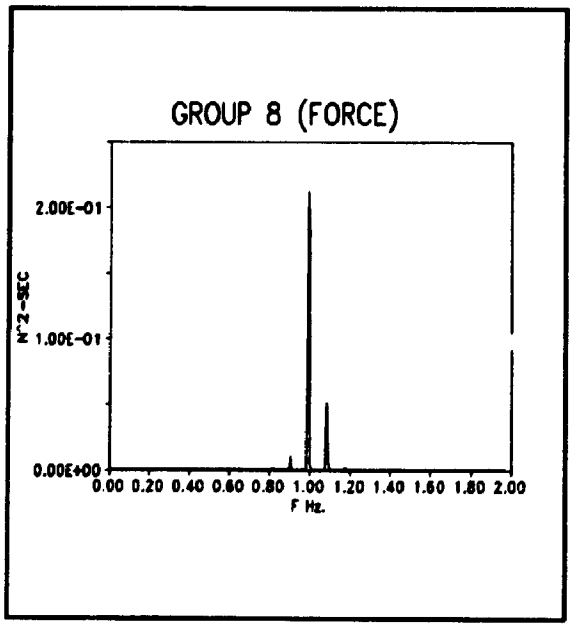

FIGURE E.3 Measured wave elevation and wave force spectra (bichromatic waves).

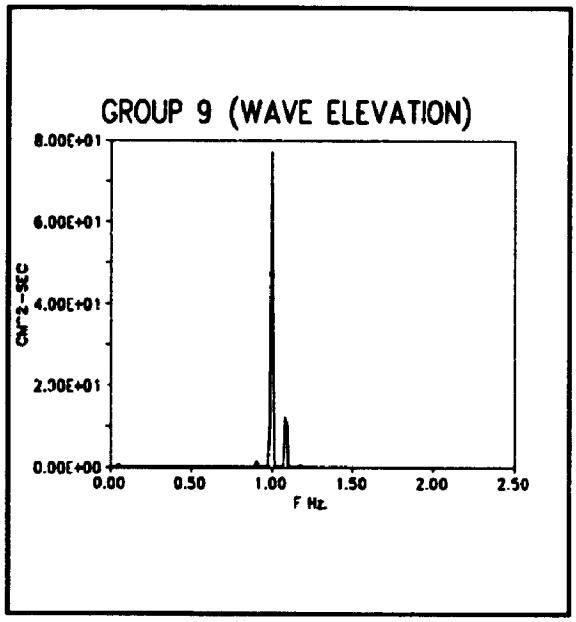

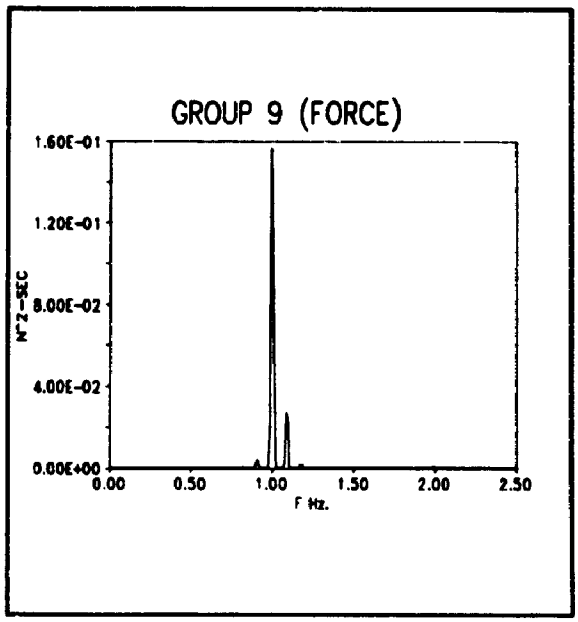

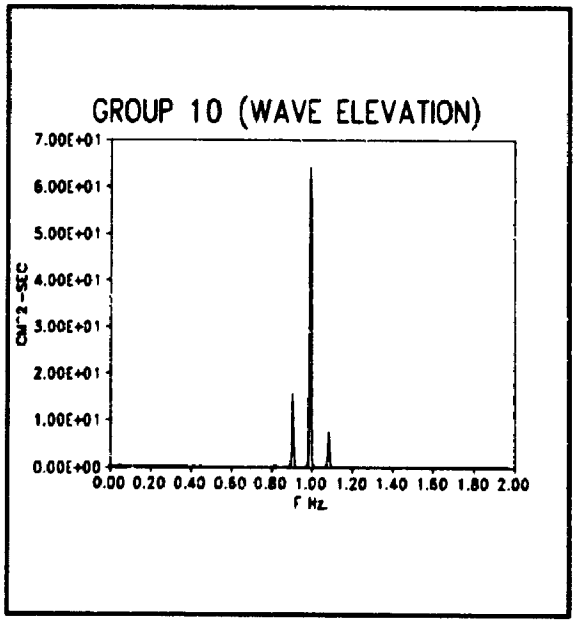

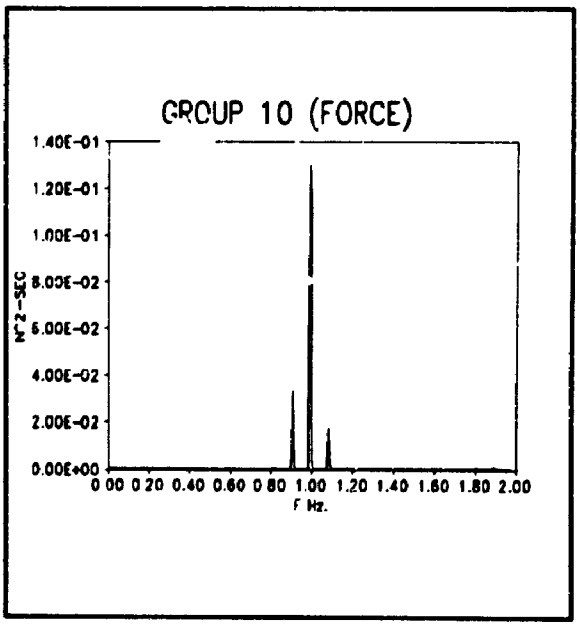

FIGURE E.4 Measured wave elevation and wave force spectra (bichromatic waves).

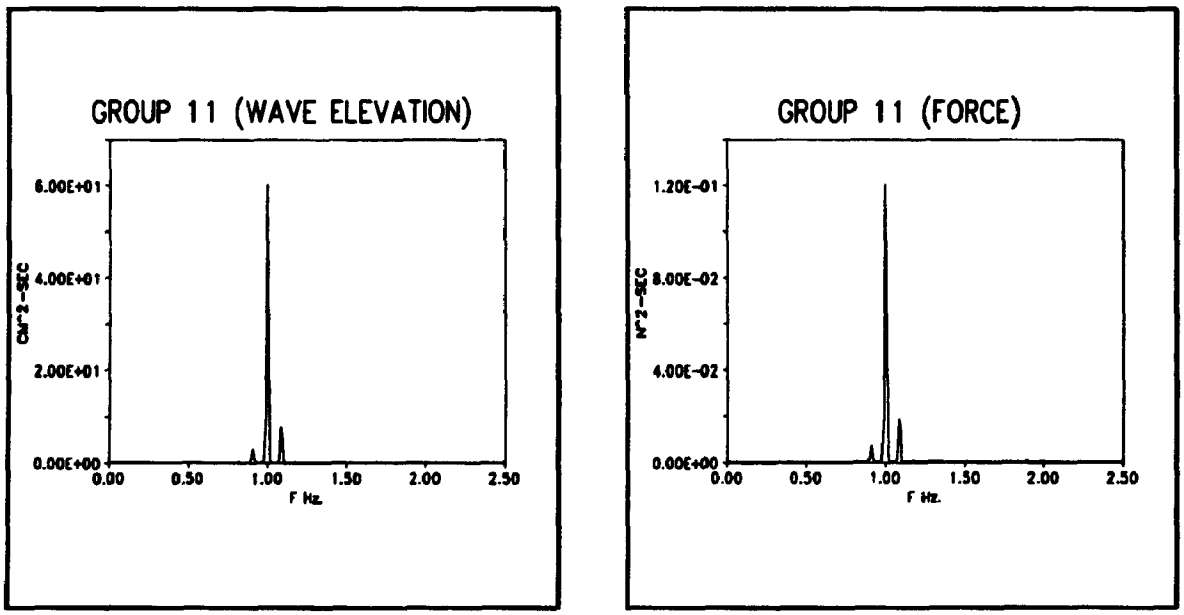

FIGURE E.5 Measured wave elevation and wave force spectra (bichromatic waves).

MEASURED AND PREDICTED DRIFT FORCES IN TIME DOMAIN (BIHCHROMATIC WAVES).

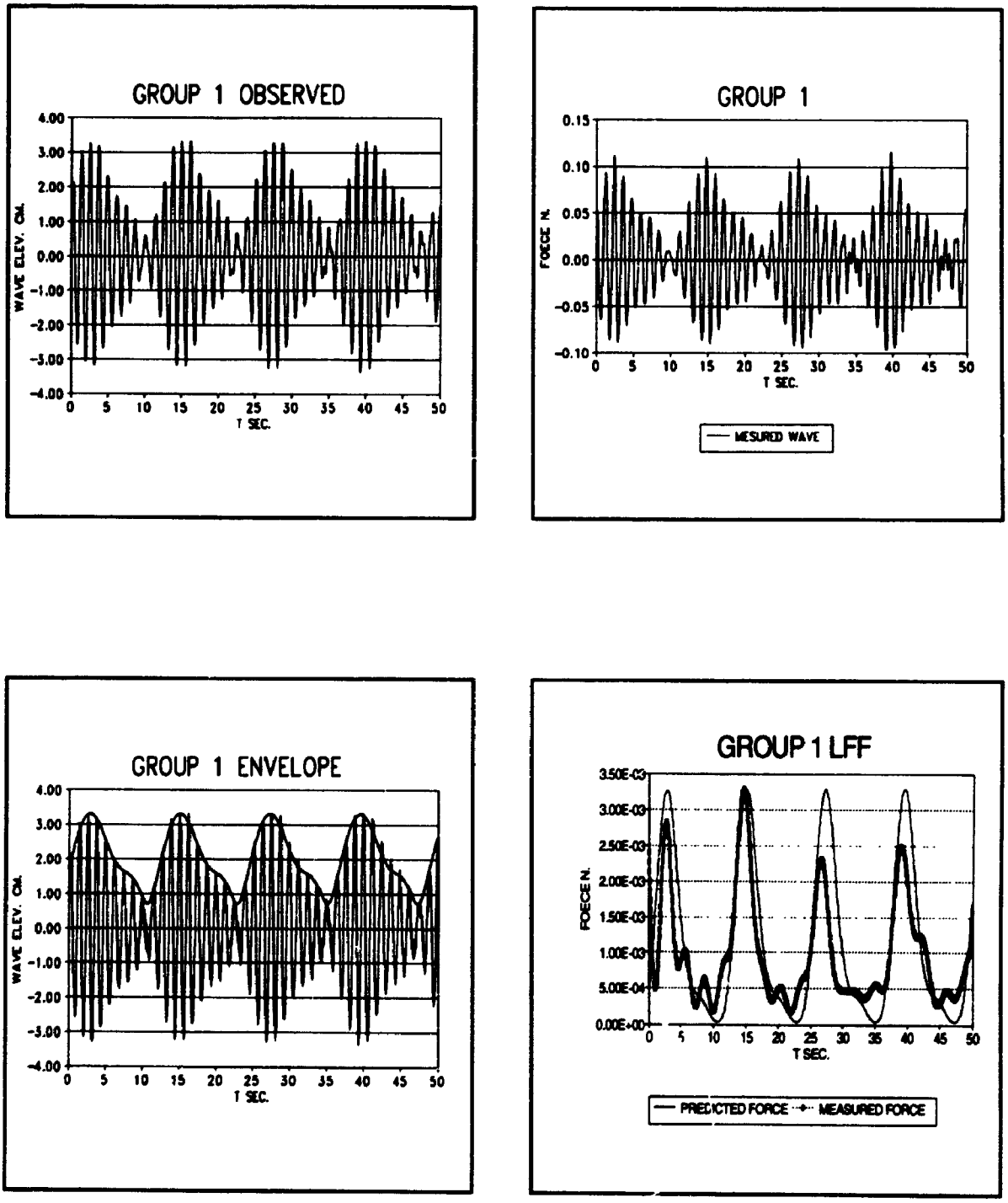

FIGURE E.6 Measured wave elevation, wave force, calculated envelope,measured and predicted drift force (bichromatic waves).

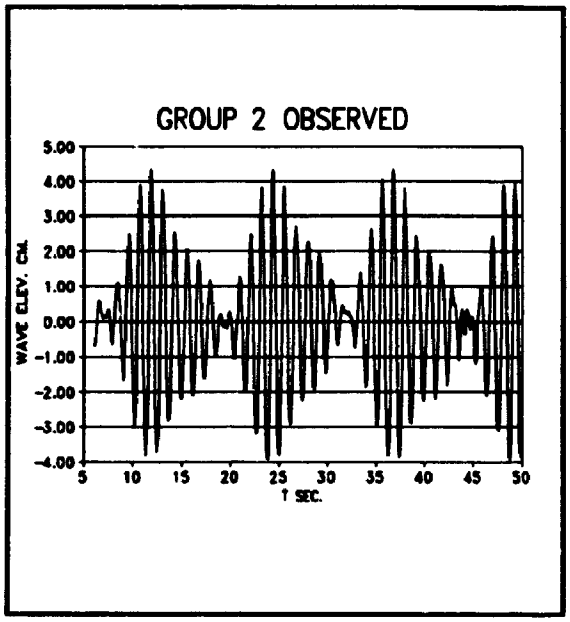

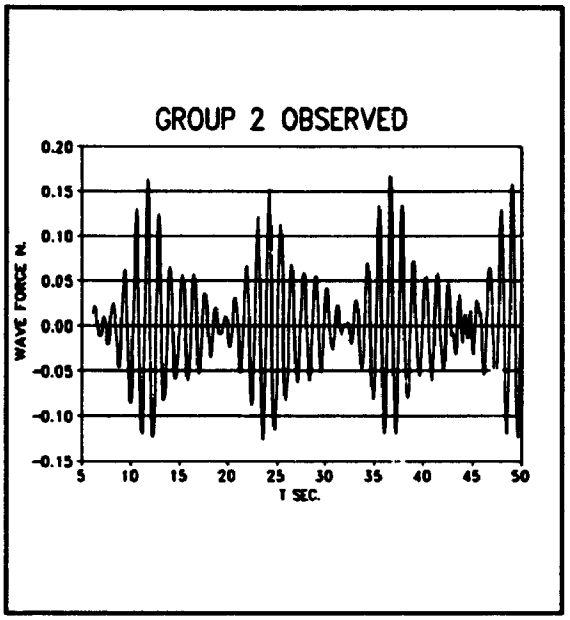

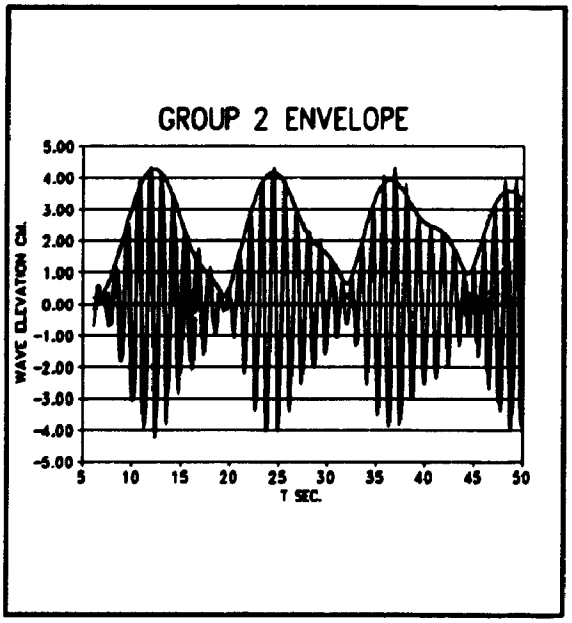

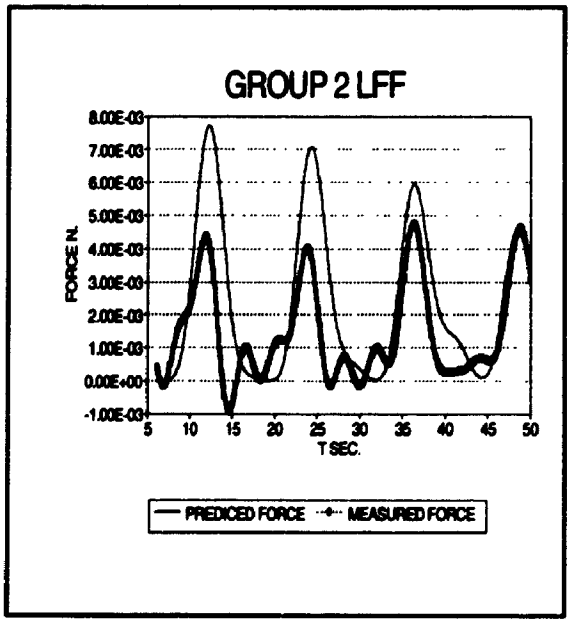

FIGURE E.7 Measured wave elevation, wave force, calculated envelope, measured and predicted drift force (bichromatic waves).

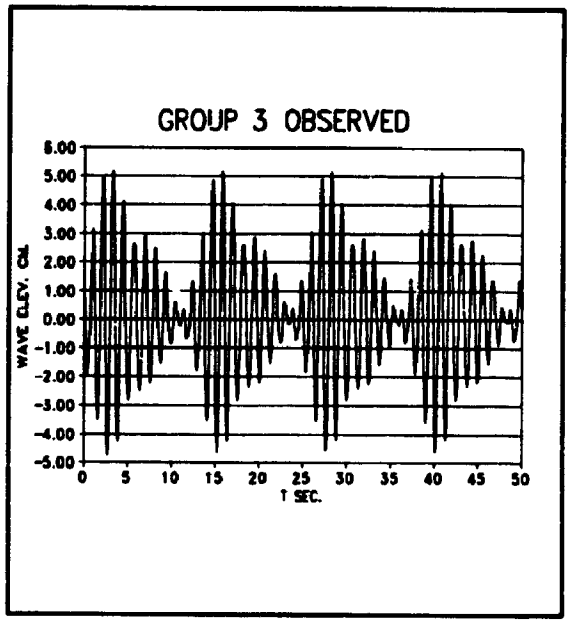

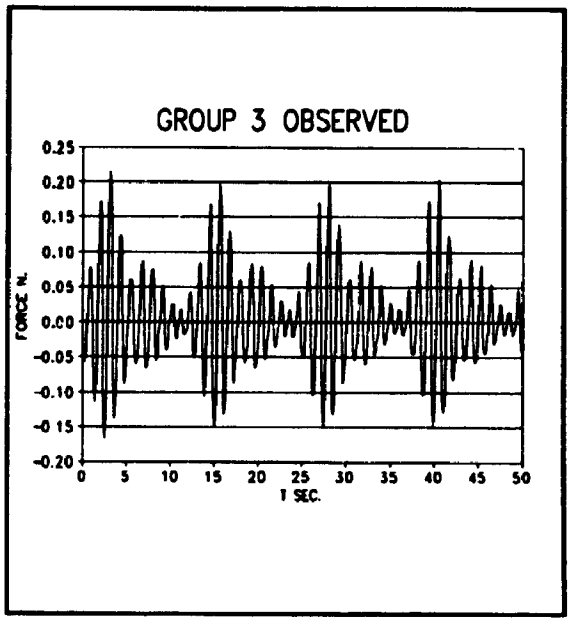

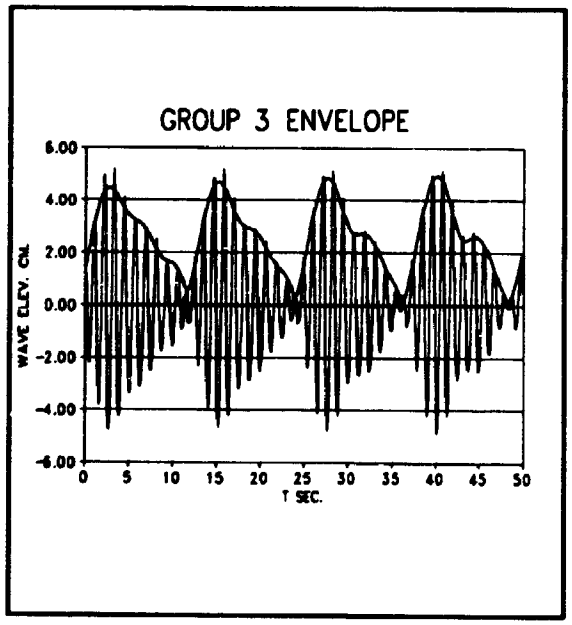

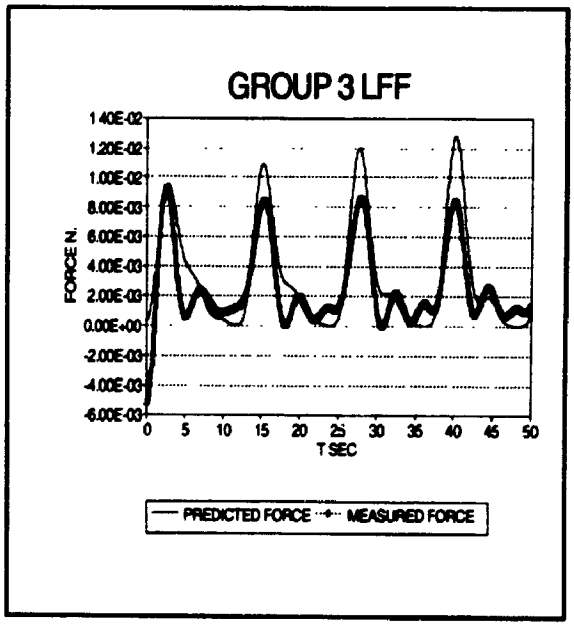

FIGURE E.8 Measured wave elevation, wave force, calculated envelope, measured and predicted drift force (bichromatic waves).

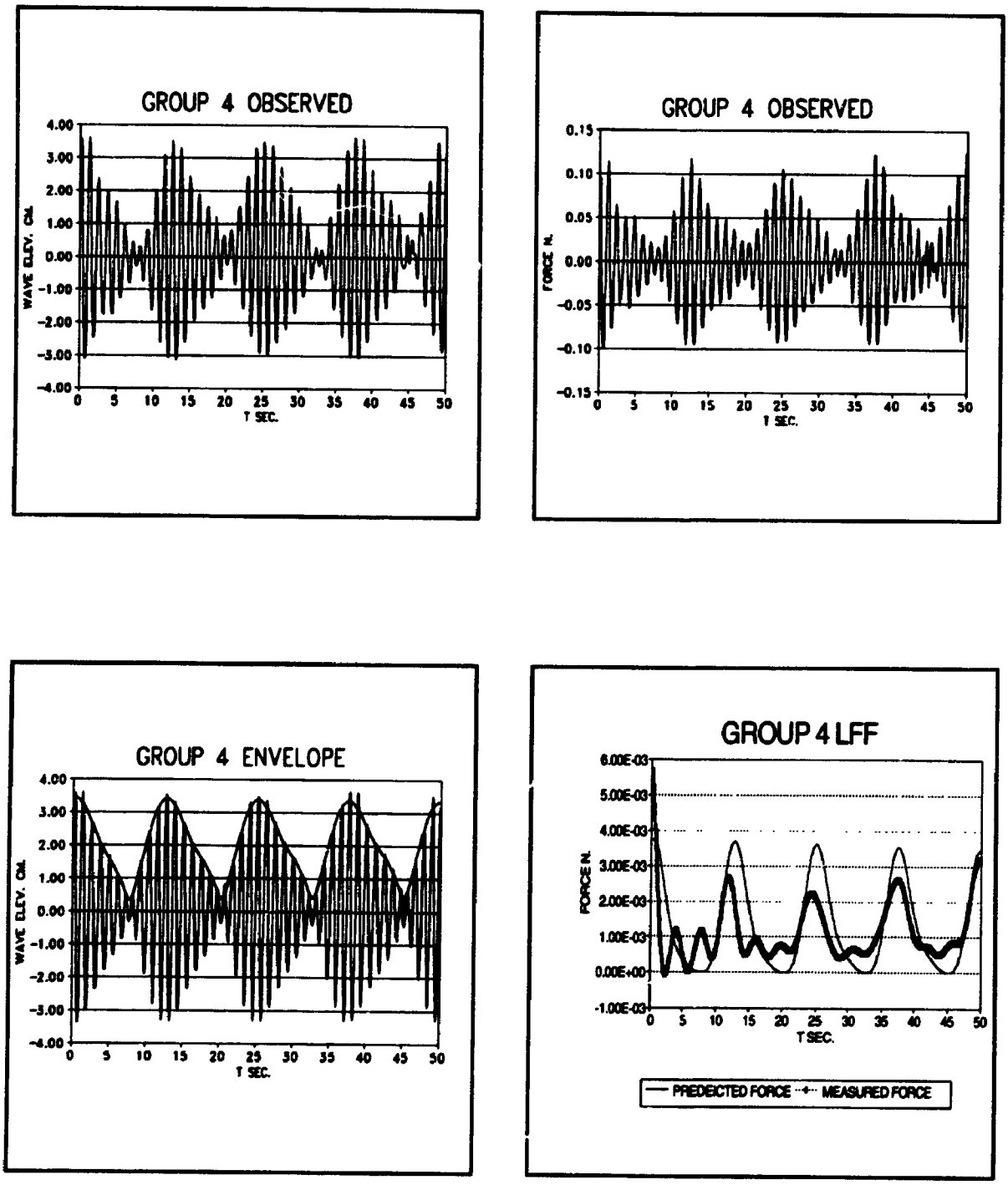

FIGURE E.9: Measured wave elevation, wave force, calculated envelope, measured and predicted drift force (bichromatic waves).

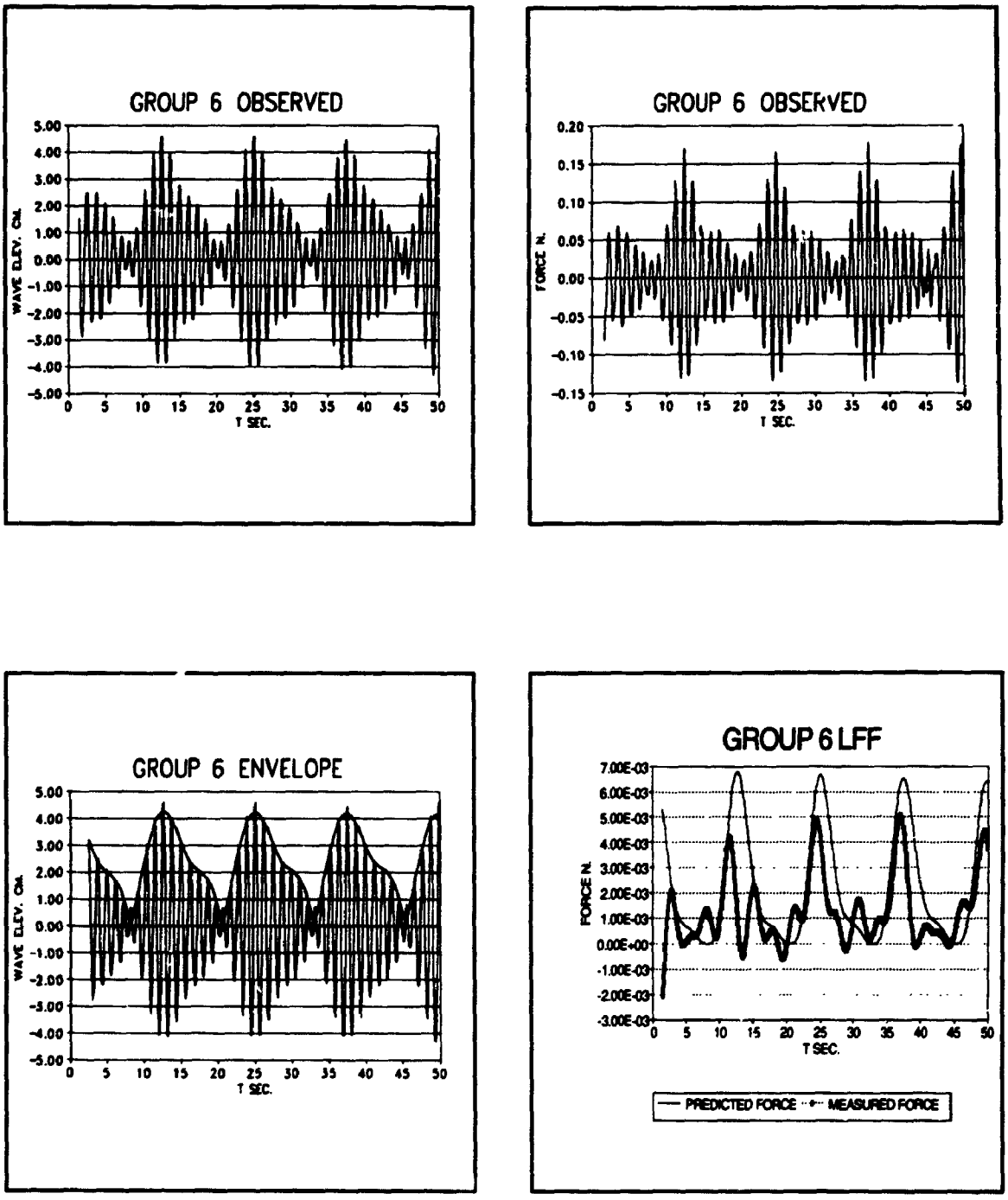

FIGURE E.10: Measured wave elevation, wave force, calculated envelope, measured and predicted drift force (bichromatic waves).

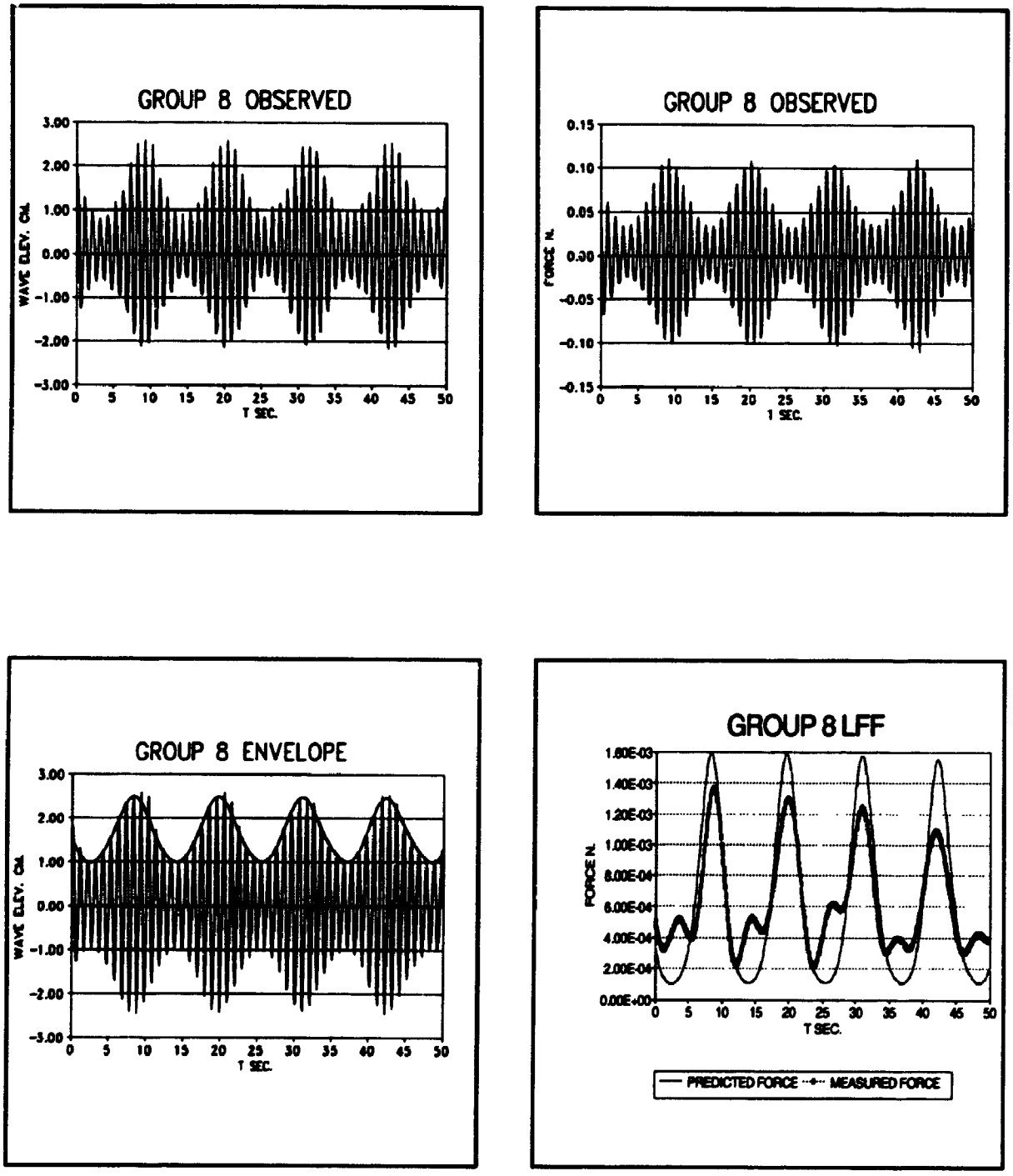

FIGURE E.11: Me- d wave elevation, wave force, calculated envelope, measured and predicted drift force (bichromatic waves).

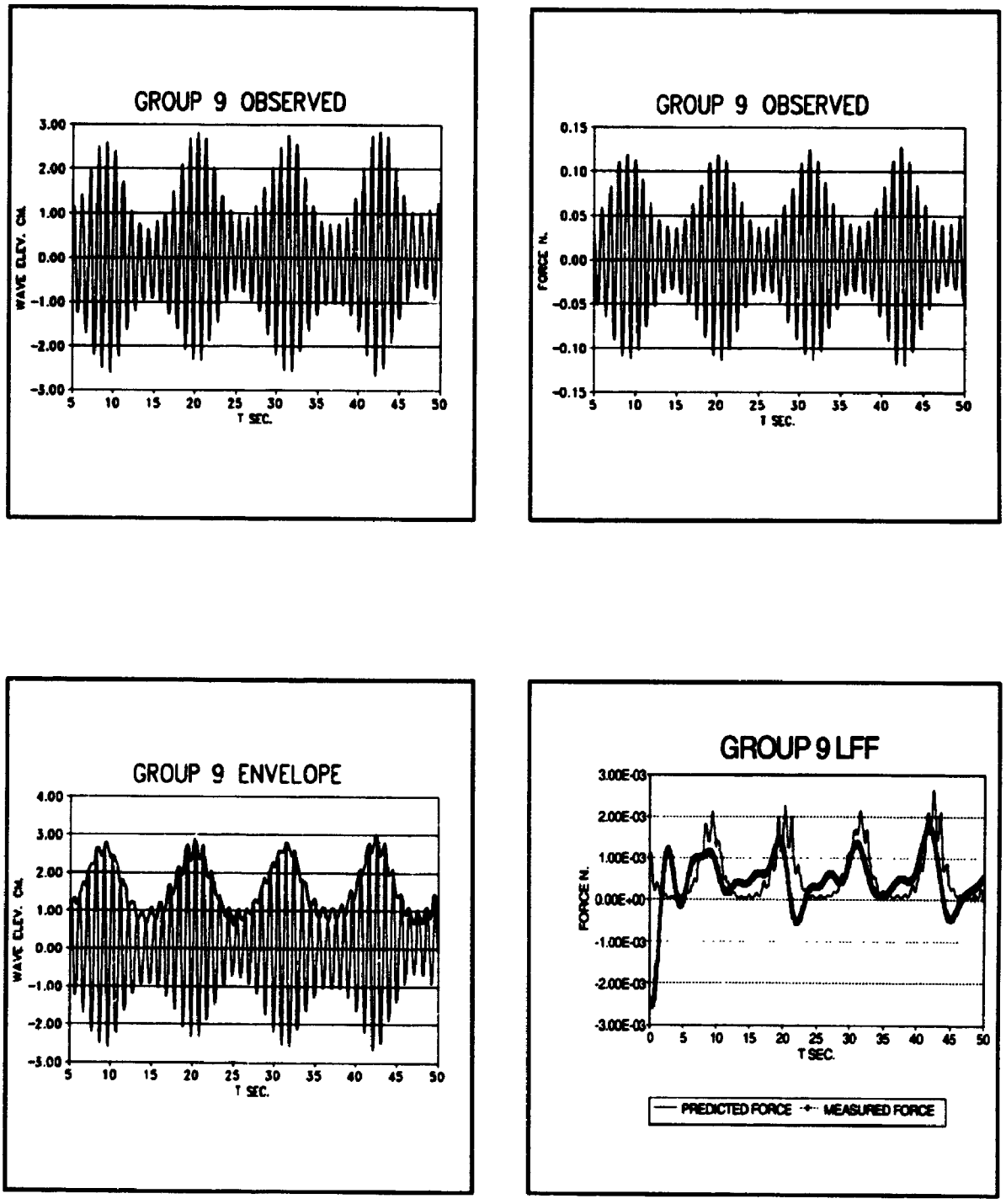

FIGURE E.12: Measured wave elevation, wave force, calculated envelope, measured and predicted drift force (bichromatic waves).

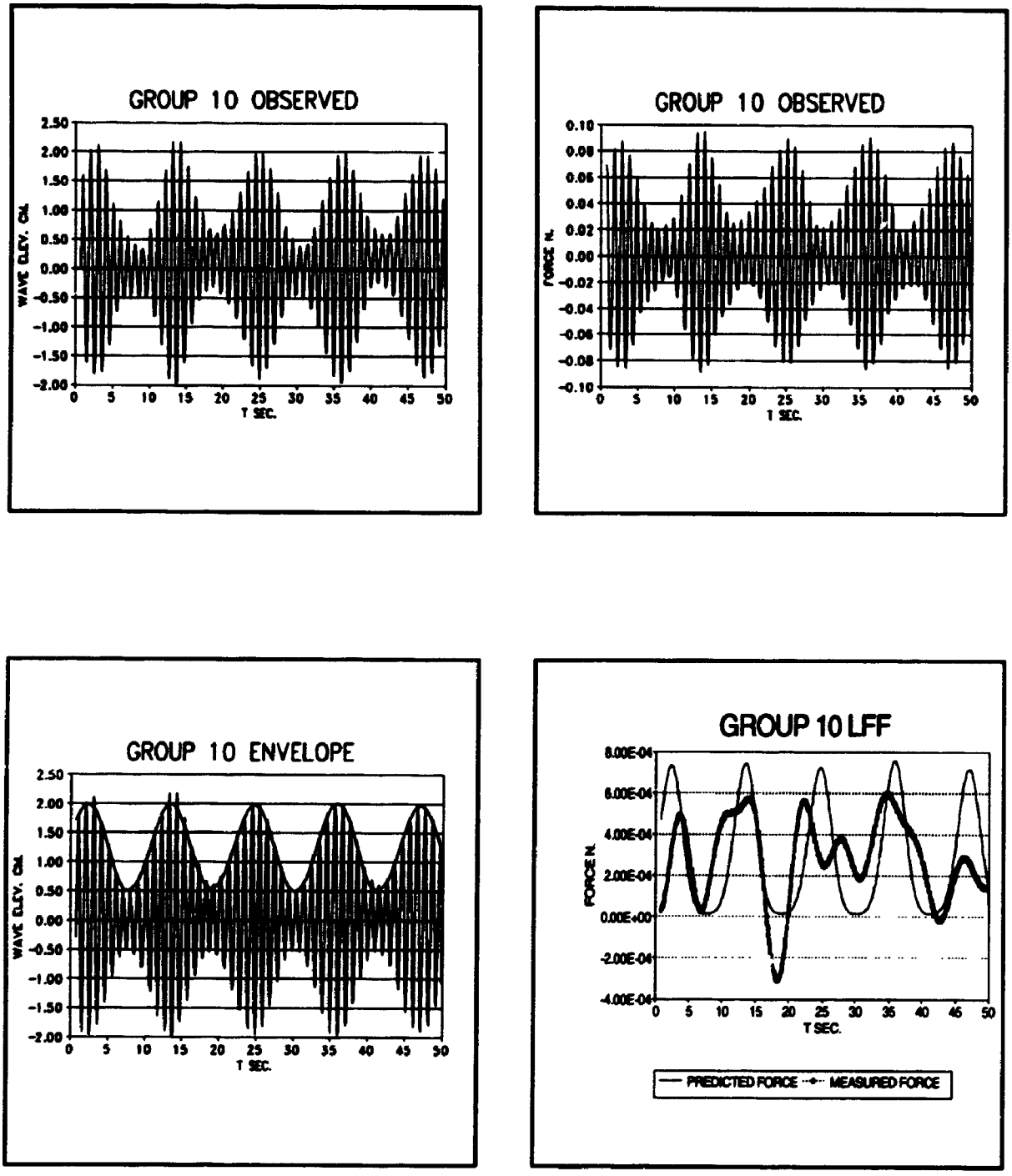

FIGURE E.13: Measured wave elevation, wave force, calculated envelope, measured and predicted drift force (bichromatic waves).

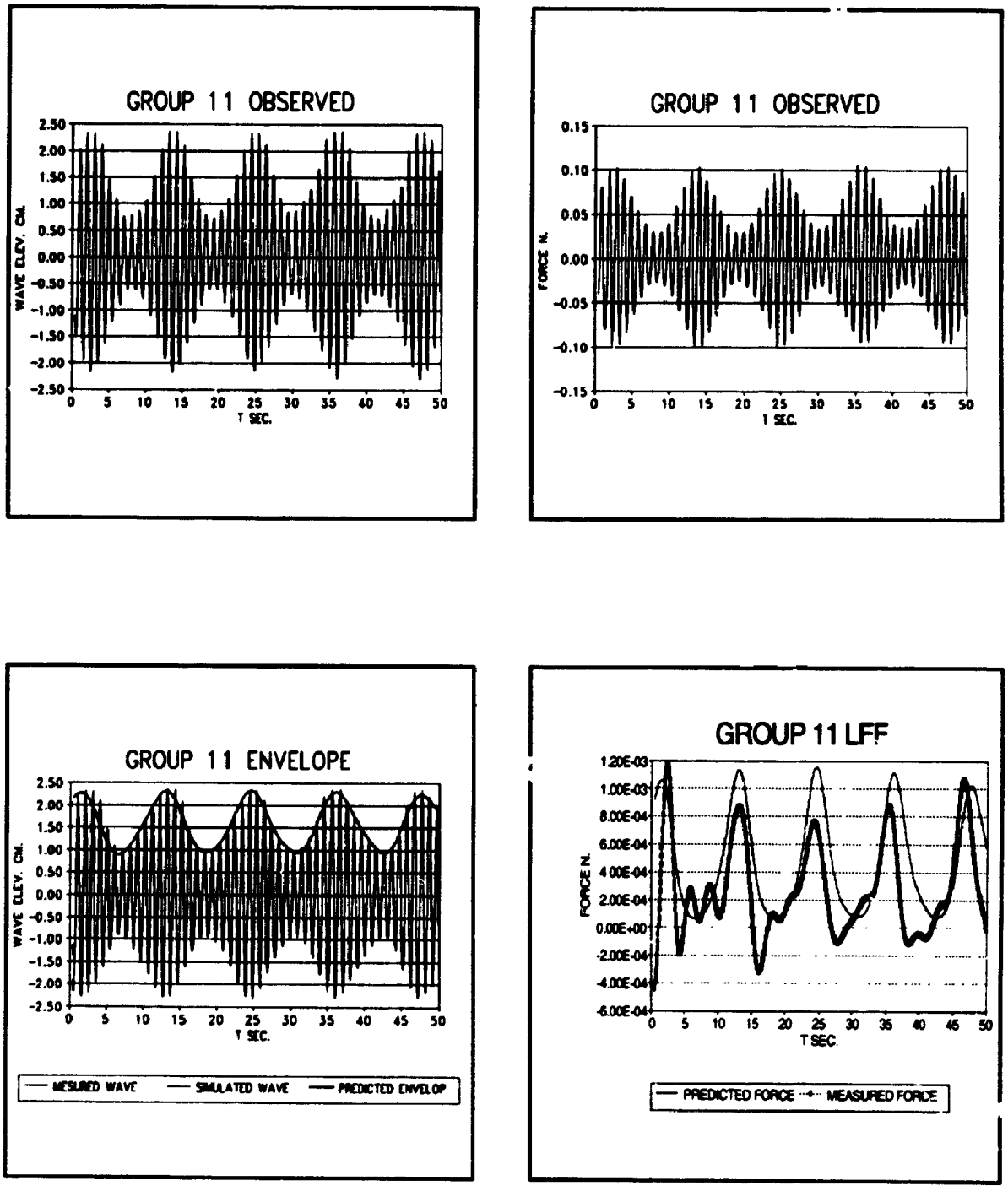

FIGURE E.14 Measured wave elevation, wave force, calculated envelope, measured and predicted drift force (bichromatic waves).

MEASURED AND PREDICTED DRIFT FORCE SPECTRA (BICHROMATIC AND RANDOM WAVES)

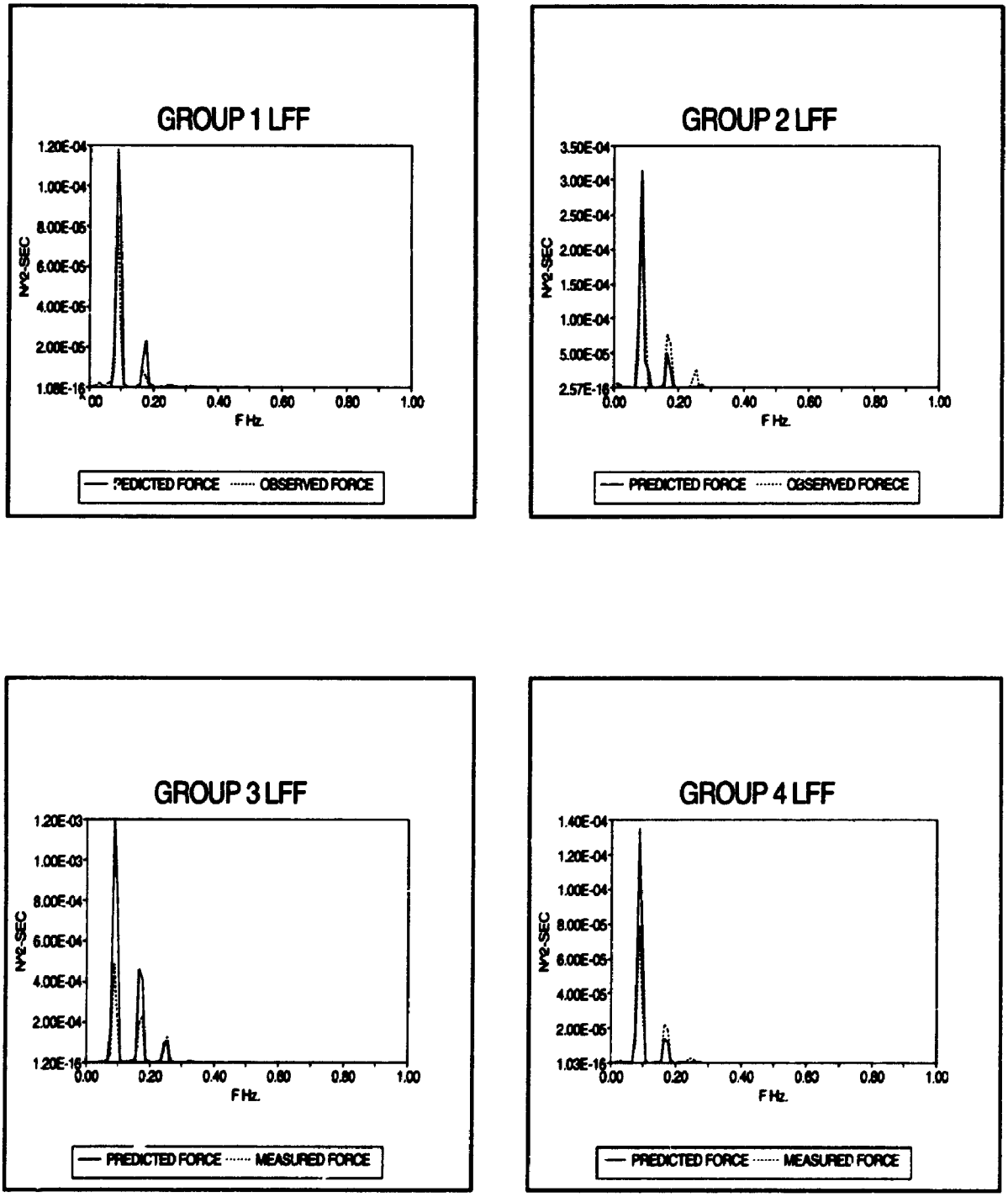

FIGURE E.15: Measuerd and predicted drift force spectra (Groups 1,2,3,4)

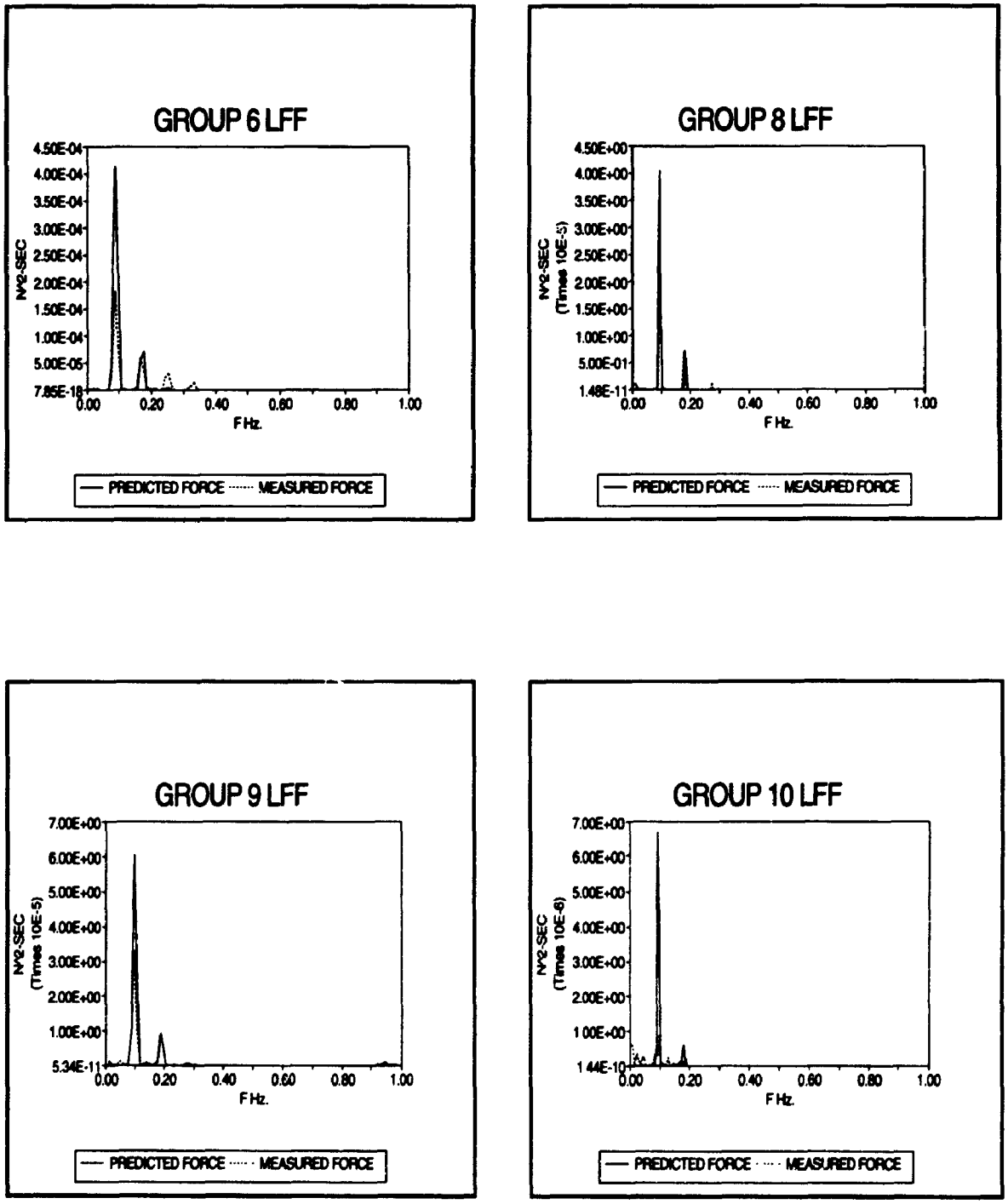

FIGURE E.16: Measuerd and predicted drift force spectra (Groups 6,8,9,10)

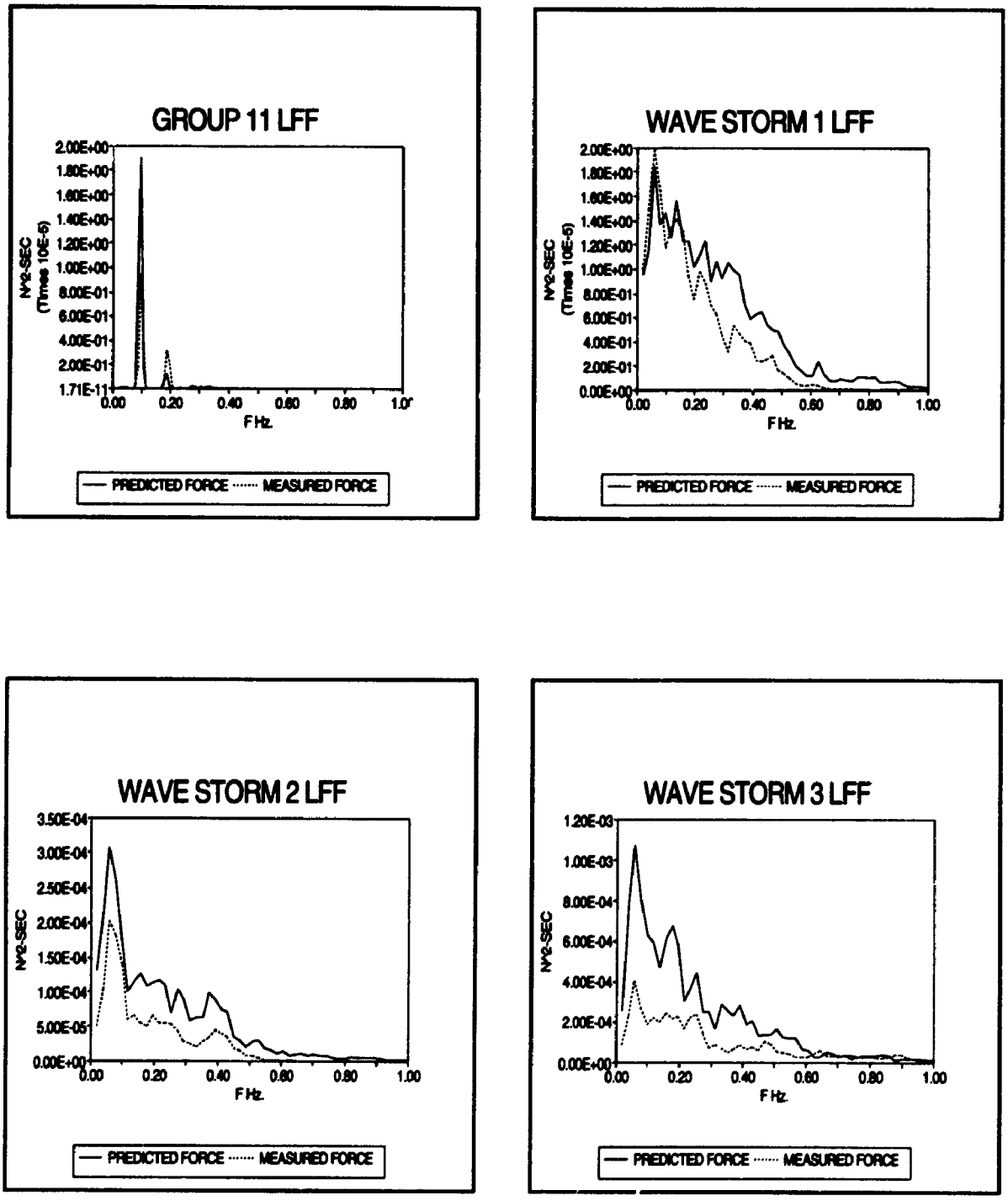

FIGURE E.17: Measuerd and predicted drift force spectra (Group 11, and Wave Storms 1,2,3)

APPENDIX F

MEASURED LOWER DECK LEVEL SURGE RESPONSE SPECTRA FOR THE THREE STRUCTURAL CONFIGURATIONS A,B,C.

This appendix presents the measured lower deck level surge response spectra for the three structural configurations.

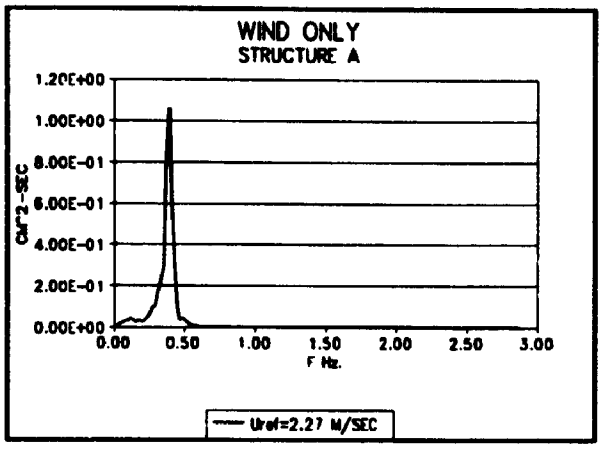

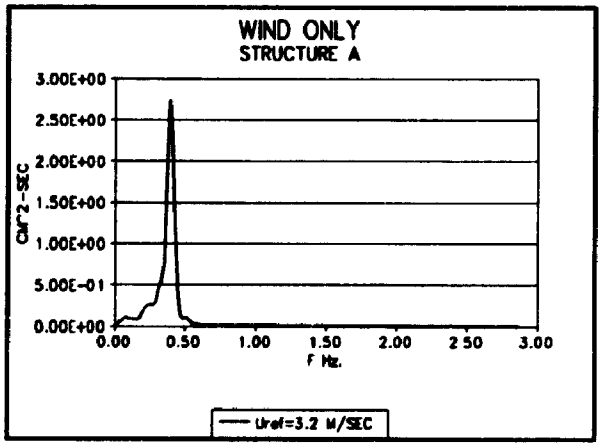

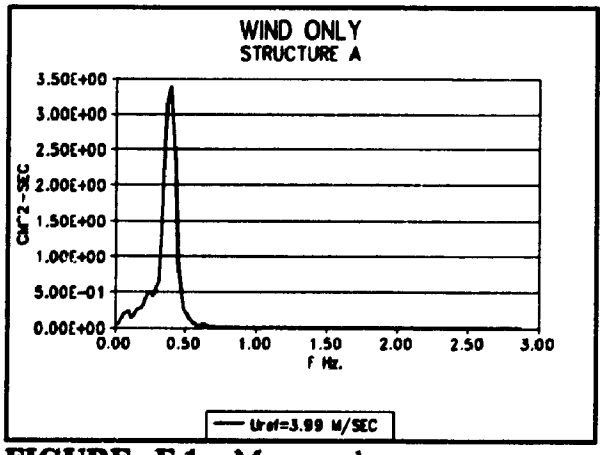

FIGURE F.1: Measured surge response spectra for different mean wind velocities (STRUCTURE A, WIND ONLY)

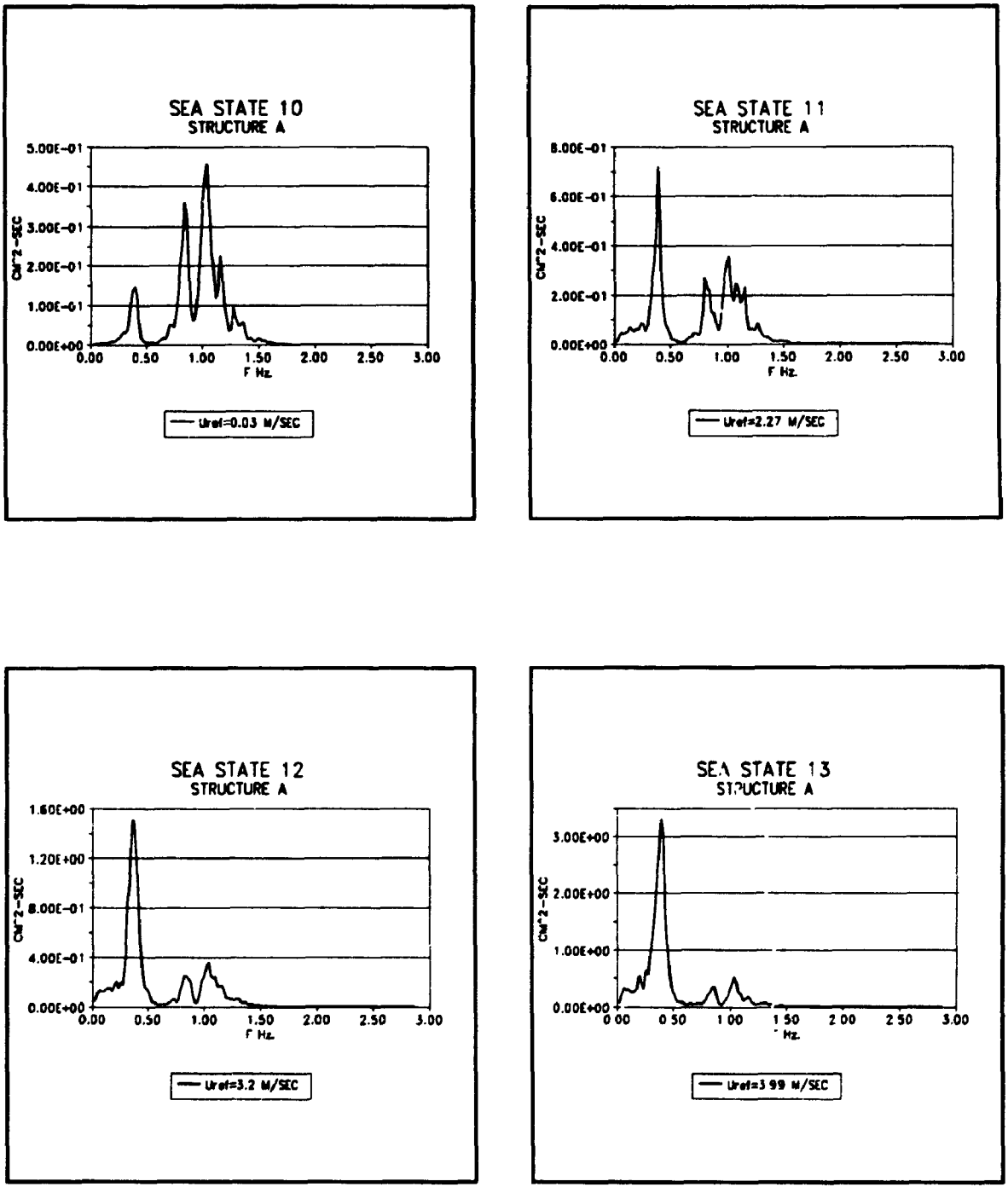

FIGURE F.2: Measured surge response spectra for different mean wind velocities (STRUCTURE A, WAVE STORM 1)

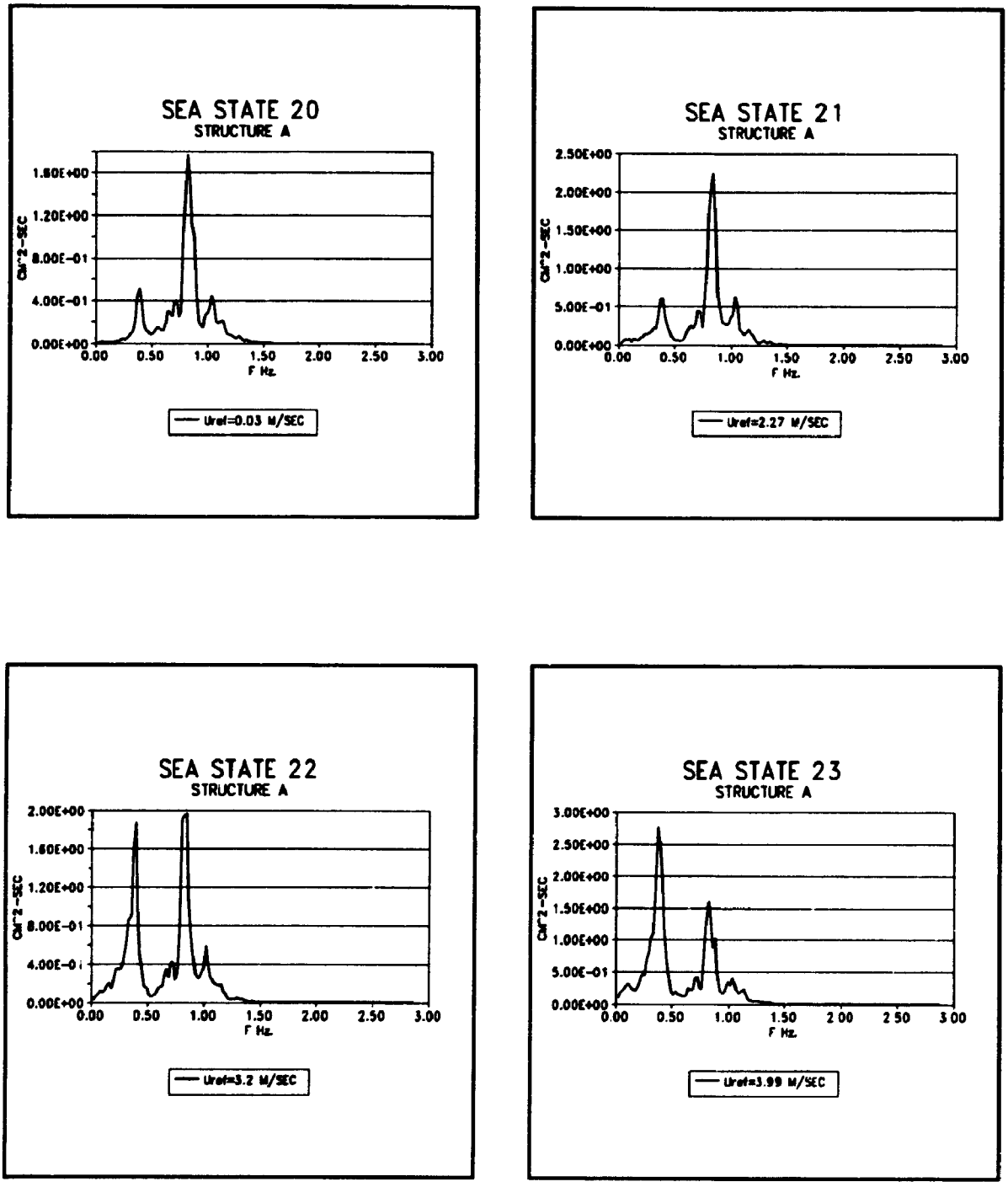

FIGURE F.3: Measured surge response spectra for different mean wind velocities (STRUCTURE A, WAVE STORM 2)

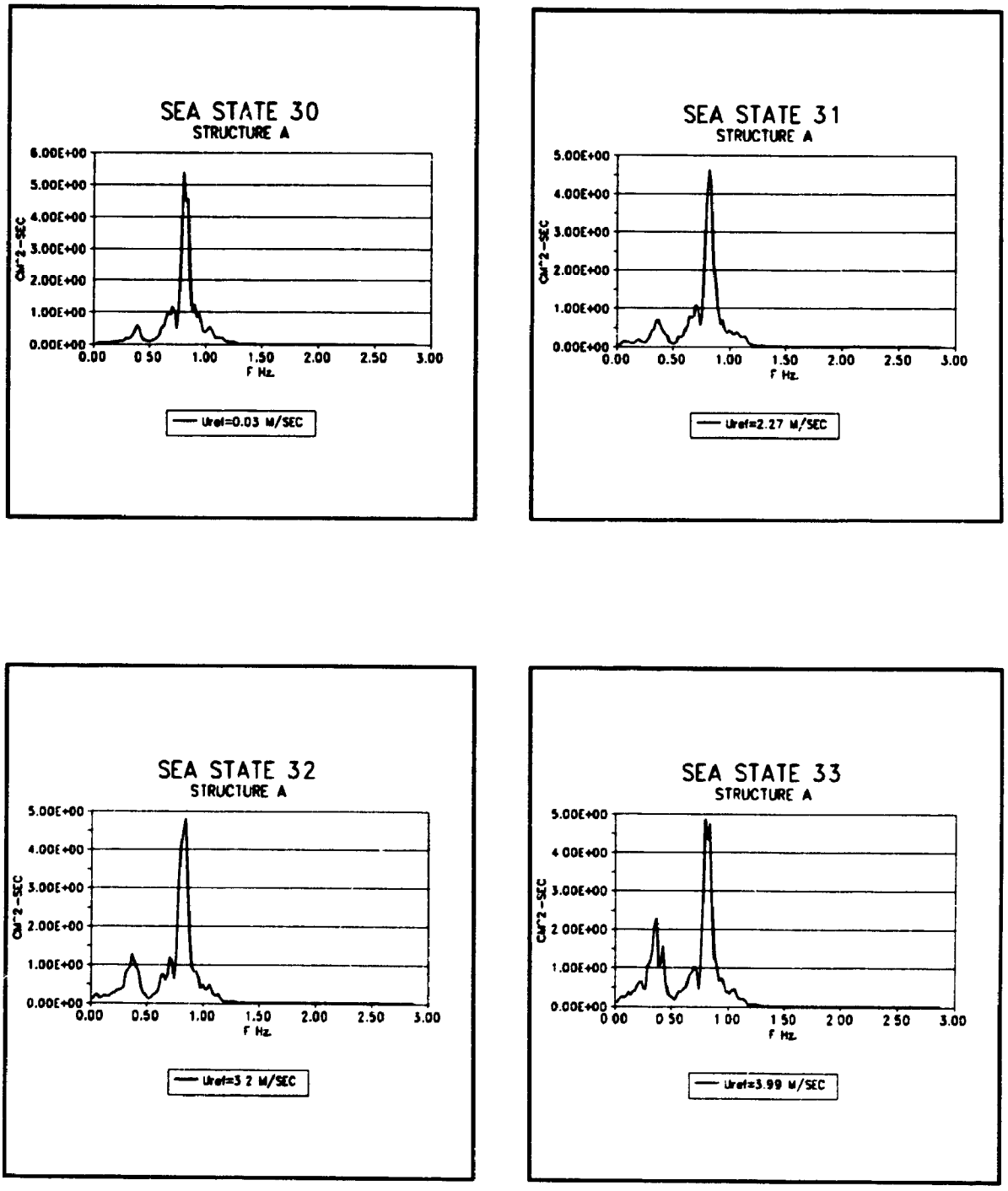

FIGURE F.4: Measured rms surge response spectra for different mean wind velocities (STRUCTURE A, WAVE STORM 3)

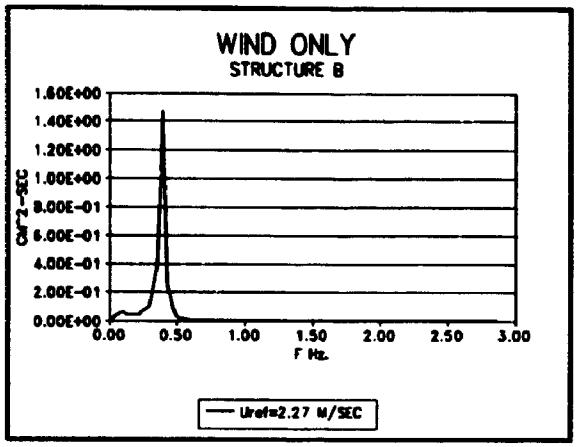

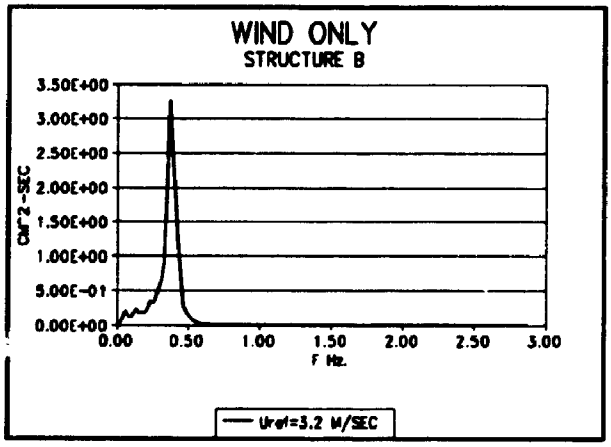

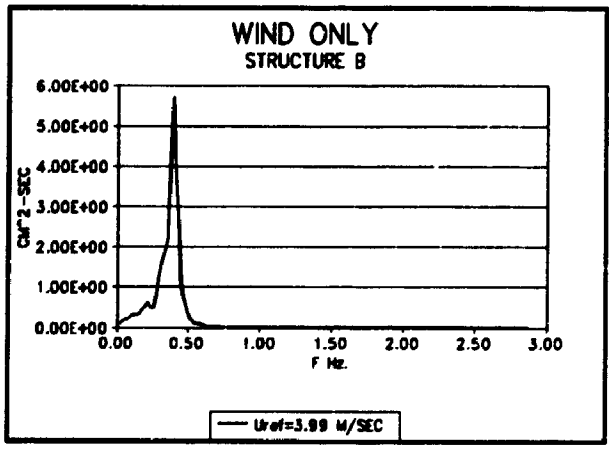

FIGURE F.5: Measured surge response spectra for different mean wind velocities (STRUCTURE B, WIND ONLY)

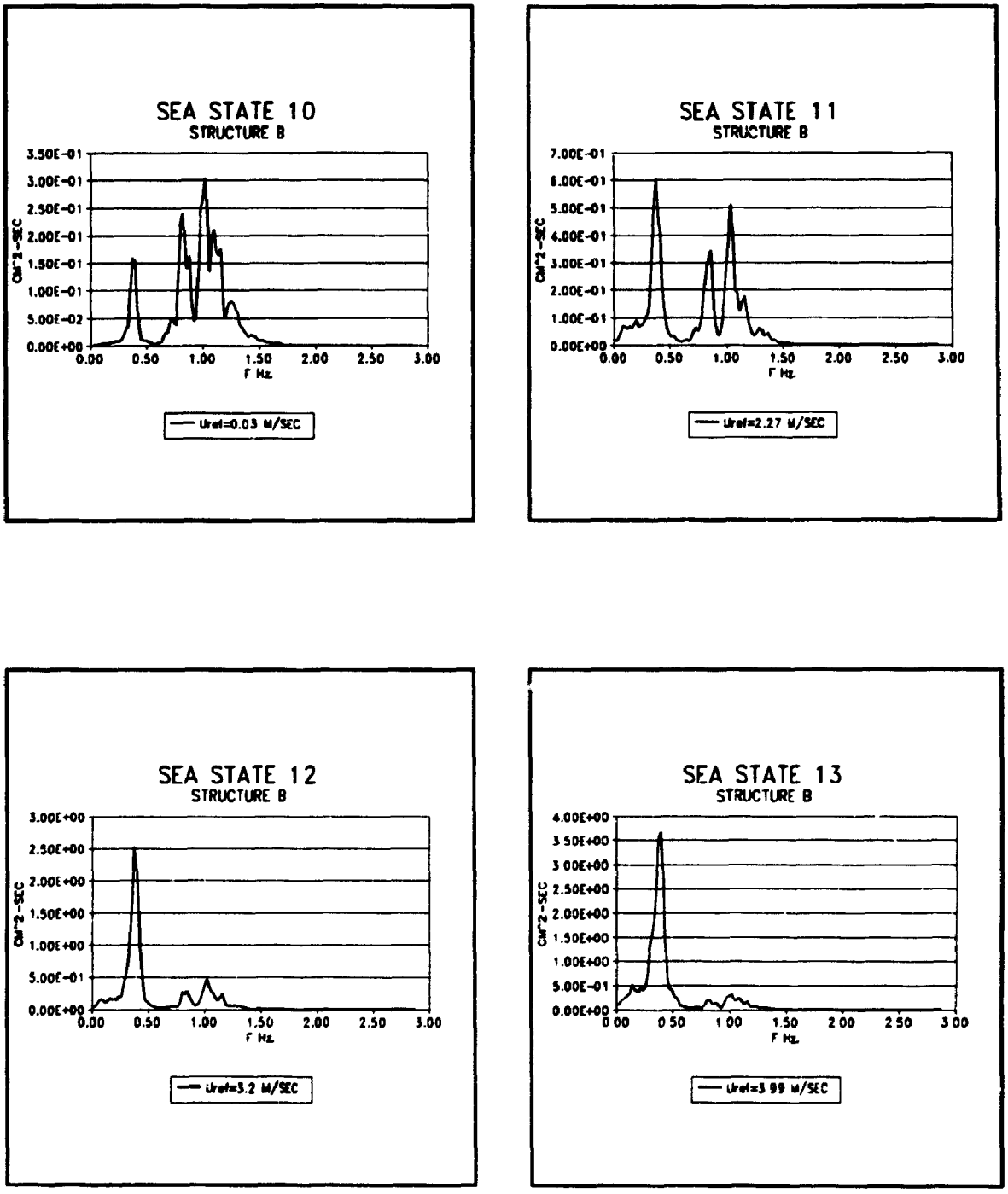

FIGURE F.6: Measured surge response spectra for different mean wind velocities (STRUCTURE B, WAVE STORM 1)

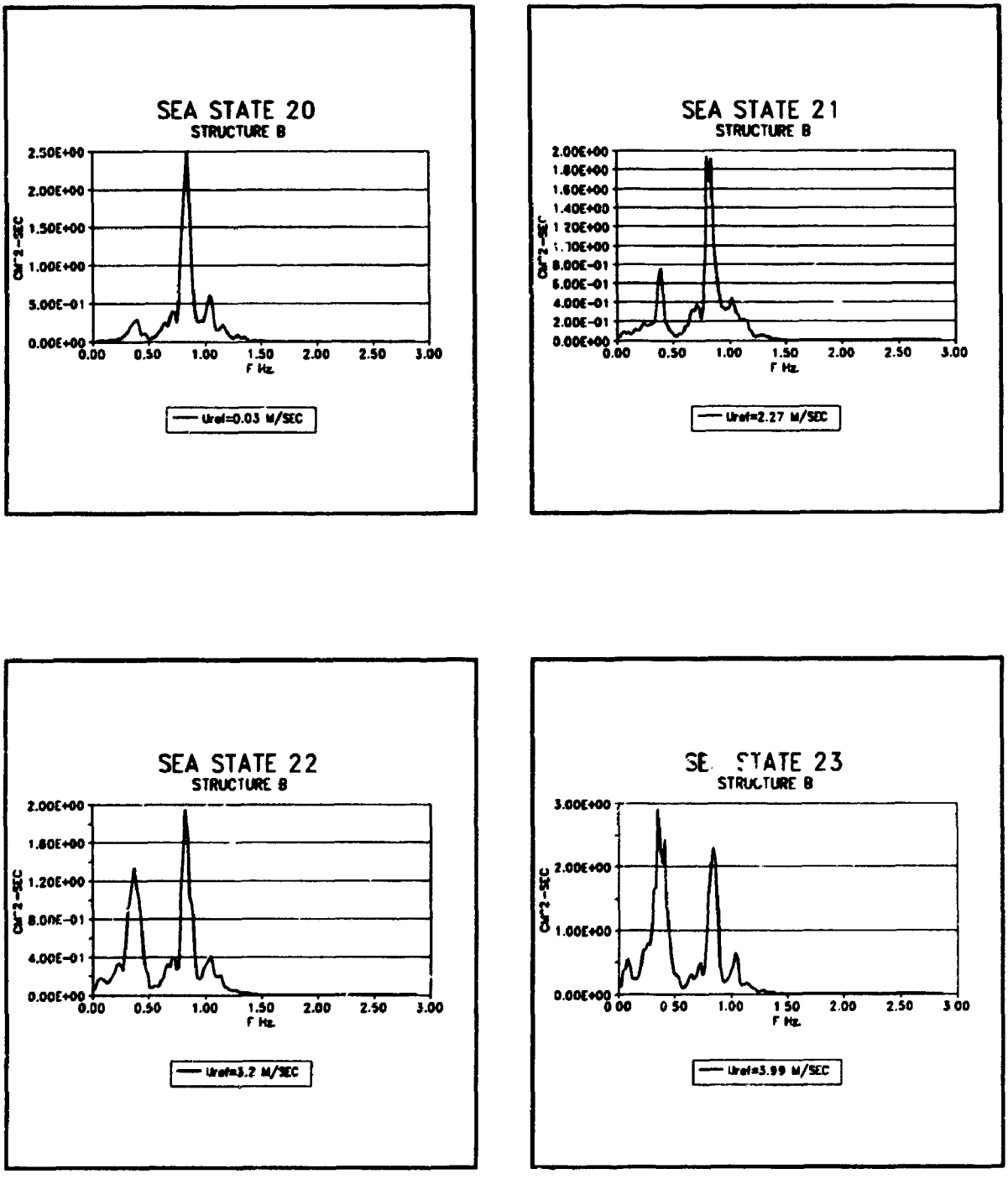

FIGURE F.7: Measured surge response spectra for different mean wind velocities (STRUCTURE B, WAVE STORM 2)

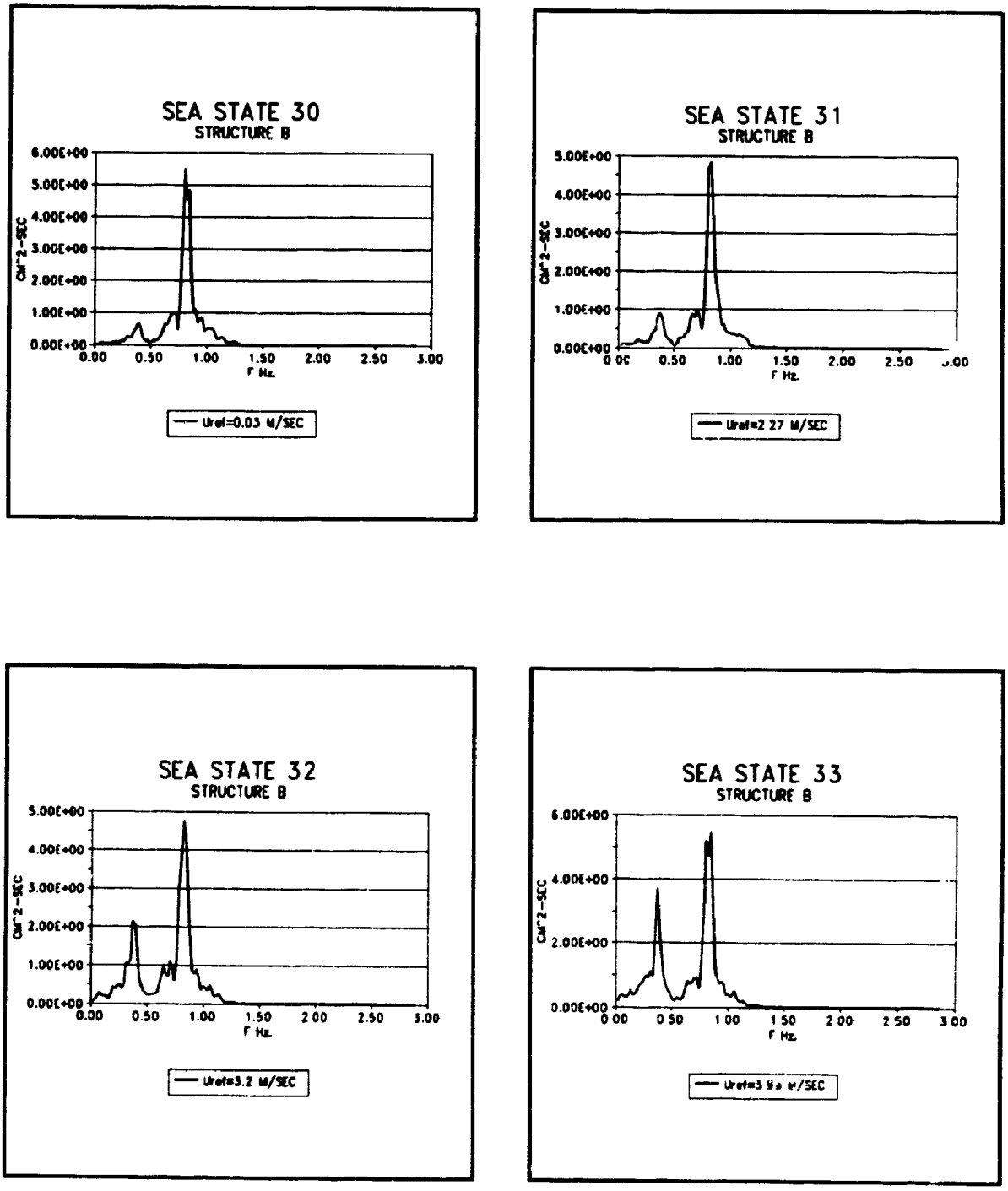

FIGURE F.8: Measured surge response for different mean wind velocities (STRUCTURE B, WAVE STORM 3)

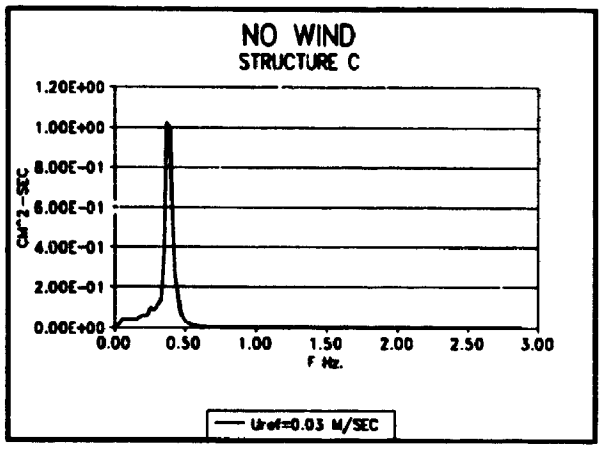

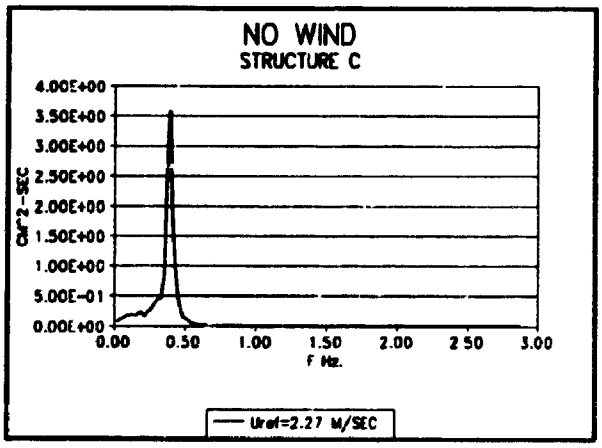

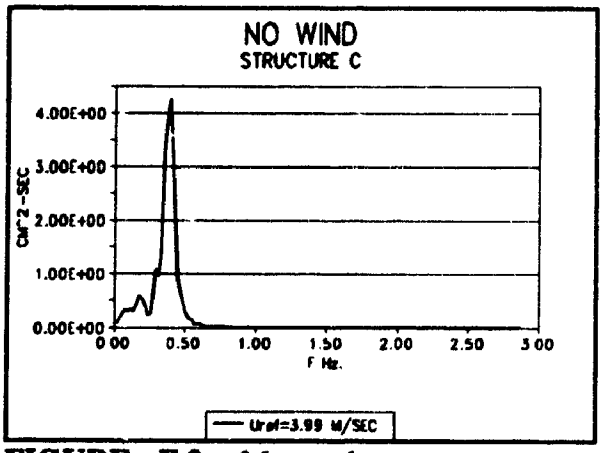

FIGURE F.9: Mesured surge response spectra for different mean wind velocities (STRUCTURE C, WAVE ONLY).

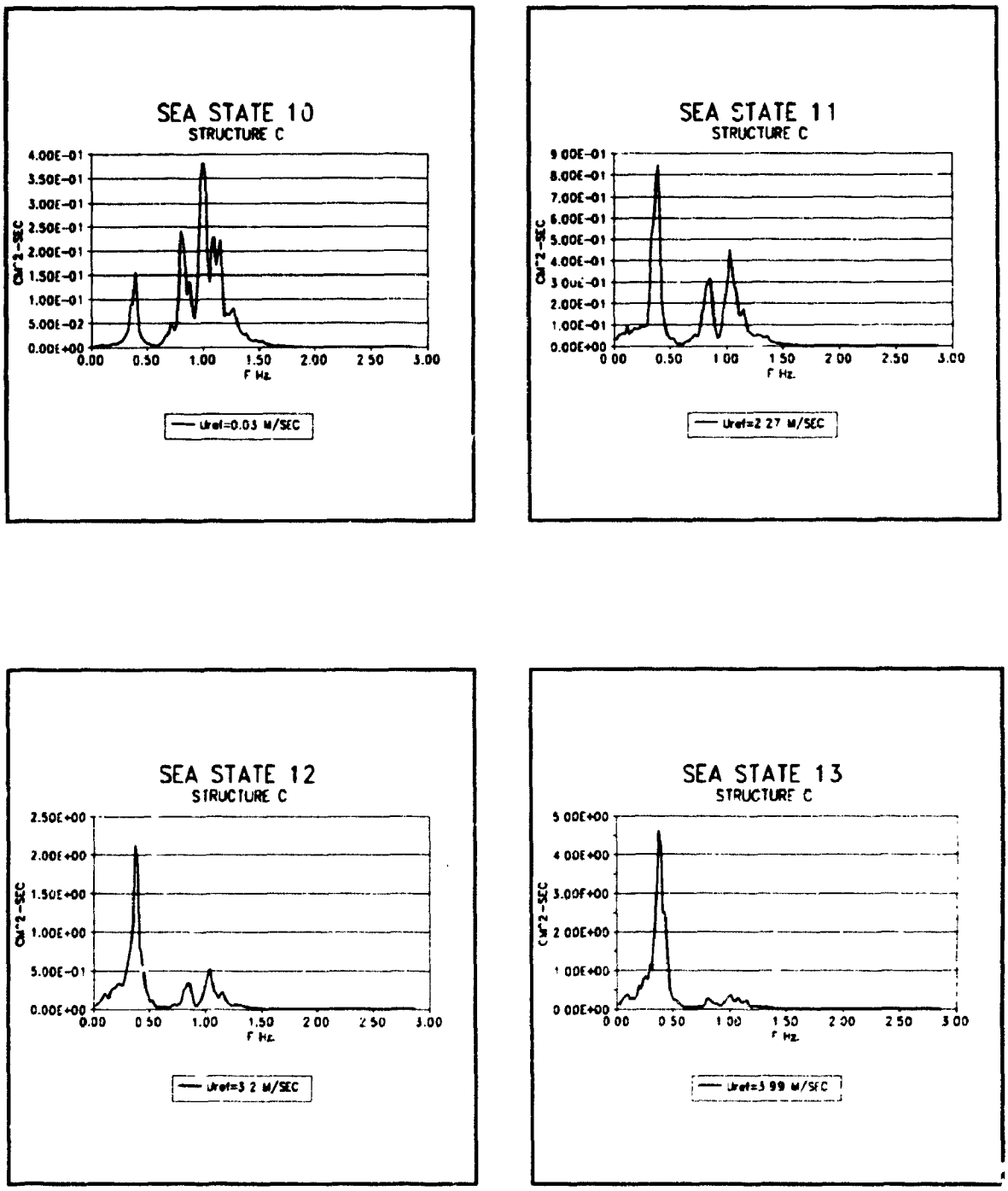

FIGURE F.10: Measured surge response spectra for different mean wind velocities (STRUCTURE C, WAVE STORM 1)

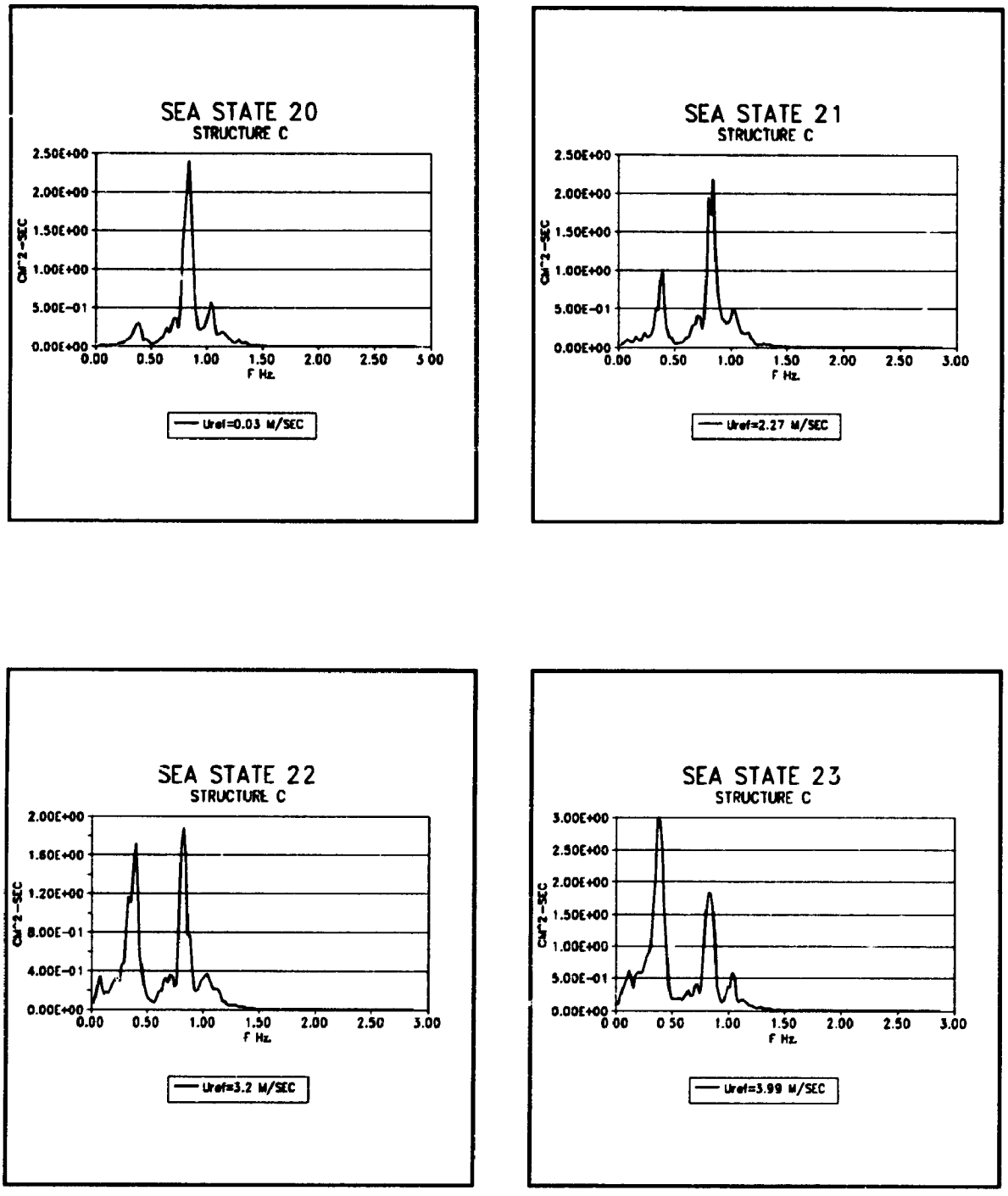

FIGURE F.11: Measured surge response spectra for different mean wind velocities (STRUCTURE C, WAVE STORM 2)

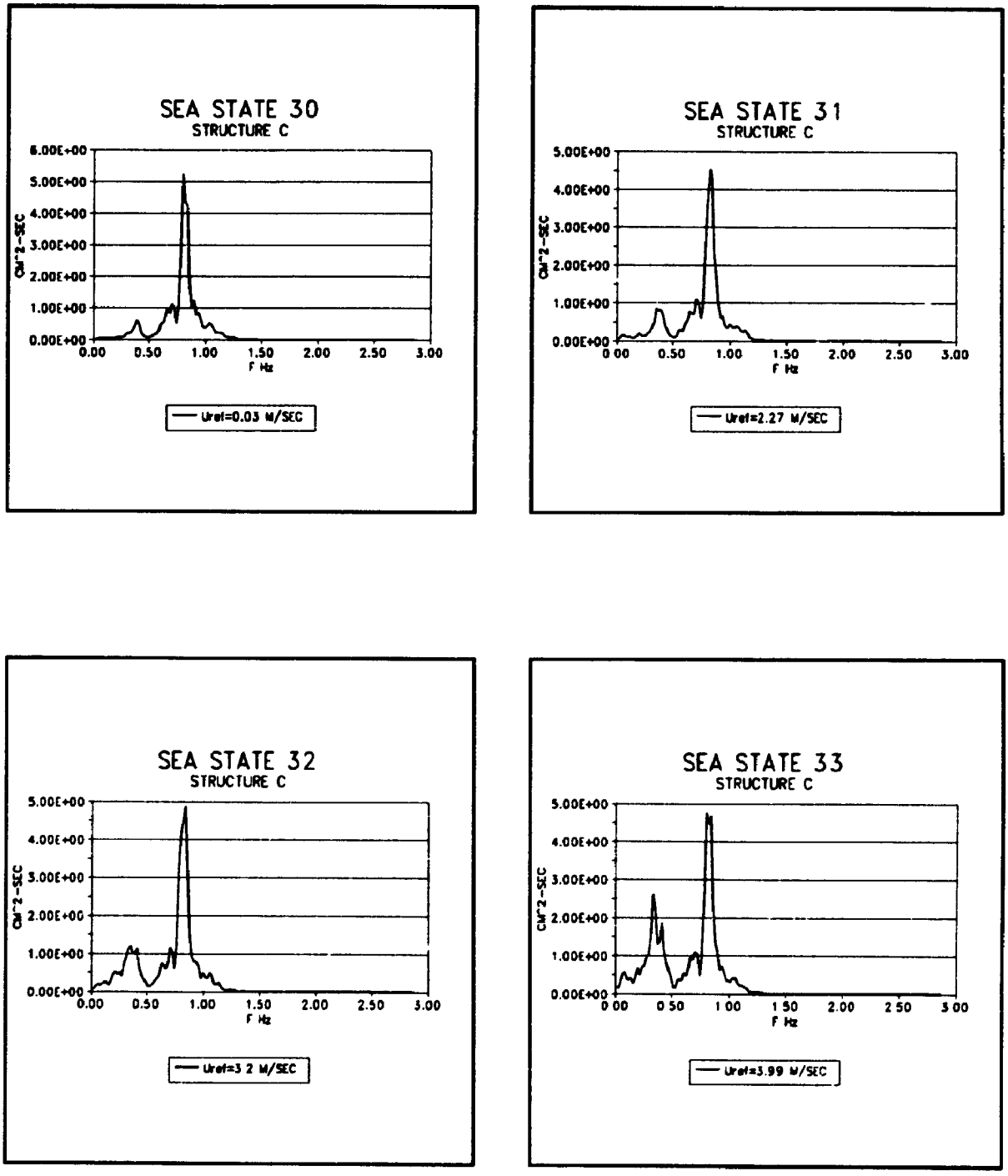

FIGURE F.12: Measured surge response spectra for different mean wind velocities (STRUCTURE C, WAVE STORM 3)

APPENDIX G

LOWER DECK LEVEL SURGE RESPONSE SPECTRA (TIME DOMAIN) FOR THE THREE STRUCTURAL CONFIGURATIONS A,B,C.

This appendix presents the lower deck level surge response spectra obtained based on time domain analysis. In each case the analysis is performed with and without inclusion of the free surface effects. The wind and wave loads employed in the computer program are those observed during the tests.

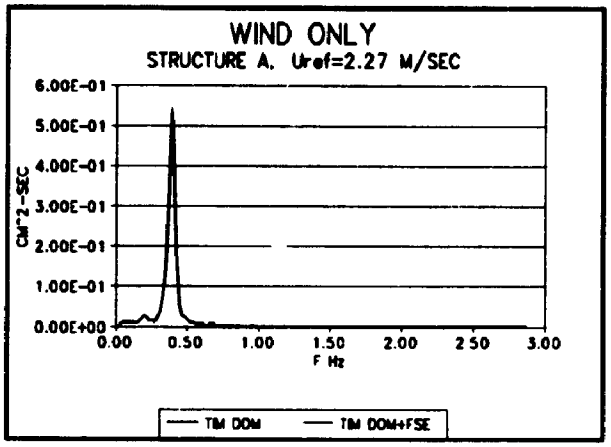

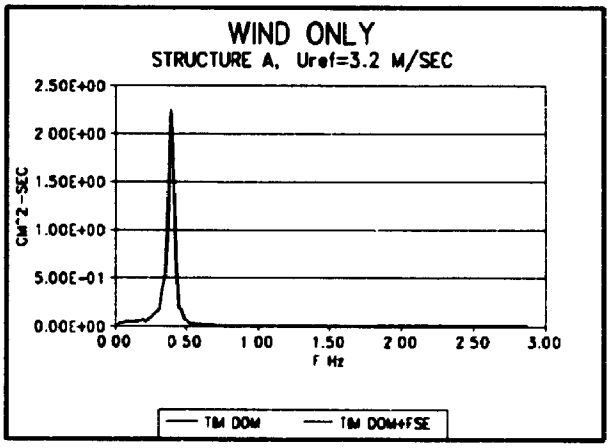

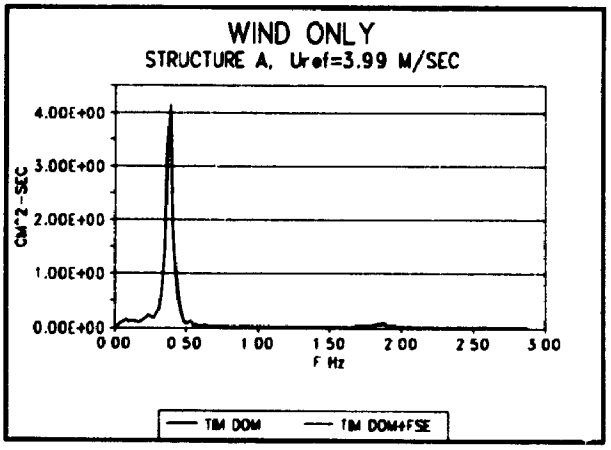

FIGURE G.1: Time domain surge response spectra (without and with inclusion of free surface drift effect) for different mean wind velocities (STRUCTURE A, WIND ONLY).

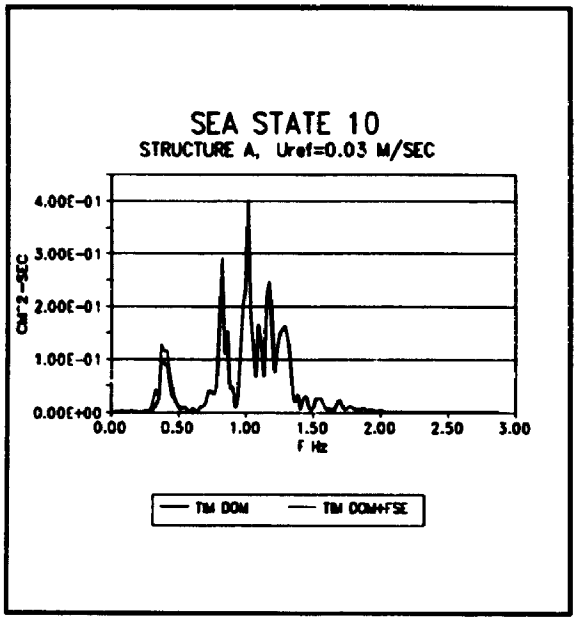

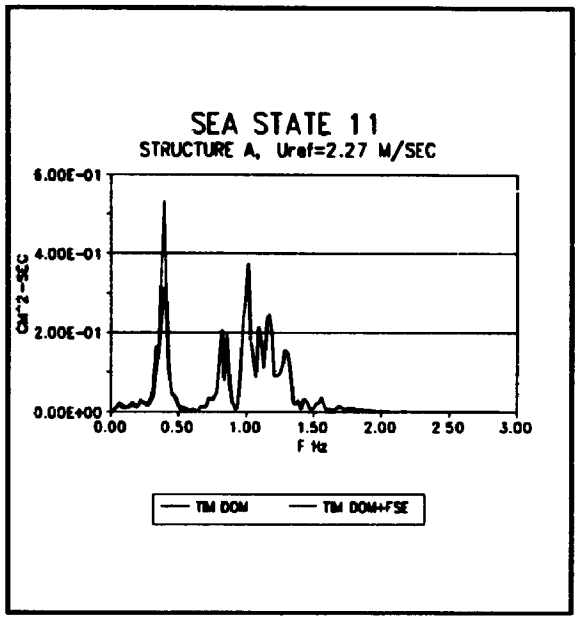

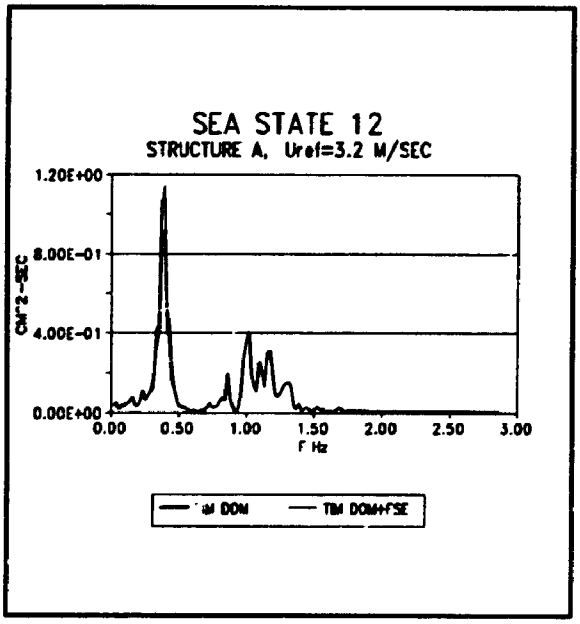

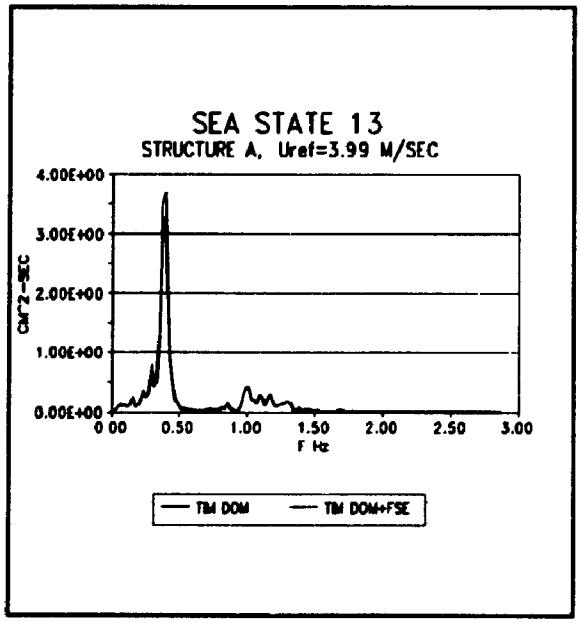

FIGURE G.2: Time domain surge response spectra (without and with inclusion of free surface drift effect) for different mean wind velocities (STRUCTURE A, WAVE STORM 1).

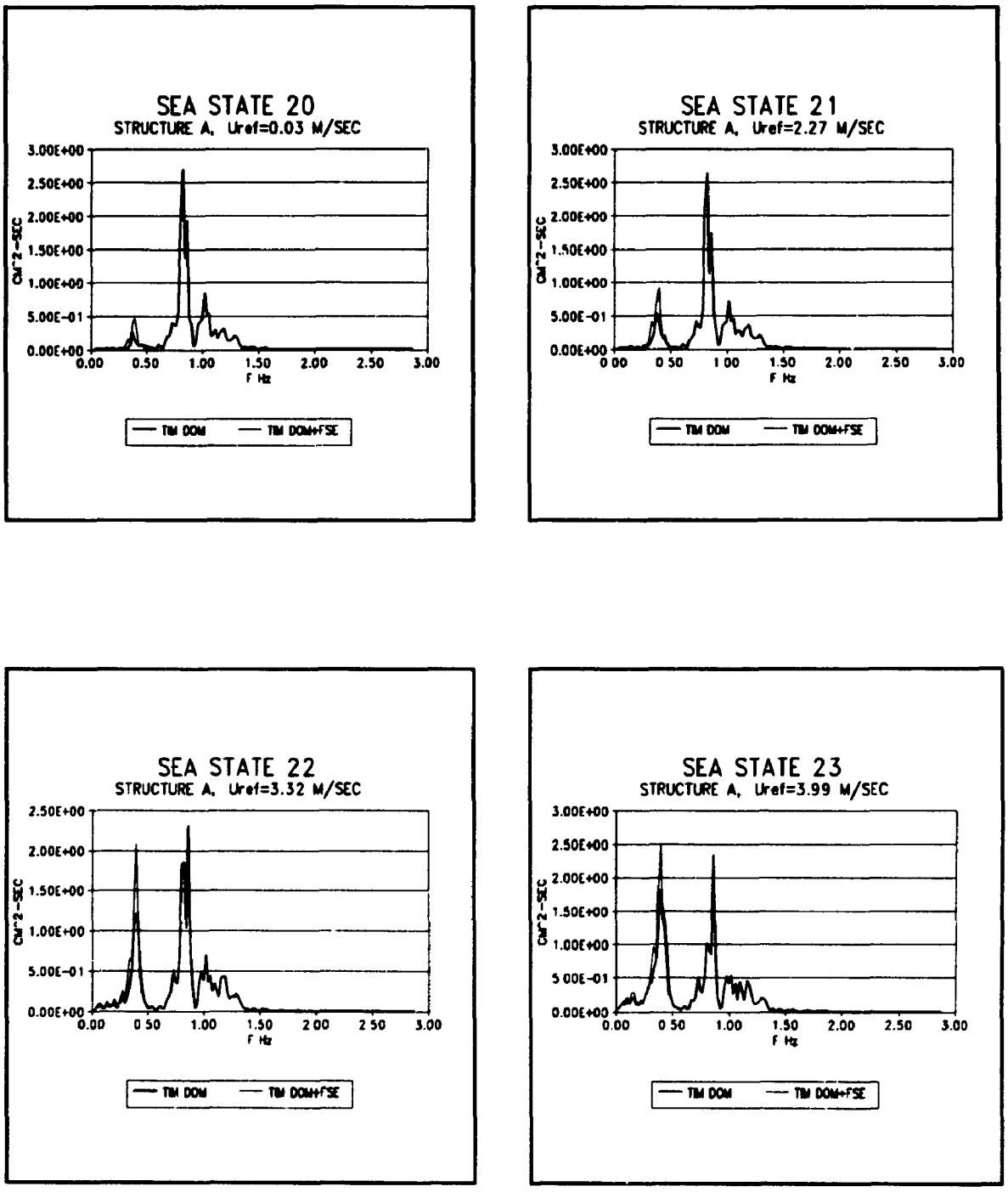

FIGURE G.3: Time domain surge response spectra (without and with inclusion of free surface drift effect) for different mean wind velocities (STRUCTURE A, WAVE STORM 2).

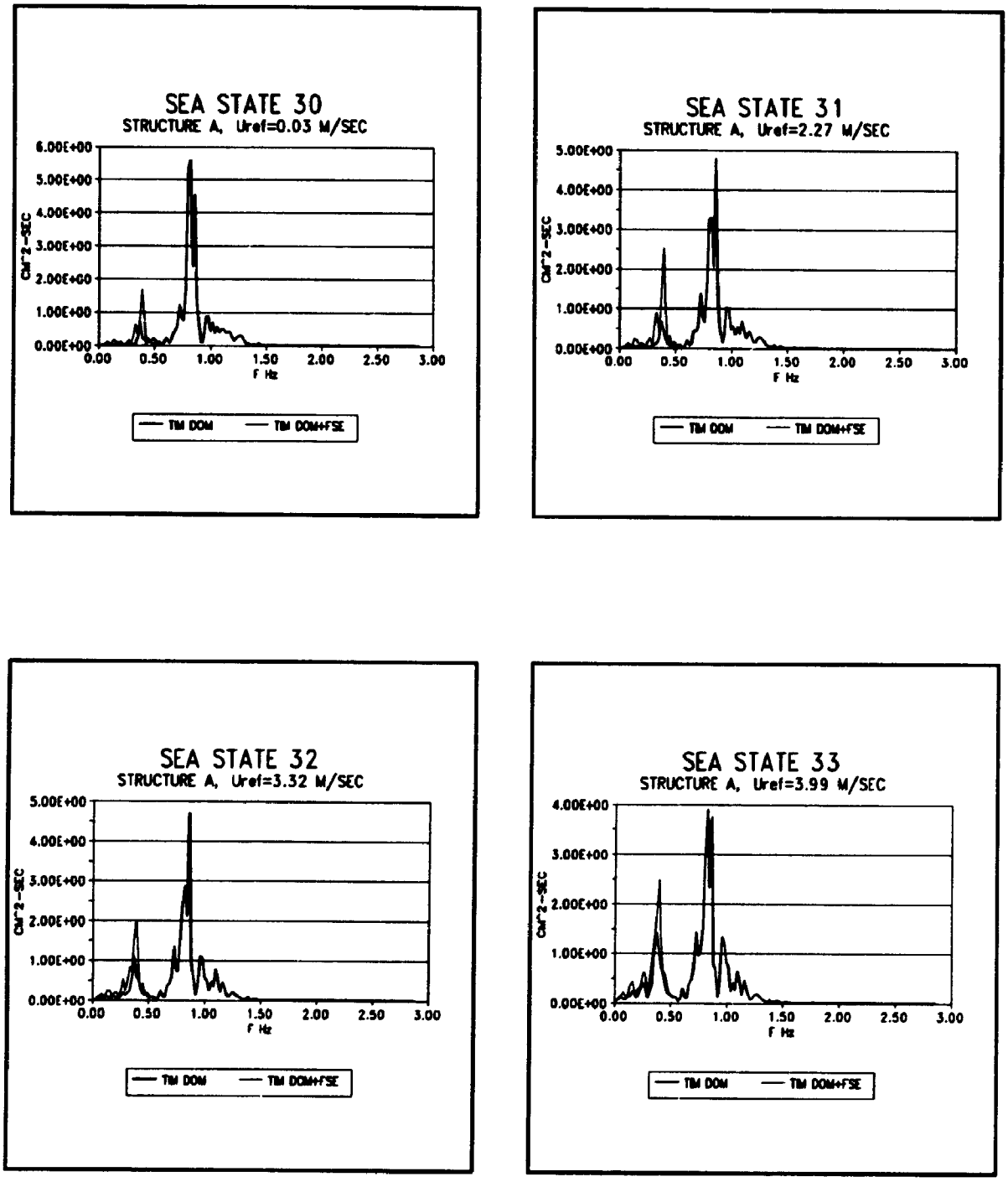

FIGURE G.4: Time domain surge response spectra (without and with inclusion of free surface drift effect) for different mean wind velocities (STRUCTURE A, WAVE STORM 3).

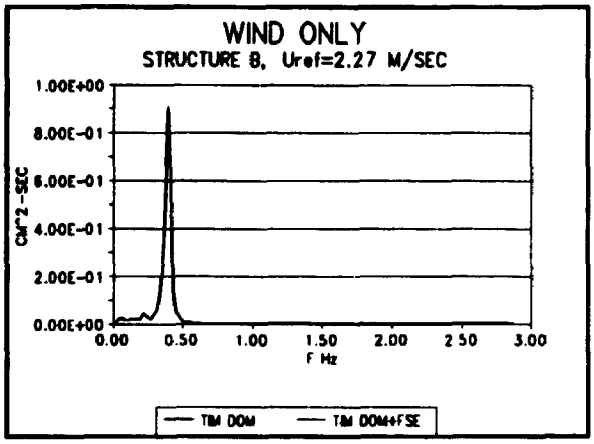

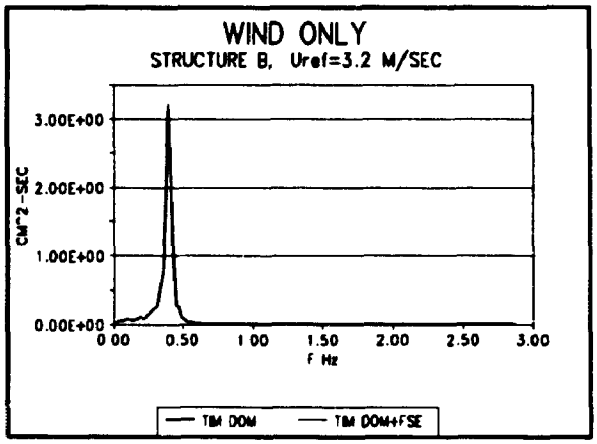

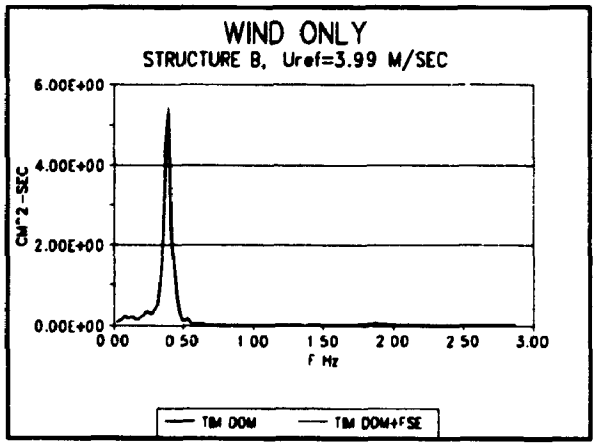

FIGURE G.5: Time domain surge response spectra (qwithout and with inclusion of free surface drift effect) for different mean wind velocities (STRUCTURE B, WIND ONLY).

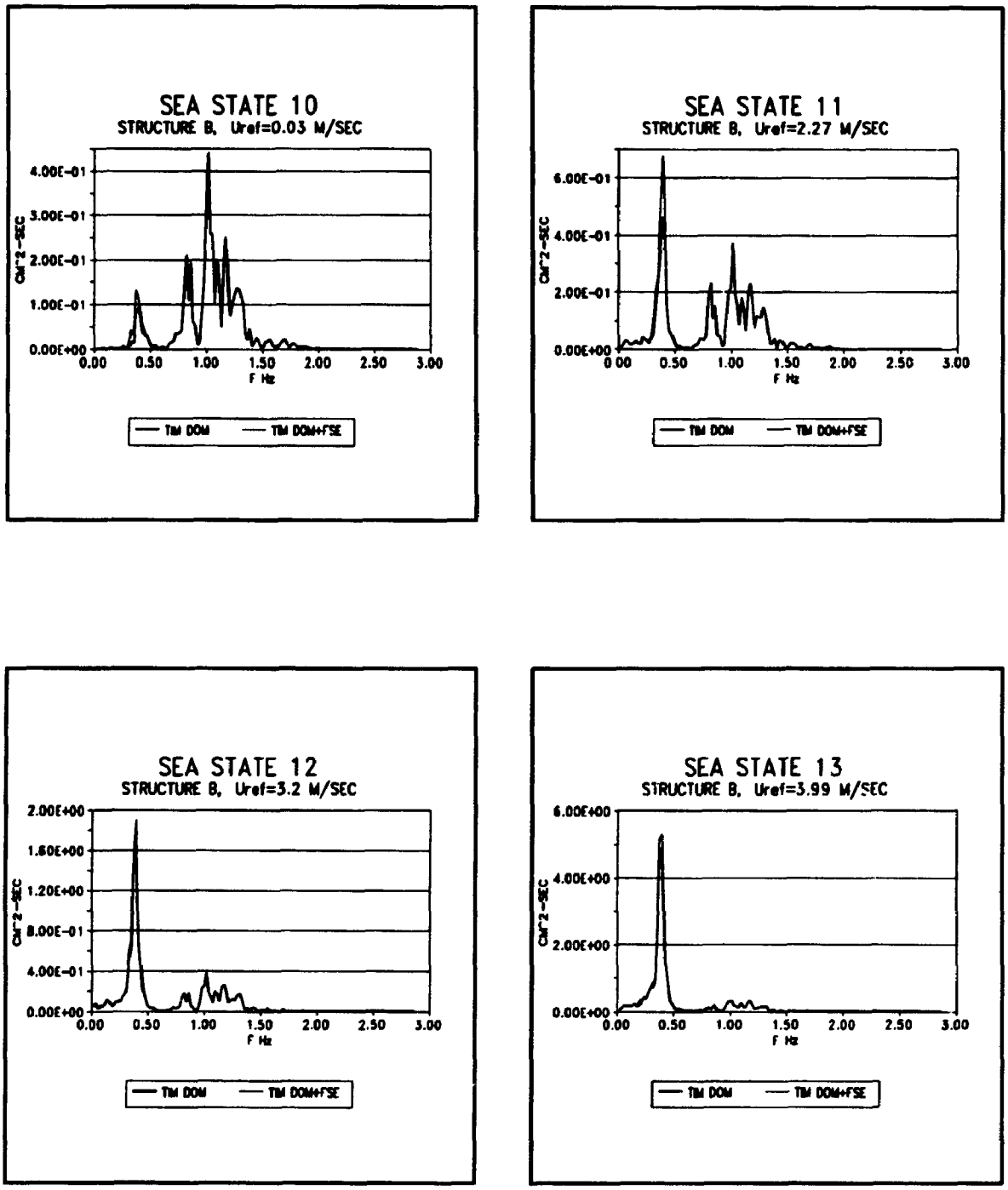

FIGURE G.6: Time domain surge response spectra (without and with inclusion of free surface drift effect) for different mean wind velocities (STRUCTURE B, WAVE STORM 1).

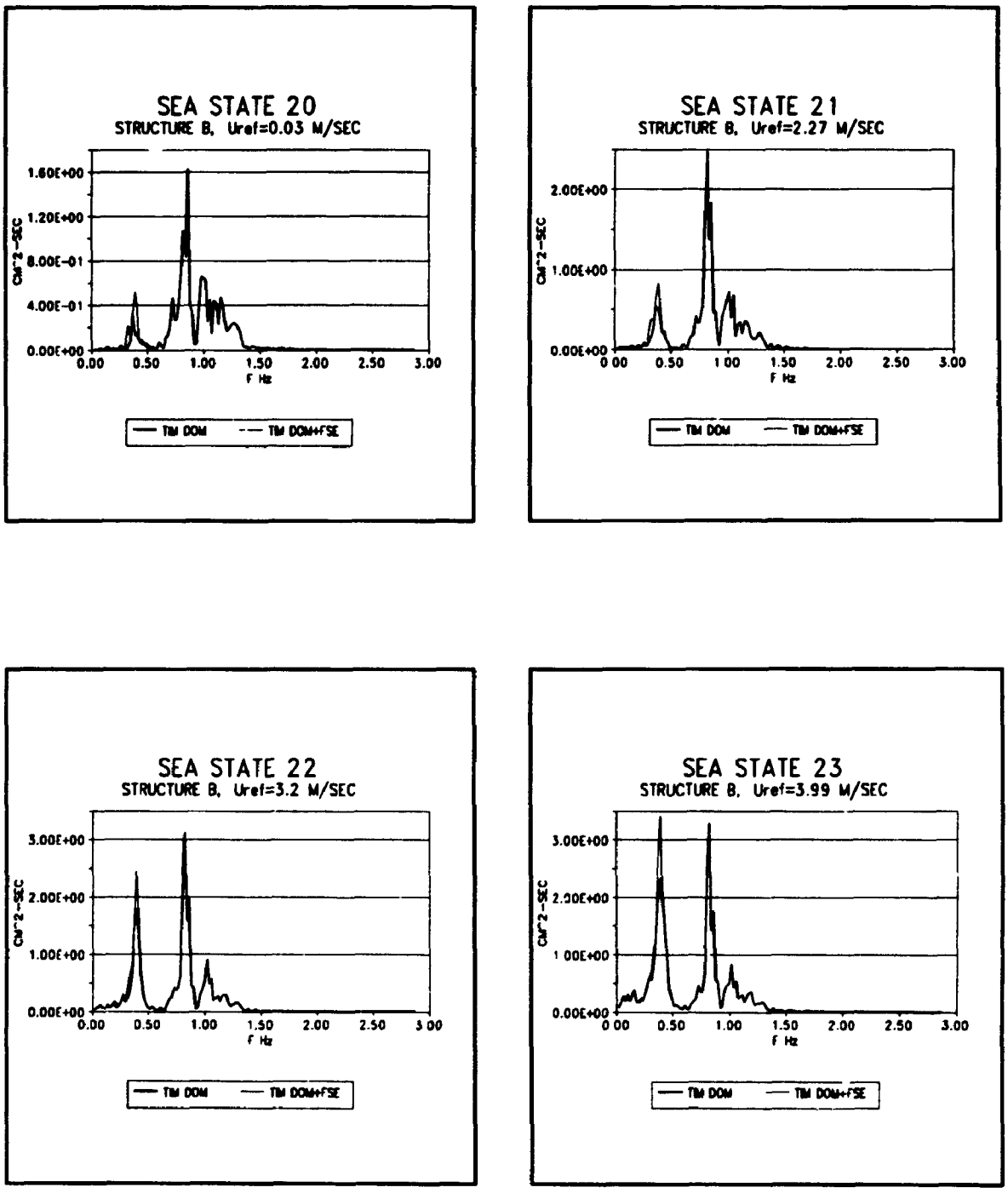

FIGURE G.7: Time domain surge response spectra (without and with inclusion of free surface drift effect) for different mean wind velocities (STRUCTURE B, WAVE STORM 2).

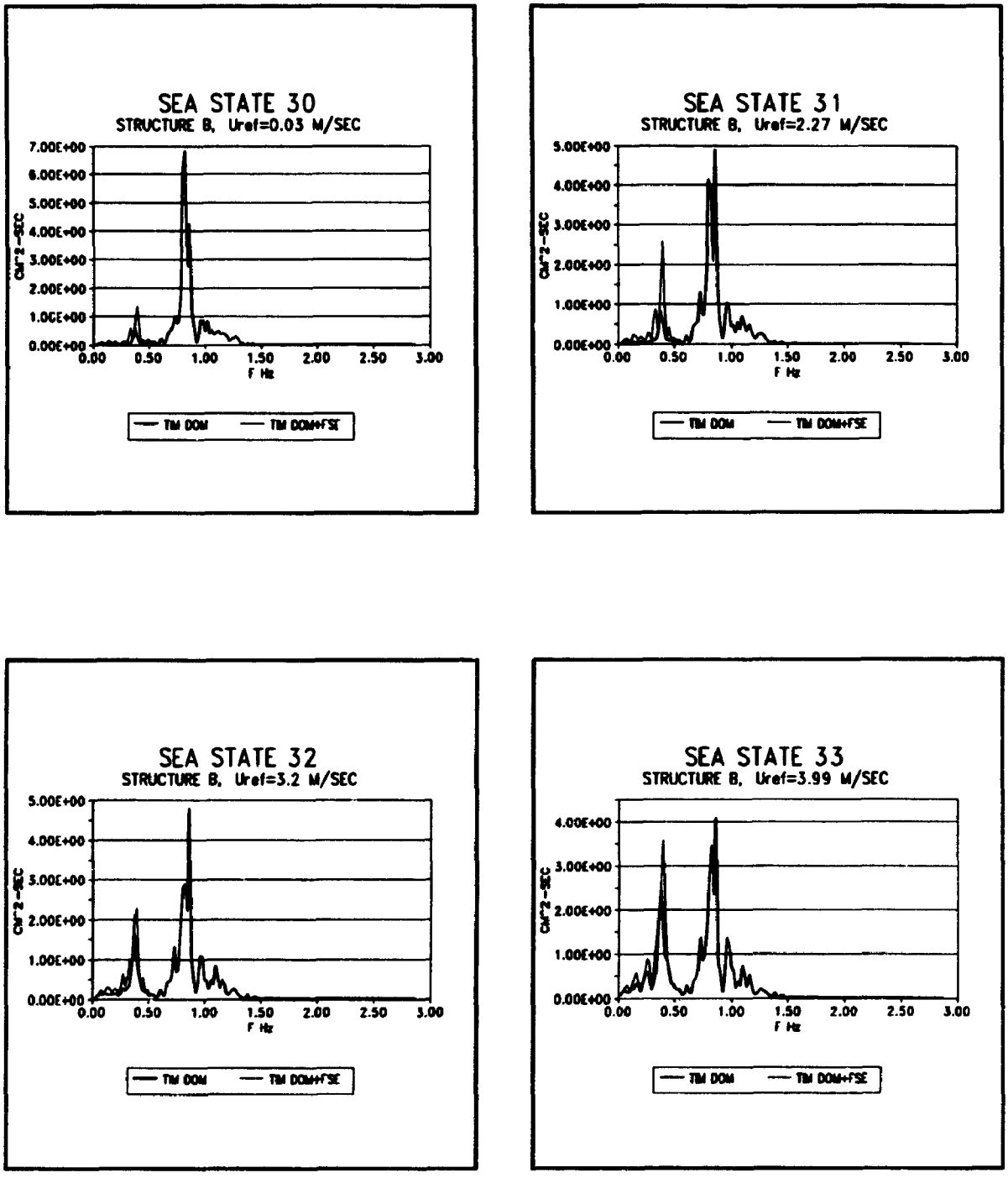

FIGURE G.8: Time domain surge response spectra (without and with inclusion of free surface drift effect) for different mean wind velocities (STRUCTURE B, WAVE STORM 3).

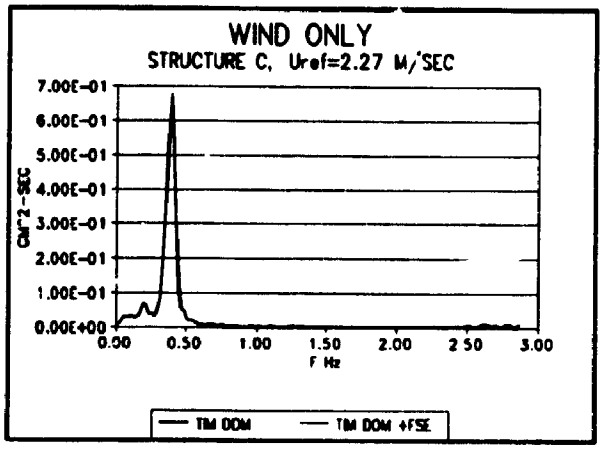

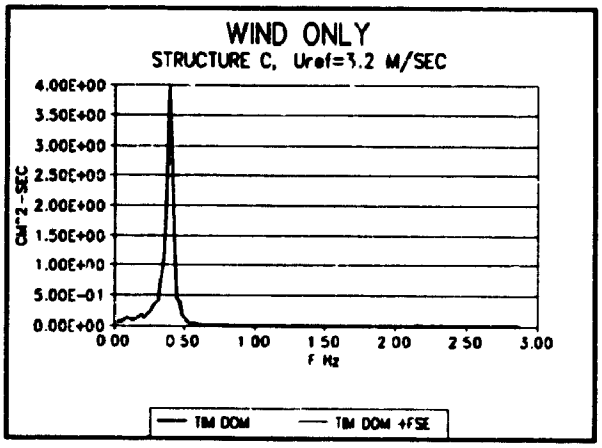

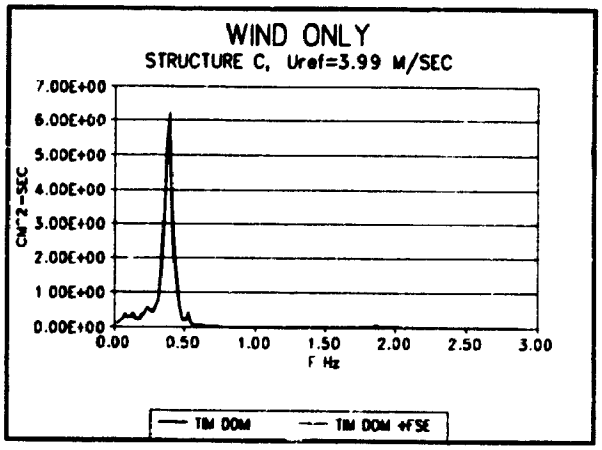

FIGURE G.9: Time domain surge response spectra (without and with inclusion of free surface effect) for different mean wind velocities (STRUCTURE C, WIND ONLY).

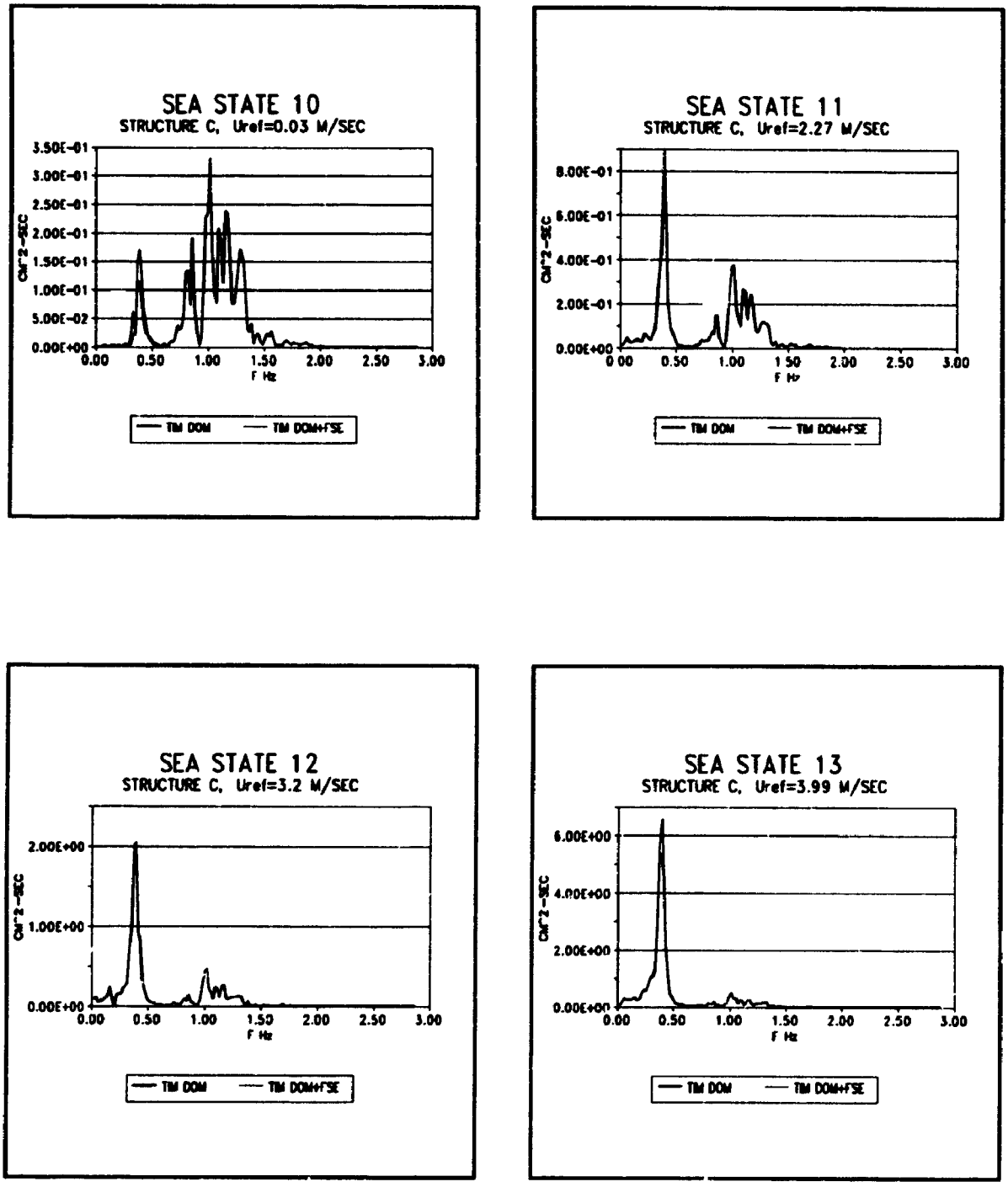

FIGURE G.10: Time domain surge response spectra (without and with inclusion of free surface drift effect) for different mean wind velocities (STRUCTURE C, WAVE STORM 1).The heavy line shows the result without the free surface effect.

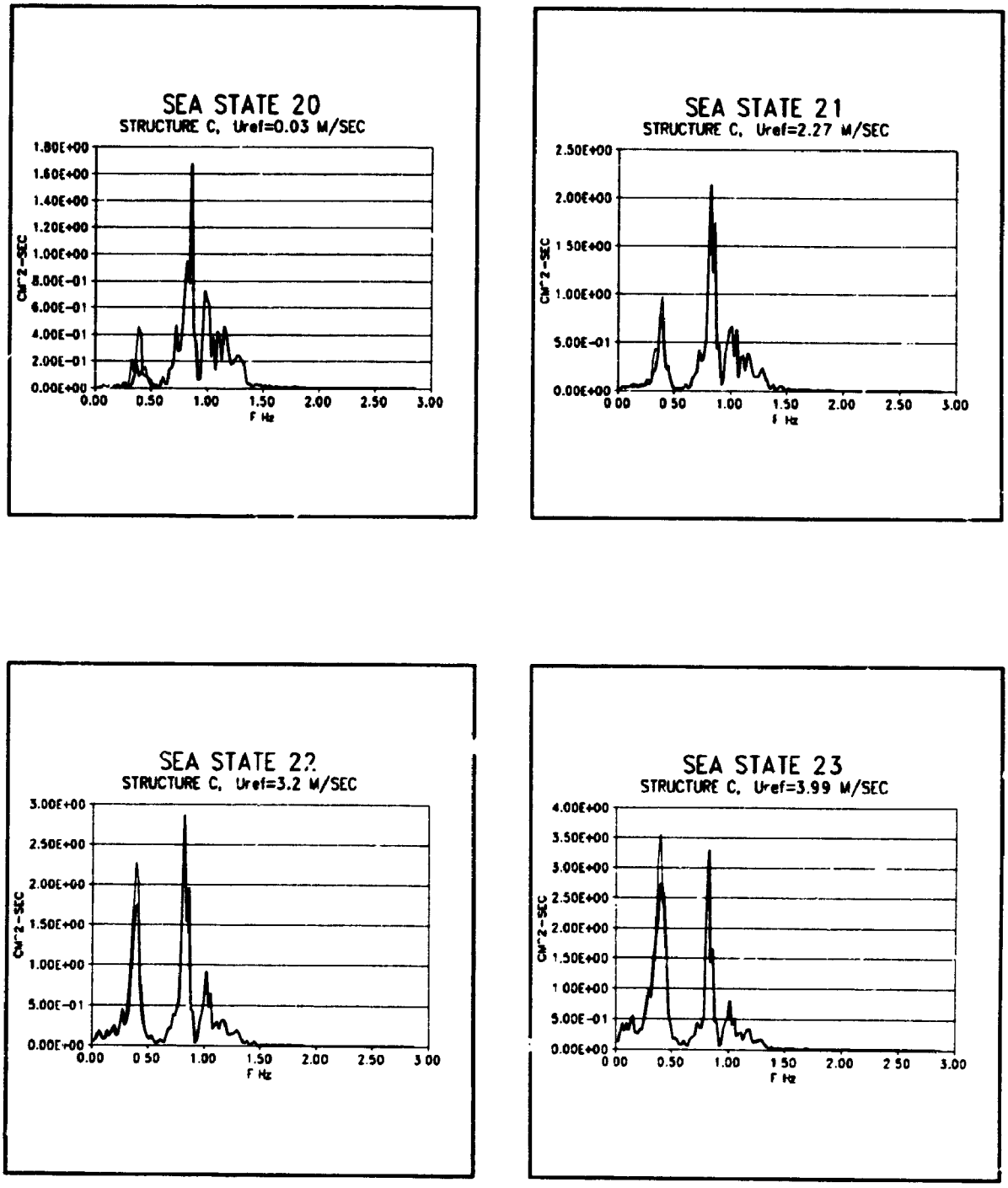

FIGURE G.11: Time domain surge response spectra (without and with inclusion of surface drift effect) for different mean wind velocities (STRUCTURE C, WAVE STORM 2).The heavy line shows the result without the free surface effect.

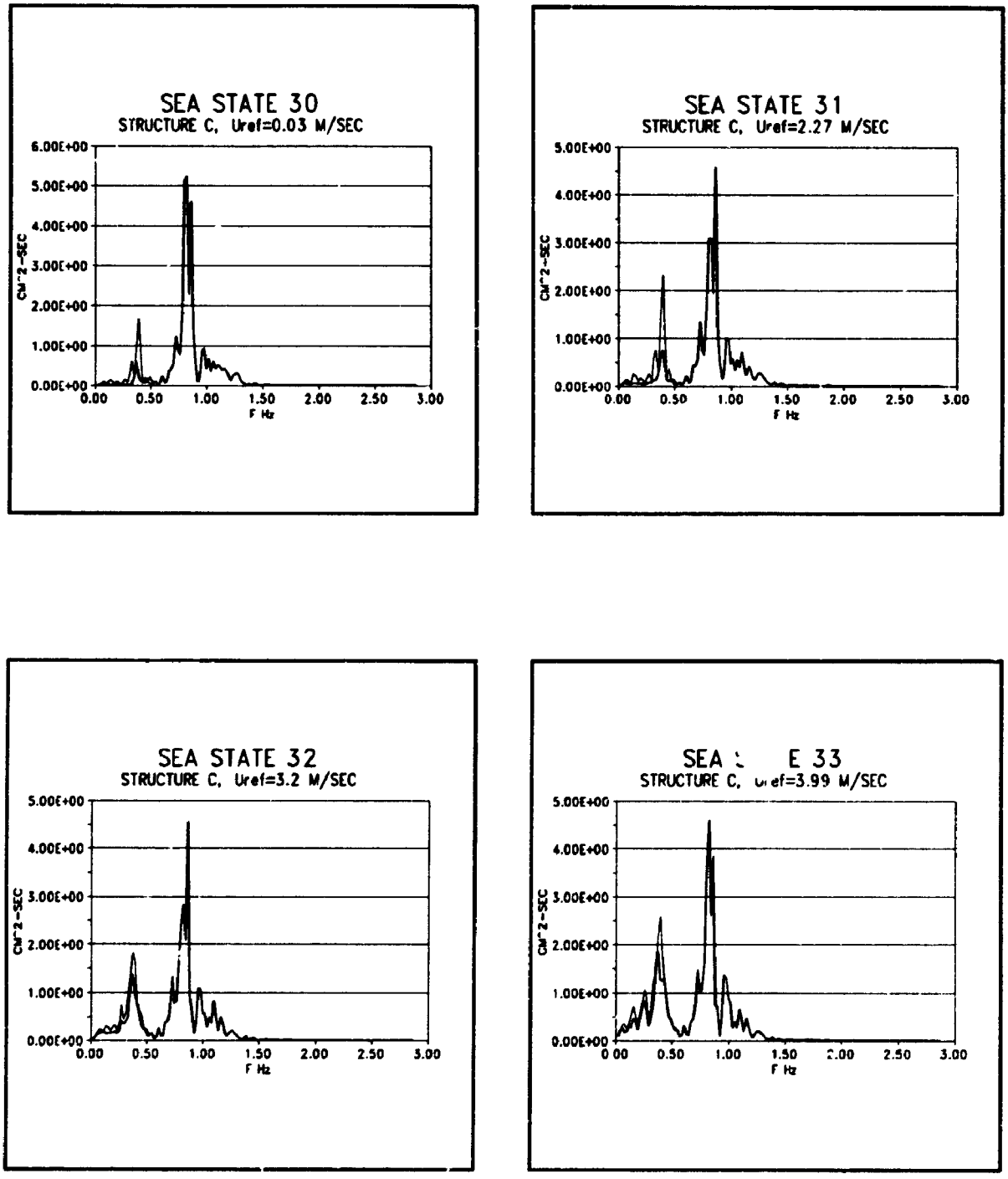

FIGURE G.12: Time domain surge response spectra (without and with inclusion of surface drift effect) for different mean wind velocities (STRUCTURE C, WAVE STORM 3).The heavy line shows the result without the free surface effect.

APPENDIX H

LOWER DECK LEVEL SURGE RESPONSE SPECTRA (BASED ON THE LINEARIZED FREQUENCY DOMAIN ANALYSIS) FOR THE THREE STRUCTURAL CONFIGURATIONS (A,B,C).

This appendix presents the lower deck level surge response spectra obtained based on frequency domain analysis. The wind and wave loads employed in the computer program are those observed during the tests.

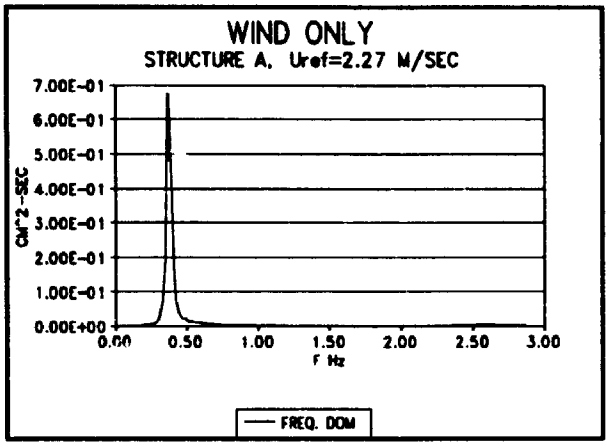

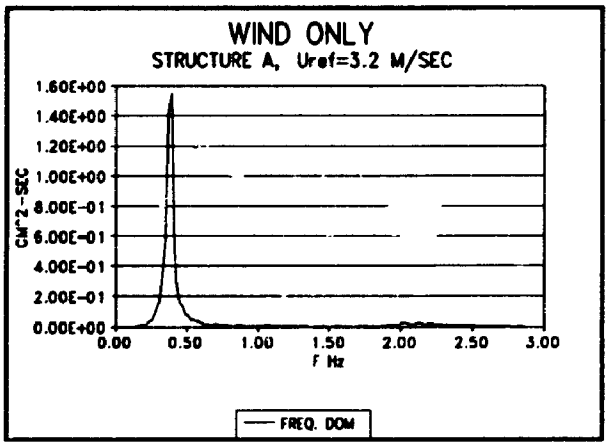

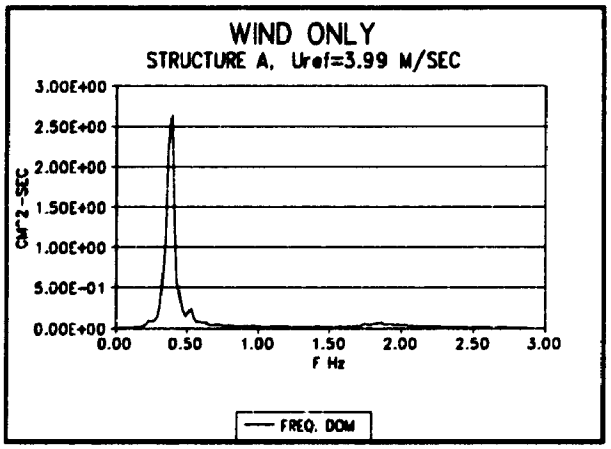

FIGURE H.1: Linearized frequency domain surge response spectra for different mean wind velocities (STRUCTURE A, WIND ONLY).

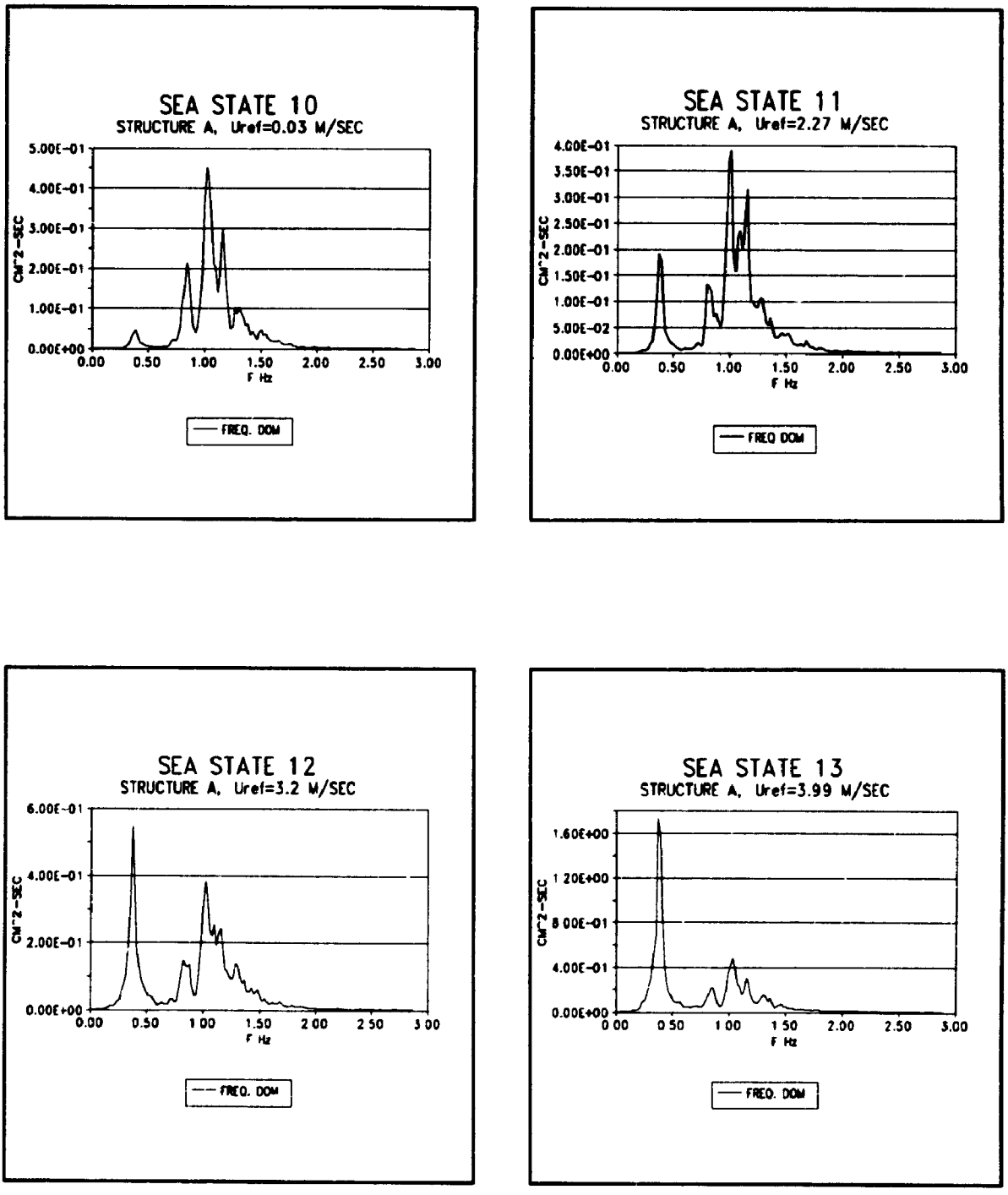

FIGURE H.2: Linearized frequency domain surge response spectra for different mean wind velocities (STRUCTURE A, WAVE STORM 1).

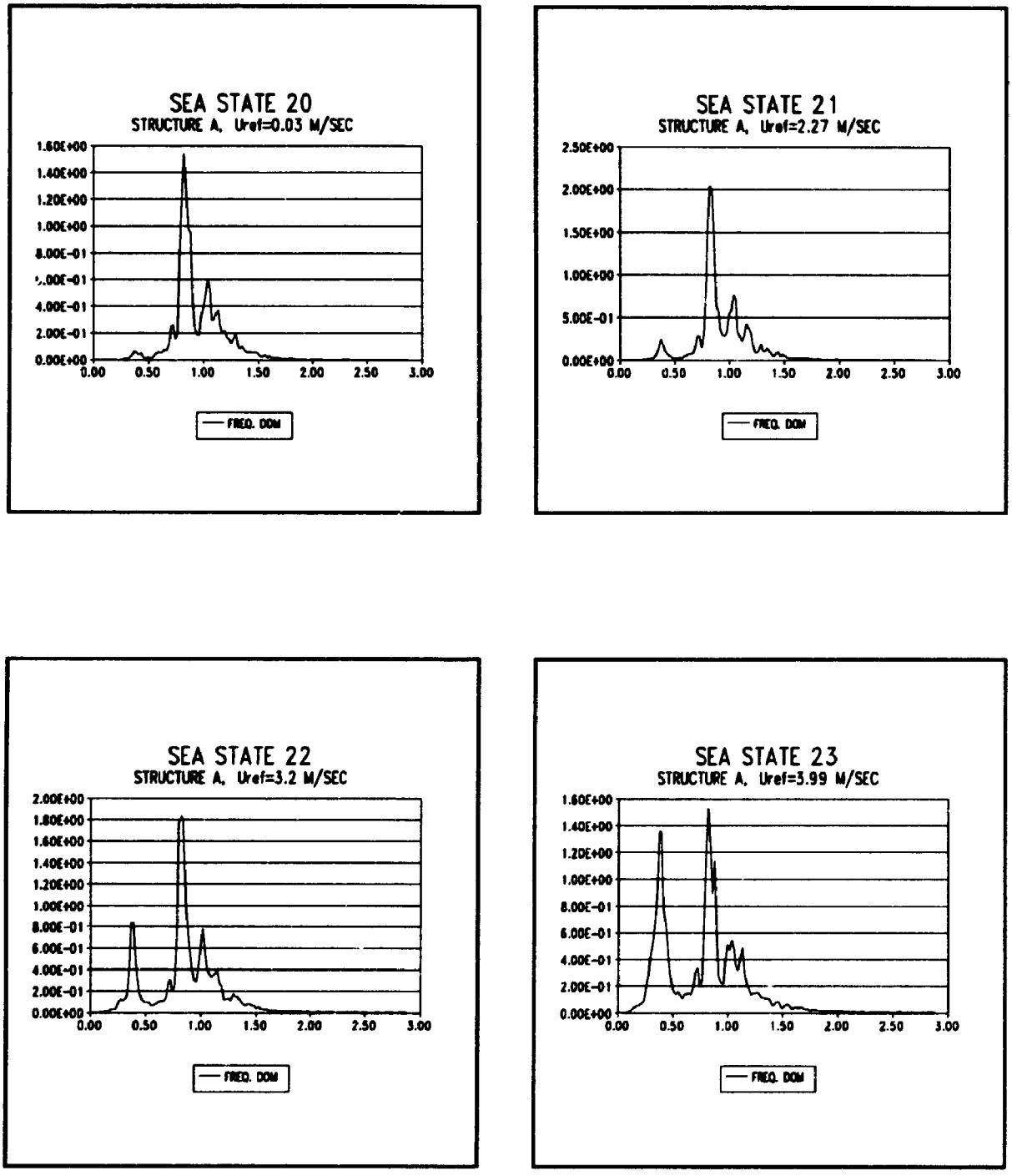

FIGURE H.3: Linearized frequency domain surge response spectra for different mean wind velocities (STRUCTURE A, WAVE STORM 2).

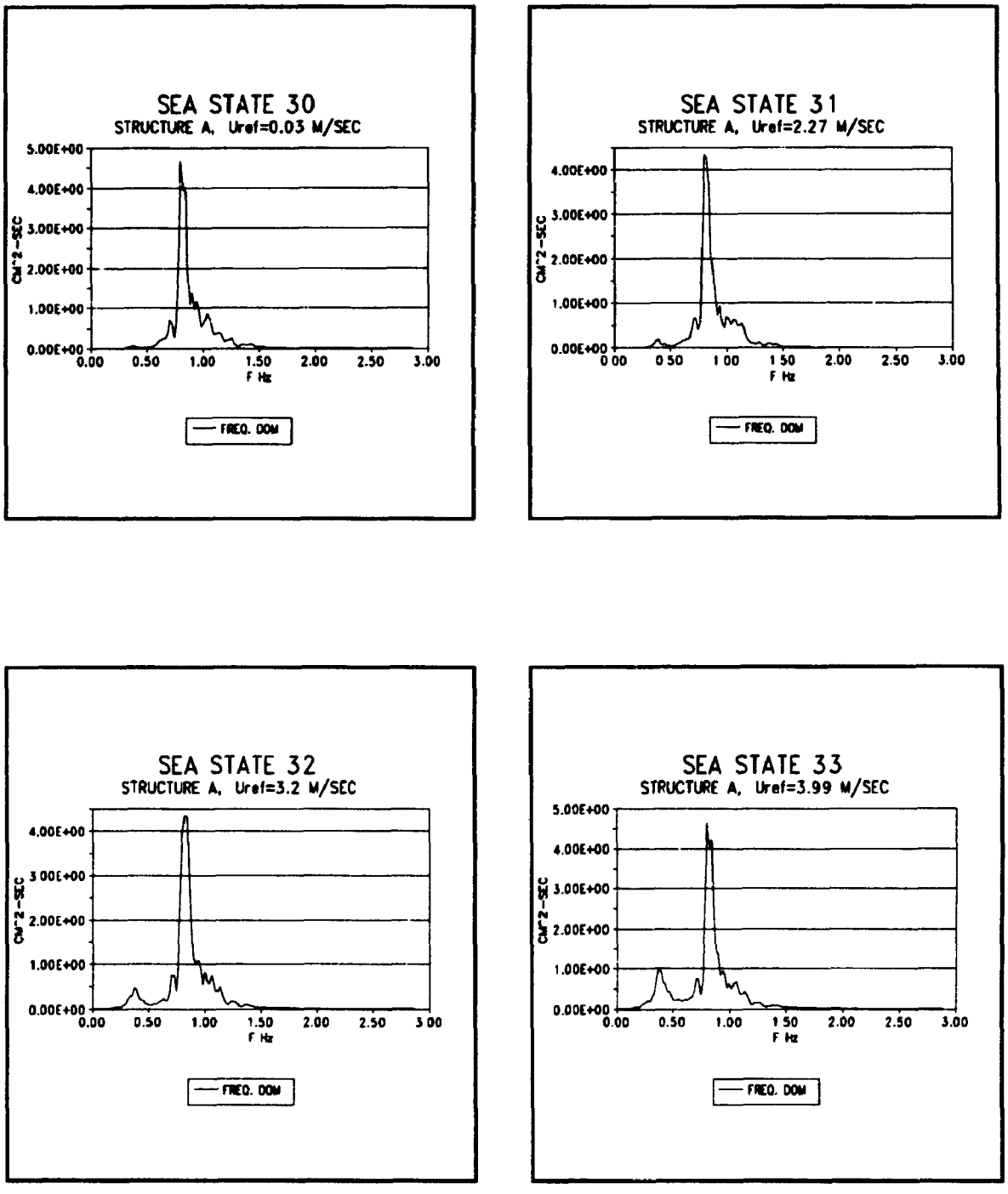

FIGURE H.4: Linearized frequency domain surge response spectra for different mean wind velocities (STRUCTURE A, WAVE STORM 3).

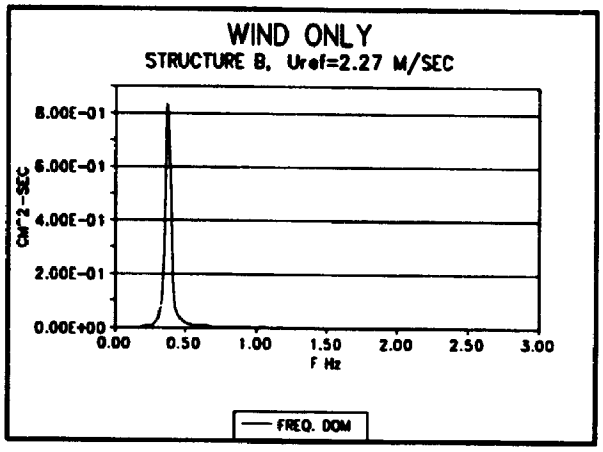

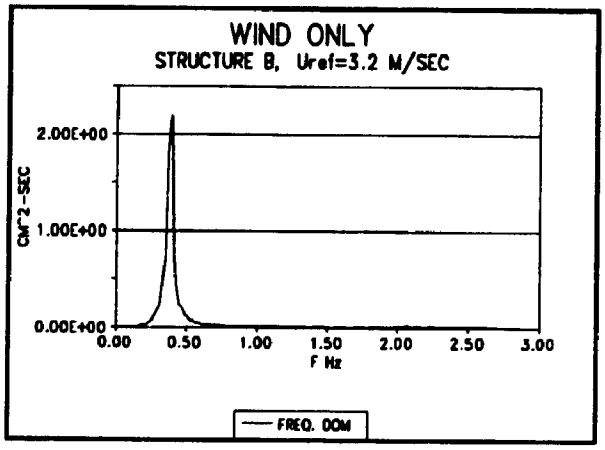

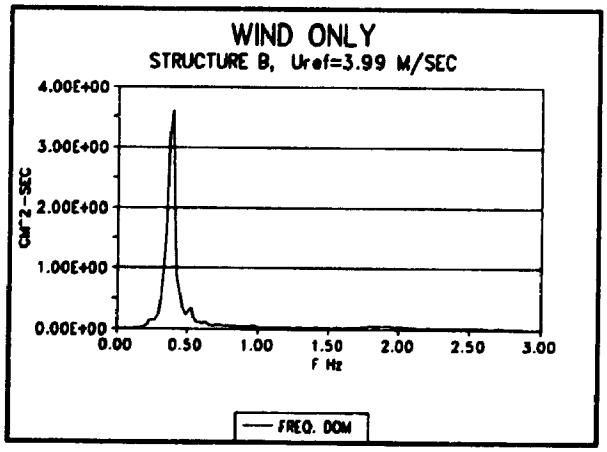

FIGURE H.5: Linearized frequency domain surge response spectra for different mean wind velocities (STRUCTURE B, WIND ONLY).

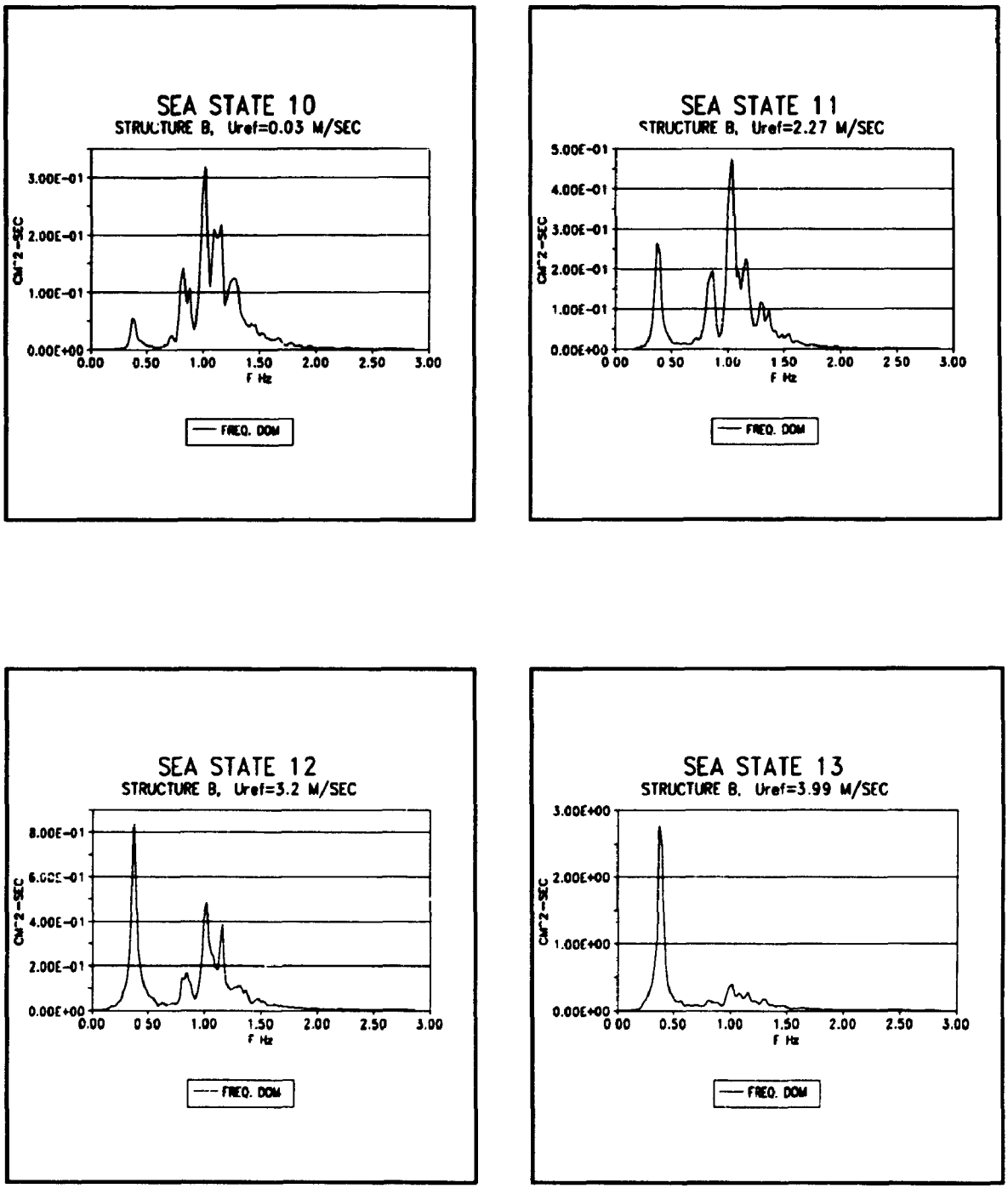

FIGURE H.6: Linearized frequency domain surge response spectra for different mean wind velocities (STRUCTURE B, WAVE STORM 1).

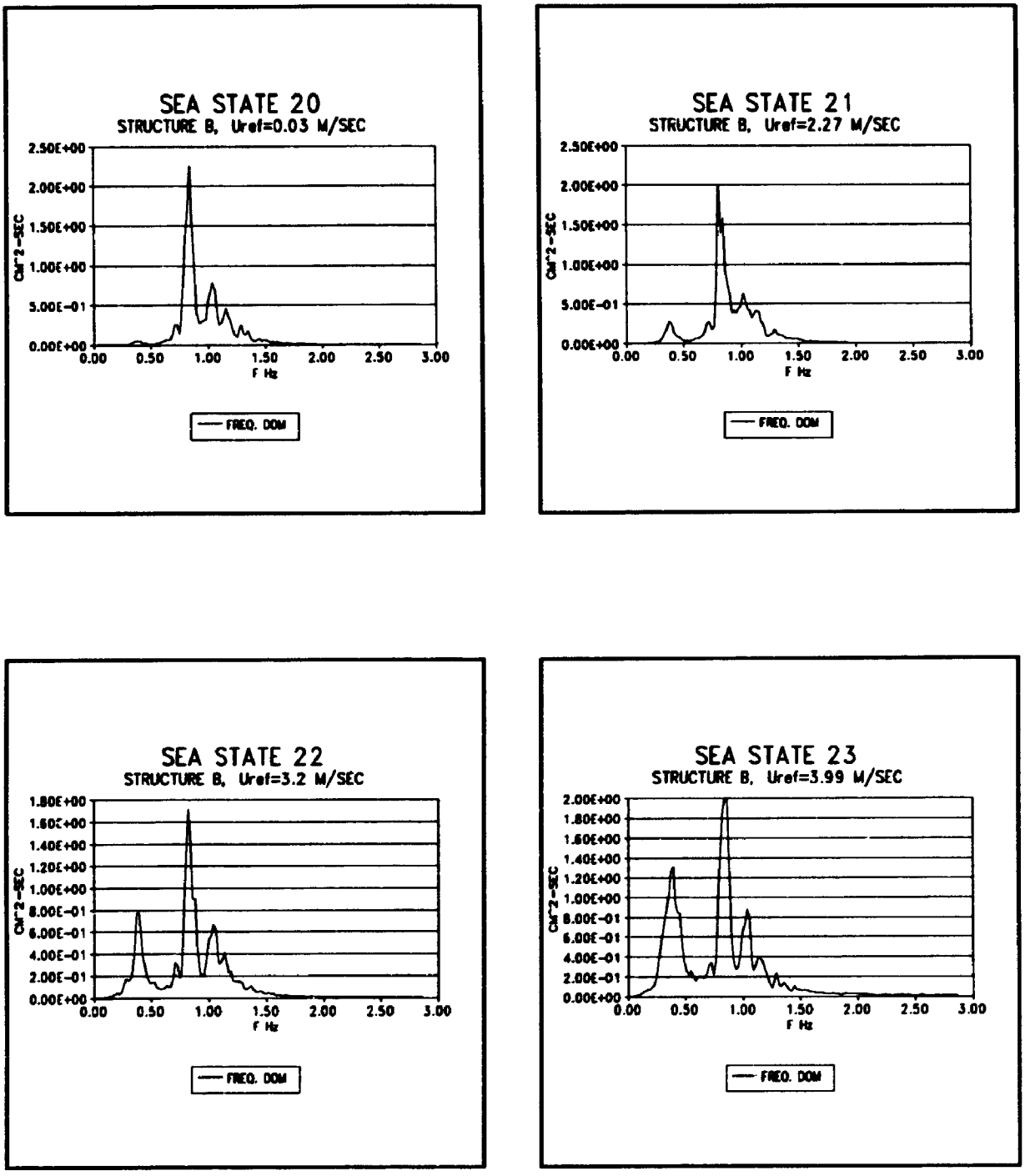

FIGURE H.7: Linearized frequency domain surge response spectra for different mean wind velocities (STRUCTURE B, WAVE STORM 2).

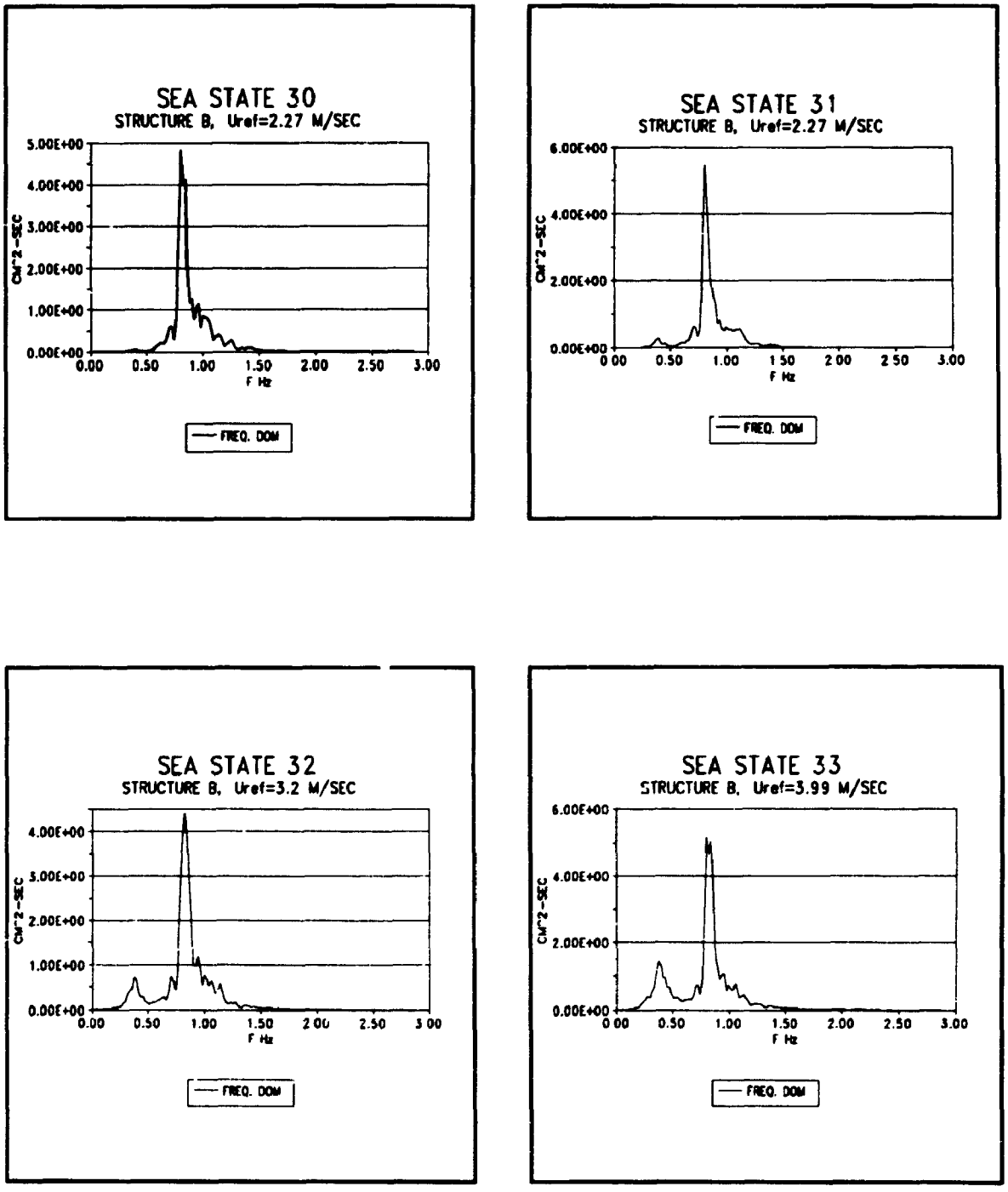

FIGURE H.8: Linearized frequency domain surge response spectra for different mean wind velocities (STRUCTURE B, WAVE STORM 3).

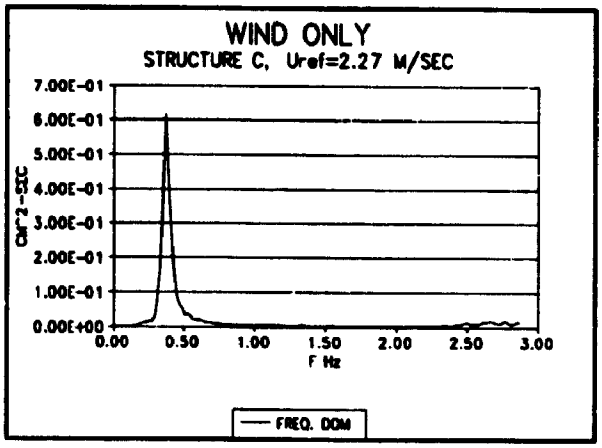

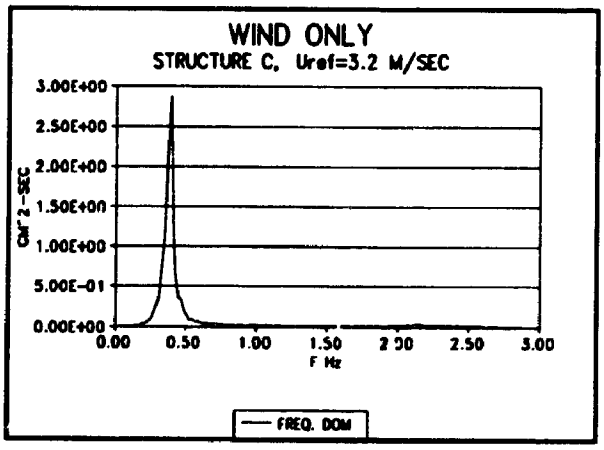

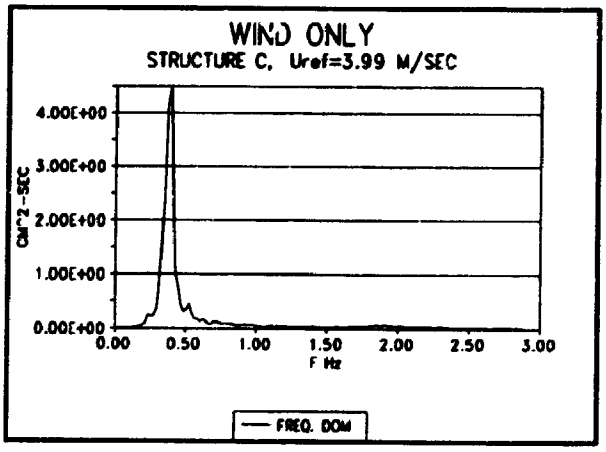

FIGURE H.9: Linearized frequency domain surge response spectra for different mean wind velocities (STRUCTURE C, WIND ONLY).

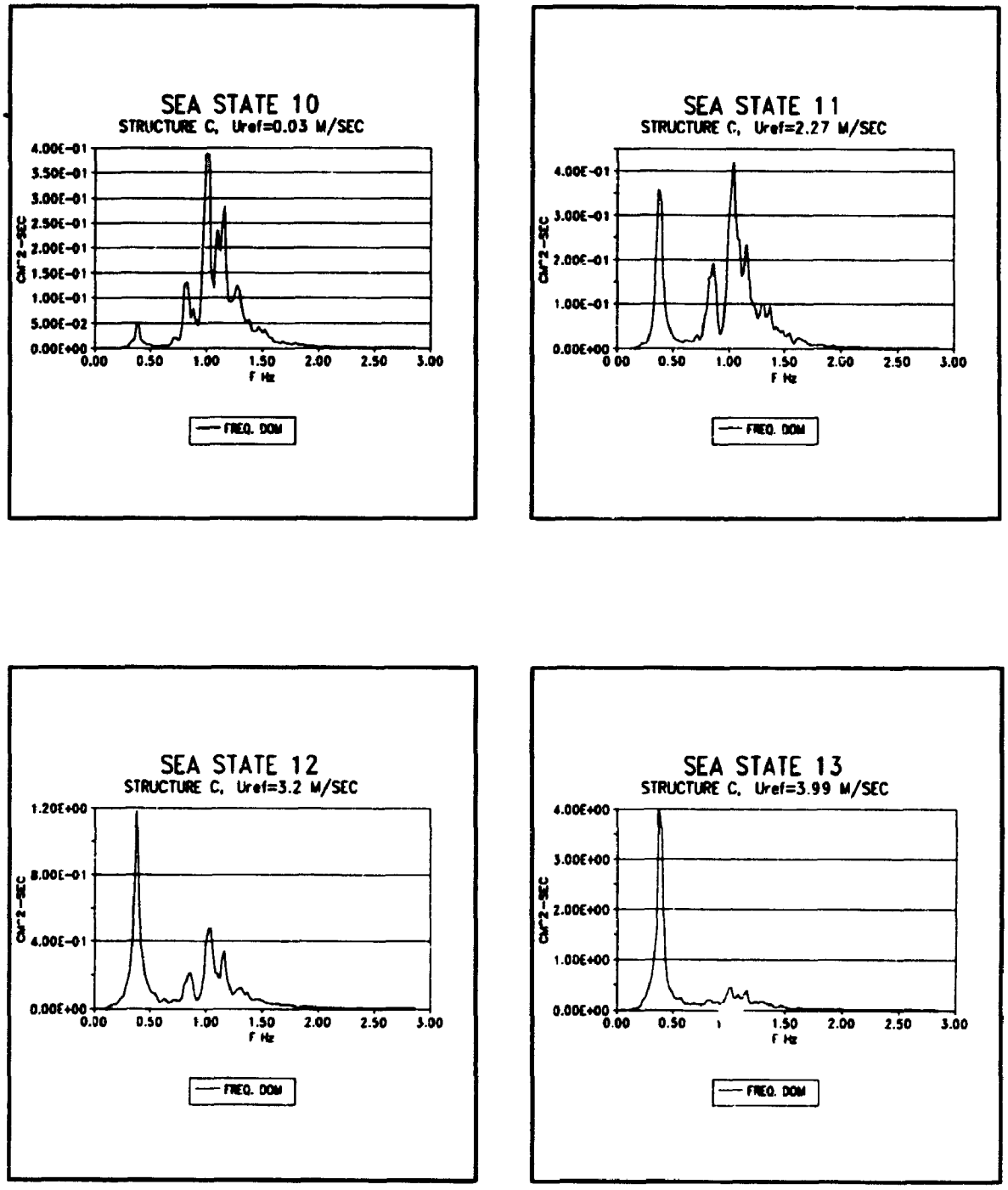

FIGURE H.10: Linearized frequency domain surge response spectra for different mean wind velocities (STRUCTURE C, WAVE STORM 1).

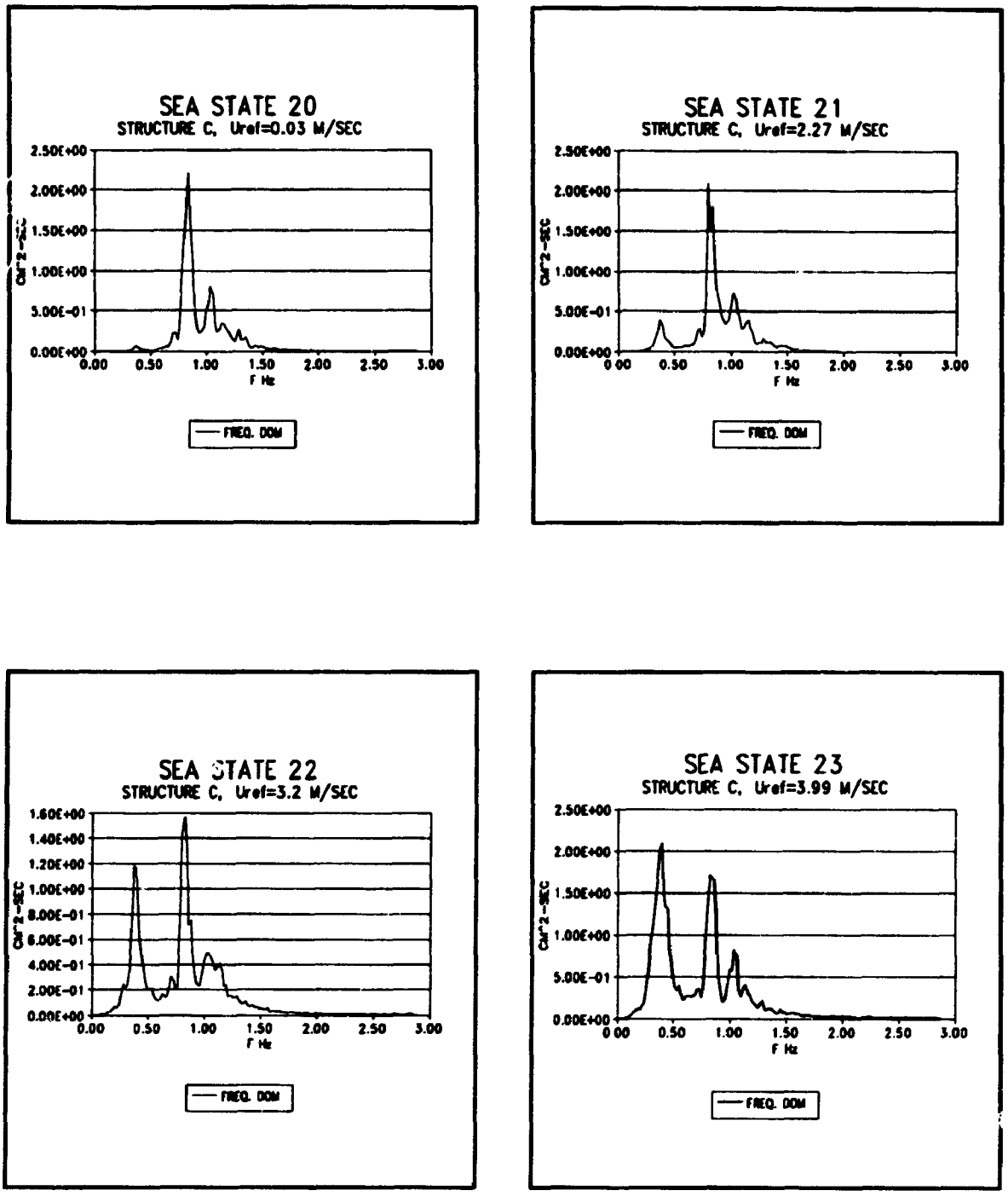

FIGURE H.11: Linearized frequency domain surge response spectra for different mean wind velocities (STRUCTURE C, WAVE STORM 2).

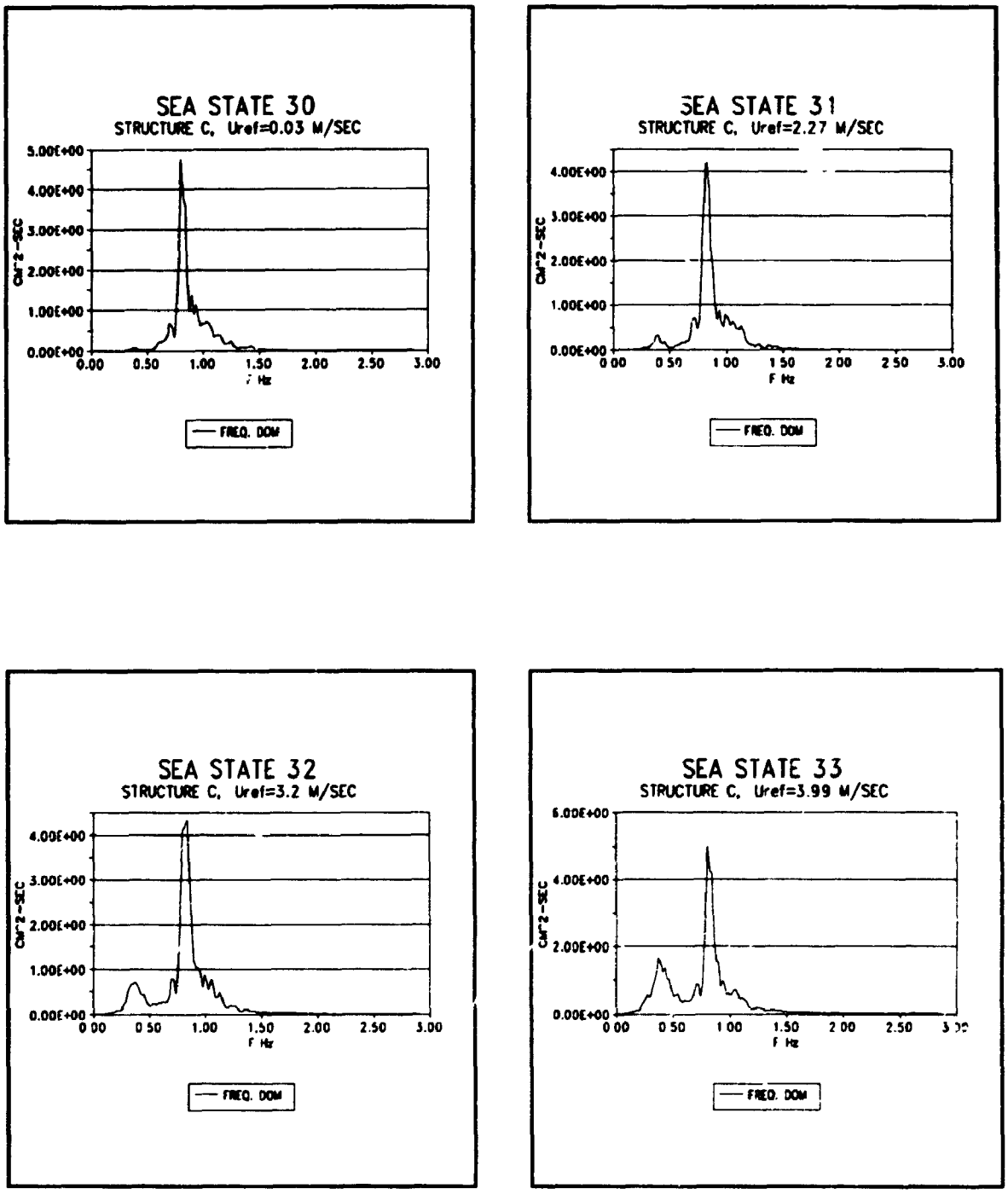

FIGURE H.12: Linearized frequency domain surge response spectra for different mean wind velocities (STRUCTURE C, WAVE STORM 3).

APPENDIX I

WIND PROFILES and SPECTRA

This appendix presents the wind velocity and intensity profiles as well as the typical wind spectra. The profiles for the 'wind only' case were measured at a wind speed of 4.9 m/s. The wind speed in the case of wave storms 1,2, and 3 was 3.9 m/sec.

The wind spectrum shown is the one for the sea state 33 (wave storm 3 and wind speed U=3.9 m/s). The measured spectrum is compared with ESDU (1975, 1985) results.

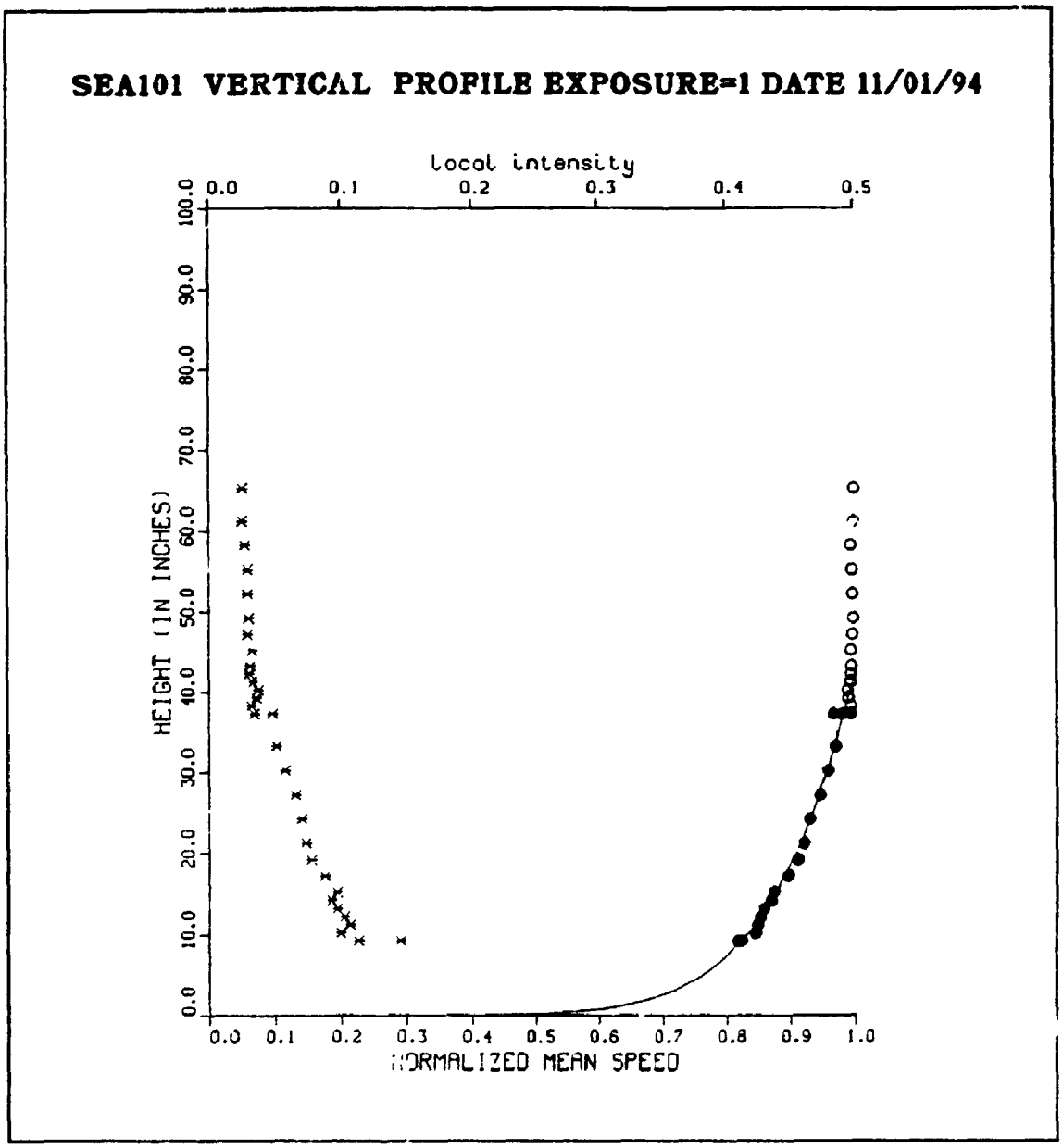

FIGURE I.1: Wind velocity and turbulence intensity profiles for wind only case (U_{ref}=4.9 m/s).

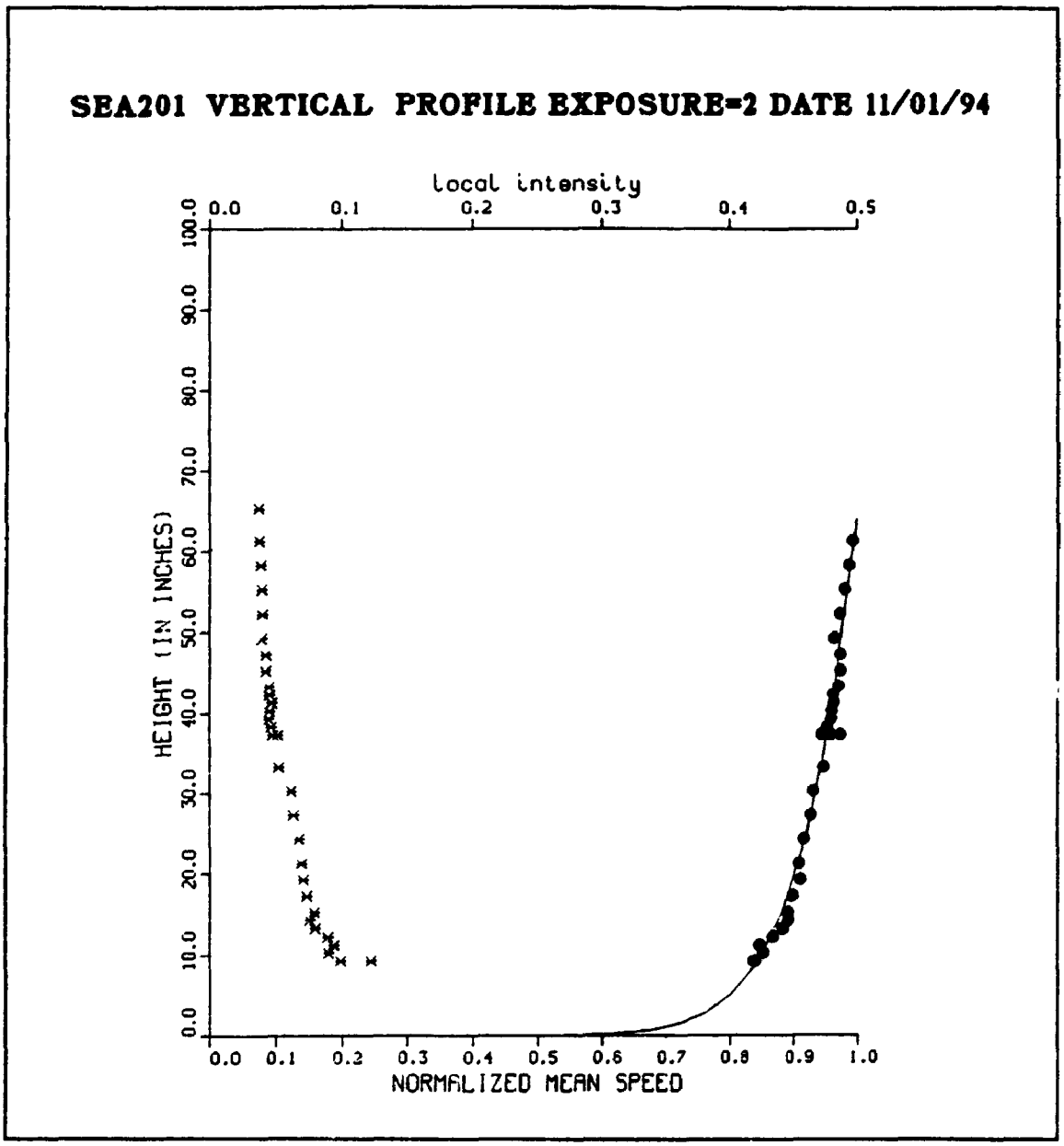

FIGURE I.2: Wind velocity and turbulence intensity profiles for wave storm 1 (U_{ref}=3.9 m/s).

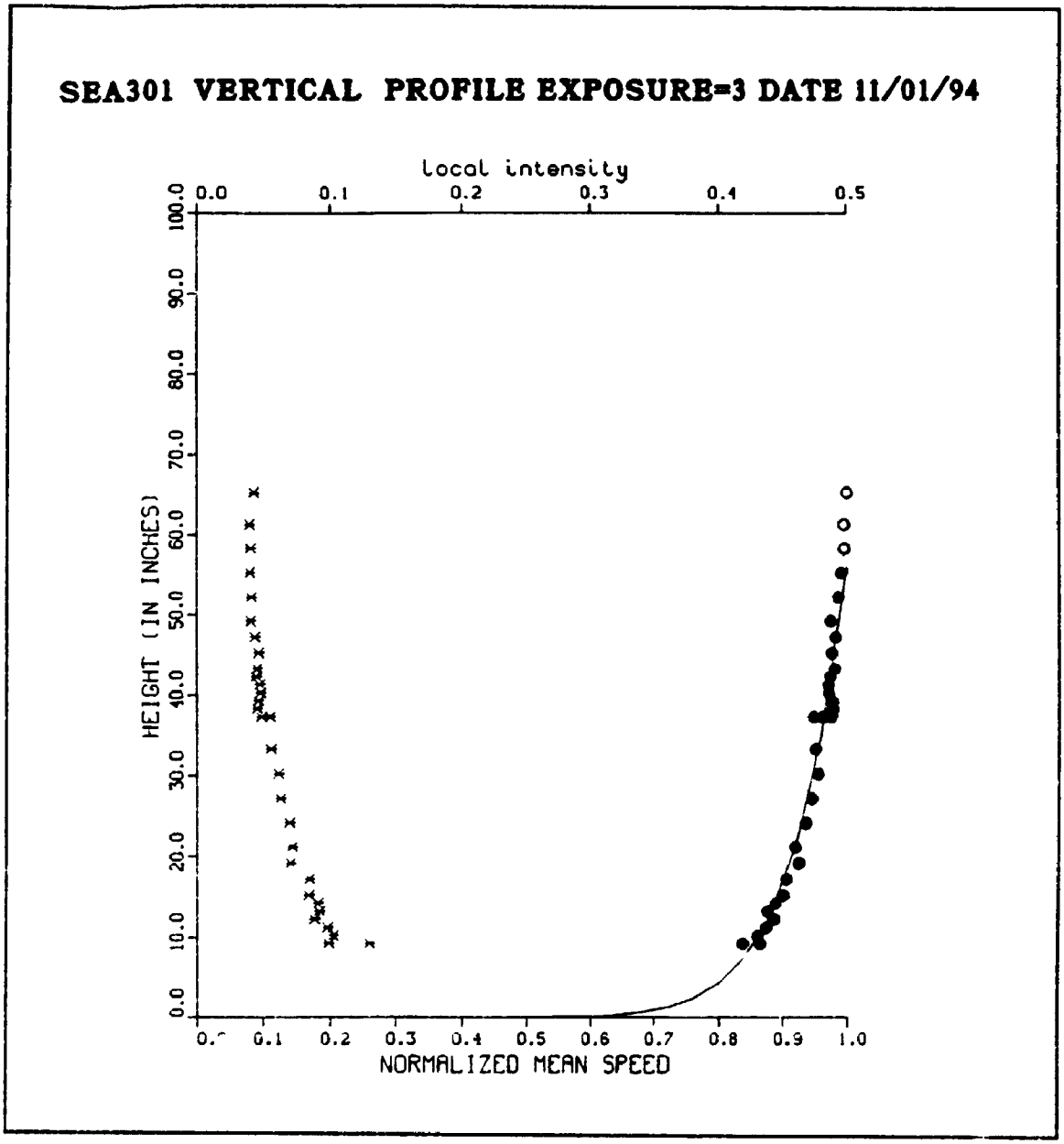

FIGURE 1.3: Wind velocity and turbulence intensity profiles for wave storm 2 (U_{ref}=3.9 m/s).

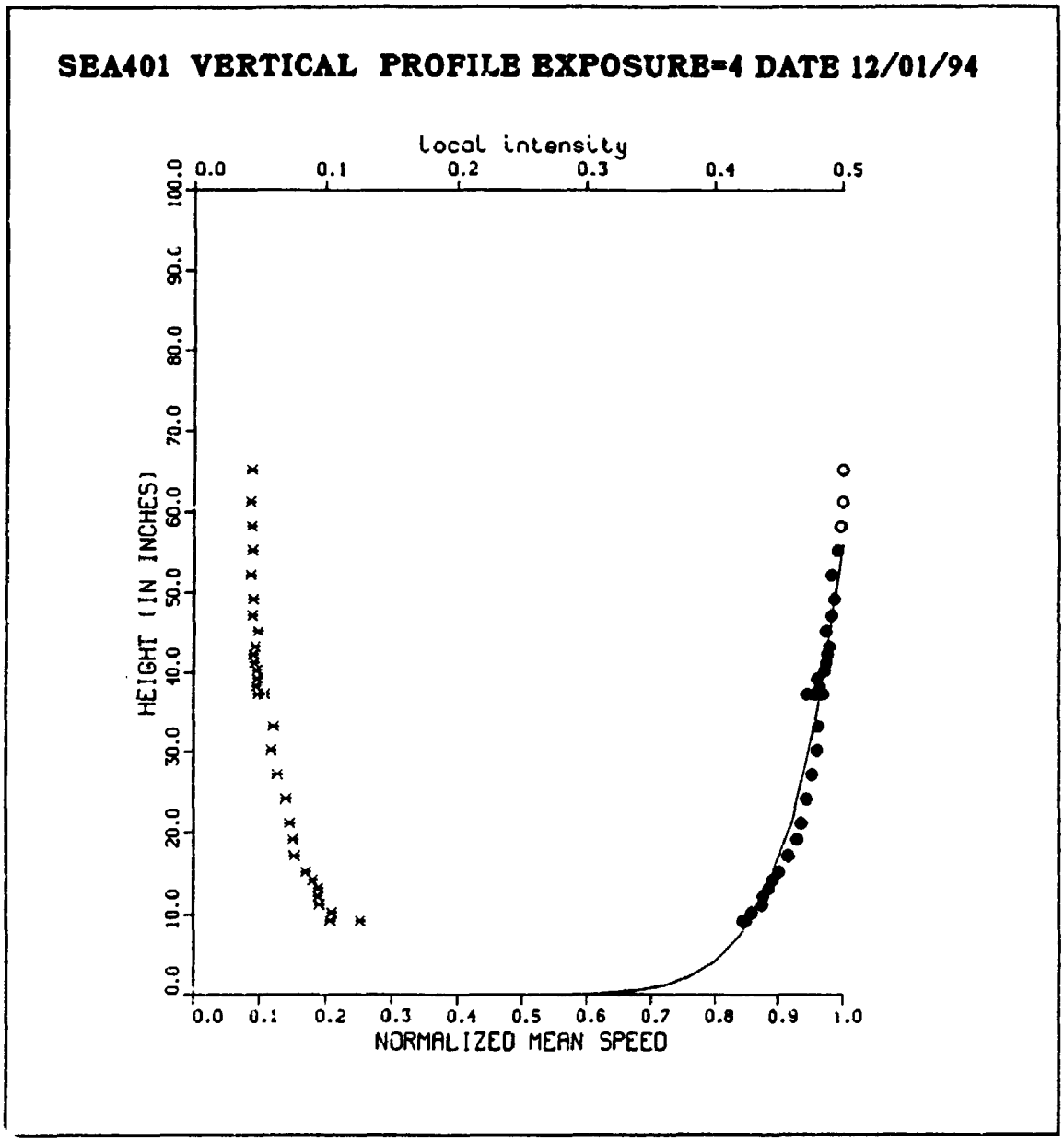

FIGURE I.4: Wind velocity and turbulence intensity profiles for wave storm 3 (U_{ref}=3.9 m/s).

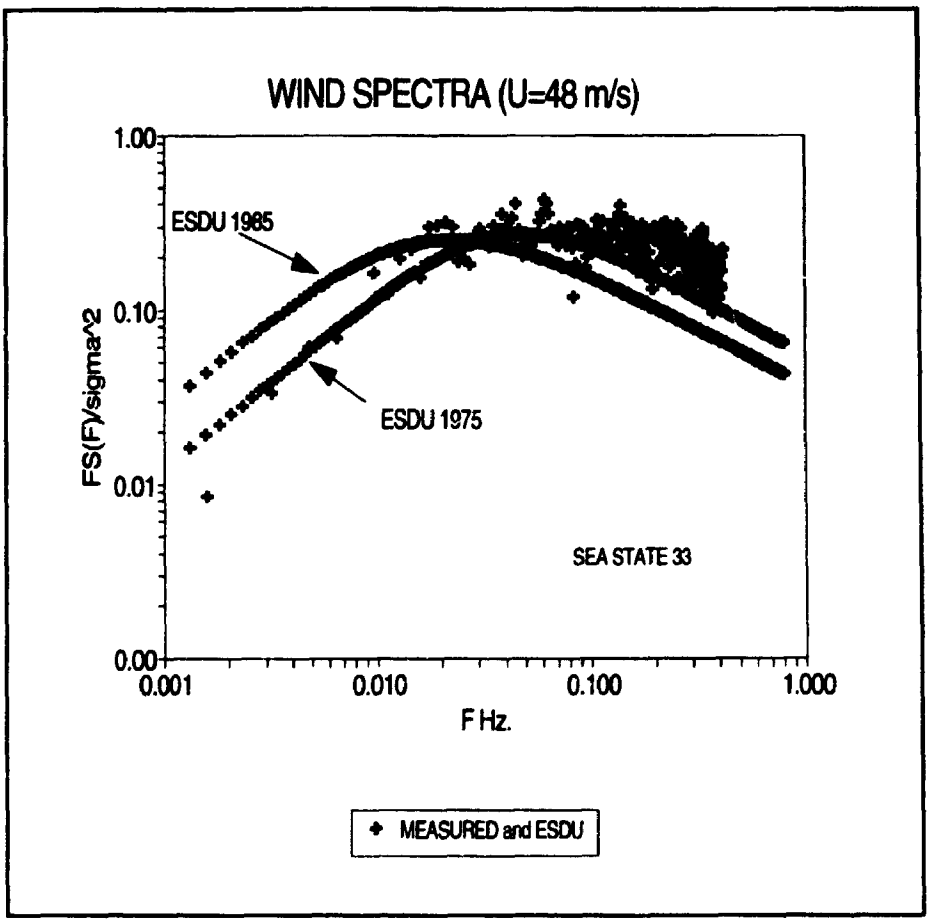

FIGURE I.5: Wind spectra (measured, ESDU 1975, ESDU 1985)

REFERENCES

Amorocho, J., J.J. Devries (1980). A new evaluation of wind stress coefficient over water surfaces. *J. of Geophysical Resor.*, Vol. 85 pp. 433-442.

Anastasiou, K., Tickell, R.G., J.R. Chaplin (1982). The nonlinear properties of random wave kinematics. *Proc. of BOSS'82 Conf.*

Andrier, B.L., Delepine, Y, J. Gauvrit (1986). Roseau: A deepwater compliant platform. *Proc. of OTC.* Houston, OTC 5256.

Barltrop, N.D.P., A.D. Adams, (1991). *Dynamics of fixed marine structures.* Butterworth Heinemann.

Bartel, V., Mansard, E.P.D., Sand, S.E., F.C. Vis (1983). Group bounded long waves in physical models. *J. of Ocean Engg.* Vol 0, No. 4, pp 261-294.

Bearman P.W., Graham, J.M.R., Naylor M.R., E.D. Obasaju (1981). The role of vortices in oscillatory flow about bluff cylinders. *Proc. os int. Symp. on Hydrody. in Ocean Engg.*, Vol. 2, pp 621-635.

Bearman, P.W., Lin X.W, P.R. Mackwood (1992). Measurement and prediction of response of circular cylinders in oscillating flow. *Proc. of BOSS'92 conf.*, London.

Bendat J.S., A.G. Piersol (1986). *Random data, Analysis and measurement procedures.* John Wiley & Sons.

Berge, B., J. Penzien (1974). Three-dimensional stochastic response of offshore towers to wave forces. *Proc of OTC, Houston*, Texas, OTC 2050.

Blevins, R.D., (1977). Flow induced vibration. *Van Nostrand, Reinhold Company.* New York.

Borgman, L.E. (1969). Ocean wave simulation for engineering design. *J. of Waterways and Harbours Div.*, ASCE, Vol. 95, No. WW4.

Borgman, L.E. (1976). Spectral analysis of ocean wave forces on piling. *J. of waterways and harbours Div., ASCE, Vol. 93.*

Bosma, J., H.J. Vugts (1981). Wave kinematics and fluid loading in irregular waves, *proc. of int. symp. on Hydrodynamics in Ocean engg.*, The Norwegian Institute of Technology.

Bostrom, T., T. Overvik (1986). Hydrodynamic force coefficients in random wave conditions. *Proceedings of Int. Symposium on Offshore Mechanics and Arctic engineering*, Tokyo.

Bowers, E.C. (1977). Harbour resonance due to set down beneath wave groups. *J. of Fluid Mech.*, Vol. 79, No. 1. pp 71-92.

Chakrabarti, S.K. (1971). Discussion on 'Dynamics of single point mooring in deep water. *J. of WaterWays*, Harbour and Coastal Eng. Div. ASCE.

Chakrabarti, S.K. (1987). Hydrodynamics of offshore structures. *Computational Mechs. Publication, Springer Verlag.*

Chakrabarti, S.K., D.C. Cotter (1984). Hydrodynamic coefficients of a mooring tower. *J. of Energy Resource Technology*, ASME, Vol. 106.

Chakrabarti, S.K. (1988). Forces on vertical cylinder due to random waves. *J. of Waterway, Port, Coastal, and Ocean Engineering*, ASCE, Vol. 114

Chakrabarti, S.K. (1980). Inline forces on fixed vertical cylinder in waves. *J. of Water Way, Port, Coastal and Ocean Division*, ASCE, Vol. 106.

Chakrabarti, S.K. (1989). Approximate methods in short-term wave response Distribution. *J. of Ocean Engg.*, Vol. 16, No. 4, pp 373-399.

Clough, R.W., J. Penzien (1975). Dynamics of structures. *McGrow-Hill International Book Company.*

Daneshvaran, M.T.S., B.J. Vickery (1994). Hydrodynamic damping of a compliant tower in waves. *Proc. of BOSS Conf.* MIT.

Dao, B.V., J.Penzien (1980). Treatment of nonlinear drag forces acting on offshore

platforms. *Earthquake Engg. Research Center. U.Cal.Ber. Report NO. UCB/EERC-80/13.*

Davenport, A.G., E.C.Hambly (1984). Turbulent wind loading and dynamic response of jackup platform, *OTC*, Houston, OTC 4824

Dean R.G. (1965). Stream function representation of nonlinear ocean waves. *J. of Geophysical Research*, Vol. 70, No. 18.pp 4561-4572.

Davenport A.G. (1961). The spectrum of Horizontal gustiness near the ground in high winds. *J. of the Roy. Meter. Soc.*, Vol. 87, pp 194-211.

Demirbilek, Z., G. Moe, P.O. Yttervoll (1987). Morison's formula: relative velocity vs. independent flow fields formulations for a case representing fluid damping. *Proceedings of Int. Symposium on Offshore Mechanics and Arctic Engineering.*

Engevic L., (1987). A new approximate solution to the surface wave problem, *Applied Ocean Research*, Vol. 9.

ESDU (1985). Characteristics of atmospheric turbulence near the ground. Part III, Variations in space and time for strong winds (Neutral atmosphere) *ESDU*, No. 86010, London, UK.

ESDU (1985). Characteristics of atmospheric turbulence near the ground. Part II, Single point data for strong winds (Neutral atmosphere) *ESDU*, No. 85020, London, UK.

ESDU (1974). Characteristics of atmospheric turbulence near the ground. Part I. Single point data for strong winds (Neutral atmosphere) *ESDU*, No. 74030, London, UK.

Falinsen O.M., B. Sortland (1987). Slow drift eddy making damping of a ship, *Appl Ocean Research*, 9, 1.

Faltinsen O.M. (1990). Sea loads on ships and offshore structures. *Cambridge University Press.*

Foster, E.T. (1970). Model for nonlinear dynamics of offshore towers. *J. Engg. Mech. Div., ASCE, Vol. 96, No. EM1.*

Garrison, C.J. , J.B. Field, M.D. May (1977). Drag and inertia forces on a cylinder in

periodic flow. *J. of Water way, Port, Coastal and Ocean Division*, ASCE, Vol. 103. pp 95-108.

Goda, Y., Y. Suizuki, (1976). Estimation of incident and reflected waves in random wave experiments. Proc. of 15th Int. Conf. on Coastal Engg., Hawaii, USA.

Gudmestad, O.T., J.J. Connor (1984). Linearization methods and the influence of current on the nonlinear hydrodynamic drag force. *J. Applied Ocean Research, Vol. 5, No. 4.*

Garrison, C.J. (1980). A review of drag and inertia forces on circular cylinders. *Offshore Technology Conference*, Houston, OTC 3760.

Gudmestad, O.T., J.J. Connor (1986). Engineering approximation to nonlinear deepwater waves. *App. Ocean Research.* Vol. 8, No. 2.

Gudmestad, O.T., Johnson, J.M., Skjelbrea,J., A. Toerum (1988). Regular water wave kinematics. *Proc. of BOSS'88 Conf.*

Gudmestad O.T. (1990). A new approach for estimating irregular deep water wave kinematics. *J. of Appl. Ocean Research*, Vol 12, No. 1.

Guyan R.J. (1965). Reduction of stiffness and mass. *AIAA J.*, Vol. 3.

Harris R.I. (1990). Some further thoughts on the spectrum of gustiness in strong winds. *J. of Wind Engg. and Indust. Aerod.*, Vol 33 pp 461-477.

Harris R.I., D.M. Deaves (1980). The structure of strong winds. Paper no. 4, *CIRIA Conf. on wind engineering*, London.

Hasselman, K., et al. (1973). Measurement of wind wave growth and swell decay during the Joint North Sea Wave Project (JONSWAP), *Deutschen Hydrographischen Zeitschrift*, Vol 13, No A.

Hogben N. (1976). Wave loads on structures. *Proc. of BOSS'76 Conference.*

Houmb, O.G., T. Overik, (1976). Parametrization of wave spectra and the long term joint distribution of wave heigth and period. *Proc. of BOSS'76*, Trondheim.

Isaacson, M., (1979). Nonlinear inertia forces on bodies. *J. of Waterway Port Coastal and Ocean Div.*, ASCE, Vol. 105, No. WW3.

Judge, P.M. (1991). Experimental measurement of low frequency forces on a slender cylinder. M.Sc. Thesis, *Univ. of Western Ont.*

Kaplan, P (1986). A new interpretation of the Morison wave force. *Proceedings of Int. Symposium on Offshore Mechanics and Arctic engineering, Tokyo.*

Keulegan, G.H., L.H. Carpenter (1958). Forces on cylinders and plates in an oscillating fluid. *J. of Res. Nat. Bureau of Standards*. Vol. 60. No.5.

Kinsman B. (1965). Wind waves their generation and propagation.. Englewood Cliffs, N.J. Prentice-Hall Inc.

Laya, E.J., J.J. Connor, S.Shyam Sunder (1984). Hydrodynamic forces on flexible offshore structures. *J.of Engineering Mechanics*, ASCE, Vol. 110, No. 3.

Lighthill, M.J. (Sir) (1962). Physical interpretation of the mathematical theory of wave generation by wind. *J. of Fluid Mech.* Vol. 14 (3)

Longuet Higgins M.S., R.W. Stewart (1964). Radiation stresses in water waves, a physical discussion with applications. *Deep Sea Research*, Vol. 11, pp 529-569.

Longuet-Higgins, M.S., R.W. Stewart (1961). The changes in amplitude of short gravity waves on steady non-uniform currents. *J of Fluid Mech.*, Vol. 10, pp 529-549.

Malhotra, A.K., J. Penzien (1970). Response of offshore structures to random wave forces. *Proc. of ASCE, J. Struc. Div. Vol 96, No. ST10.*

Malhotra, A.K., J. Penzien (1970). Nondeterministic analysis of offshore structures. *J. of Engineering Mechanics Div. ASCE, Vol. 96, No EM6.*

Mansard, E.P.D. Sand S.E., P. Klinting (1986). Sub and Super Harmonics in natural waves. *Proceedings of Int. Symposium on Offshore Mechanics and Arctic engineering*, Tokyo.

Miles J.W. (1957-1962). On the generation of surface waves by shear flows. *J. of Fluid*

Mech., 1957 Vol. 3, pp 185-204; Vol. 6, pp 568-582 (1959a); Vol. 6, pp 583-598 (1959b); Vol. 7, pp 469-478 (1960); Vol. 13, pp-433-448.

Mo, O., T. Moan (1984). Environmental load effect analysis of guyed towers. *Third Int. Offshore Mech. and Arctic Enging Symp., New Orleans.*

Moan, T., S. Haver (1975). Stochastic dynamic response analysis of offshore platform, with particular reference to gravity type platforms. *Proc. of OTC,* Houston, Texas, OTC 2407.

Moe, G., R.L.P.Verley (1980). Hydrodynamic damping of offshore structures in waves and currents. *Proceeding of the OTC*, Paper No. 3798.

Morison, J.R., O'Brien, M.P., Johnson, J.W. S.A. Schaaf (1950). The force exerted by surface waves on piles. *AIME Trans*, Vol. 189, pp 149-154.

Newman, J.N. (1986). Marine hydrodunamics. *MIT Press.*

Ng, J.Y. (1988). The dynamic response of a deepwater compliant platform. MSc thesis, *Univ. of Western Ontario.*

Ochi M.K. (1982). Stochastic analysis and Probability prediction in random seas. *Advances in Hydroscience*, Vol. 13, pp 217-375.

Ottesen Hansen N.E. (1978). Long period waves in natural wave trains. Report 46, Institute of Hydrodyn. and hydraulic Engg., Tech. Univ. of Denmark, pp 13-24

Paz M. (1991). *Structural Dynamics: theory and computation.* Van Nostrand Reinhold, New York.

Phillips, O. (1957). On the generation of waves by turbulent wind. *J. of Fluid Mech.* 2(5).

Sand, S.E., E.P.D. Mansard (1986). Reproduction of higher harmonics in irregular waves. *J. Ocean Engg.*, Vol. 13, No. 1, pp 57-83.

Sand, S.E. (1982). Long wave problems in laboratory models. *J. of Waterways, Port, Coastal Ocean Div. ASCE*, 108, WW4. pp 492-503.

Sarpkaya, T., M. Isaacson (1981). Mechanics of wave forces on offshore structures. Van Nostrand Reinhold Co. New York.

Sarpkaya, T. (1976). Vortex shedding and resistance in harmonic flow about smooth and rough circular cylinders. *Proceeding of the first BOSS Conference*, Vol. 1, 220-235.

Sarpkaya, T. (1986). Force on a circular cylinder in viscous oscillatory flow at low Keulegan-Carpenter numbers. *J. of Fluid Mech.*, 165, pp 61-71.

Sarpkaya, T. (1976). Inline and transverse forces on cylinders in oscillatory flow at high Reynolds numbers. *Proc. of Offshore Tech. Conf.*, OTC 2533, Houston.

Schwartz, L.W., (1974). Computer extension and analytical continuation of Stokes expansion for gravity waves. *J. Fluid Mech.* 62.

Shiotani, M. (1975). Turbulence measurements at the sea coast during high wind. *J. meter. Soc. Japan*, 53.

Skjelbreia, L., J.A. Hendricksen (1961). Fifth order gravity wave theory. *Proc. of 7th Conf. on Coastal.* Engg. pp 184-196.

Slezak, R.A. 1986. Microcomputer control of spectral conditions in a wave tank. M.E.Sc. Thesis, *Univ. of Western Ontario, London, Ca.*

Taylor, R.E., A. Rajagopalan (1982). Dynamics of offshore structures part II, Stochastic averaging analysis. *J. of sound and vibration, Vol 83*

Taylor, R.E., A. Rajagopalan (1982). Dynamics of offshore structures part I, Perturbation analysis. *J. of sound and vibration. Vol. 83.*

Telionis D.P. (1981). Unsteady viscous flows, New York, Springer Verlag New York Inc.

Thomas, R.G. 1987. The development of a wave absorber for BLWTL II. M.Eng. Thesis. Univ. of Western Ontario, London, Ca.

Vickery B.J. (1982). Wind loads on compliant offshore structures.

Vickery B.J. (1969). On the reliability of gust loading factors. *U.S. Dept. of Commerce,*

National Bureau of Standard Bldg. Sci. series.

Vickery P.J. (1988). Wind and wave loads on a tension leg platform: theory and experiment. Ph.D. thesis, Univ. of Western Ontario. London, Ca.

Vickery, B.J. (1965). On the flow behind a course grid and its use as a model of atmospheric turbulence, *proc. 2nd Australasian conf. on hydraulics and fluid mechanics.*

Vickery B.J. (1983). A wind tunnel investigation of the mean and dynamic loads on an offshore guyed tower drilling platform. Univ. of Western Ontario Engg. Science Research Rep., BLWT-ss18-1983.

Vughts, J.H. Hines J.M R. Nataraja (1979). Modal superposition versus direct solution techniques in the dynamic analysis of offshore structures. *Proc. of BOSS Conf.* London.)

Wang C.Y. (1968). On high frequency oscillating viscous flows, *J. of Fluid Mech. Vol. 32, pp 55-68.*

Wheeler, J.D. (1970). Method for calculating forces produced by irregular waves, *J. of Petroleum Technology*, march. pp 359-367

Williamson, C. H. K (1985). Sinusoidal flow relative to circular cylinders. *J. Fluid Mech., Vol. 155, pp 141-174.*

Wilson E.L. (1977). Numerical methods for dynamic analysis. *Numerical Methods in Offshore Engineering*, Zienkiewicz, O.C., Chap.6, John Wiley & Sons.)

Wu, S.C. J.R. McDermott (1976). The effect of current on dynamic response of offshore platforms. *Proc. of OTC*, Houston, Texas. OTC2540